Effect of Surface Porosity on Tribological Properties of Automotive Al-Si Alloys

by

Md. Aminul Islam

Submitted in partial fulfilment of the requirements
for the degree of Master of Applied Science

at

Dalhousie University
Halifax, Nova Scotia
August 2010

DALHOUSIE UNIVERSITY

DEPARTMENT OF PROCESS ENGINEERING AND APPLIED SCIENCE

The undersigned hereby certify that they have read and recommend to the Faculty of Graduate Studies for acceptance a thesis entitled "Effect of Surface Porosity on Tribological Properties of Automotive Al-Si alloys" by Md. Aminul Islam in partial fulfillment of the requirements for the degree of Master of applied science.

Dated: August 20, 2010

Supervisor: _____

Readers: _____

_____

_____

DALHOUSIE UNIVERSITY

DATE: August 20, 2010

AUTHOR: Md. Aminul Islam

TITLE: Effect of Surface Porosity on Tribological Properties of Automotive Al-Si Alloys

DEPARTMENT OR SCHOOL: Department of Process Engineering and Applied Science

DEGREE: MASc CONVOCATION: October YEAR: 2010

Permission is herewith granted to Dalhousie University to circulate and to have copied for non-commercial purposes, at its discretion, of the above thesis upon the request of individuals or institutions.

Table of Contents

List of Tables

List of Figures

Abstract

Al-Si based alloys are commonly used in the automobile industry due to their superior properties, high strength to weight ratio, corrosion resistance, recyclability, etc. These alloys are fabricated by casting and powder metallurgy techniques in which porosity is a common feature. The presence of pores is accompanied by a decrease in mechanical properties, i.e., a drop in hardness and ductility of the materials. In the present study, an attempt was made to understand the effect of surface porosity on the tribological property. A380M and Al-6wt% Si alloys were used to prepare specimens containing 2.6 to 6.9% porosity via casting and 1 to 6.7% porosity via powder metallurgy techniques, respectively. Dry sliding wear behavior was investigated in the load range 6-20 N against an AISI 52100 bearing steel ball using a reciprocating ball-on-flat configuration at a frequency range of 4-20 Hz for cast and 15 Hz for P/M samples.

List of Abbreviations and Symbols Used

Symbols	Description
A	Area of contact
AA	Aluminum association
A_{A_i}	The area fraction of the porosity of i^{th} field
$\overline{A_A}$	The average area fraction of porosity of the 'n' field
Ar	Real area of contact
AFM	Atomic force microscope
CFH	Cubic feet per hour
dp/dh	Slope at maximum load
E^*	Composite elastic modulus
E_1	Elastic modulus for the Berkovich indenter
E_2	Elastic modulus for test material
EDS	Energy-dispersive spectroscopy
F_N	Normal force
F_T	Tangential force
95% CI	95% confidence interval
% RA	Percent relative accuracy
HIP	Hot isostatic pressing
h_c	Contact depth

h_{max}	Maximum indentation depth
H	Hardness
H_S	Hardness of the softer material
HPDC	High pressure die casting
K	Wear coefficient
MPIF	Metal powder industries federation
P_{max}	Maximum applied load
P/M	Powder metallurgy
PDF	Powder diffraction file
P_g	Equilibrium pressure of dissolve gases
P_s	Pressure drop due to shrinkage
P_{atm}	Atmospheric pressure
P_H	Pressure due to metallostatic head
$P_{s\text{-}t}$	Pressure due to surface tension
ρ_{Green}	Green density of the compact
ρ_{water}	Water density
$\rho_{Sintered}$	Sintered density of compact
S	Standard deviation
τ_i	Shear strength at the interface
τ_{max}	Maximum shear stress
μ_a	Adhesion component of friction

ν_1	Poisson's ratio of Berkovich indenter
ν_2	Poisson's ratio of test material
$Vol\ \%\ porosity$	Volume percentage of porosity
W	Wear volume
XRD	X-ray diffraction

Acknowledgements

The author would like to acknowledge the guidance, words of encouragement and unwavering support offered by Dr. Zoheir Farhat throughout the entirety of this project. The author would like to thank Auto-21 for financial assistance, Magna Powertrain for providing A380M aluminum alloy and Bodycote International for performing HIP experiments. The efforts of Dr. George Jarjoura and Dr. Su-Ling Brooks are greatly appreciated. Furthermore, the author would like to thank Dr. D.P Bishop and Randy Cooke for their assistance with sample preparation. Thanks are also extended to the materials engineering group at Dalhousie University including, Bradley Collier, Winston Mosher, Meisam Shahirnia, Aboulwahab Ibrahim and David Walker. The excellent technical support offered by Mr. Dean Grijm and Mrs. Patricia Scallion is greatly appreciated.

Finally, the author would like to acknowledge the support of his family and friends, who have always been there for him throughout his academic career.

CHAPTER 1 INTRODUCTION

Objectives and Overview

Weight reduction technology has attracted an increasing amount of attention in the global automotive industry due to energy saving and environmental issues. The use of new materials with high strength and low density is the most effective method for automobile weight reduction and thus replacement materials for steel have been widely developed. Among these light materials, Al-Si alloys, the most representative of light metals, are commonly used in the automobile industry due to their enhanced properties. However, the relatively low wear resistance of these alloys as compared to steels has limited their uses in components where high wear resistance is required.

Wear of materials is a complex phenomenon and occurs whenever surfaces come in contact, even in the presence of a lubricant. Friction causes dissipation of energy and wear leads to loss of material and dimension and ultimately limiting the life of components. Wear is affected by many material and environmental variables. In particular, porosity in one, or both, of the sliding pair plays an important role during wear. For cases where material loss might result in lifetime-limiting damage, reducing the overall wear rate is of utmost importance. For designers and engineers, who have to make optimal decisions in situations where tribological considerations are significant, it is crucial to have a sound understanding of the wear process.

Magna Powertrain Inc. is a major supplier for the global automobile industry in the field of powertrain design, development, testing and manufacturing. The company produces double-sided clutch housing for high end automobiles using high pressure die casting process. Their high pressure die cast (HPDC) components are prone to porosity formation which leads to poor tribological characteristics and failures. Such defects can be very costly in high volume production facility. The top view of double sided clutch housing is shown in Figure 1.1. The cavity, as shown in the figure, is known as a piston cavity and the surrounding surface of the cavity is known as the ‘seal surface.’ Porosity in the seal

surface region causes loss of pressure tightness and decreases strength. Figure 1.2 shows how the clutch housing fits within the center support assembly. A piston slides into the piston cavity with a linear reciprocating back and forth motion. Due to the presence of porosity, reciprocating friction between the piston and seal surface creates wear damage, leading to premature failure.

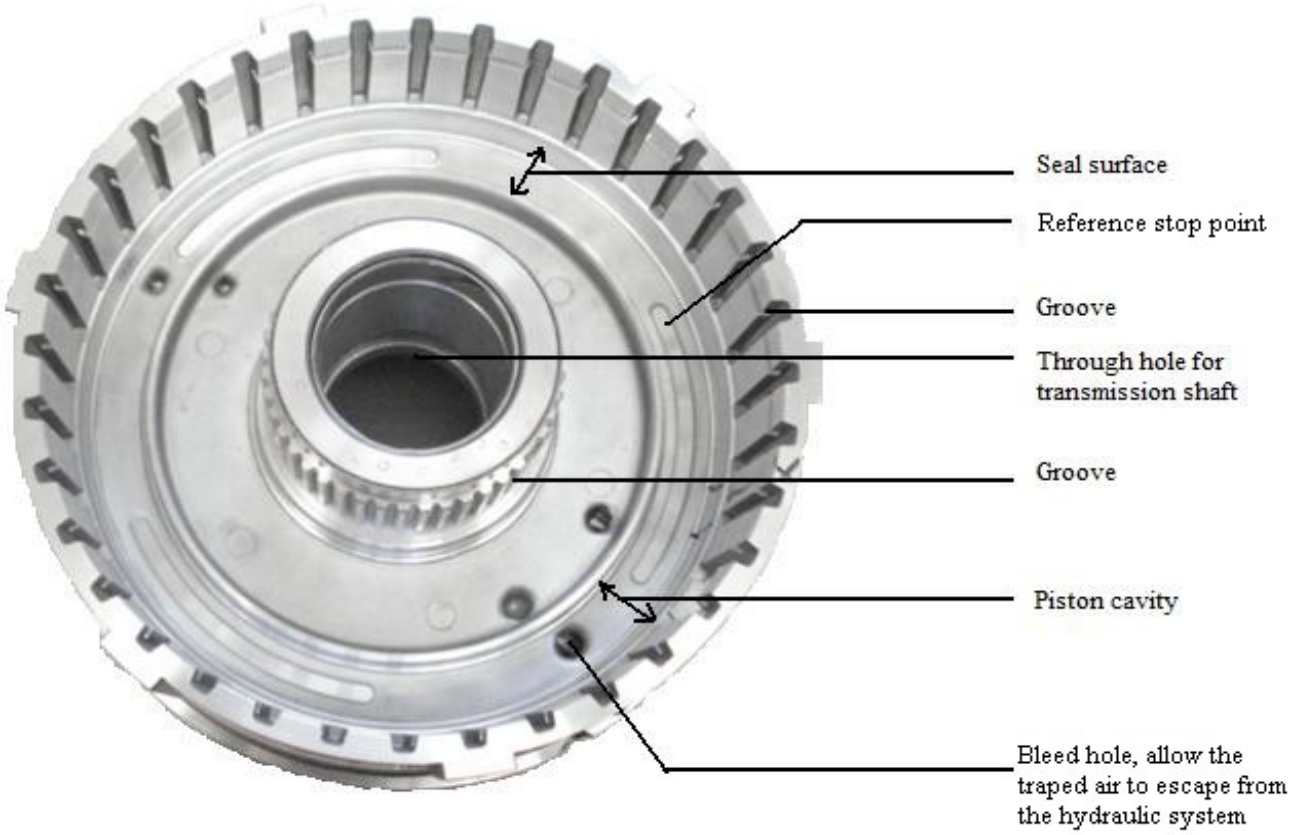

Figure 1.1 Top view of the double sided clutch housing

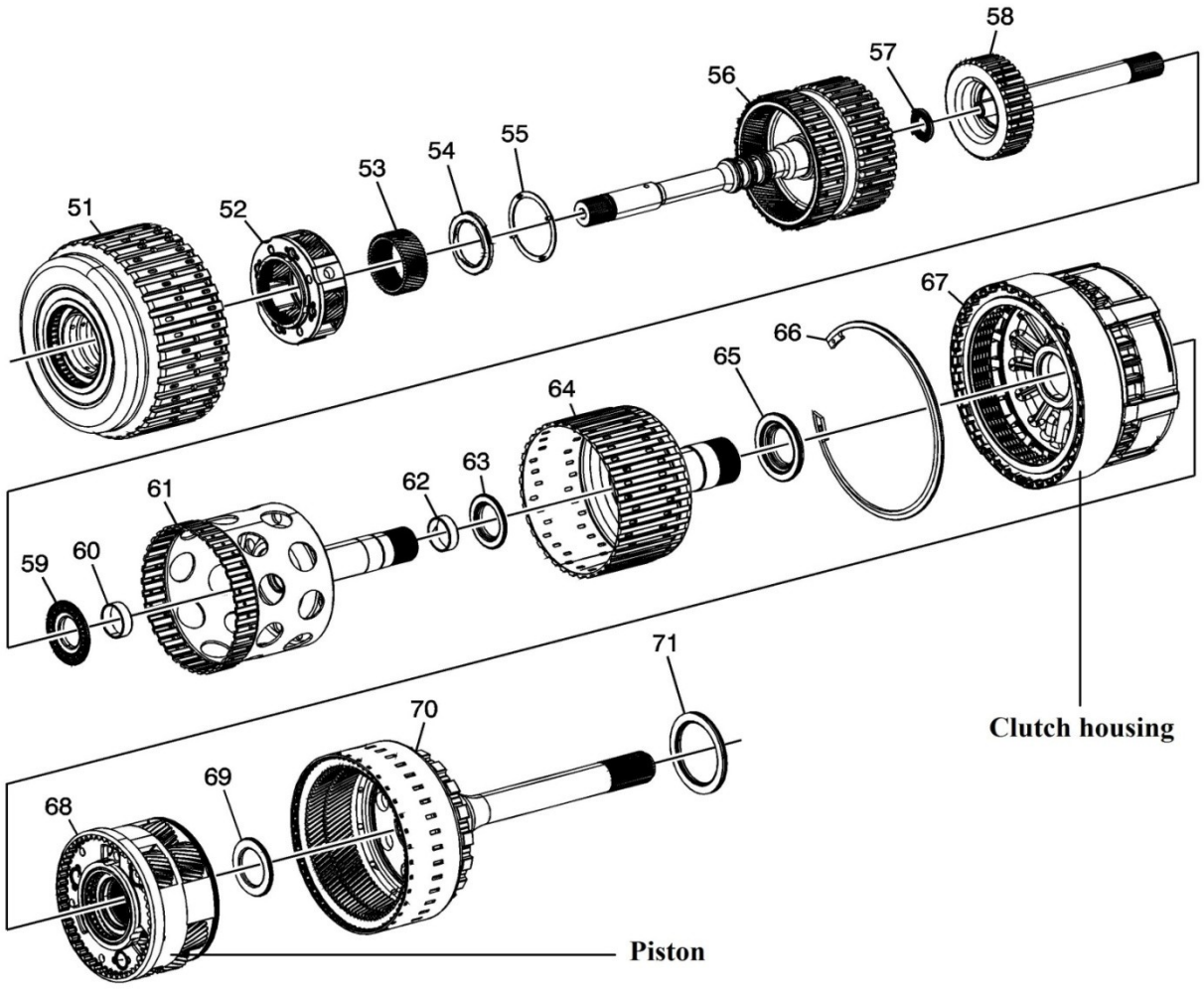

Figure 1.2 Detailed figure of center support assembly (Magna Inc, unpublished work)

In order to mitigate the detrimental effect of surface porosity, it is essential to establish a fundamental and comprehensive understanding of how porosity influences wear. The objectives of this work are:

i. To study the effect of surface porosity on the tribological characteristics of Al-Si alloys.
ii. Assess the effect of hot isostatic pressing treatment (HIP) as means for mitigating the effect of surface porosity.

In order to achieve the objectives of this work, A380M and Al-6 wt% Si specimens with different porosity levels were fabricated and investigated through a series of reciprocating wear tests.

The organizational outline of this thesis is as follows. A review of pertinent background information on fabrication techniques, i.e., casting and powder metallurgy, are provided in Chapter 2. This is followed by an up-to-date review of wear behavior and wear maps of Al-Si alloys and the effect of porosity on wear. Materials and experimental methods used to achieve the research objectives are outlined in detail in Chapter 3. Experimental results and relevant discussions are given in Chapter 4. Conclusions of this research and recommendations for future work are summarized in Chapter 5.

CHAPTER 2 LITERATURE REVIEW

Automakers strive to offer consumers a vehicle with excellent fuel efficiency, reduced emissions and enhanced performance. One of the main strategies adopted to achieve this is to use lighter materials. Because of their excellent strength-to-weight ratio, aluminum-based alloys have emerged as the principal competitor to steel. In enhancing the mechanical properties of aluminum to a level comparable to steel, alloying tends to perform the best. Each alloying element is added alone or in combination with others to achieve the desired properties. Copper (Cu) substantially increases the strength, permits precipitation hardening and reduces corrosion resistance and ductility. Manganese (Mn) and magnesium (Mg) increase strength through solid-solution strengthening and improve work-hardening ability. Silicon (Si) increases strength and wear resistance and, in combination with magnesium, induces precipitation hardening (Mathers, 2002). Thus, alloying has received considerable attention. Aluminum alloys are classified according to their alloying element and are presented in detail in the following sections.

2.1 Specification of Aluminum Alloys

Specifications for aluminum alloy chemistries include the effects of major, minor and impurity elements. Major alloying elements define the ranges of elements that control castability and property development. Minor alloying elements control solidification behaviour, modify eutectic structure, refine primary phases, control grain size and shape, promote or suppress phase formation, and reduce oxidation. Impurity elements influence castability and the form of insoluble phases that at times limit or promote desired properties.

Alloy nomenclature and designation systems for aluminum alloys are not internationally standardized. Many nations have developed and published their own standards. It is convenient to divide aluminum alloys into two major categories: casting composition and wrought compositions. A further differentiation for each category is based on the primary mechanism of property development. Wrought and cast aluminum alloys use different identification systems. The term "wrought aluminum" refers to aluminum alloys that have been mechanically worked to improve the grain structure and physical properties.

Wrought aluminum is in a form of sheet, foil, plate, rod, bar, or tubing and it leaves the mill in an "as formed" condition.

Forming operations, thermal treatments, and/or aging alter the cast ingot metallurgical properties and crystalline structure. This strongly influences the strength, corrosion resistance, and several other properties of the finished product. The aluminum classification numbering system has been established by the American National Standards Institute (ANSI) and the Aluminum Association (AA). This classification system uses an alpha-numeric code to identify major alloying elements and heat treating conditions of the material. The primary alloy groups are designated by a four-digit code. Table 2.1 and Table 2.2 show the wrought and cast alloy classifications, respectively. The first digit indicates the major alloying element. The second digit indicates modifications to the alloy formulation. When a new alloy is first introduced, the second digit is zero. Later, if modifications to the chemical composition are made, a sequential number of 1 through 8 is used to designate the modified alloy. Within the 10xx aluminum group, a zero in the second digit indicates there is no special control on individual impurities. Digits other than zero indicate the number of impurities that are specifically controlled.

In the AA alloy designation, there are four numeric digits, with a period between the third and fourth. First digit refers to the principal alloying constituent while second and third digits refer to specific alloy designation (number has no significance but is unique). The fourth digit is 0, 1 or 2. 0 denotes casting, 1 denotes standard ingot and 2 denotes ingot having composition ranges narrower than but within those of standard ingot (Polmear, 1995). Variation in the composition limits that are too small to require a change in numeric designation are indicated by a preceding letter (A, B, C etc). As for example, 380.0, contains no letter prefix; the first version has an A, e.g., A380.0, the second version has a B and so forth.

Table 2.1 Wrought alloy classification (Aluminium alloy, 2010)

Designation	Major alloying element	Properties
1XXX	99% Al	Ductile, corrosion-resistant and has good formability.
2XXX	Cu	Heat treatable, aging increases strength and hardness.
3XXX	Mn	Increases strength either in solid solution or as a precipitated inter-metallic phase.
4XXX	Si	Most Al-Si wrought alloys are not heat treatable, except 4032 containing 1% Mg and 4145 containing 4% Cu.
5XXX	Mg	Al-Mg are not heat treatable, can be strengthened by cold work (strain hardening) and have moderate mechanical strength combined with relatively high ductility in annealed condition.
6XXX	Mg – Si	Precipitation upon age-hardening forms fine precipitate, increasing strength of these alloys.
7XXX	Zn	Al-Zn alloys containing other elements offer the highest combination of tensile properties.
8XXX	Other element	Al-Li alloys were developed to reduce weight in aircraft and aerospace structures.

Table 2.2 Cast alloy classification (Aluminium alloy, 2010)

Designation	Major alloying element	Properties
A1XX.X	99 % Al	Ductile, corrosion-resistant and has good formability.
A2XX.X	Cu	Good high temperature strength, increases precipitation hardening and reduces corrosion resistance.
A3XX.X	Si alloy with Cu and/or Mg	Low cost. With Cu is heat treatable. Both Cu and Mg increase strength and hardness.
A4XX.X	Si	Moderate strength and high ductility
A5XX.X	Mg	Moderate to high strength and toughness. High corrosion resistance in marine atmosphere.
A7XX.X	Zn	Good finishing characteristics and good corrosion resistance. High strength through natural aging without heat treatment.
A8XX.X	Sn	Developed for bearing applications. Sn imparts lubricity.

2.2 Al-Si Alloys

The composition of alloys determines the potential for achieving specific physical and mechanical properties. The interaction of alloying elements is recognized in promoting desired micro-structural phases and solid solution effects for the development of these properties. The outstanding effect of silicon additions to aluminum and its alloys is the improvement in casting characteristics. The aluminum casting industry is based on aluminum-silicon alloys and their many variations. Binary aluminum-silicon alloys exhibit excellent fluidity, castability and corrosion resistance. However, these alloys display low strength and poor machinability. The strength, ductility and castability of hypoeutectic aluminum-silicon alloys can be further improved by modification of the aluminum-silicon eutectic. Aluminum-silicon alloys exhibit low specific gravity and coefficients of thermal expansion (Tahat, 2010). In hypereutectic aluminum-silicon alloys, refinement of the proeutectic silicon phase by phosphorus additions is essential for casting and product performance.

Among the most widely used aluminum casting alloys are those that contain silicon and copper. The amounts of both additions vary widely, so that copper predominates in some alloys and silicon in others. Copper contributes to strengthening and machinability and silicon improves castability and reduces hot shortness. The addition of magnesium (Mg) greatly increases the response of the Al-Si alloys to heat treatment by forming the Mg_2Si constituent, which, because its solid solubility varies with temperature, permits substantial heat treating effects. The Al-Si-Mg alloys are characterized by excellent castability, good response to heat treatment, and high resistance to corrosion. An Al-Si-Mg-Cu multi-component system produces alloys that, when heat treated and aged, provide an excellent combination of castability and strength. Silicon provides good wear resistance and casting characteristics; copper and magnesium improve machinability and strength on heat treatment (Van Horn, 1967). Alloys containing greater than eutectic silicon concentrations display low specific gravity and elevated temperature strength and are often used in applications requiring a high degree of wear resistance. While wear resistance is usually associated with surface hardness resulting from matrix properties, wear resistance in these alloys results from the presence of a large volume fraction of

hard primary silicon particles in the microstructure. Application of these alloys includes pistons, clutch housings, center support assemblies, cylinder blocks, brake rotors and cylinder liners.

2.3 Powder Metallurgy Processing

Powder metallurgy (P/M) is a metal synthesis technology used to fabricate metal parts in a near- net shape. By definition, P/M is "the art of producing metal powders and utilizing metal powders for production of massive materials and shaped objects" (ASM committee on Definitions of Metallurgical Terms, 1992). It represents an attractive fabrication method for many industries due to inherent advantages such as lowering or in some cases eliminating machining costs, less material wasted in the form of scrap, and the ability to fabricate complex parts. Current P/M processes have been established using a "press and sinter" approach. A typical "press and sinter" P/M process consists of several steps, including raw powder mixing to produce a homogeneous alloy blend, compaction (consolidation) of powder into green compact, and sintering of the compact. A secondary machining operation is then added based on the specifications required of the finished product.

2.3.1 Powder Blending and Mixing

Powders are blended to mix all of the alloying elements to achieve a homogeneous composition. Powder mixing is generally incorporated into P/M processing when a new powder composition is required. Powder mixing may incorporate elemental or pre-alloyed powders. Since pre-alloyed powders tend to be hard, the accurate combination of master alloy powder and elemental powder must be determined to ensure that the powder blend is compactable. It is essential that, during mixing, a lubricant be added. Lubricants prevent the powder blends from cold welding to the metal dies during compaction.

2.3.2 Powder Compaction

Once the desired alloy is blended, it is then compacted. Compaction can be performed using a single action or double action approach. In single action, the compact is pressed from one direction, whilst in the latter, compressive forces are applied in two directions. In some cases, isostatic compression is utilized, where the compact is subjected to

compressive forces from all directions simultaneously. Industrial methods of powder compaction consist of die compaction (Kalpakjian & Schmid, 2003), hot/cold isostatic compaction (Price & Kohler, 1984), direct powder forging and metal injection molding (Erikson & Wiech, 1984).

The most commonly used technique is uniaxial die compaction, whereby powders are loaded and axially compacted in a hard, rigid die made from tool steel or cemented carbide to form “green compact”. An example of conventional uniaxial powder compaction is shown in Figure 2.1. The die provides the cavity into which the powder is pressed and prevents lateral flow while loading is applied through punch motion. Most compaction is performed in a manner such that both the upper and lower punches move. In this regard, the upper punch is retracted during powder filling, while the lower punch remains in the die (the so-called fill position). After filling, the lower punch drops to the pressing position and the upper punch is brought into the die. This aspect of the cycle is termed "under fill" and is used to reduce the amount of powder that is splashed out of the die when the top punch first contacts the loose powder. Both punches are then loaded to generate stress within the powder mass. Finally, the upper punch is removed and the lower punch is then used to eject the compact from the die. The cycle then repeats with a new fill of powder (German R. , 1994).

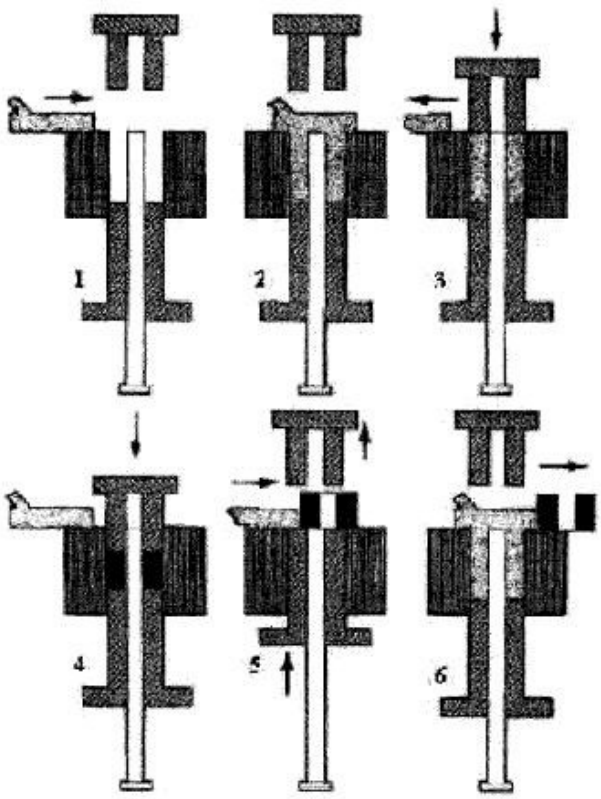

Figure 2.1 Sequence for die compaction (Powder Metallurgy Design Solutions, 1999)

There are several stages of movement that the powder will experience as the punches are inserted and compaction pressure increases. In the first stage, a rearrangement of powder particles to fill the larger voids occurs. In the second stage, localized deformation occurs wherein simple point contacts deform into flatted surfaces. Homogeneous deformation begins in the next stage, where the pores begin to collapse and powders become work hardened. In the final stage of compaction, powder particles are heavily work hardened and act as a solid, incompressible body. Particles undergo appreciable strain hardening, making it increasingly difficult to compact to a higher density (Helwiget al., 2009).

The largest problem encountered in uniaxial die compaction is the occurrence of die wall friction. Die wall friction causes the applied pressure to decrease with the depth traveled into the powder bed. The consequence of this is that the green body density is non-uniform. Both single action (pressure applied from one side only) and double action

(pressure applied from both sides) compaction experience this problem. In the former the density is greatest near the applied load and decreases as the distance from the load increases. Double action compaction causes the density of the green body to be highest at both punch faces and lowest at an intermediate point termed the density split (German R. , 1994) (Figure 2.2).

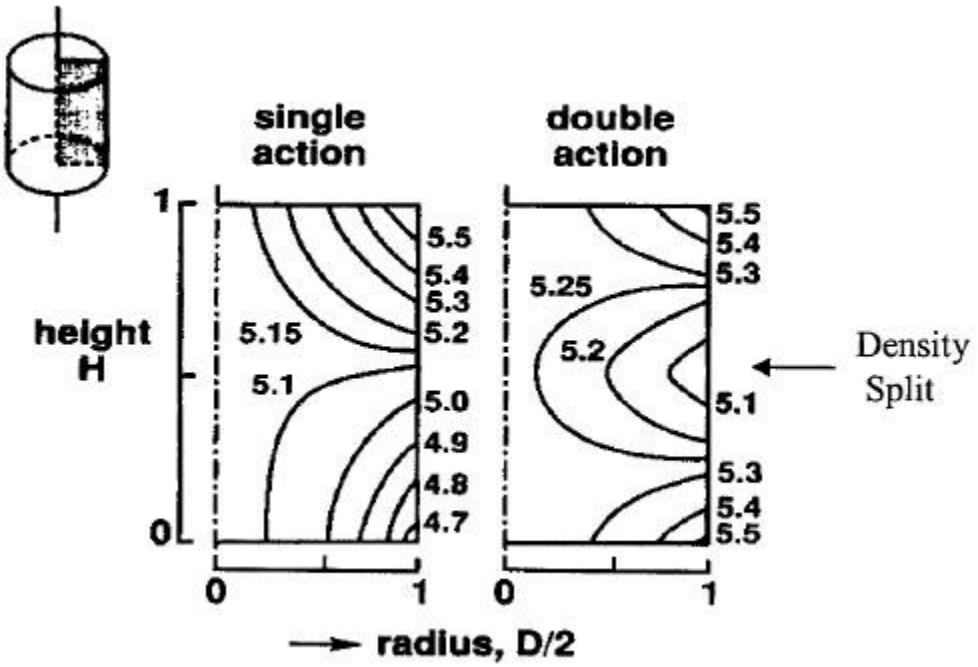

Figure 2.2 Density profile in single action and double action compaction (German R. , 1994)

2.3.3 Sintering

Once green bodies of an appropriate density and geometry have been compacted, they are sintered in a controlled atmosphere. Sintering is a thermal process which increases the strength of a powder mass by bonding adjacent particles via diffusion or related atomic level events. In this, the diffusion amongst adjacent powder particles and alloy additions result in the formation of strong inter-particle bonds which improve mechanical properties. When sintering reactive metals such as Al, an essential consideration is the surrounding atmosphere. In order to avoid any deleterious reactions with oxygen that may impede densification, inert or reducing atmospheres are frequently used (Schaffer & Hall, 2002).

When green bodies are heated, the compact will attempt to reduce its energy by lowering its overall surface area. To accomplish this, a variety of thermally-activated mass transport mechanisms engage to form necks between adjacent particles. Such mechanisms are commonly divided into the categories: surface-transport and bulk transport. Surface transport involves the migration of atoms from one surface to another and can be accomplished by evaporation/condensation, surface diffusion, or volume diffusion (German & Munir, 1975). Conversely, bulk transport involves the migration of atoms from the bulk central mass of a particle to a surface. This can be accomplished by volume diffusion, grain boundary diffusion, or plastic flow (German & Munir, 1975).

From a practical perspective, the two most significant factors in sintering are sintering time and temperature, with the latter being regarded as the most important variable. Particle size, compact porosity, and powder type (elemental or master alloy) also influence sintering response. The majority of P/M materials are sintered in a solid-state manner at approximately 0.6 to 0.8 of the absolute melting point (or solidus) of the material. While sintering proceeds, the micro structure changes considerably as the temperature is increased and the time prolonged. The associated evolution sequence can be broken down into three key stages – initial, intermediate and final.

The initial stage is primarily focused on the growth of sinter bonds (necks) that form between the contacts that exist in green compacts. Although all mass transport mechanisms are involved at this stage, the lower temperature mechanisms of evaporation-condensation and surface diffusion are also important. Vapour flows into the neck due to the vapour pressure difference and atoms diffuse to the neck in response to the locally high concentration of vacancies that exist. The respective size and shape of the pore is an important gauge in assessing the stage or degree of sintering. In the initial stage, the porosity is coarse and shows only slight rounding. The strength of a sintered product after initial stage will be very low and is said to be "under sintered". The intermediate stage is generally the most important of the three as it governs the extent of densification and largely determines the properties of the sintered product. This stage is characterized by simultaneous pore rounding, densification and grain growth. Since the curvature gradients are largely eliminated during the initial stage of sintering, the driving force for

continued sintering becomes the elimination of surface area energy through changes in the pore structure. At this stage the pores can be thought of as cylindrically-shaped regions with a high concentration of vacancies. Consequently, vacancies diffuse away from pores, while a corresponding flux of atoms (mass) flows into them. This reduces the amount of porosity and surface area contained within the compact and is manifested as densification. The cylindrical pores eventually pinch-off into smaller, highly rounded pores that are located at grain boundary intersections.

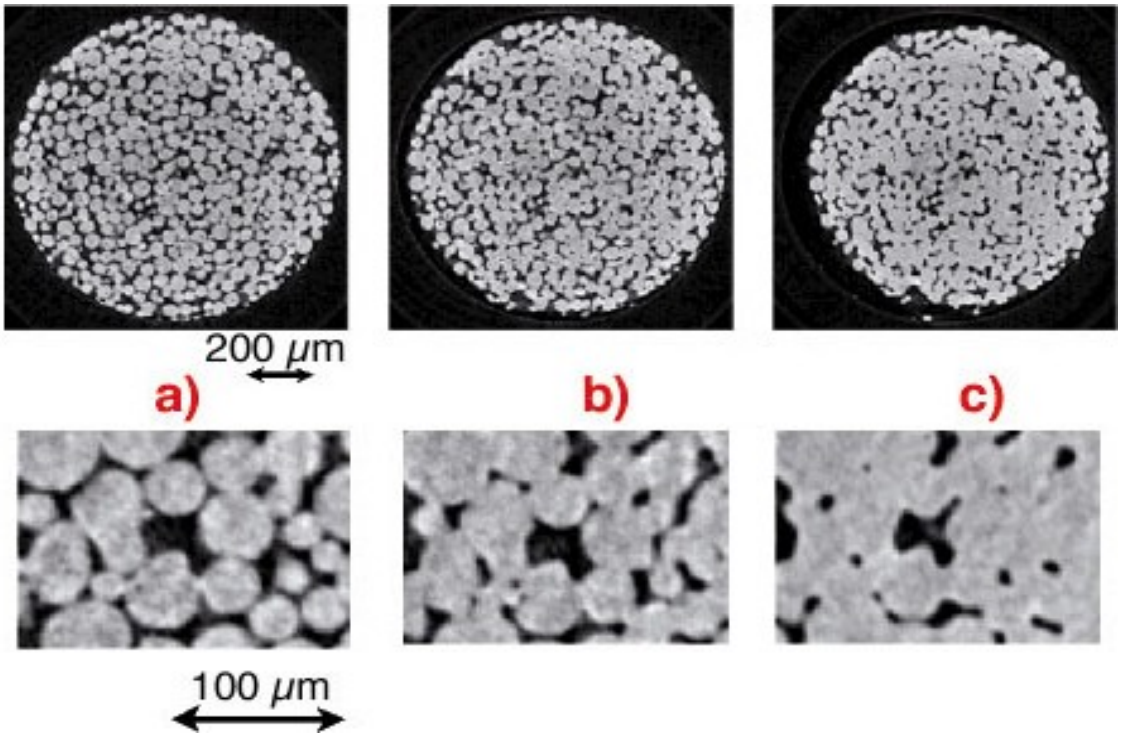

Figure 2.3 Different stages of sintering, (a) initial stage, (b) intermediate stage, (c) final stage (ESRF, 2006)

At this point, the third "final stage" of sintering begins. When compared to the initial and intermediate stages of sintering, the final stage is a very slow process and is rarely attained in commercial applications for P/M. The final stage of sintering commences when closed, highly rounded pores exist at grain boundary intersections. The driving force for continued densification in the final stage is exclusively the reduction of surface area of atoms and surface energy. Densification and creep occurs by grain boundary diffusion (Riedel, et. al, 1994). Since much of the surface area is eliminated in the

preceding stages, the relative magnitude of the driving force has diminished greatly. In order to attain further improvements in densification and strength during this stage the interaction between grain boundaries and porosity must be examined.

The presence of porosity in the compact is common in the P/M process. Energetically speaking, pores are bound to grain boundaries because they lower the grain boundary area and thus the overall energy of the sintered compact. As the sintering process continues, the porosity and the binding energy of the pore-to-grain boundary diminish. In this scenario, the pores can eventually break free from grain boundaries by two mechanisms. One possibility is attributed to increased grain boundary mobility. This occurs at higher sintering temperatures and longer times such that the grain boundaries move faster than the pores and eventually break free (Figure 2.4). A second possibility is Ostwald ripening. In essence, this means that large pores will grow at the expense of smaller ones. For this to occur at an appreciable rate, the pores must lie along grain boundaries which act as paths for rapid diffusion. However, if grains grow too quickly the pores will become separated from the grain boundaries. From a practical perspective, once pores break away from grain boundaries by either mechanism, densification stops at this point.

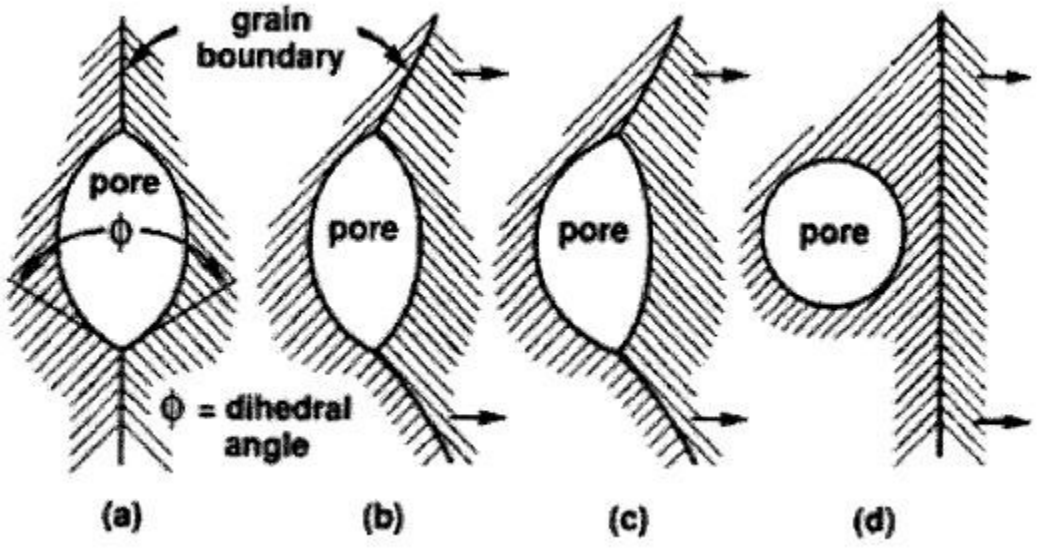

Figure 2.4 The sequence of steps leading to pore isolation and spheroidization in the final stage of sintering via grain boundary mobility (ESRF, 2006)

2.4 Casting

Initially, aluminum alloy was cast using processes that historically have been used for other metals. The relatively attractive engineering properties of aluminum, such as low melting point and ease of castability, quickly led to developments that broadened the means by which engineered shapes could be produced from molten metal. There is a large number of casting processes, and each imposes different rates of heat extraction, solidification rates, and means of compensating for solidification-related microstructural tendencies. Many factors influence the selection of a casting process for producing a specific part. Process selection is strongly influenced by part requirements that are often the basis for defining alloy candidates that in turn influence the range of process choices. The most important process selection criteria are: requirements for fluidity, resistance to hot tearing, minimization of shrinkage tendencies, volume, productivity, process yield, material costs, tooling costs, cost of machining, welding and heat treatment (Kaufman & Rooy, 2004). Many aluminum alloy castings can be produced by any of the available methods. In most cases, dimension, design features and material property requirements limit the range of candidate processes. Compromises in specified criteria are made to facilitate the use of the most cost effective process.

High-pressure die casting (HPDC) is the trendy method for producing aluminum parts. Because of their excellent dimensional accuracy and smooth surfaces, most HPDCs require no machining except the removal of flash around the edge and possible drilling and tapping holes. High-pressure die casting production is fast and inexpensive relative to other casting processes. Aluminum is used in 80-90% of the HPDC alloys available in the world today (Mukhopadhyay, 2007). In the process, molten metal (aluminum) is injected under pressure into water-cooled dies. Pressure is maintained until the part has solidified (Asensio-Lozanoa & Suárez-Peña, 2006). Molten metal usually enters the mold by the action of a hydraulic ram in a containment chamber (shot chamber), resulting in rapid filling of the mold cavity. There are two variants of the die-casting machine: cold chamber and hot chamber. In cold chamber die casting, a metered quantity of metal is poured into the shot sleeve and injected into the die at 5-500 MPa pressures by a piston. When the metal has solidified, the die is opened and the casting is ejected. A typical

working principal of cold chamber die casting is shown in Figure 2.5. The principals of directional solidification and gravity-based gating and risering are essentially inapplicable to die casting. Gates and runners are used to convey metal from the shot chamber to the die cavity. Geometrical considerations are observed to minimize turbulence, air entrapment and fragmentation of the metal stream. Techniques are used to intensify pressure during the solidification phase to decrease the volume fraction of internal porosity.

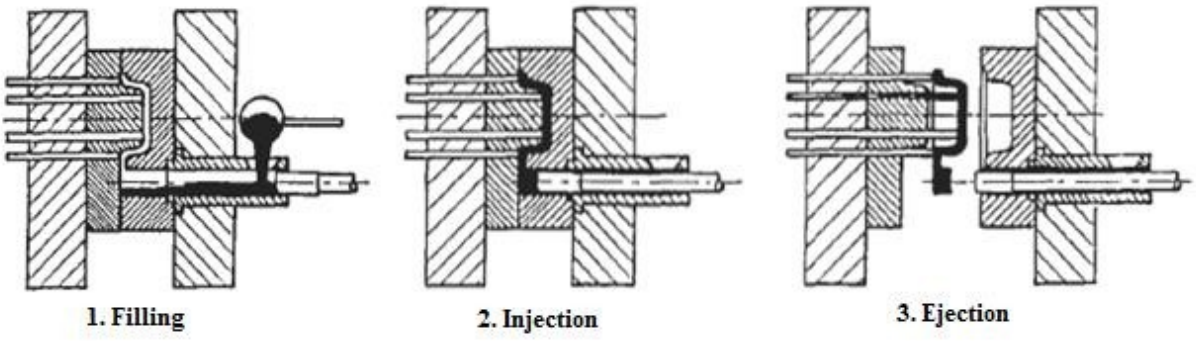

Figure 2.5 Working principles of horizontal cold chamber high-pressure die casting machine (EAA, 2009)

In hot chamber die casting (Figure 2.6), the shot tube is located below the surface of a reservoir of liquid metal and fills automatically when the plunger is withdrawn. This greatly increases the rate of production and, presumably, reduces defects caused by chill in the shot tube. The hot chamber machine is simple, easy to operate, and permits even higher production rates than the cold chamber machines. It operates at lower pressures and is particularly suitable for thin-walled castings in magnesium alloy and the lower aluminum content zinc alloys. Aluminum and the higher aluminum content zinc alloys attack the parts of the machine with which they come in contact; consequently, they are not really suitable for hot chamber high-pressure die casting.

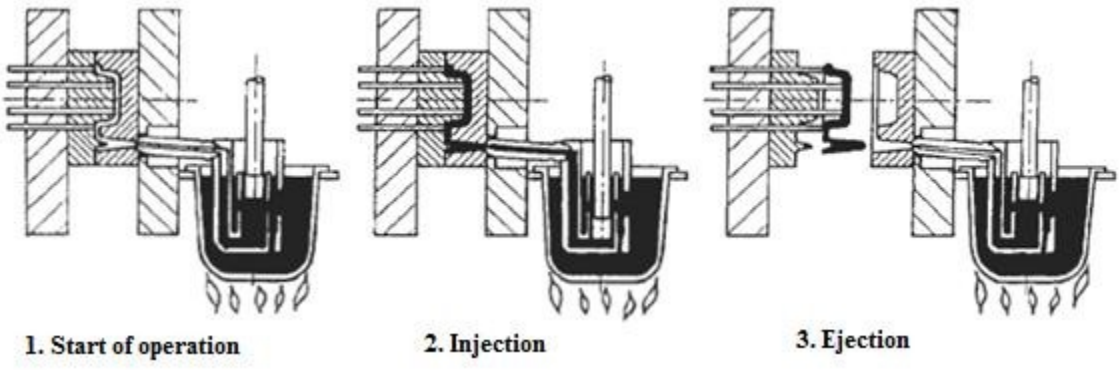

Figure 2.6 Working principles of piston-operated hot chamber high-pressure die casting machine (ODC, 2004)

Alloy compositions of cast and wrought aluminum are parallel in many respects. Hardening and desired properties are achieved through the addition of alloying elements and heat treatment (Kaufman & Rooy, 2004). Since work hardening plays no significant role in the development of casting properties, the use and purpose of some alloying elements differ in casting and wrought alloys. Castability is the most important consideration in differentiating wrought and casting alloy compositions. For pressure die casting, the criteria of castability are resistance to hot cracking, fluidity, die soldering and surface finish. Fluidity is a complex function that can be quantified and strongly affected by temperature above the liquidus or degree of super heat. Improved fluid characteristics are usually associated with narrow solidus-liquidus ranges and in greater percent liquid at the eutectic temperature. The tendency for solidification and post solidification cracking is dominated by element effects on elevated temperature strength and on solidification rate. The casting alloys used in greatest volumes contain silicon. Solidification results in shaped casting are improved by fluidity, elevated temperature resistance to cracking and feeding characteristics that sufficient amounts of silicon impart (Kaufman & Rooy, 2004). The optimal concentration of silicon depends in part on the casting process. Feeding, the compensation for internal shrinkage also varies as a result of gradients in the solidification zone that are process controlled. In general, castability is associated with alloys of reduced solidification range.

2.4.1 Porosity in Al Casting

Porosity is the most common defect in Al casting and is the major cause of rejection. Porosity is the term used to indicate voids or cavities that form within a casting during solidification. It is often the cause of degraded mechanical properties in rejected casting, including limited strength and ductility, variable fracture toughness, irregular crack initiation and propagation characteristics, and lack of pressure tightness (Boileau & Allison, 2001; Sigworth, et. al 1994; Kim, et. al 1997). Porosity in aluminum is caused by the precipitation of hydrogen from liquid solution or by shrinkage during solidification, and more commonly by a combination of these effects. Blow holes, entrapped gas and mold reactions also result in porosity that adversely affects mechanical properties as well as physical acceptability. Nonmetallic inclusions entrained before solidification influence porosity and mechanical properties.

2.4.1.1 Types of Porosity

The solidification condition determines the structural features that affect the physical and mechanical properties of an alloy. When the first metal injected into the die cavity, rapid freezing causes the formation of so-called 'skin' having a thickness of 0.1-0.2 mm (Kiuchi & Kopp, 2002). Spherical gas porosity, interdendritic porosity and 'flow line' porosity can be found between the skin and the central region of the casting. Depending on the origin, porosity in high-pressure die castings is usually classified as:

a. shrinkage porosity,
b. gas porosity,
c. flow porosity.

The affinity for the formation of shrinkage porosity is related to both the liquid/solid volume fraction at the time of final solidification and the solidification temperature range of the alloy. Shrinkage occurs during solidification due to volumetric differences between liquid and solid states. Shrinkage porosity occurs when the gate area (from which the molten metal is injected into the die cavity) solidifies before solidification in other areas of the casting is completed (since in this case, the passage for molten metal to feed the shrinkage due to solidification is cut off) (Tian, et. al 2002). Thermal conditions of the

die (dictated by its water cooling system, the spray settings, the thermal conductivity of the die material, the cycle time, etc.) and the temperature of the molten metal are the major factors affecting the amount of shrinkage porosity for a given alloy composition and casting geometry. A typical example of shrinkage porosity is shown in Figure 2.7 (a). Gas porosity is caused mainly by trapped air, steam and burning products of organic lubricants used in the shot sleeve. Two features of conventionally produced HPDCs are the extreme turbulence experienced by the molten metal as it is forced at high speed into a die, and the very rapid rate at which it then solidifies (Lumley, et. al 2008). Because of this, castings usually contain internal pores in which gases such as air, hydrogen or vapours formed by the decomposition of organic die wall lubricants are entrapped. An example of gas porosity is shown in Figure 2.7 (b).

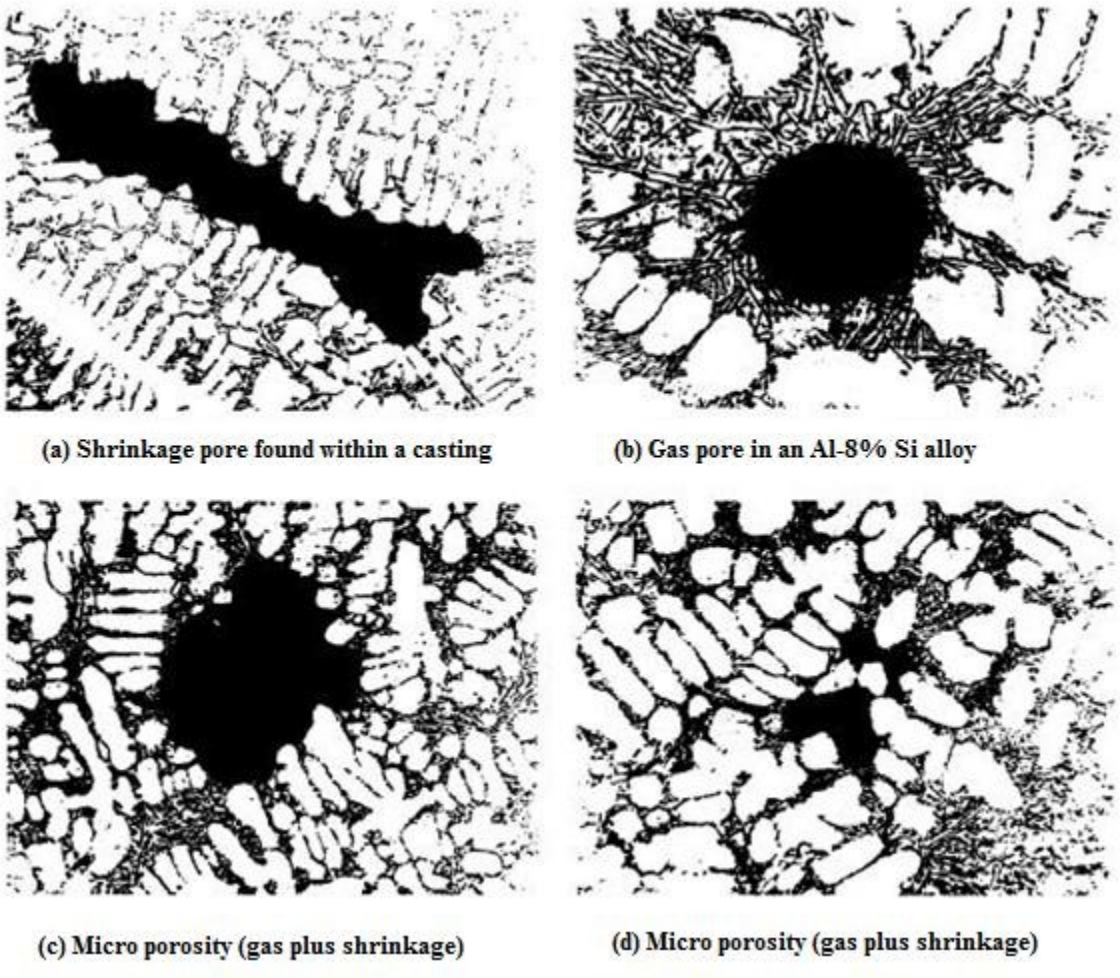

Figure 2.7 Typical porosity in cast aluminum alloy (Anson & Gruzleski, 1999)

The vast majority of porosity encountered in casting is due to a combination of gas and shrinkage. Small amounts of dissolved hydrogen significantly increase pore size when shrinkage voids form. These pores typically occur in the interdenderitic regions, which are the last parts of the structure to freeze. Some examples are shown in Figure 2.7 (c) and (d). Flow porosity results from insufficient pressure toward the end of cavity filling. Factors affecting the porosity levels in the castings can be numerous. For example, any factors affecting the fluid flow conditions during cavity filling (such as the moving speed of the piston in the shot sleeve, the velocity of the molten metal flowing through the gate, the geometry and the location of the gate for a given casting, pressure applied, etc.) may potentially affect the amount and/or distribution of entrained air. Planar defects such as oxide skins and cold shuts may also be present.

2.4.1.2 Effect of Hydrogen

Hydrogen is the only gas that is appreciably soluble in aluminum and its alloys and is thus the leading contributor to gas porosity in these alloys. The solubility of hydrogen in aluminum varies directly with temperature and square root of pressure. Solubility increases rapidly with increasing temperature above the liquidus. Hydrogen solubility is considerably greater in liquid than in the solid state as shown in Figure 2.8 (Kaufman & Rooy, 2004). The solubility of hydrogen in aluminum just above the liquidus is 0.69 ppm and just below the solidus is 0.04 ppm, which varies slightly for most casting alloys.

During cooling and solidification, dissolved hydrogen in excess of the extremely low solid solubility may precipitate in molecular form, resulting in the formation of primary and/or secondary voids. Most hydrogen into molten aluminum comes from the dissociation of water vapour at the surface of the liquid aluminum according to the reaction (Khorasani, 1996),

$$2Al\ (Liquid) + 3\ H_2O \rightarrow Al_2O_3 + 6H \qquad \textbf{Equation 2.1}$$

where hydrogen gas dissolves in liquid aluminum according to an atomistic process that involves: (a) dissociation of diatomic hydrogen gas into the atomic form at the boundary between the atmosphere and the melt, (b) dissolution of the atomic hydrogen into the

boundary layer, and (c) transport of atomic hydrogen into the bulk of the melt through a diffusion process.

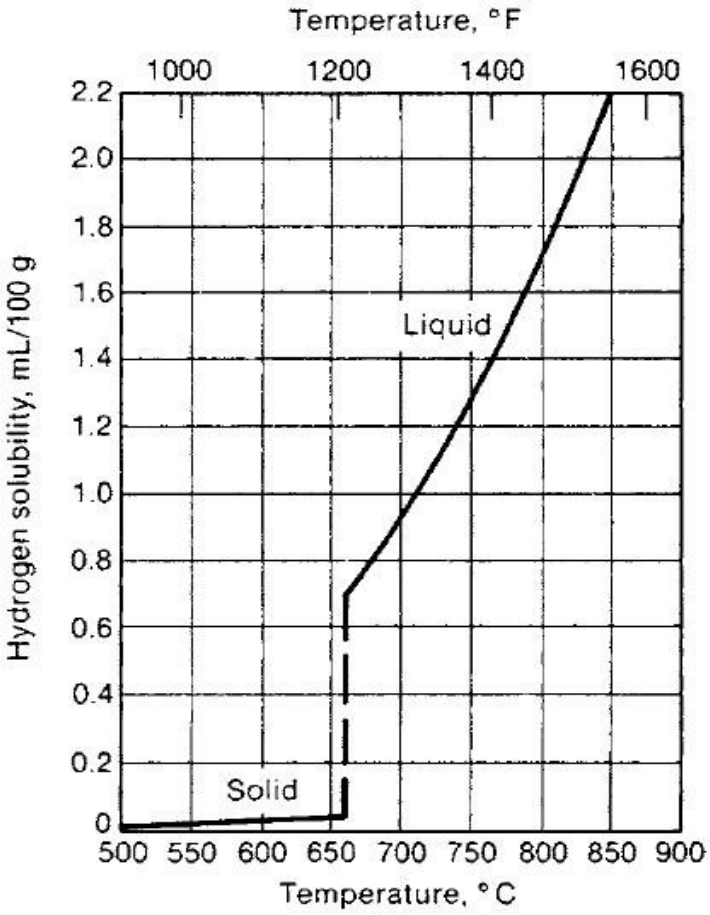

Figure 2.8 Solubility of hydrogen in aluminum at 1 atm hydrogen pressure (Kaufman & Rooy, 2004)

Primary or interdendritic porosity forms when hydrogen contents are sufficiently high that hydrogen is rejected at the solidification front, resulting in supercritical saturation and bubble formation. Secondary (micro-size) porosity occurs when dissolved hydrogen contents are low, and void formation occurs at characteristically subcritical hydrogen concentration. Hydrogen bubble formation is strongly resisted by surface tension forces by increased liquid cooling and solidification rates after diffusion, and by an absence of nucleation sites for hydrogen precipitation such as entrained oxides. The precipitation of hydrogen obeys the law of nucleation and growth and consists of:

a. Diffusion of hydrogen atoms within the molten pool.
b. Formation of subcritical nuclei as a function of time and temperature.
c. Random emergence of stable precipitates that exceed the critical size required for sustained growth.
d. Continued growth as long as dissolved hydrogen atoms remain free to diffuse to the precipitated bubble.

The result is a general distribution of voids occurring throughout the solidified structure. There is a threshold hydrogen value for any composition that must be exceeded for hydrogen porosity to occur. The pore volume fraction and pore size decrease with decreased hydrogen content above a threshold value and pore volume fraction and size decrease with increased cooling rate as illustrated in Figure 2.9.

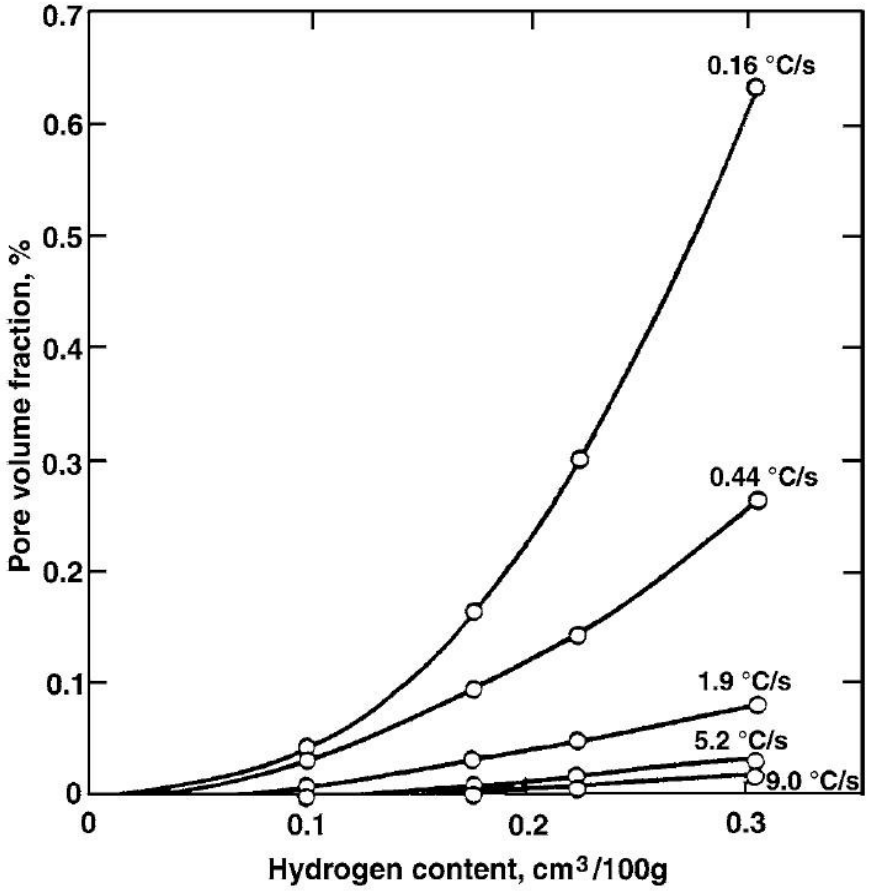

Figure 2.9 Hydrogen content, pore size and cooling rate relationship (Kaufman & Rooy, 2004)

2.4.1.3 Theory of Porosity Formation

The following equation can be considered to describe the conditions under which a pore is stable and can grow (Gruzleski & Closset, 1990):

$$P_g + P_s \geq P_{atm} + P_H + P_{s\text{-}t} \qquad \textbf{Equation 2.2}$$

where,

P_g = Equilibrium pressure of dissolve gases in the melt,

P_s = Pressure drop due to shrinkage,

P_{atm} = Pressure of the atmosphere over the system,

P_H = Pressure due to metallostatic head,

$P_{s\text{-}t}$ = Pressure due to surface tension at the pore/ liquid interface.

In order for a pore to exist, its internal pressure ($P_i = P_g + P_s$) must be sufficient to overcome all the external forces ($P_{ext} = P_{atm} + P_H + P_{s\text{-}t}$) which can act to cause it to collapse. The dissolved gas pressure P_g and the pressure drop due to shrinkage P_s are the main driving forces for porosity formation. Hydrogen precipitation and shrinkage porosity formation are usually considered separate and independent phenomena. There are interactive mechanisms that affect both. Small amounts of dissolved hydrogen significantly increase pore size when shrinkage voids form. In this respect, the effects of gas and shrinkage on pore volume fraction can be considered additive. Since, by definition, shrinkage voids form in areas of reduced pressure relative to atmospheric conditions, hydrogen solubility is reduced in the surrounding liquid and facilitates the precipitation of hydrogen into the forming void. The important measures of these pores morphology, density, size and volume fraction of pores are affected by hydrogen.

The formation of hydrogen voids and effects of hydrogen on internal shrinkage are influenced by entrained inclusions that nucleate precipitates. Inclusion strongly facilitates bubble formation even at very low levels of dissolved hydrogen.

2.5 Wear

Wear is the progressive loss of material, due to relative motion between a surface and a contacting substance. The loss of material from a surface, transfer of material from one surface to another or movement of material within a single surface is known as wear. This includes the degradation by the displacement of material within the surface (leading to changes in surface topography without loss of material), as well as the more usual case of material removal. The wear process is common in machines with or without the presence of a lubricant.

2.5.1 Mechanism of Wear

The continuous unidirectional or reciprocating relative motion between two moving bodies in contact under load is known as sliding wear. Sliding wear mechanisms are identified based on the type of material removal process. Many different mechanisms of sliding wear are proposed in the literature (Rigney, 1988; Jahanmir, 1980; Bhushan & Gupta, 1991). However, the most commonly cited mechanisms of wear in the literature include adhesion, abrasion, surface fatigue and delamination, which are described in detail in the following sections.

2.5.1.1 Adhesive Wear

When two nominally mating surfaces are brought together, they touch at the tips of the highest asperities and the total area of intimate contact is determined by the deformation of the material in these regions under the applied load. It is assumed that these asperities, deformed plastically, welded together by high local pressure and form asperity junctions (Finkin, 1978; Stolarski, 1994; Bowden & Tabor, 1950). Continued sliding results in a tangential force which causes the junctions to be sheared, and separation of surfaces occurs in the bulk of the softer material. If the weld is sufficiently weak, shearing will take place at the interface, with the resulting wear being sensibly zero. This fact immediately suggests that the presence of an oxidized surface layer at the interface reduces friction, so weakening the weld ensures that the break will occur at the oxidized surface layer (Gohar & Rahnejat, 2008). On the other hand, if failure occurs within the bulk of the softer material, because of the high weld interface strength, a fragment might

be plucked out and carried away by the harder material and with subsequent rubbing, becomes detached as wear debris (Figure 2.10).

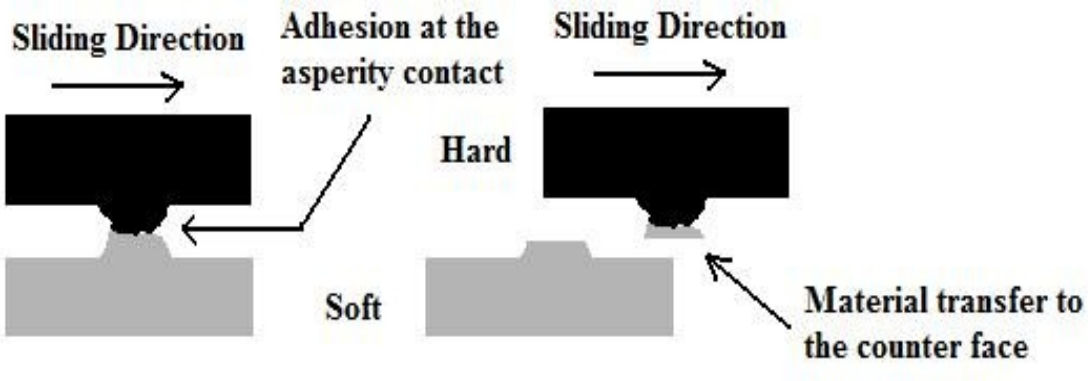

Figure 2.10 Adhesive wear (Surface Engineering, 2007)

Adhesive wear can well be described by Archard's law of wear (Archard, 1953),

$$W = K\frac{F_N}{H_S} \qquad \textbf{Equation 2.3}$$

where W is the volume worn per unit sliding distance, F_N is the applied load, H_S is the hardness of the softer materials in contact and K is the wear coefficient. Moreover, Bowden and Tabor (1964) suggested that the adhesion component of friction is due to the formation and rupture of interfacial bonds. These bonds are the result of interfacial interatomic forces developing between two surfaces in contact. If sliding is to take place, a friction force is needed to shear the weakest tangential planes at the area of contact.

If the shear strength at the interface is τ_i, which is assumed to be the bulk shear strength of the weaker material, the force required to break a junction between two asperities in contact will be given by $\tau_i A_r$, that is, F_T. Using the relationship $A_r = F_N / H_S$, the adhesion component of friction (μ_a) becomes,

$$\mu_a = \frac{F_T}{F_N} = \frac{\tau_i}{H_S} \qquad \textbf{Equation 2.4}$$

Where, H_S is the hardness of the softer material.

2.5.1.2 Abrasive Wear

When two surfaces come into contact, wear occurs on both surfaces. Abrasive wear, as defined by ASTM (Standard Terminology Relating to Wear and Erosion, 1987), is due to hard particles or hard protuberances that are forced against and move along a solid surface. The rate at which the surfaces abrade depends on the characteristics of each surface, the presence of abrasives between the first and second surfaces, the speed of contact, and other environmental conditions. The loss rate is not inherent to a material. Abrasion is typically categorized according to types of contacts as well as contact environment (ASM, 1992). Types of contacts include two- or three-body wear, as shown in Figure 2.11. The former occurs when an abrasive slides along a surface, and the latter, when an abrasive is caught between one surface and another. Particles enter the clearance space between a component's two moving surfaces, bury themselves in one of the surfaces, and act like cutting tools to remove material from the opposing surface. Particle sizes causing the most damage are those equal to and slightly larger than the clearance space. Ultimately, abrasive wear will result in dimensional changes, leakage and lower efficiency.

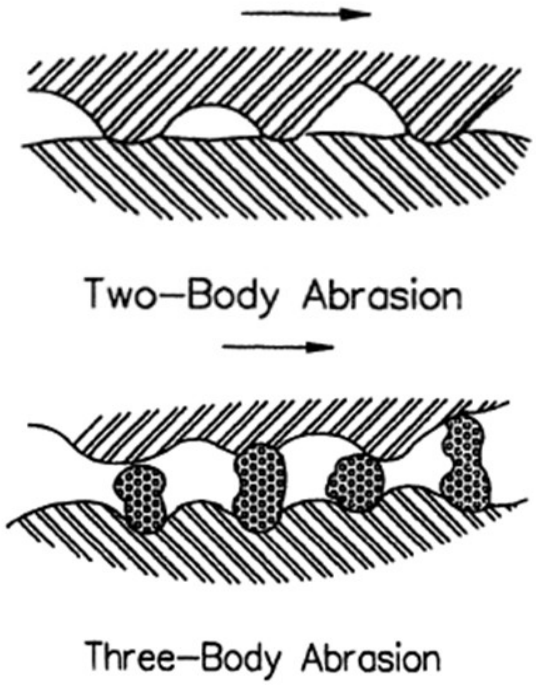

Figure 2.11 Two- and three-body abrasive wear (Surface Engineering, 2005)

Several mechanisms have been proposed to explain how material is removed from a surface during abrasion. These mechanisms include fracture, fatigue and melting. Because of the complexity of abrasion, no one mechanism completely accounts for all the loss (Harsha & Tewari, 2003). Abrasion loss rates are not intrinsic to a material. Environmental factors such as the type of abrasive and its characteristics, temperature, speed of contact, and load affect the wear rate. The hardness of the abrasive particles is important to the rate of abrasion of the subject material. If the hardness of the abrasive exceeds that of the wear material, abrasive wear typically becomes more severe (Nathan & Jones, 1966-67), as shown in Figure 2.12. If the abrasive hardness exceeds the hardness of the material, it would penetrate the surface and cut/remove material without having its cutting edges broken or rounded. The shape of the abrasive particle is important, because it influences the shape of the groove produced in the material. It also influences the contact load and the transition from elastic to plastic contact. Experiments have confirmed that less wear occurs when materials are abraded by rounded rather than sharp particles (Nathan & Jones, 1966-67).

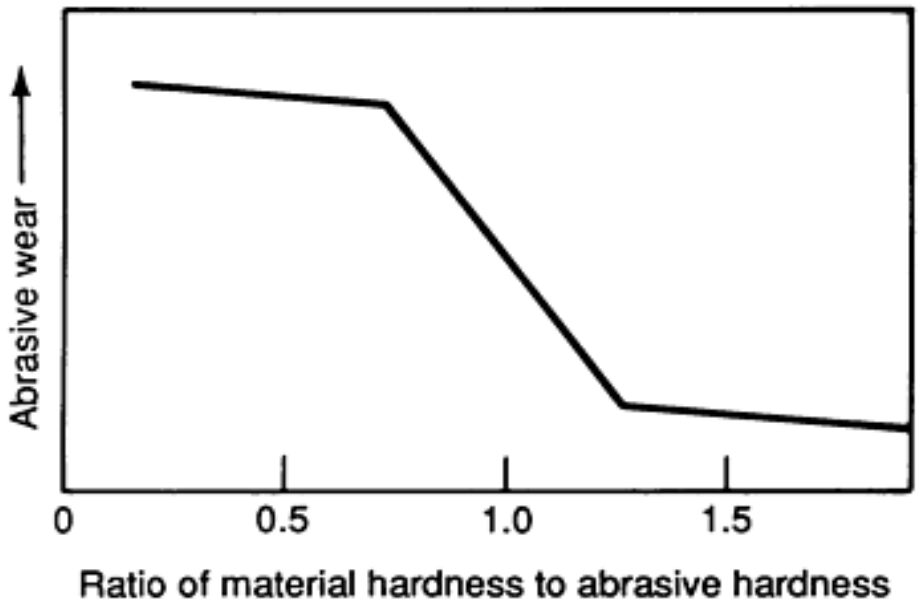

Figure 2.12 Abrasive wear rate vs material hardness/abrasive hardness ratio (Nathan & Jones, 1966-67)

It is expected that abrasive wear would increase as the temperature rises, because the hardness and yield strength decrease. Instead, for aluminum and copper (Soemantri, et al 1985), when the temperature is increased from ambient to 673 K, very little change in the abrasive wear rate is observed. It has been proposed that the reason for this small change is that during abrasion, small areas beneath the abrasive particles are adiabatically heated. At higher initial temperatures, the metal flow stress is reduced. This results in less heating in the material during the abrasion process and similar abrasion rates are observed. The rate of abrasive wear has been found to slightly increase with increasing speed in the range from 0 to 2.5 m/s (Tylczak & Oregon, 1992). Abrasive wear has been shown to be proportional to load, following Archard's equation. However, this proportionality effect breaks down when the load is high enough to fracture the abrasive particles. If the forces do fracture the abrasive particles and create new sharp edges, wear can increase. If the abrasive particle edges are rounded, wear will decrease.

2.5.1.3 Surface Fatigue

Repeated loading and unloading cause cyclic stress on a surface, eventually resulting in the formation of surface or subsurface cracks. The surface ultimately fractures and large fragments are lost, leaving pits. This phenomenon can occur only in systems where abrasive and adhesive wear are not present, for example, in systems with high surface contact loads. An area of surface must be stressed repeatedly, without constant removal of particles, to fail in fatigue. Fretting, erosion, and cavitations are typical examples of this type of wear. Bearing surfaces are subjected to fatigue failures as a result of repeated stress caused by particles trapped between the two moving surfaces (Pall, 2007). At first, the surfaces are dented and then cracking begins. These cracks spread after repeated stress by the bearing load, even without additional particulate damage, and eventually the surface fails, producing a spall. A typical type of surface fatigue is shown in Figure 2.13.

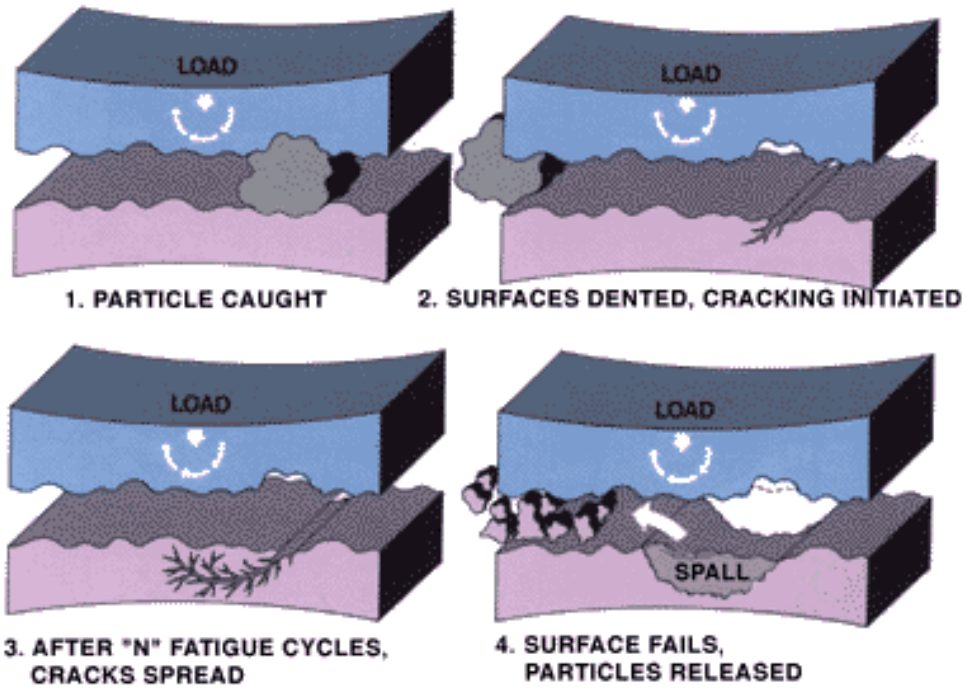

Figure 2.13 Surface fatigue (Kopeliovich, 2008)

2.5.1.4 Fretting wear

Fretting is a small-amplitude oscillatory movement that may occur between contacting surfaces, which are usually nominally at rest. One of the immediate consequences of the process in normal atmospheric conditions is the production of oxide debris; hence, the term "fretting wear" or "fretting corrosion" is applied to the phenomenon. The movement is usually the result of external vibration, but in many cases it is the consequence of one of the members of the contact being subjected to a cyclic stress (that is, fatigue), which gives rise to another and usually more damaging aspect of fretting, namely the early initiation of fatigue cracks. This is termed "fretting fatigue" or "contact fatigue." Fatigue cracks may also be initiated where the contacting surfaces are under a very heavy normal load or where there is a static tensile stress in one of the surfaces (Tehrani & Saket, 2009). Because vibration is one of the main causes of the fretting movement, it follows that the most likely area for it to occur is in machinery. The contacts between hubs, shrink- and press-fits, and bearing housings on loaded rotating shafts or axles, are particularly prone to fretting damage; however, because the movement arises from alternating stresses in the shaft surface, the problem is more one of fatigue than wear (Styles, 1980).

It is generally agreed that when fretting wear is taking place between two flat surfaces, the progress with time (or number of cycles) can be recognized as occurring in three stages (Hurricks, 1970; Aldham, et. al 1985):

a) Initial stage of a few thousand cycles when metal-to-metal contact is prevalent, resulting in local welding, roughening of the surface, high friction, and low contact resistance. Fatigue cracks are initiated in this stage if the movement is a result of cyclic stressing (Waterhouse, 1977).
b) Formation of beds of compacted oxide with a fall in coefficient of friction and erratic behavior of contact resistance as it oscillates between high and low values.
c) Onset of a steady state in which the friction is more or less constant and the contact resistance is generally high with occasional momentary falls to a low value.

2.5.1.5 Erosion Wear

Erosive wear is caused by particles that impinge on a component surface or edge and remove material from that surface due to momentum effects. This type of wear is especially noticed in components with high velocity flows, such as servo and proportional valves (Affatato, et. al 2008). Particles repeatedly striking the surface may also cause denting and eventual fatigue on the surface. The damaging effects of erosive wear can be seen in dimensional changes to equipment, leakage, lower efficiency, and the generation of additional particles, which leads to further contamination and wear throughout the system.

2.5.2 Delamination Wear Theory

Delamination is a process of the initiation and propagation of a sub-surface crack, as shown in Figure 2.14. The propagation of sub-surface cracks can help maintain relative stability in a certain load range. Suh (1973) proposed that at low sliding speeds, wear debris formation could be described by a delamination wear theory. Wear processes such as adhesive wear, fretting and fatigue were all related to this same mechanism. Suh stated that wear occurred by the following sequential steps:

a) Cyclic plastic deformation of surface layers by normal and tangential loads.

b) Crack or void nucleation in the deformed layers at inclusions or second-phase particles.
c) Crack growth nearly parallel to the surface.
d) Formation of thin, long wear debris particles and their removal by extension of cracks to the surface.

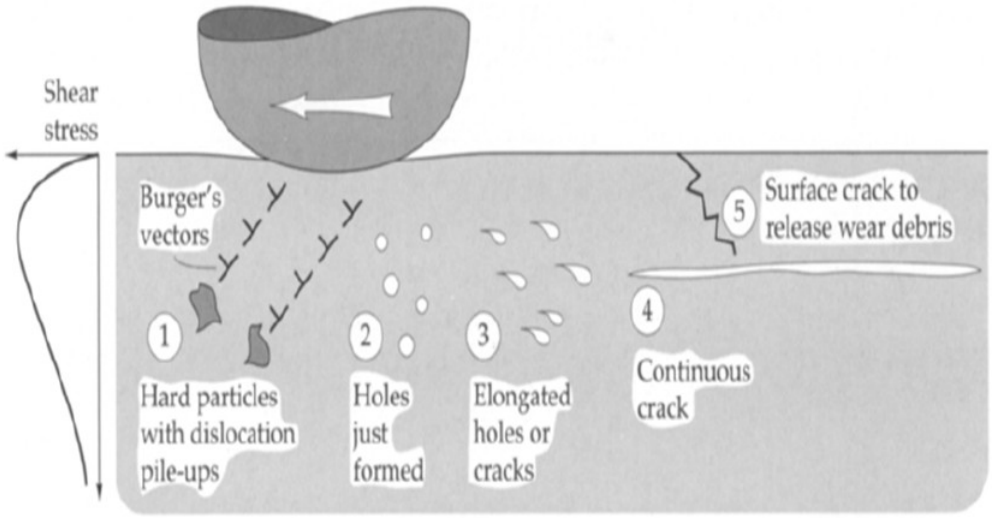

Figure 2.14 Delamination wear (OCPL, 2003)

The rate-determining mechanism of wear shows dependence on the metallurgical structure. When sub-surface deformation controlled the wear rate, hardness and fracture toughness were both considered to be major influencing factors. Jahanmir and Suh (1977) showed that for microstructures containing hard second-phase particles, if sufficient plastic deformation occurred during sliding wear, crack nucleation was favoured at these particles. In this situation, where inter-particle spacing is an important variable, crack propagation controlled the wear rate. Void formation was primarily attributed to the plastic flow of the matrix around these hard particles and occurred very readily around the hard particles but crack propagation occurred very slowly. Void size tends to increase with increased friction coefficient and applied load.

Suh's delamination theory proposed that voids only nucleated at a defined depth below the sliding wear surface. Void formation was related to the hydrostatic pressure which existed directly under a contact region. Voids therefore nucleated below a level where hydrostatic pressure was not large enough to suppress their formation and above a depth

where plastic deformation was sufficient to nucleate voids around the hard particles. The existence of this critical depth dictated the resultant dimensions of the wear particle debris, especially the thickness of plate-like particles. The existence of a depth below the worn surface where void formation and eventual shear instability occurred was confirmed by Rosenfield (1987).

In a study of dry sliding wear of dispersion hardened alloys, delamination wear theory was identified as a major wear process (Deuis, et. al 1997). Hardness and friction coefficients played a major role in the overall wear process. The wear resistance decreased with increased volume fraction of the oxide phase, even when hardness was increased. Crack propagation was considered to be the wear-rate controlling factor. Cracks were initiated at the particle/matrix interface or by fracture of the particles. For crack nucleation at particle/matrix interfaces, the following conditions were necessary:

a) Tensile stress across the interface should exceed the interfacial bond strength.
b) Elastic strain energy released upon decohesion of the interface should be sufficient to account for the surface energy of the crack created.

For second-phase particles to be a significant factor in the nucleation of a void or micro-crack, they must possess a diameter in excess of 2.5 μm in order to satisfy the energy conditions. Therefore, for good wear resistance it is desirable to have an alloy reinforced with a large volume fraction of very small coherent particles.

2.5.3 Wear Mechanisms Map

D. Tabor (1983) suggested constructing wear mechanism maps which summarize data and modes of wear, showing how the mechanisms interface and allowing the dominant mechanism for any given set of conditions to be identified. Lim and Ashby (1987) constructed the first wear mechanism maps based on physical modeling in order to systematize empirical wear data on steels. These maps allowed prediction of dominant wear mechanisms under a given set of test conditions in terms of a few key dimensionless parameters, and how various mechanisms of wear interface with one another. There are many mechanisms of wear, each dependent in a different way on operating conditions. The dominant mechanism, at any given normal load and sliding velocity is the one

leading to the fastest rate of wear. In order to find an overall framework which reveals the relationships between the mechanisms and, for given sliding conditions, identifies the dominant one, Ashby and Lim (1990) follow two converging routes – empirical and physical modeling. For empirical routes, data from wear experiments are plotted on suitable axes and identified by wear rates and mechanisms, as shown in Figure 2.15.

Boundaries are drawn to separate classes of behavior, separating all data points associated with one mechanism from those associated with another. The result identifies the field of dominance of each mechanism. The second route is that of physical modeling, as seen in Figure 2.16. The individual mechanisms of wear are identified. A wear rate equation is derived for each mechanism. The dominant mechanism is identified with the mechanism which, at a given normal load and sliding velocity, gives the fastest wear rate.

Many researchers (Childs, 1988; Kato, et. al 1994; Ashby, et. al 1991; Wang & Rodkiewicz, 1994; Hokkirigawa, 1991; Kong & Ashby, 1992; Lim, et. al 1993; Lim, et. al 1996) have been involved in the construction of wear mechanism maps. They worked with different sliding pairs, lubricating systems and test conditions, ultimately using their individually-favored approach to constructing their wear map. Antoniou and Subramanian (1988) developed a qualitative map to organize wear data on aluminum and its alloys, as shown in Figure 2.17. This diagram was produced from direct experimental evidence from both the worn surfaces and associated debris. Within the wear mechanism map for aluminum alloys five wear mechanisms have been identified by Antoniou. The method of identification relies heavily on the topography and microstructure of the wear debris and associated worn surface. These five mechanisms are: (a) formation of fine equiaxed particles, (b) delamination of compacted equiaxed particles, (c) delamination of deformed aluminum alloy, (d) gross material transfer and (e) melt wear.

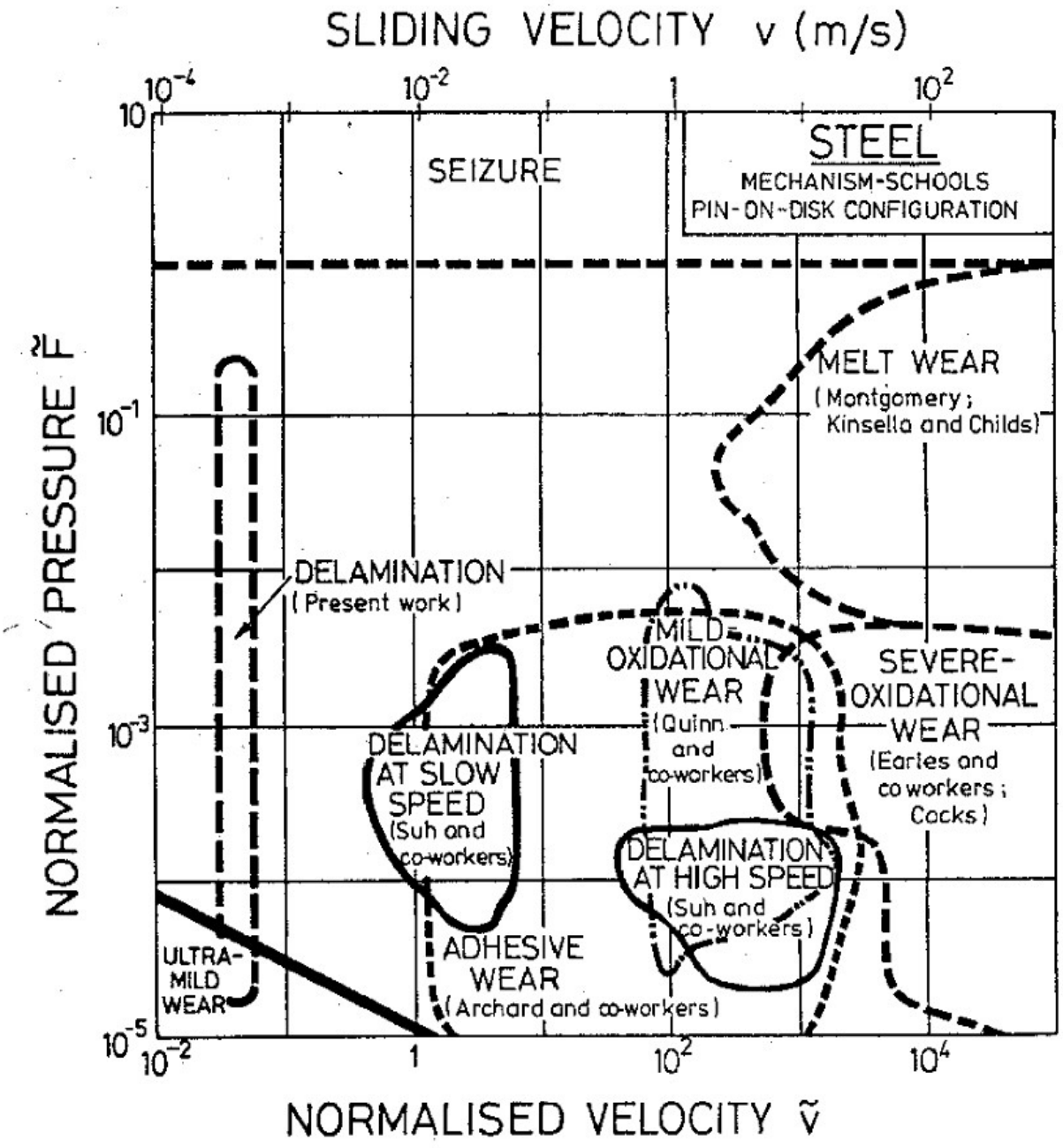

Figure 2.15 Empirical wear mechanism map for medium carbon steel sliding on itself (Ashby & Lim, 1990)

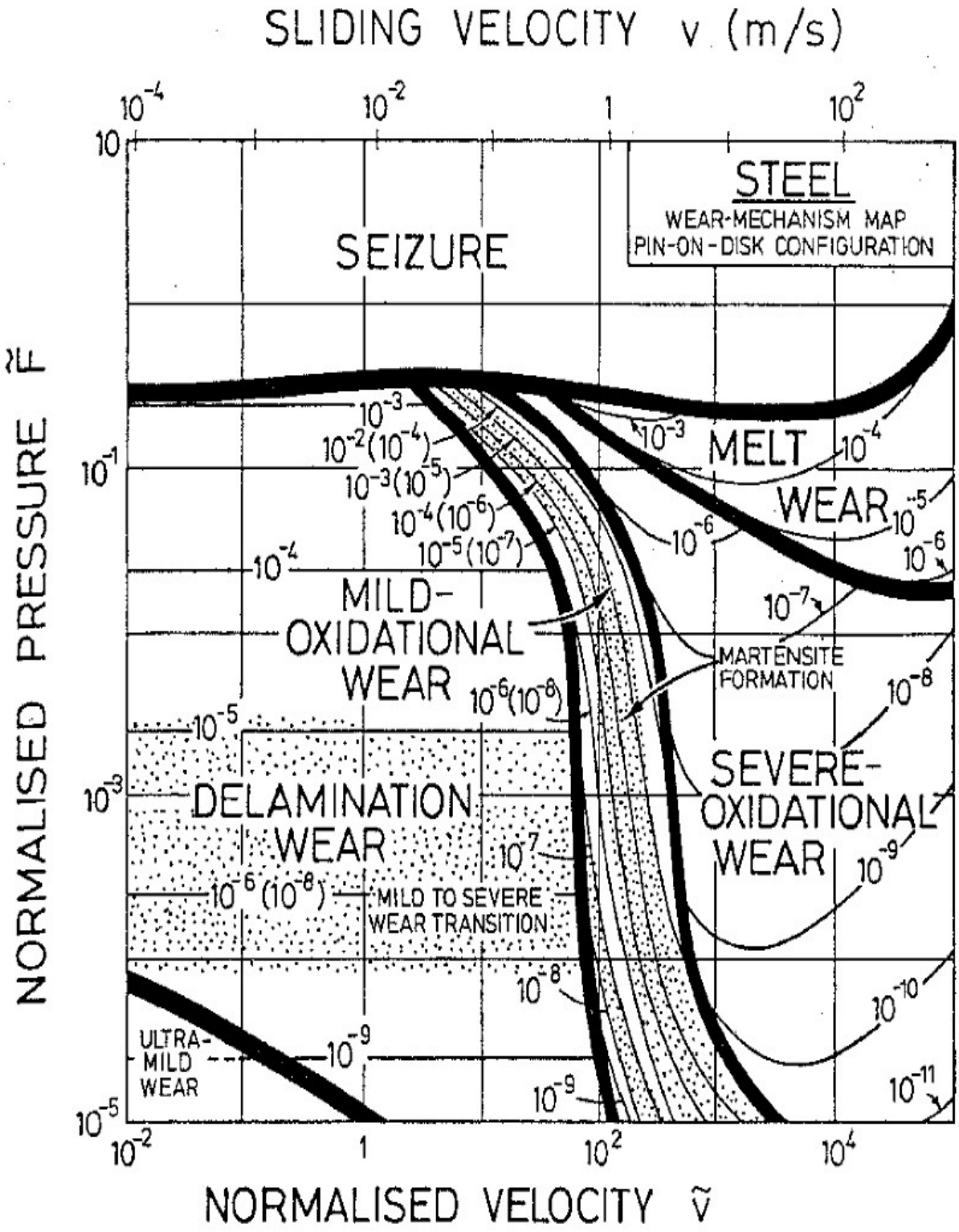

Figure 2.16 Wear mechanism map for low carbon steel based on physical modeling (Ashby & Lim, 1990)

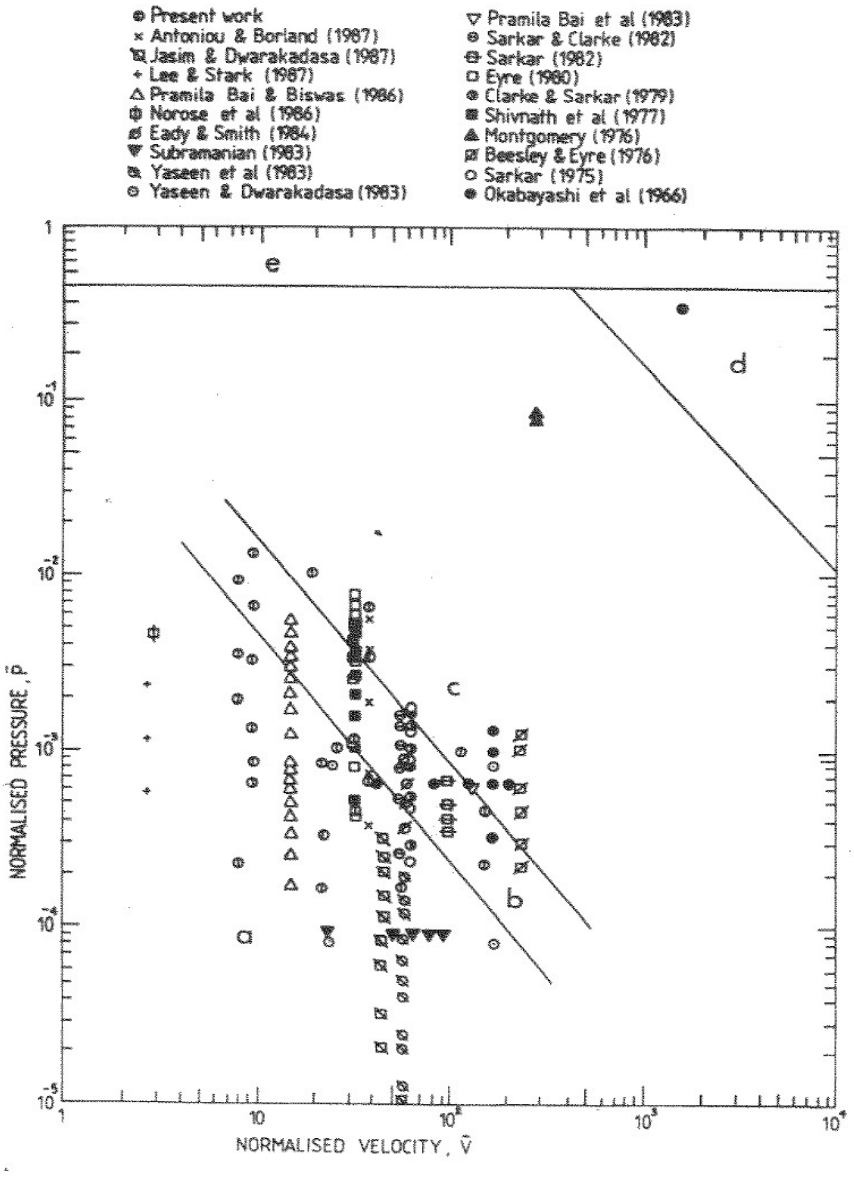

Figure 2.17 Wear mechanism map for aluminum alloys (Antoniou & Subramanian, 1988)

Y. Liu et al. (1991) presented a wear mechanism map for aluminum alloys, based on the physical modeling approach suggested by Lim and Ashby. They used new model equations based on a different state-of-stress criterion suitable for aluminum and its alloys, calibrated with the help of available experimental data. Models for four different wear mechanisms were developed: (a) oxidation dominated wear, (b) delamination wear, (c) melt lubrication wear and (d) seizure. Figure 2.18 shows the wear mechanism map

developed by Y. Liu et al. For the unlubricated sliding of aluminum and aluminum alloys on steel.

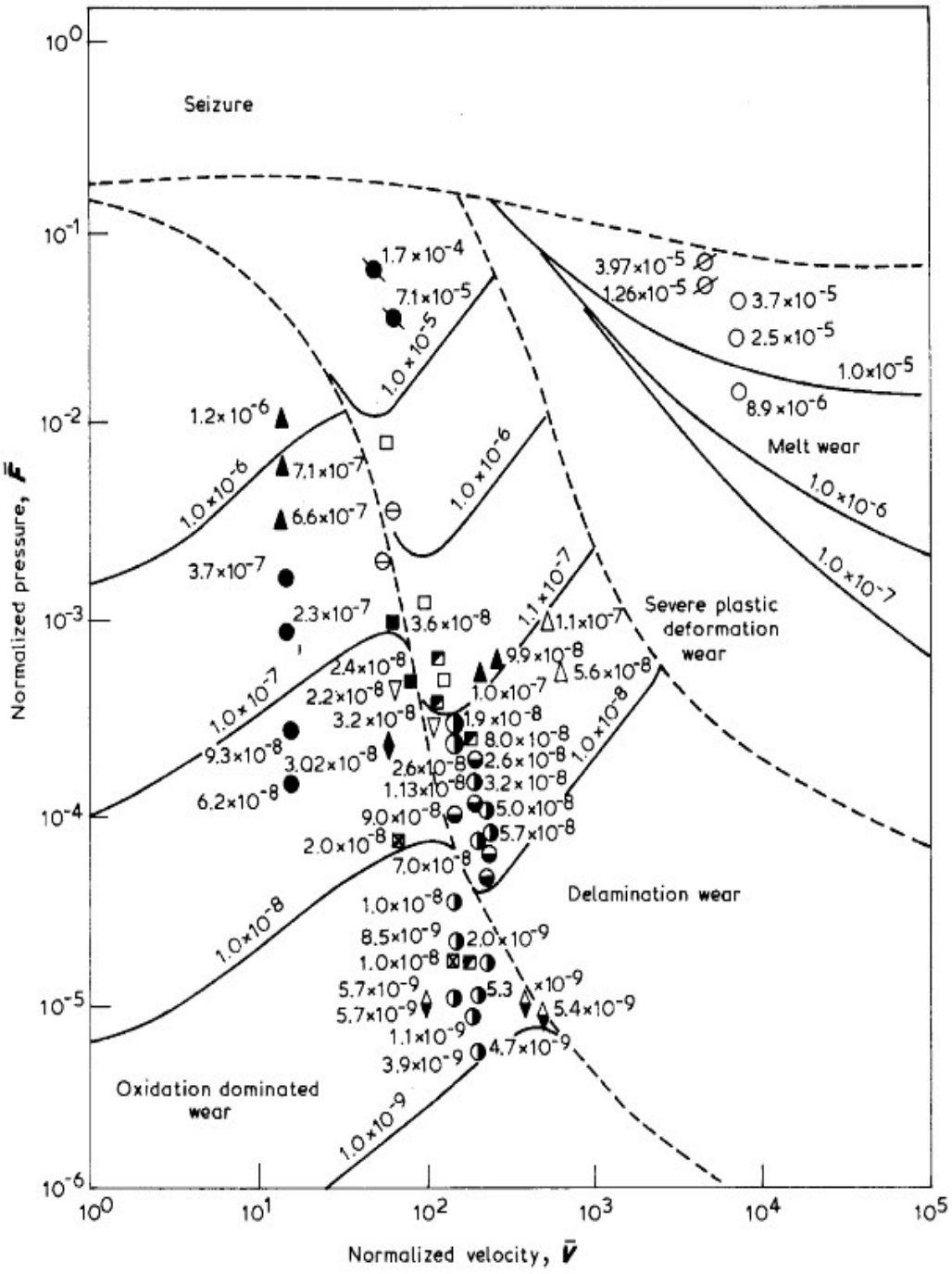

Figure 2.18 Wear mechanism map for aluminum alloys developed by modeling (Liu, et. al 1991)

Lim (1998) offered some personal views on future directions for research in wear mapping.

a) Wear maps for different tribological conditions should be constructed; they should not be limited to describe only the wear of unidirectional sliding. Effort to construct time dependent wear transition maps should be encouraged.
b) More wear maps designed to serve primarily as diagnostic tools, such as 'failure maps' and 'operating conditions maps', should be prepared.
c) Wear maps should have a sufficient wide range of sliding (or operating) conditions. Even if these maps are of an empirical nature, they will still be able to provide an overall framework for the better understanding of wear behavior.
d) There is a need to address the paucity of wear maps describing lubricated conditions as real life tribo systems almost always operate in a lubricated condition.
e) Wear maps should be constructed with an aim to serve the end users.

2.5.4 Wear Behavior of Aluminum

The principal factors that influence the sliding wear of aluminum include: extrinsic factors such as sliding distance, sliding speed, applied load, atmospheric condition, etc. (Torabian, et. al, 1994) and some intrinsic factors such as reinforcement type, shape, size, volume fraction and distribution, interface between the reinforcement particle and matrix, porosity and so on (Saka, et. al, 1977). Wilson and Alpas (1997) have clearly demonstrated that there is strong interaction between normal load and sliding speed in causing the wear of a material. Wear rate increases with an increase in normal load and sliding velocity, which has been investigated by several researchers (Tu, et. al, 2003; Bindumadhavan, et. al, 2001; Mahmoud, et. al, 2008). Wear mechanism maps developed by Liu et al. (1991) suggest that wear of aluminum alloy occurs by several mechanisms, i.e., oxidation-dominated wear, delamination wear, melt lubrication wear, and seizure. At relatively low sliding speeds and loads, a purely oxidative mechanism controls the process (mild wear). At higher loads, metal-metal contact leads to severe wear when the surface temperature of the contact area exceeds the recrystallization temperature of the material (Ling & Saibel, 1957). Plastic deformation and damage accumulation below

contact surfaces play an important role in sliding wear of ductile materials and the wear rate, after prolonged rubbing, depends upon the properties of the generated skin rather than on the properties of the original materials (Menezes, et. al, 2009; Moore & Tegart, 1952).

Archard and Hirst (1957) suggested that a mild wear process can be divided into three stages. In the initial stage, as the surfaces first rub together, the load is borne by a relatively small number of contact areas and wear occurs by the transfer of materials to the counter-face. As the experiment proceeds, the surfaces in contact achieve greater conformity, and the load becomes supported by a larger number of contact areas. In the final stage, most of the load is borne by the loose wear debris and an increase in wear rate is observed due to abrasion of the surfaces by these particles. Subramanian (1991) suggested that the wear rate of Al-Si alloy decreases with increasing sliding speed. He attributed the decreasing trend of wear rate to a reduction in the number and size of the transferred fragments. Jasim et al. (1993) found that, the depth of the subsurface damage decreases with increasing sliding speed, indicating that the decrease in wear rate is a consequence of shallower subsurface damage as sliding speed increases. Other researchers concluded that wear rate initially decreases and then increases as sliding speed is steadily increased (Biswas & Bai, 1981). It is pertinent to point out that wear resistance depends not only on the properties of the materials involved but also on the geometry of the contact (Simchi & Danninger, 2004). Strain hardening may also play a role since the density of dislocations would increase during wear, which could influence the hardness and thus wear resistance.

2.5.5 Effect of Porosity on Wear

Porosity is the most distinguishing feature of a cast and sintered product and also the most common but serious microstructural defect which has a negative impact on its mechanical properties. The presence of pores promotes the formation of surface or subsurface cracks (He, et. al, 1997) and acts as preexisting incipient cracks in the system, waiting to become unstable at appropriate stress levels. The pores increase the surface roughness of the materials, decrease the real area of contact between two sliding surfaces,

and consequently increase the contact pressure and promote particle detachment during sliding (Vardavoulias, et. al, 1993).

The influence of porosity on the wear behavior of materials has been found to be rather complex and has not been clearly identified. It is pertinent to note that as often occurs in tribology, different researchers used different testing conditions in terms of both tribological parameters and geometrical configurations. This makes it difficult to derive a useful comparison between published data or to form a unifying view. Both beneficial and detrimental effects of porosity on wear resistance have been reported.

The increase in porosity content decreases both the yield and ultimate tensile strength values of the produced samples. Fatigue strengths, hardness, facture toughness and elongation (%) all decrease with increasing porosity. Porosity appears to impact the process not merely by softening the material alone but also by promoting subsurface cracking and delamination. The pores affect stress distribution and metal deformation of subsurface layers during dry sliding. Accumulation of subsurface damage results in nucleation of cracks that further expand by shearing. The influence of the pores on crack initiation and crack propagation under cyclic loading was determined by several researchers (Bergmark, et. al, 2002; Gerard & Koss, 1990).

Suh (1977) observed that an increase in porosity content reduces the length of crack propagation required to link up with other cracks and cause delamination. The propagation of subsurface cracks at a critical depth parallel to and eventually up to the surface results in the formation of flake-like debris (Simchi & Danninger, 2004) This reduction in properties is not only influenced by the total vol % porosity but also by pore size and shape as well as pore interconnectivity (Bocchini, 1986). At high porosity, materials have more interconnected pores, lower strength, and are much easier to deform and to be torn off. A decrease in the density of voids results in enhanced wear resistance since the voids may act as stress raisers and thus increase the probability of cracking or fracture (Ye, et. al, 2001). From the point of view of fracture behavior, pore size is more critical than the overall porosity content (Tekmen, et. al, 2003) (Danninger, et. al, 1993).

The influence of porosity on the wear behaviour of materials also depends on wear conditions. Porosity acts as lubricant reservoirs in wet sliding conditions, which provides a considerable advantage in wear process (Hoffman, et. al, 1999). In contrast, in dry sliding condition, the wear rate increases gradually with increasing volume fraction of porosity content due to its combined effect on both the real area of contact and subsurface cracking (Hamid, et. al, 2008). In their experiments, A. Hamid et al. (2008) found that, in dry sliding conditions, the wear rate increases gradually with increasing volume fraction of porosity up to 4 vol. %, but beyond that, the wear rate increases rapidly with further increasing porosity. Similar results were found by other researchers (Mahmoud, et. al, 2008).

Gui et al. (2000) investigated the influence of porosity on the dry sliding wear behavior in spray-deposited, Al-based composite and found that, at low load, porosity in the as-sprayed composite has very little effect on wear behavior. This is because the pores beneath the worn surface remain stable and cannot propagate significantly, whereas with an increasing load, sub-surface deformation and strain-induced stress increase. The pores beneath the worn surface become unstable and cracks originating from these pores can propagate during the wear process, resulting in delamination wear. Porosity would exert a significant influence on wear rate when the applied load is sufficiently large to render the pores beneath the worn surface unstable. Plastic deformation and fracture are considered the main causes of severe wear. If strain-induced shear stress is larger than the shear strength of the material itself in the subsurface, severe wear will occur. Thus the occurrence of severe wear depends on the shear strength of the material and strain-induced shear stress. The presence of pores decreases the shear strength of the material since shear fracture takes place directly through these pores. In addition, the increase of applied load can promote the enlargement of the size of the deformation zone beneath the worn surface, so that more pores can influence the wear process.

Under certain conditions porosity may act as a trap for wear debris. Dubrujeaud et al. (1994) found that, for all porosities, the values of volume loss resulting from measuring the wear facet diameter are always higher than the values resulting from measuring the mass loss. This difference in values is more pronounced for high porosities and was

attributed to the entrapping of wear debris by the pores. The presence of porosity is associated with its capacity to entrap the wear debris is also reported by S. C. Lim and J. H. Brunton (1986). Trapping of wear debris on surface pores decreases wear rate by decreasing the contact pressure and plastic deformation near pores (Chen, et. al, 2009).

Pore size is the most important parameter in terms of entrapping wear debris. In the case of specimens with low porosity and small mean pore size, the capture of debris by the pores is difficult. These pores may be partially or completely closed by plastic deformation, decreasing the probability of pore filling by the debris. In contrast, for high porosity levels and larger mean pore sizes, plastic deformation results in filling the pores with metallic particles (Dubrujeaud, et. al, 1994). According to Dubrujeaud, the filling of pores with wear debris enhances the dry sliding wear resistance of the material by reinforcing the porous material. A type of composite is created at the surface and porosity in the surface decreases significantly. The real contact area between sliding surfaces increases which results in decreasing the contact pressure. The possibility of particle agglomeration during sliding and formation of large abrasive agglomerates is diminished. The complete filling of pores precludes plastic deformation near the pores and creation of metallic debris.

Sub-surface pores elongate in the direction of sliding and in some places close locally. During repeated sliding, the elongated pores near the surface eventually propagated up to the sliding surface to form flake-like debris. In other words, the formation of surface cracks and attendant debris may be a consequence of pore deformation and pore coalescence in the sub-surface layers and/or microcrack nucleation at the subsurface pores. If pore closing occurs, it is understandable that the wear rate decreases considerably and the compact behaves similarly to a material of lower porosity. This behavior was amply reported in previous investigations (Amsallem, et. al, 1973; Dubrujeaud, et. al, 1994; Wang & Danninger, 2001).

For abrasive wear process, hardness may be the main factor determining the wear behavior. An increase in hardness gives rise to a reduction in wear rate (Straffelini & Molinari, 2001), but is often altered by porosity, wear test conditions and so on (Jun-an & Danninger, 2001). Wang et al. (2003) shows that, under the same wear test conditions,

and owing to high hardness and low porosity, the wear coefficient becomes much smaller. This implies that low porosity and high hardness are mainly responsible for the low wear coefficient in the running-in process.

2.6 Hot Isostatic Pressing

Hot isostatic pressing is very significant process refinement available to deal with internal porosity, commonly referred to as HIP or HIPing. Hot isostatic processing of casting is recognized as a means of providing improved internal soundness or integrity, increased density and improved properties. While die compaction and sintering provide a closer to net shape than is possible in all but the most advanced and expensive HIPing processes, the small levels of porosity present in conventional P/M parts limit their use in fatigue critical applications and in situations where mechanical property requirements normally specify a wrought material. By producing a pore free P/M product, HIP can compete with forgings (Mashl, 2008). It has proved capable of substantially eliminating micro-porosity resulting from the precipitation of hydrogen and formation of internal shrinkage during solidification. HIP has no effect on cracks, shrinkage and other defects that communicate to the casting surface.

The HIP process subjects a component to both elevated temperature and isostatic gas pressure in a high pressure containment vessel. The pressurizing gas most widely used is argon. An inert gas is used, so that the material does not chemically react. The chamber is heated to a temperature that is below the solidus but high enough to maximize plastic flow and enhance atom or vacancy diffusion within the material. Under the simultaneous influence of hydrostatic pressure and elevated temperature, a pore will collapse and shrink, initially by plastic flow, then by diffusional mechanisms. During a typical HIP cycle, the unit is loaded with parts and sealed. A vacuum system removes air from the vessel, and then the vessel is filled with argon. The unit is then pressurized with inert gas while the furnace is heating. An increase in pressure occurs from both the mechanical action of the compressor and temperature induced pressure rise that occurs while heating gas in an enclosed volume. Once the desired temperature and pressure are achieved, the dwell portion of the HIP cycle begins. Since plastic deformation via yielding occurs very rapidly, the pore shrinkage that takes place due to plastic flow is complete once the dwell

temperature and pressure are reached. The remaining portion of the dwell time allows additional pore shrinkage via diffusion as well as solid state bonding across the collapsed pore interface. A typical schematic diagram of HIP is shown in Figure 2.19 (Mashl, 2008). The principals of HIP are as follows (Kaufman & Rooy, 2004):

a) At elevated temperatures and under increased pressure, limited but significant dissolution of hydrogen in the aluminum alloy matrix occurs, permitting the collapse and healing of voids surfaces formed by hydrogen precipitation during solidification.
b) At elevated temperatures and under increased pressure, precipitated hydrogen in excess of the solubility limit is compressed and repartitioned, resulting in increased structural density and integrity.
c) At elevated temperatures and under increased pressure, shrinkage voids uncontaminated by hydrogen are compressed and healed by the collapse of the surrounding structures when yield strength is reduced sufficiently for plastic deformation to occur during the densification cycle.
d) In the case of shrinkage voids contaminated by hydrogen, resolution of hydrogen and collapse and metallurgical bonding of internal void surfaces occur by a combination of these effects.

Temperature, time and pressure are the three critical process variables to be determined when choosing the processing parameters for a new material. In some cases, heating and cooling rates also must be considered. A temperature should be chosen that will lower the flow stress of the metal as much as possible, thus maximizing the amount of densification that occurs by plastic flow as well as self diffusion will occur at an acceptable rate, thereby enhancing the final stages of densification. Heating and cooling rate must be selected in such a way so as to strike a balance between short cycle times and other metallurgical factors that are affected by heating and cooling rates. The materials that are in contact with a casting during HIP must also be considered.

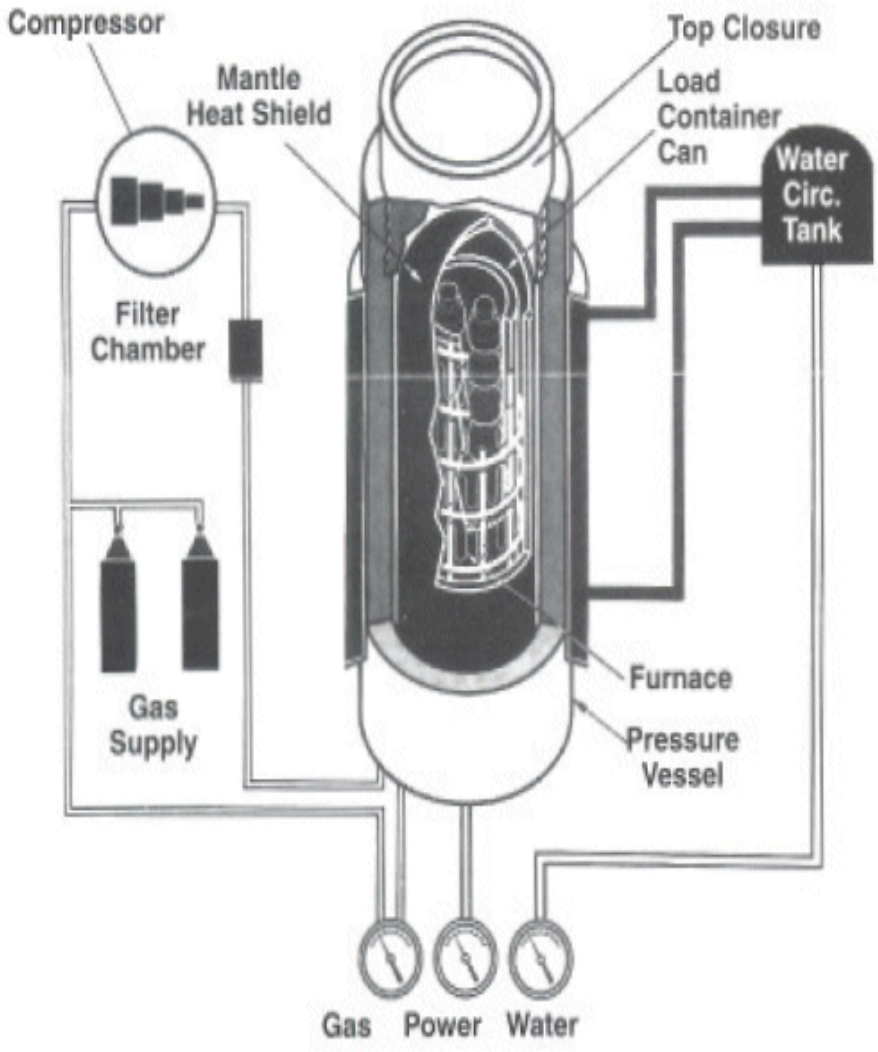

Figure 2.19 Schematic diagram of typical HIP chamber (Mashl, 1999)

The presence of surface-connected porosity is the most common cause for dissatisfaction in solving a porosity problem, as there must be a gas-tight layer of material surrounding the pores for HIP to work. The vast majority of a pore network can be sub-surface, but if there is even so much as one pinhole penetration of the surface that opens the pore network to the external high pressure gas, the gas will penetrate the pore network. Once the gas pressure within the pore network has equalized with the external pressure, no densification will occur. Figure 2.20 illustrates the concept of surface-connected porosity.

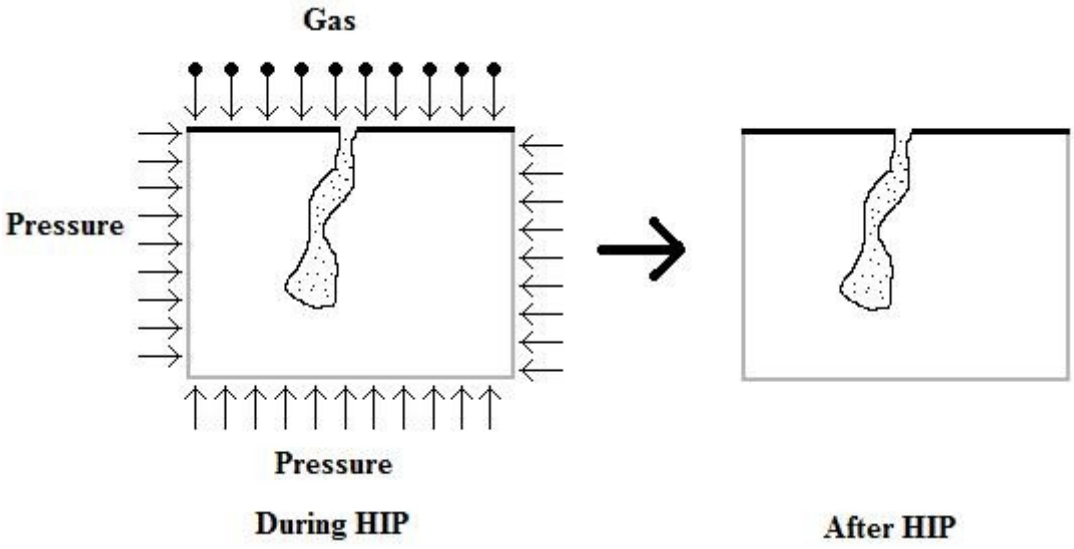

Figure 2.20 Schematic diagram showing the effect of HIP on surface connected pore (Mashl, 1999)

The best solution to surface-connected porosity is to eliminate its occurrence in the casting operation through modification of the mold deign by incorporating chills into the mold or by using any other technique that will help to ensure that a solid layer of metal is formed on all surfaces. In some cases, a surface sealing process, such as weld overlay, can be used to seal surface connected porosity. The sealed pore will contain air, so HIP could create a network of oxides in the region where the pore had been. Nevertheless, if the end result is acceptable, sealing off a surface connected pore network is one way to salvage an expensive casting that would otherwise become scrap.

CHAPTER 3 EXPERIMENTAL METHODES

3.1 Materials Preparation

3.1.1 Casting

High-pressure die cast A380M aluminum alloy was obtained from Magna Powertrain. The composition of A380M was determined using inductively coupled plasma mass spectrometry and is summarized in Table 3.1. The letter 'M' in A380M indicates higher manganese content. High silicon content helps to increase fluidity and improve corrosion resistance (Sarkar & Clacke, 1980; Tingler, 2008; Sarkar & Clarke, 1979). Furthermore, the presence of silicon as an alloying element in these alloys improves wear resistance significantly. However, there is no universal trend in wear behavior of Al-Si alloys with respect to silicon content (Gomes, et. al, 2005). In other words, increasing the Si content in the alloy does not always increase the wear resistance. The presence of magnesium improves hardenability, while copper is added to increase low-temperature strength (Ma, 2008).

Table 3.1 Composition of A380M aluminum alloy

	Composition (Weight %)					
Al	Si	Cu	Fe	Mn	Mg	Zn
85.2	8.35	3.06	0.87	0.31	0.06	2.15

The A380M was tested in the as received condition and re-melted for further testing. An SP-16A induction heater (manufactured by MTI Corporation, Richmond, CA, USA) was used for melting purposes. During induction, an alternating electric (AC) current is passed through a metal coil which creates a magnetic field. When a metal is introduced into the magnetic field, an electrical current passes through the metal and causes it to heat. The choice of the frequency of the AC used depends on the object size, material type, and the penetration depth. A suitable casting setup was designed, as shown in the Figure 3.1 to obtain different and controlled amounts of porosity in the casting. The set-up consists of crucible and crucible holder inside a sealed 60 mm diameter quartz glass tube. The

whole quartz glass tube (chamber) is placed in the water cooled alternating current solenoid coil. The crucible used is made of graphite to avoid oxidation. The chamber was first evacuated using a vacuum pump and then filled with gas mixture (Ar + 5.17% H_2) through a 2 mm glass tube inserted from the top of the chamber. These steps were done two to three times to ensure all the moisture was removed from the chamber. The alloy was melted at 700° C, at which point the solubility of hydrogen is about 0.9 mL/100g (Kaufman & Rooy, 2004). In order to supply a sufficient amount of hydrogen, the chamber was filled with the gas mixture before heating. Solidification rate, which ensures differing amounts of porosity in the casting, was controlled by changing the gas mixture and water flow rates. A pressure gauge was used to control the gas mixture flow rate and a water gauge to control the water flow rate through the Cu coil. Casting was done at a gas mixture flow rate of 10 CFH (cubic feet per hour) and without gas flow. The change in temperature during solidification was measured using an optical pyrometer.

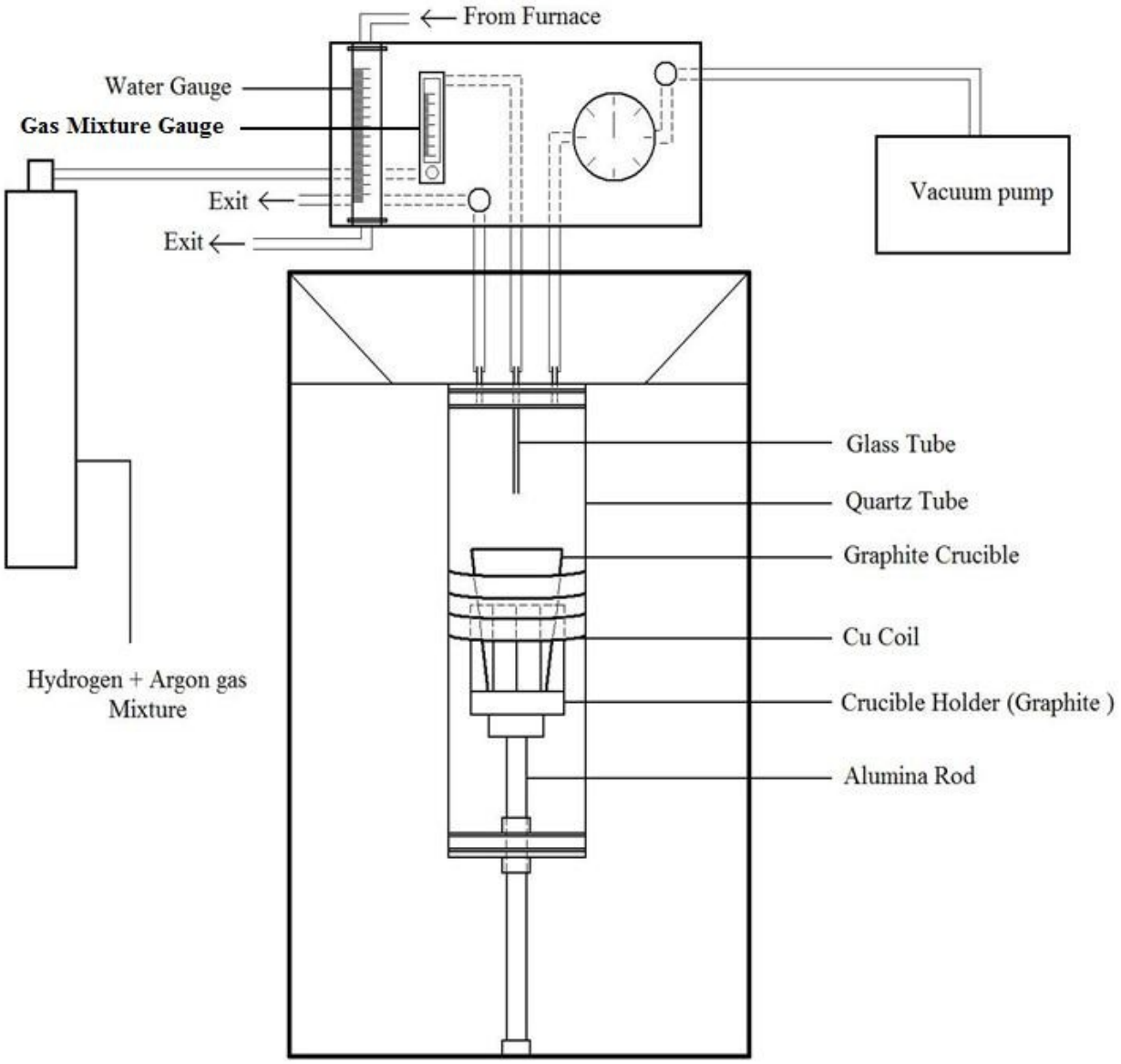

Figure 3.1 Schematic diagram of the induction furnace setup

3.1.2 P/M Processing and Sintering

In order to achieve a more uniform distribution of porosity, samples were also prepared using the powder metallurgy method. Two powders (i.e., Al-Si master alloy, 88 wt% Al + 12 wt% Si, and Al-Mg master alloy, 90 wt% Al + 10 wt% Mg) were used to produce sintered aluminum with a composition of 6 wt% Si and 0.5 wt% Mg. A Lico wax C was used as a pressing lubricant. The exact composition of Al-Si alloy is given in Table 3.2.

Table 3.2 Composition of Al – Si alloy

Element	Weight %
Al	88.8
Mg	0.5
Cu	4.5
Sn	0.2
Si	6.0

Specimens were pressed at 100, 200 and 600 MPa and sintered in a tube furnace in the presence of nitrogen gas at 560° C for 20 minutes and then slow cooled to 480° C. Some of the sintered 600 MPa samples were then swaged to further reduce the amount of porosity. The temperature profile during sintering is shown in Figure 3.2.

3.1.3 Swaging

Swaging is a method of working a material analogous to extrusion, in which the dimensions of an item are altered using a die or dies, where the item is forced. In this process a cylindrical billet is drawn out into a rod of a reduced diameter. As a billet is forced through the swaging unit, its diameter is reduced through the sequential impacts from four die segments. Prior to swaging, all bars were machined to a required diameter and placed in a furnace set to 470° C for 1 hour to reach equilibrium. After this time, the bar was swaged and returned to the furnace for 15 more minutes.

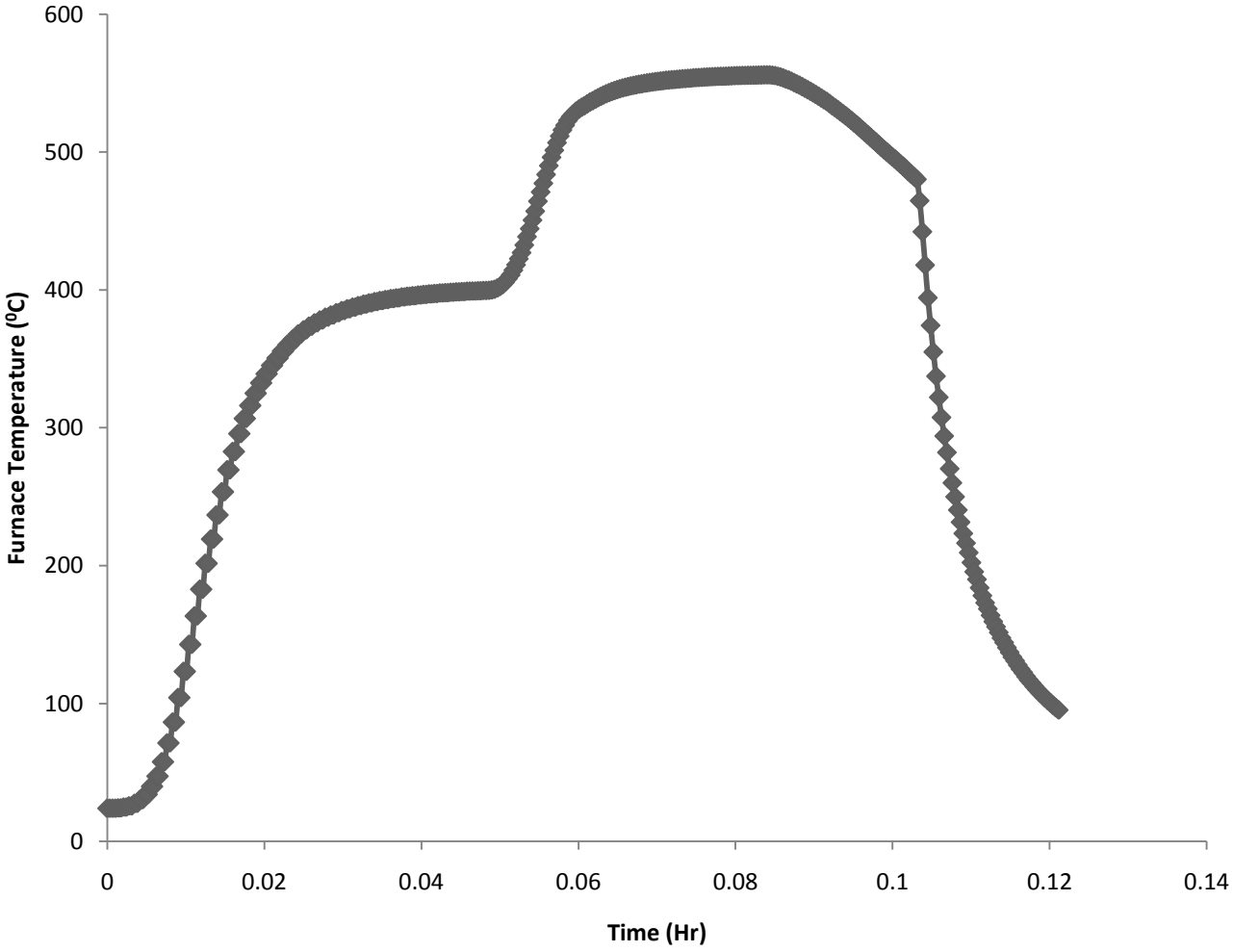

Figure 3.2 Temperature profile during sintering of Al-6wt% Si

3.2 Materials Microstructural Characterization

3.2.1 Optical Microscopy

Specimens were carefully prepared to produce acceptable quality surfaces for image analysis. Specimens were cut (20 mm × 10 mm × 5 mm), mounted and ground using 240, 320, 400 and 600 grit SiC abrasive papers and then polished using 1 μm, 0.3 μm and 0.05 μm gama alumina suspension. Keller's solution (1vol% HF + 1.5 vol% HCl + 2.5 vol% HNO_3 + 95 vol% H_2O) was used as an etching reagent and the specimens were emerged in the solution for 10-12 seconds. Olympus BX51 research microscope (Figure 3.3), equipped with bright-field objectives was used to analyze the microstructure at high resolution.

Figure 3.3 Olympus BX51 research microscope

3.2.2 Porosity Measurement

3.2.2.1 Volume Percent Porosity

The green and sintered densities of samples were determined in accordance with MPIF (Metal powder industries federation) Standard 42 (2002). In order to measure the un-sintered (green) density of the compact, the weight of the samples were taken in air (w_{air}) and after immersion in water (w_{water}). The temperature of the water was also recorded. The green density was then calculated using the following equation,

$$\boldsymbol{\rho_{Green} = \frac{W_{air} \times \rho_{water}}{W_{air} - W_{water}}} \qquad \textbf{Equation 3.1}$$

where, ρ_{water} is the density of water measured using,

$$\boldsymbol{\rho_{water} = 7 \times 10^{-8} T^3 - 1 \times 10^{-4} T + 0.9996} \qquad \textbf{Equation 3.2}$$

where T is the measured temperature of the water in degree Celsius. In order to seal the surface-connected porosity the parts/test pieces are oil impregnated or the pores are filled with a suitable material. The sintered density was performed by weighing the samples in air, prior to infiltrating them with ESSO-NUTO H46 hydraulic oil under vacuum for 30 min. The vacuum was released and the specimens were placed on a screen to drip dry for 5-7 minutes before continuing. Specimens were then lightly wiped, cleaned and weighed in air (with oil impregnation). Finally, oil-impregnated samples were weighed in water and the sintered density was calculated as follows:

$$\boldsymbol{\rho_{Sintered} = \frac{W_{air} \times \rho_{water}}{W_{ao} - W_{wo}}} \qquad \textbf{Equation 3.3}$$

where, W_{ao} is the weight of the oil infiltrated specimen in air and $W$is the weight of the oil infiltrated specimen in water. The volume percentage of porosity =

$$\boldsymbol{Vol\,\%\,porosity = 100 - \left(\frac{\text{Sintered density}}{\text{Theoretical density}} \times 100 \right)} \qquad \textbf{Equation 3.4}$$

Here, the theoretical density of the alloy was calculated to be 2.75 g/cc according to the 'rule of mixture' (Equation 3.5)

Table 3.3 Theoretical density calculation

Element	Density (g/cc)	Weight %
Al	2.70	88.8
Mg	1.73	0.5
Cu	8.72	4.5
Sn	7.31	0.2
Si	2.33	6.0

$$\rho_{Theoretical} = \frac{1}{\left(\frac{wt\,\%\,Al}{\rho_{Al}} + \frac{wt\,\%\,Mg}{\rho_{mg}} + \frac{wt\,\%\,Cu}{\rho_{Cu}} + \frac{wt\,\%\,Sn}{\rho_{Sn}} + \frac{wt\,\%\,Si}{\rho_{Si}}\right)} \qquad \textbf{Equation 3.5}$$

$$= 2.75 \text{ g/cc}$$

3.2.2.2 Area Percent Porosity

Surface porosities of samples were calculated by using image analysis software (Image-Pro Plus, version 6.3.0.512). A series of images were taken to cover the whole surface area of the sample. Porosities were identified based on their gray-level intensity differences compared to the matrix. Gray-level threshold settings were selected to permit independent detection of porosity, using the 'flicker method' of switching back and forth between porosity and the matrix. Second-phase particles and dendrite may be counted as porosity because their gray-level range is similar to that of porosity. The grey-level thresholds as well as boundary conditions (i.e., aspect ratio, min radius and area) were carefully controlled in order to avoid the identification of second-phase particles and dendrite as porosity. A counting protocol was chosen to correct for edge effects so that a porosity lying across a field boundary is counted only once (Standard Practice for Determining the Inclusion or Second-Phase Constituent Content of Metals by Automatic Image Analysis, 2008).

For each field, the area fraction of the detected area of porosity was measured by dividing the detected area of porosity by the area of the measurement field. The area fraction of the porosity of ith field (A_{A_i}) was calculated using following equation:

$$\boldsymbol{A_{A_i} = \frac{\sum_{j=1}^{j=m} A_j}{A_T}} \qquad \textbf{Equation 3.6}$$

where A_T is the total field area (μm^2) and A_j is the area of the detected jth pore (μm^2) of total 'm' pore present in the ith field. The average area fraction of porosity of the total 'n' field ($\overline{A_A}$) was calculated by:

$$\boldsymbol{\overline{A_A} = \frac{\sum_{i=1}^{i=n} A_{A_i}}{n}} \qquad \textbf{Equation 3.7}$$

where n is the number of fields measured or total number of images taken to cover the surface area of the sample. The standard deviation (*S*), 95% confidence interval (95% CI) and percent relative accuracy (% RA) was calculated by using the following equations:

$$\boldsymbol{S = \left[\frac{\sum\left(A_{A_i} - \overline{A_A}\right)^2}{n-1}\right]^{1/2}} \qquad \textbf{Equation 3.8}$$

$$\boldsymbol{95\%\, CI = \frac{St}{\sqrt{n}}} \qquad \textbf{Equation 3.9}$$

$$\boldsymbol{\%\, RA = \frac{95\%CI}{\overline{A_A}} \times 100} \qquad \textbf{Equation 3.10}$$

The value of percent porosity is expressed as the mean value plus or minus the 95% CI. Here, 't' is a constant, the value of which is expressed as a function of n. Over n = 30, the value may be defaulted to a value of 2. The percent relative accuracy (% RA) is an estimate of the percent of error of each measurement as influenced by the field-to-field variability of the values.

3.2.3 Scanning Electron Microscopy (SEM)

Hitachi S-4700 cold field Scanning electron microscopy was used to exam worn surfaces of A380M and Al-6wt% Si alloy samples and wear debris collected during wear tests. The samples were mounted to aluminum sample stubs using hot glue, and a copper tape was employed for a good conductivity. Wear debris were secured by ultra smooth carbon

adhesive tabs on 15 mm diameter aluminum sample stubs. The SEM was operated at an accelerating voltage of 10 kV, beam current of 15 μA, and working distance of 12mm. An Oxford® X-Sight 7200 Energy Dispersive Spectroscopy (EDS) system was also used for chemical analysis of wear tracks and wear debris. INCA software was then used for analyzing the acquired spectra.

3.2.4 Atomic Force Microscopy

The micro-topography of the surface was characterized using an Ambios Atomic Force Microscope (AFM) system (Figure 3.4). Measurements of surface topography were performed in air and at ambient conditions and covered an area of 250 x 250 μm. Samples were scanned using a non-contact (intermittent) cantilever vibrating at a resonance frequency of 150 KHz and attached to a silicon probe having a tip radius of 20 nm. Tests were performed at a scan rate of 1 Hz. The AFM image of the polished surface is shown in Figure 3.5. The average surface roughness measured by atomic force microscope is about 1.34 μm.

Figure 3.4 Atomic force microscope

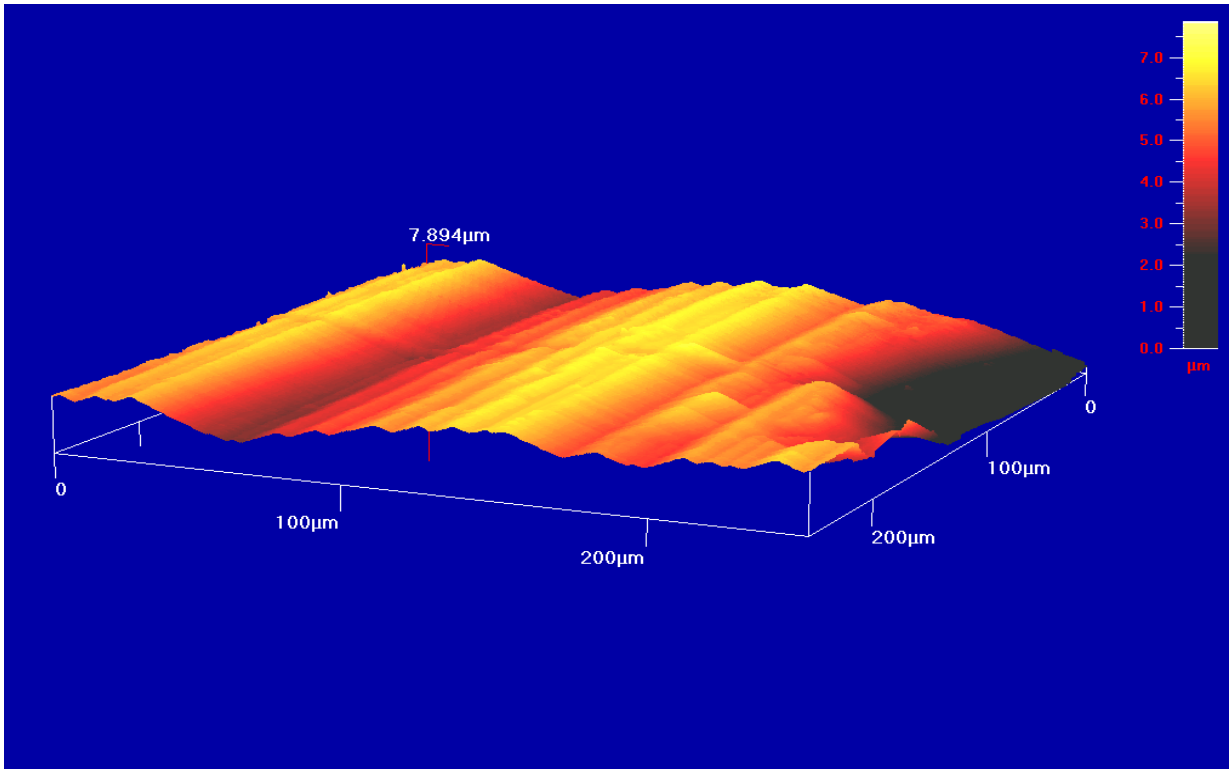

Figure 3.5 Surface topography of polished A380M sample

3.2.5 X-ray Diffraction

X-ray diffraction was conducted on as received A380M. The specimen was cut (20 mm × 10 mm × 5 mm) ground and polished down to 0.05 µm, as described in section 3.2.1. The samples were then cleaned in methanol in an ultrasonic bath and mounted in a specimen holder. X-ray diffraction (XRD) was carried out employing a high-speed Bruker D8 Advance XRD system. The XRD system uses a high-speed LynxEye^{TM} detector and CuKα radiation having a wave length of 1.54 Å, tube voltage of 40 kV and tube current of 40mA (Figure 3.6). Samples were scanned from a 2θ angle of 20° to 140° with a step size of 0.049°. Diffraction patterns were analyzed using Bruker's EVA software and compared to known diffraction patterns present in the International Centre for Diffraction Data (ICDD) powder diffraction file (PDF) database. Al and Si peaks were matched to those in the Powder Diffraction Files and identified as having an FCC crystal structures. The XRD pattern for the A380M is shown in Figure 3.7.

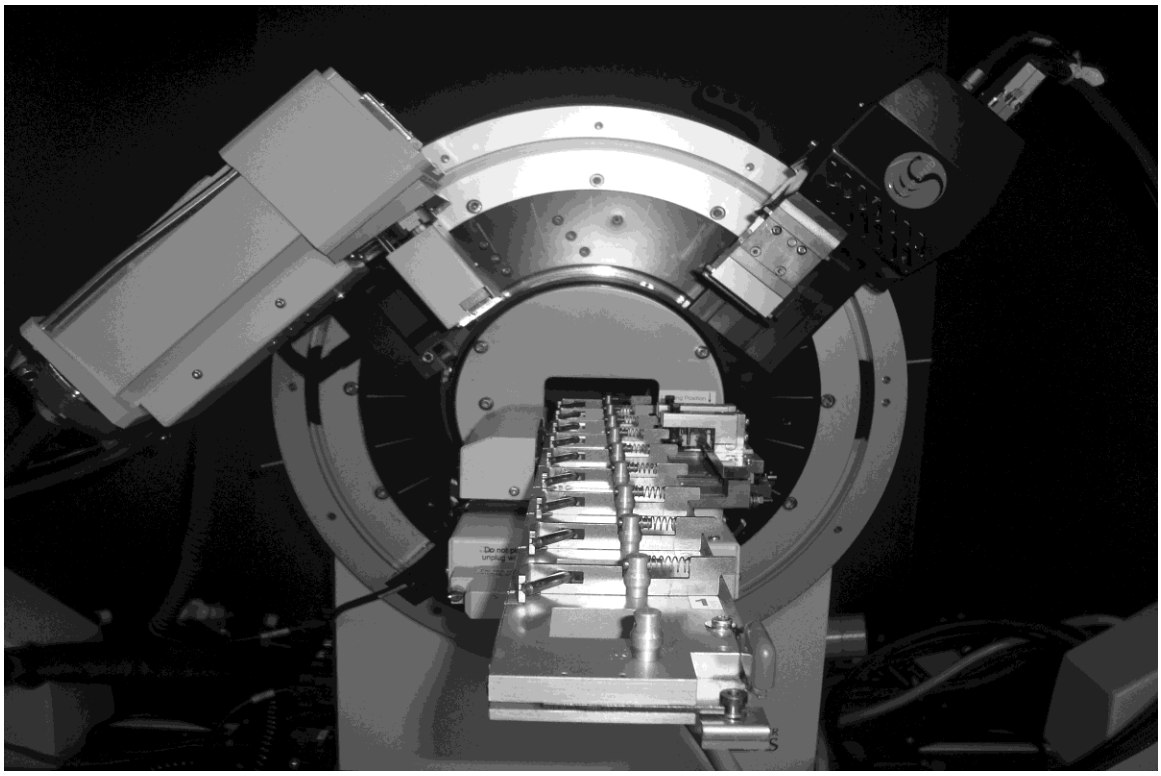

Figure 3.6 Bruker D8-Advance XRD system

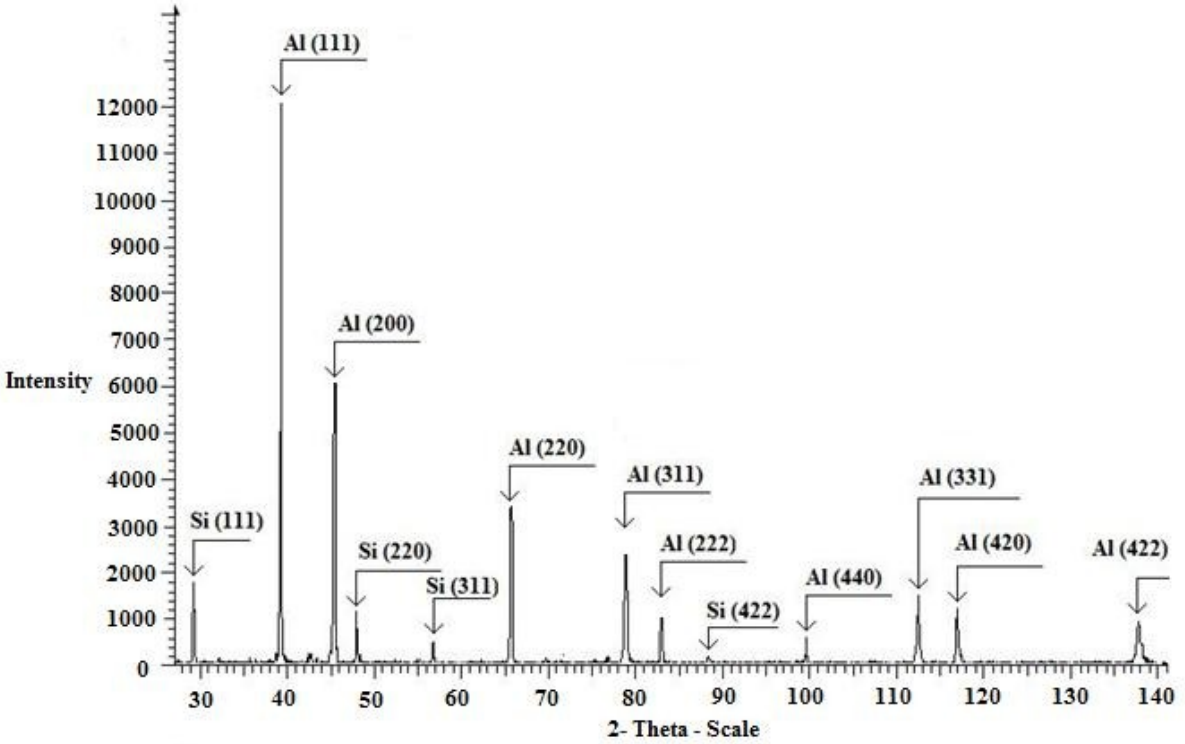

Figure 3.7 XRD patterns of A380M aluminum alloy

3.3 Macro and Micro Mechanical Properties

The macro and micro mechanical properties of the samples were investigated using Rockwell hardness testing and nanoindentation.

3.3.1 Rockwell Hardness Testing

Rockwell hardness tests were carried out in all specimens of A380M and Al-6wt% Si alloys. Tests were performed on a Leco R600 Rockwell hardness tester (Figure 3.8) using the 'A' scale under a load of 60 Kg and a diamond indenter. Prior to testing, specimens were ground and polished as above. The Rockwell hardness test device was calibrated prior to operation using standard calibration blocks. Six indentations were made at random locations for all the samples. Three of them were performed on the top face and three on the bottom.

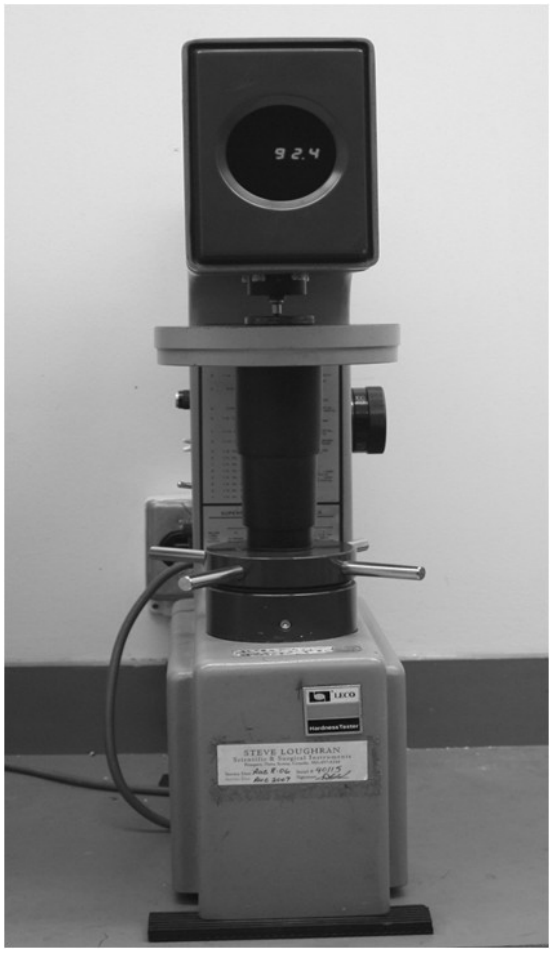

Figure 3.8 Rockwell hardness tester (Leco R600)

3.3.2 Nanoindentation

Nanoindentation experiments were conducted using a nanoindentation system (developed by CETR, USA) having a nanohardness head and a controller attached to a CETR multifunctional tribometer system. The instrument uses a Berkovich diamond pyramid (Figure 3.9) with an angle of 65.3° between the tip axis and the faces of the triangular pyramid. The displacement of the indentation and the load could be measured independently with a resolution of 0.03 nm and 0.1 μN, respectively. Twelve measurements at twelve different locations on the polished surface were produced on a given specimen using maximum load range from 50 mN to 400 mN in order to insure any irregularities in the surface will not affect the hardness values significantly. The test generates a depth versus load curves that can be used to calculate hardness and elastic modulus of the materials. The total penetration depth consists of a plastic component and an elastic recovery component which occurs during the unloading. Maximum indentation depth (h_{max}) can be expressed as:

$$\boldsymbol{h_{max} = h_c + \left[\frac{(\pi-2)}{\pi}\right]\left(\frac{2P_{max}}{\frac{dp}{dh}}\right)} \qquad \textbf{Equation 3.11}$$

h_{max}, P_{max} and slope at maximum load, dp/dh are determined from the load versus displacement profile. Hardness (H) at the maximum applied load was calculated using Oliver and Pharr method (Oliver & Pharr, 1992). The relationship between Hardness (H) and the maximum applied load (P_{max}) is as follows,

$$\boldsymbol{H = \frac{P_{max}}{A}} \qquad \textbf{Equation 3.12}$$

where A is the contact area and for Berkovich indenter is given by,

$$\boldsymbol{A = 24.5\, h_c^{\,2}} \qquad \textbf{Equation 3.13}$$

where h_c is the contact depth. The elastic modulus can be expressed as,

$$E^* = \frac{1}{2}\frac{dp}{dh}\frac{\sqrt{\pi}}{\sqrt{A}} \qquad \textbf{Equation 3.14}$$

where

$$\frac{1}{E^*} = \frac{1-\nu_1^2}{E_1} + \frac{1-\nu_2^2}{E_2} \qquad \textbf{Equation 3.15}$$

Here, E_2 and ν_2 are elastic modulus and Poisson's ratio of the test material, and E_1 and ν_1 are the same parameters for Berkovich indenter. In the current analysis E_1 and ν_1 were taken as 1141 GPa and 0.07, respectively.

Nano-indentation test was performed in A380M aluminum alloy. Figure 3.10 shows the force-displacement (penetration depth of indenter) curve for A380M aluminum alloy. The effective plastic depth of penetration h_c was computed by a regression line through the unloading curve over the upper 50% of the data, and then the hardness at the maximum load was calculated from the value of h_c. The elastic modulus, however, was calculated from the slope of the upper 50% portion of the unloading part of the curve. Table 3.4 summarizes the mechanical properties of A380M obtained from the nanoindentation test. Hardness and elastic modulus represent an average of 12 tests at different maximum loads.

Table 3.4 Nanoindentation test data for A380M

Physical properties	
Young's modulus (GPa)	49.75
Hardness (GPa)	1.03

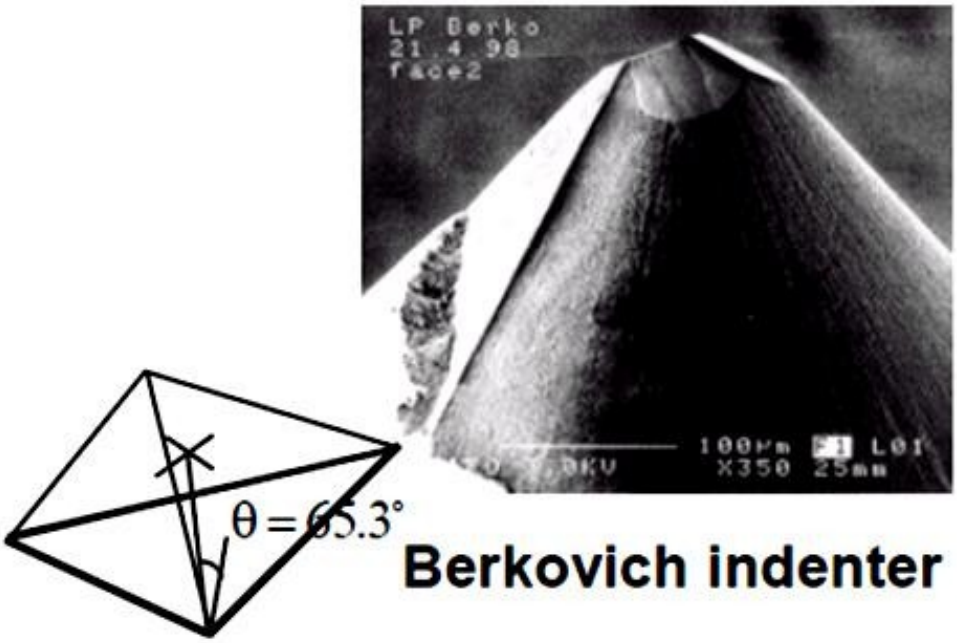

Figure 3.9 Berkovich diamond indenter (Liang, et. al, 1996)

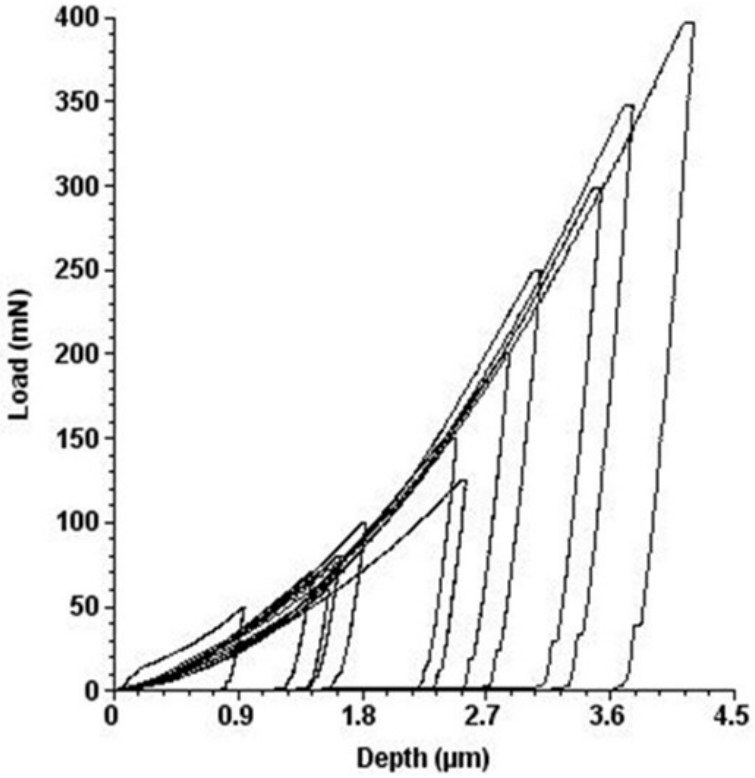

Figure 3.10 Load vs indentation depth profile for A380M

3.4 Tribological Characterization

3.4.1 Reciprocating Wear Test

Dry reciprocating wear tests were performed using a Universal Micro-Tribometer (UMT) (manufactured by CETR, USA). This test method utilizes a ball upper specimen that slides against a flat lower specimen in a linear, back and forth, sliding motion, having a stroke length of 5.03 mm. All tests were conducted at room temperature and at a relative humidity of 40-55%. The load is applied downward through the ball specimen against the flat specimen mounted on a reciprocating drive. The specimens were securely fastened inside the wear chamber. The tester allows for monitoring the dynamic normal load, friction force and depth of the wear track during the test. Figure 3.11 depicts an image of the wear chamber and the sliding ball of the UMT tribometer.

A 6.3 mm diameter AISI 52100 bearing steel ball having a hardness of HRA 83 was used as a counter-face material. The ball was mounted inside a ball holder which was attached directly to a suspension system which, in turn, is attached to a load sensor that controls and records forces during the test. The instantaneous values of calibrated normal load (F_Z), tangential load (F_X), and depth of wear track (Z) were measured and continuously recorded using a data acquisition system. The data automatically calculates the variation of the coefficient of friction, COF ($\mu = F_X/F_Z$), with time. The weight of the specimen was measured before and after each wear test to determine individual weight-loss at selected time intervals. The test condition for the reciprocating test is given in Table 3.5. For A380M aluminum alloy, four different loads (6 N, 10 N, 15 N and 20 N) were employed; each was tested under four different frequencies (4 Hz, 10 Hz, 15 Hz and 20 Hz) and five different time intervals (10 min, 30 min, 45 min, 60 min and 90 min). For the Al-Si alloy, four different loads (6 N, 10 N, 15 N and 20 N) were employed, with each being tested under 15 Hz frequency and at five different time intervals (10 min, 30 min, 45 min, 60 min and 90 min).

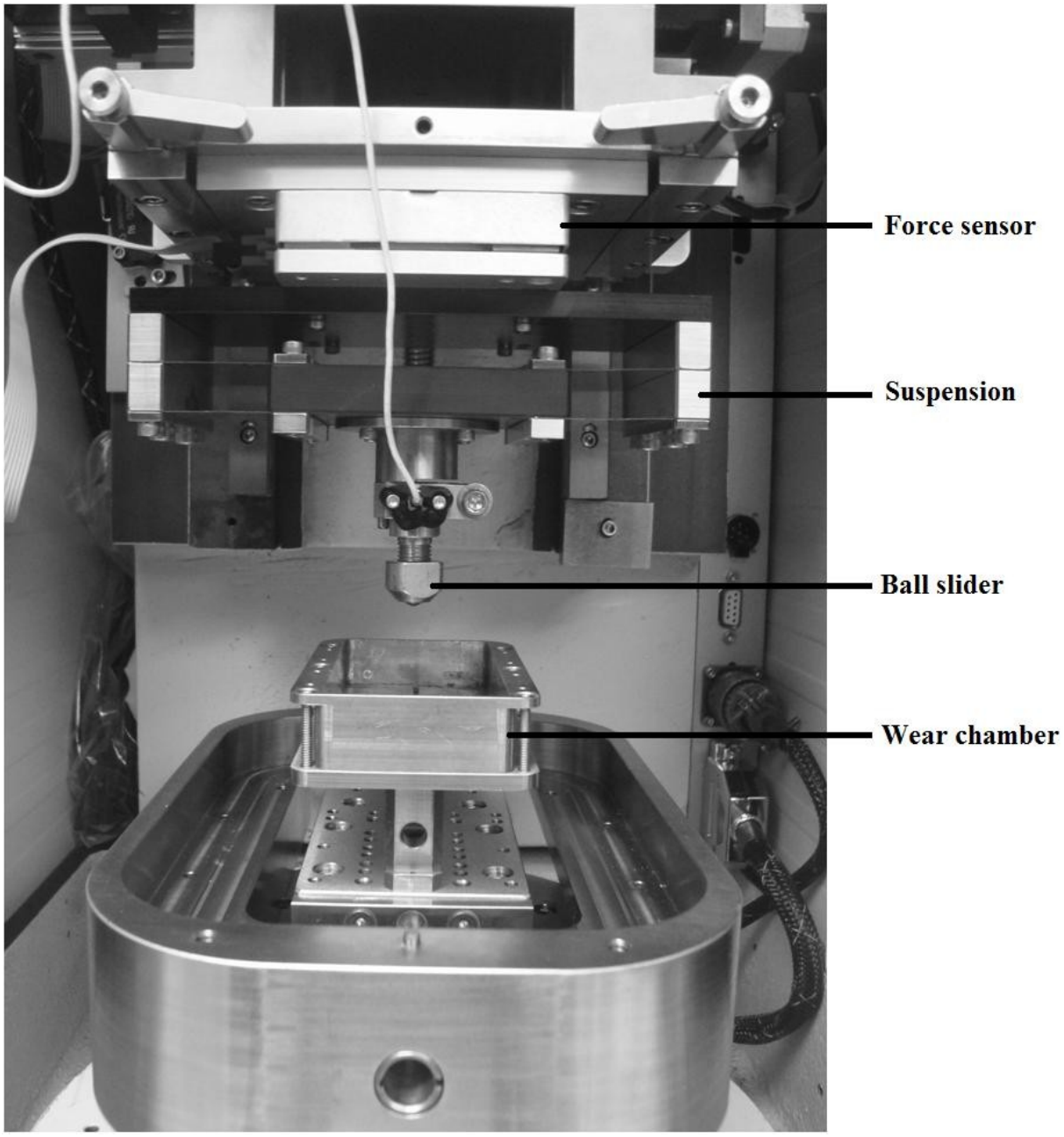

Figure 3.11 Ball-on-flat reciprocating wear tester

Table 3.5 Operating condition for reciprocating wear test

Test Conditions	
Lubricant	None
Temperature	Ambient
Pressure	1 atm
Relative humidity	40 – 55 %
Stroke length	5.03 mm

CHAPTER 4 RESULTS AND DISCUSSION

4.1 A380M Aluminum Alloy

4.1.1 Microstructural Characterization

Hydrogen is the only gas that is appreciably soluble in aluminum and its alloys. The solubility increases rapidly with increasing temperature above the liquidus (Kaufman & Rooy, 2004). Porosity in aluminum casting is caused by the bubbling of hydrogen from liquid solution or by shrinkage during solidification, though more usually by a combination of both effects. During cooling and solidification, dissolved hydrogen in excess of the extremely low solid solubility limit may bubble in molecular form, resulting in the formation of primary and/or secondary voids. Slower solidification rate allows for a longer time for H_2 evolution.

In the current study, hydrogen gas was intentionally added during casting to induce porosity. The combination of solidification rate and gas (Ar + 5.17% H_2) flow were used to control the total amount of porosity in the samples. As-received A380M aluminum alloy was melted with 10 CFH gas flow and without gas flow. The percentage of average surface porosity (gas + shrinkage) ranges from 2.6 % for the as-received to 6.9 % for the specimen melted without-gas flow (Table 4.1). The gas porosity in the table represents the total amount of porosity due to hydrogen gas evolution only. While the gas + shrinkage porosity is due to both shrinkage and gas evolution. The average porosity values in Table 4.1 represent the average of gas porosity and gas + shrinkage porosity. The optical micrographs in Figure 4.1 (a) and (b) reveal dendritic structures, typical of cast structures. Both microstructures revel a uniform distribution of Si particles having grain sizes of about 39 μm and 51 μm (Table 4.1) for specimens prepared with and without gas flow, respectively. The aluminum matrix exhibit a similar trend, i.e., the specimens cast with gas flow have a smaller aluminum grain size of 101 μm as opposed to 179 μm for specimen cast with no gas flow. The differences in grain sizes between specimens, prepared using the two different casting conditions is attributed to the variation in cooling rates. That is, the specimen prepared with gas flow undergoes faster cooling rate (as will be discussed later), hence, smaller grain size. Moreover, the pores

are irregular in shape for castings prepared with 10 CFH gas flow while those for castings prepared without gas flow are more rounded in shape. The as-received specimen microstructure (Figure 4.1 (c)) exhibits lower porosity, finer matrix and small Si particles than the specimen cast in the laboratory, with total porosity at around 2.6%. Rapid solidification, absence of hydrogen gas and high pressure during solidification are the reasons for lower porosity in the as-received specimen.

Table 4.1 Grain size and % surface porosity of cast A380M aluminum alloy

Specimen	Matrix grain size (μm)	Si particle size (μm)	Gas pore size (μm^2)	Shrinkage + gas pore size (μm^2)	% gas porosity	% gas + shrinkage porosity	% average surface porosity
As received	6.7	2.5	8.1	62.3	0.6	1.9	2.6 ± 0.11
10 CFH gas flow	101.1	39.2	17.8	96.3	1. 2	2.3	3.5 ± 0.02
Without gas flow	179.1	51.1	9.7	137.5	0.8	6.2	6.9 ± 0.08

Figure 2.8 illustrates that the solubility of hydrogen in aluminum just above the liquidus is 0.69 ppm and just below the solidus is 0.04 ppm. The higher the amount of dissolved hydrogen in the melt the higher will be the porosity (gas and gas + shrinkage) in the cast due to the evolution of gas during solidification. Contrary to expectations, the % average surface porosity for casting prepared without-gas flow (6.9%) is higher than that prepared with 10 CFH gas flow (3.5%). It is suspected that, 'dissolved hydrogen in the melt', 'solidification rate' and 'gas pressure' are the three contributing factors that control the amount of porosity and pore size in the casting, as discussed below. These three factors simultaneously work together in a complex dynamic fashion and ultimately determine the amount of porosity and size of pores.

From Figure 2.9, it is clearly seen that total percent porosity decreases with an increase in solidification rate. In this study the temperature drop measured during solidification is plotted in Figure 4.2 for the two casting conditions. The cooling rates calculated from the

slopes of the best fit lines in Figure 4.2 for the casting prepared without-gas flow and the casting prepared by injecting 10 CFH of the gas mixture are about 0.14° C/s and 0.26° C/s, respectively. The gas mixture that flows into the melting chamber during casting is at room temperature and reduces the temperature of the melt rapidly during solidification. A high solidification rate does not allow sufficient time for the evolved hydrogen to diffuse and combine with shrinkage porosity to form large gas + shrinkage porosity. Hence, it is expected that, specimens prepared with higher solidification rate (10 CFH) will have large gas porosity (less time available to diffuse and combine with shrinkage porosity) and smaller gas + shrinkage porosity (both in size and amount) compared with the specimen prepared with slower solidification rate (no gas flow). Furthermore, from Equation 2.2, a pore is stable and can grow (Gruzleski & Closset, 1990), when it satisfies,

$$P_g + P_s \geq P_{atm} + P_H + P_{s\text{-}t}$$

In the case of casting prepared by injecting 10 CFH gas mixture, additional pressure is added at the right-hand side of the equation, as the gas enters into the chamber at a relatively high velocity. The additional gas pressure makes it difficult for gas and gas + shrinkage pores to grow. So, it can be deduced that if other factors are constant, both the size and amount of gas and gas + shrinkage porosity will be less in 10 CFH casting condition.

As shown in Figure 4.1 (a), (b) and Table 4.1, the gas pore size and % gas porosity for 10 CFH gas flow (18 μm^2 and 1.2) are higher than specimens cast with no gas flow (10 μm^2 and 0.8). Although gas pressure limits the amount of porosity and pore size as explained above, the combined effect of more dissolved hydrogen and higher solidification rate (not allowing enough time for the evolved hydrogen to diffuse and combine with shrinkage porosity) are the reason for higher gas porosity (1.2%) and larger pore size (18 μm^2) in the specimens cast with 10 CFH gas flow as opposed to specimen cast with no gas flow. On the other hand, the size and % gas + shrinkage porosity for the specimens cast with 10 CFH gas flow (96 μm^2 and 2.3) are less than the specimen cast with no gas flow (138 μm^2 and 6.2). Higher dissolved gas in the specimens cast with 10 CFH is expected to result in higher amounts of gas porosity and larger gas + shrinkage pores than specimens

cast with no gas flow. However, this is restricted by higher solidification rate and higher gas pressure. Hence, it can be said that, higher dissolved hydrogen gas in the melt does not always end up with higher porosity in the cast. It is the combined effect of dissolved hydrogen, solidification rate and gas pressure which determines the final porosity characteristics.

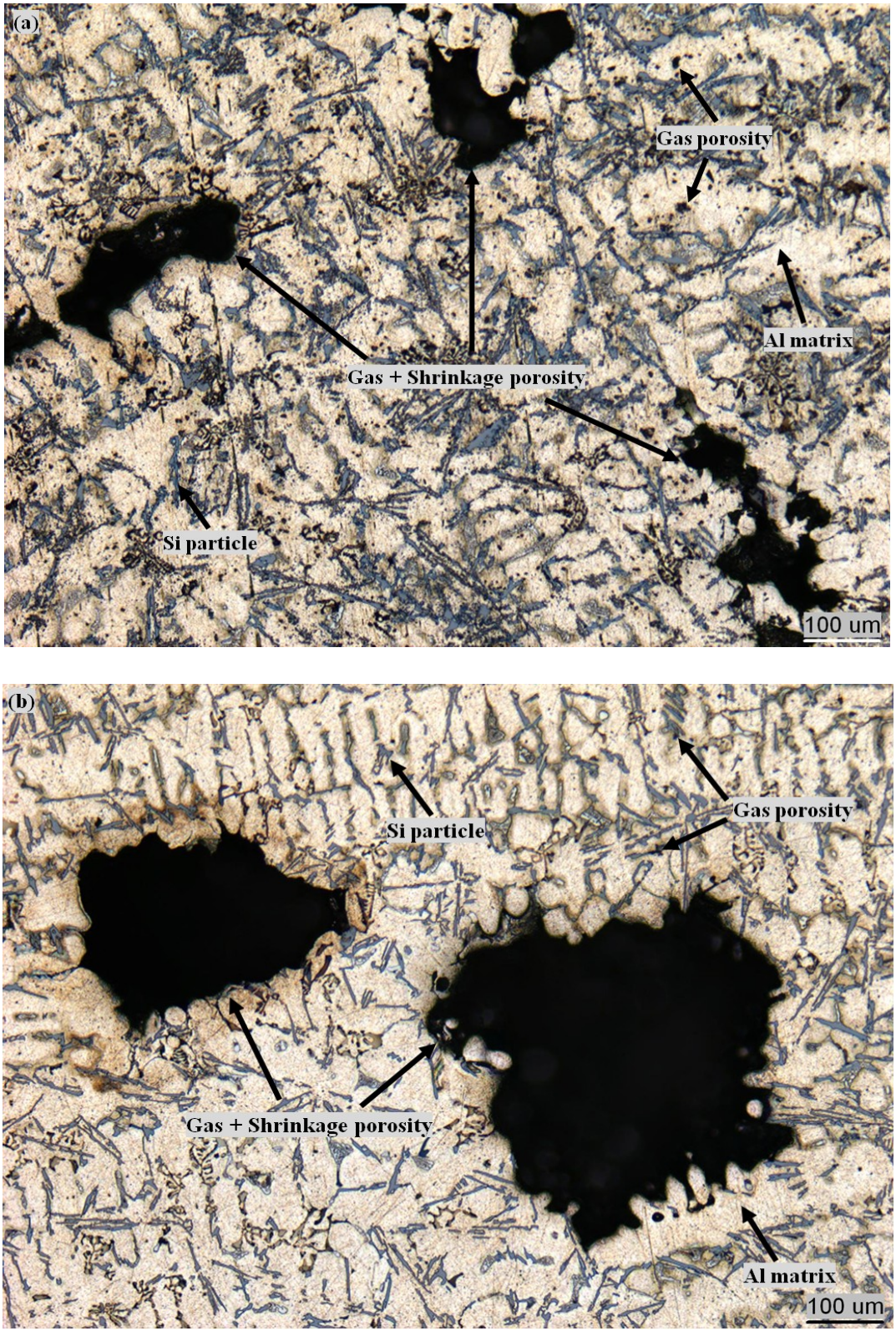

Figure 4.1 Optical micrograph of A380M (a) cast in the presence of 10 CFH gas flow, (b) cast without gas flow

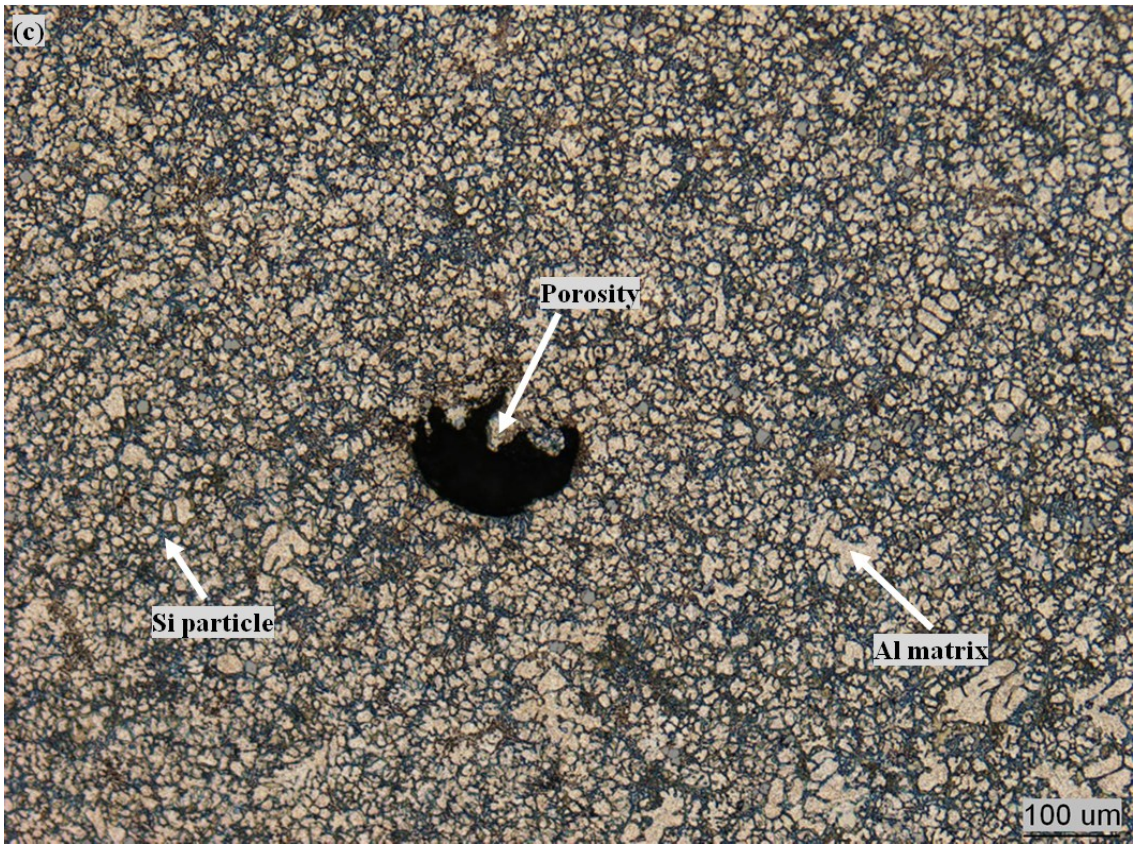

Figure 4.1 Continued, optical micrograph of (c) as received

In order to investigate the effect of porosity on the hardness of an A380M aluminum alloy, a series of Rockwell hardness measurements were conducted and plotted in Figure 4.3. As one would expect, increase in % surface porosity of the specimens decreases the hardness as a result of a weaker structure and, hence, softer material. The hardness of the specimens containing 6.9%, 3.5% and 2.6% porosity are around 47 HRA, 55 HRA and 63 HRA, respectively. This represents a reduction in hardness of around 33 % as porosity increases from 2.6% to 6.9 %.

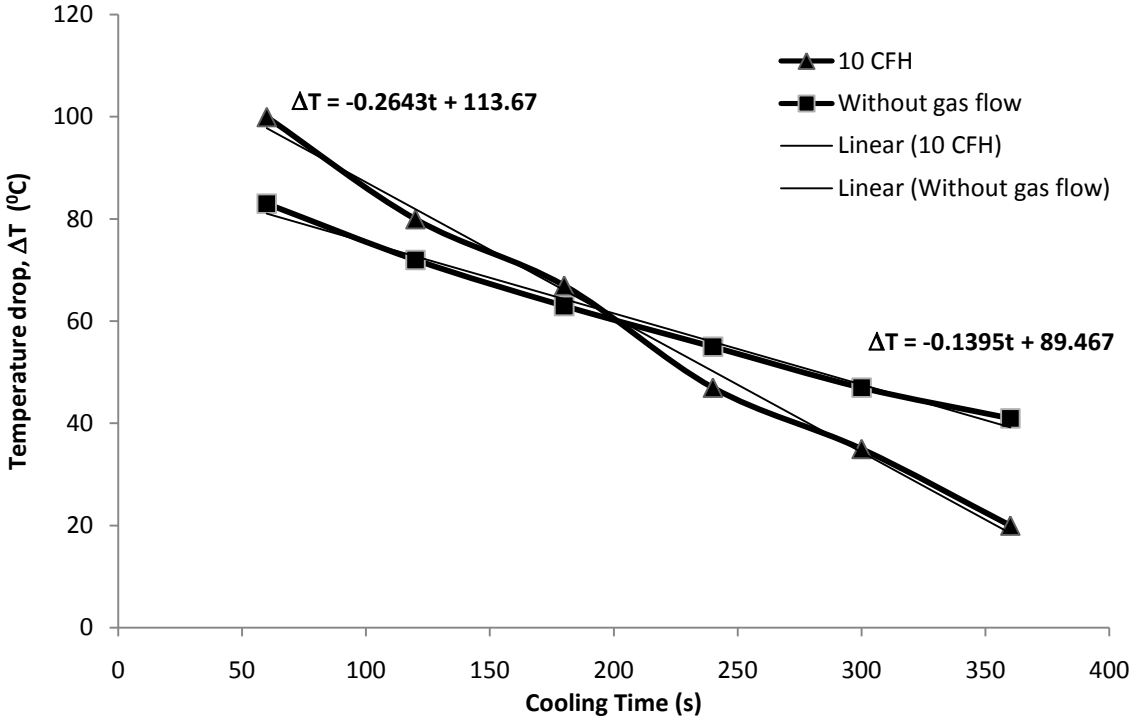

Figure 4.2 Temperature drop during solidification

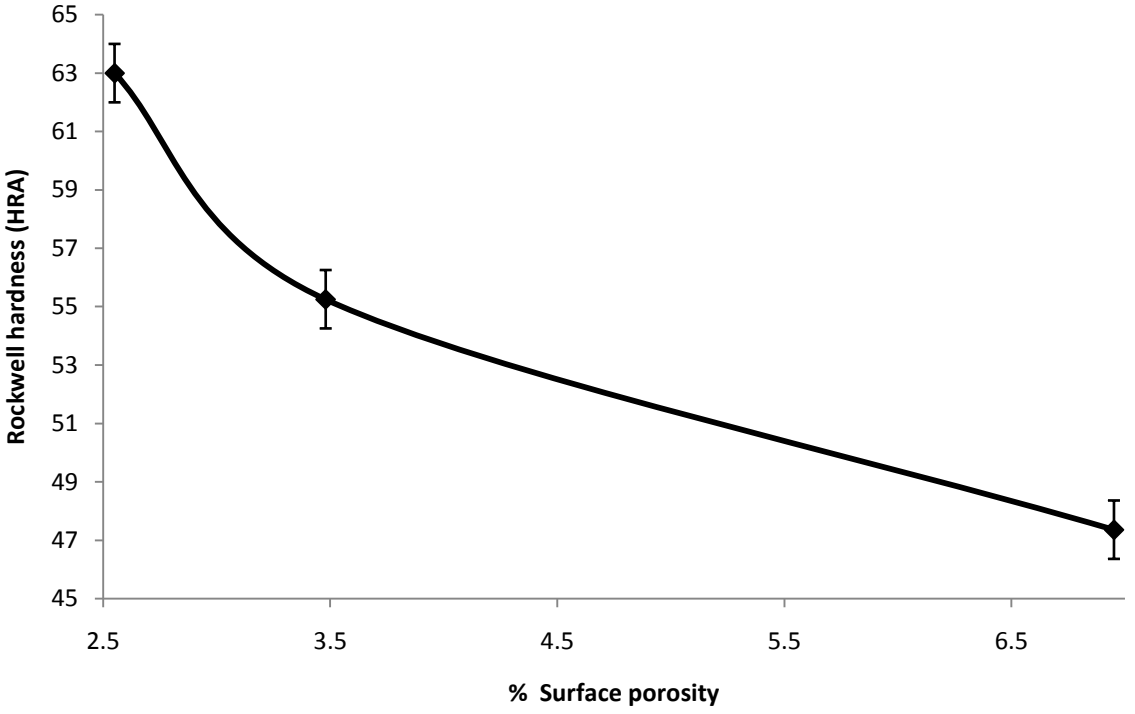

Figure 4.3 Variation of hardness with porosity content for A380M aluminum alloy

4.1.2 Tribological Behavior

4.1.2.1 Coefficient of Friction

Dry sliding wear behavior was investigated in the load range 6 – 20 N against AISI 52100 bearing steel ball using a reciprocating ball-on-flat configuration. The instantaneous values of calibrated normal force (*Fz*) and tangential force (*Fx*) were measured and continuously recorded, using a data acquisition system. The acquisition system automatically calculates the variation of the coefficient of friction, COF ($\mu = Fx/Fz$) with time. The magnitude of subsurface plastic strain and depth of highly deformed zone depend on COF (Menezes, et. al, 2009). The higher the coefficient of friction, the deeper is the deformation zone and extent of plastic strain. Figure 4.4 shows the coefficient of friction as a function of sliding frequency for as received, cast condition 1 and cast condition 2. For convenience, specimens cast with 10 CFH gas flow and without-gas flow are termed as, cast condition 1 and cast condition 2, respectively. It can be seen that, the coefficient of friction decreases gradually with an increase in sliding frequency for A380M aluminum alloy. The value of COF at highest frequency is about one half of its value at low frequency in the frequency range investigated. It is suspected that at low frequency, longer time is available for the formation and growth of asperity junctions in contact regions, which increases the force required to shear off the junction to maintain relative motion, hence, high coefficient of friction. Dwived (Dwivedi, 2006) reported similar findings for cast hypereutectic aluminum silicon alloys. Furthermore, it is observed that COF is sensitive to the applied load especially in the low frequency range and it is, in general, found to increase with load. The coefficient of friction is plotted as a function of porosity in Figure 4.5. As shown in the figure, the coefficient of friction increases with increasing porosity. The coefficient of friction in the specimens containing 2.6%, 3.5% and 6.9% porosity were determined to be 0.30, 0.32 and 0.34, respectively. Yalcin (Yalcin, 2009) found similar results (increase in COF with increasing porosity) and he further suggested that, under dry friction conditions, a decrease in the coefficient of friction results in a decrease in the mass loss of the porous material.

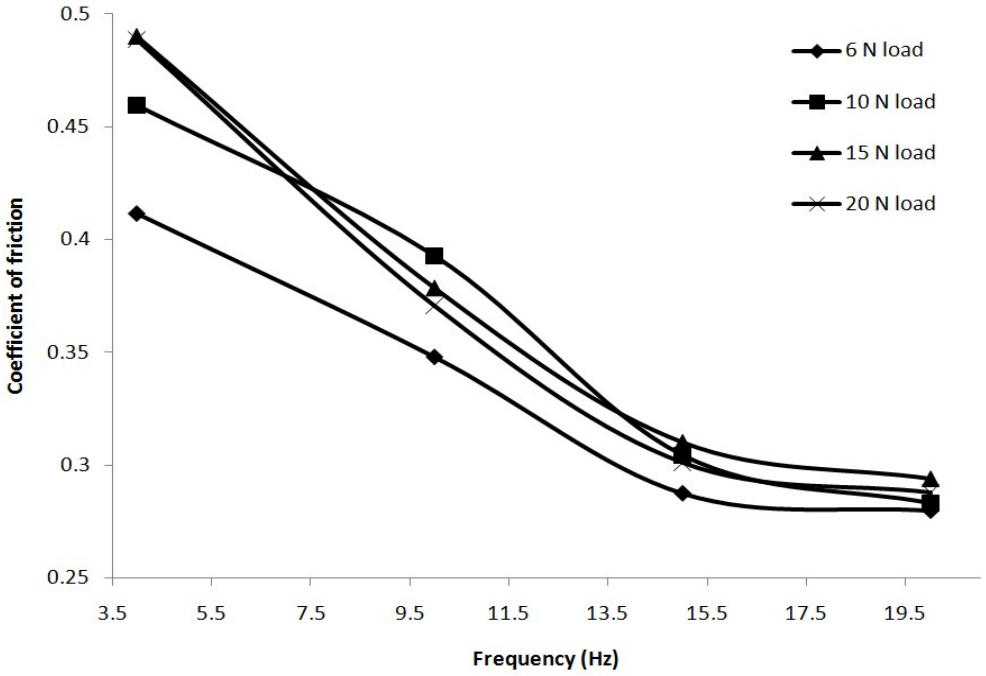

(a)

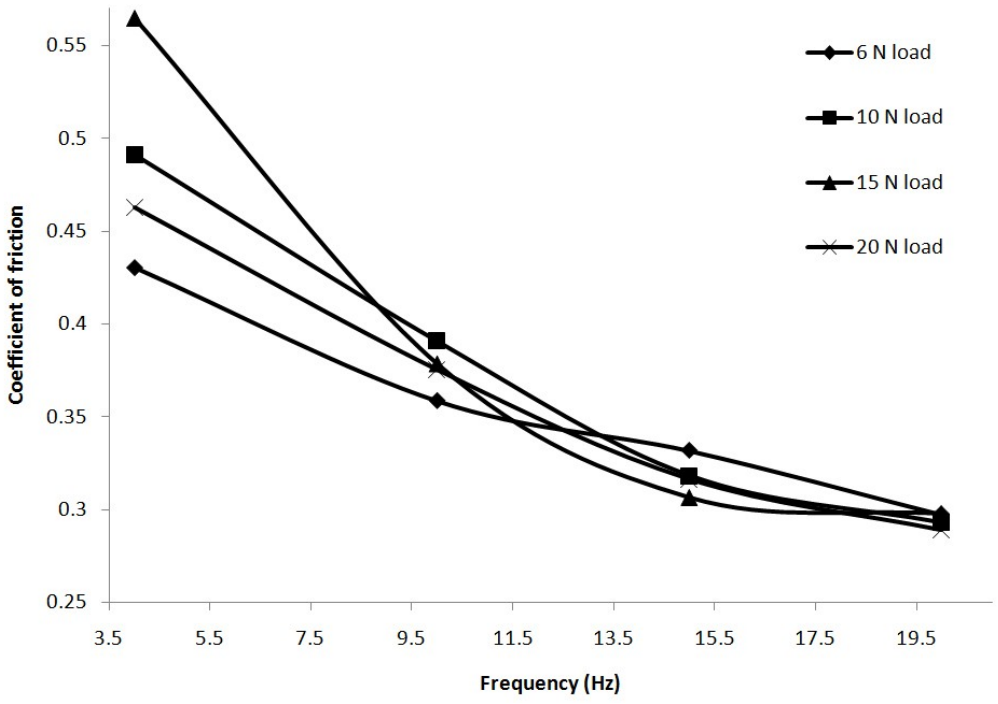

(b)

Figure 4.4 Coefficient of friction vs frequency for A380M at different normal loads (a) as received (b) cast condition 1

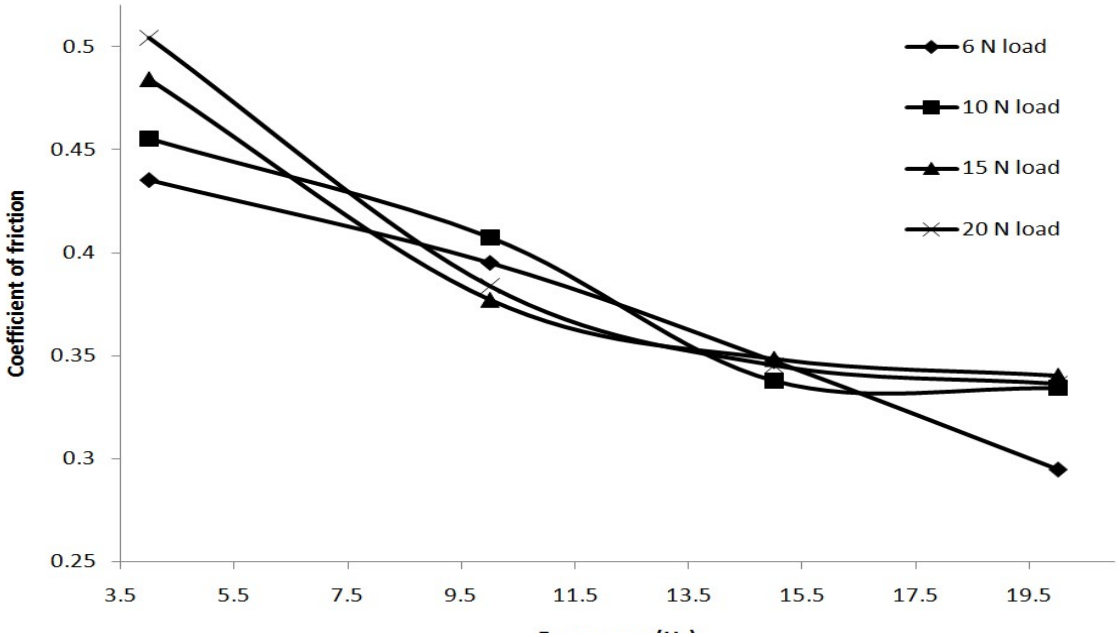

(c)

Figure 4.4 Continued, Coefficient of friction vs frequency at different normal load (c) cast condition 2

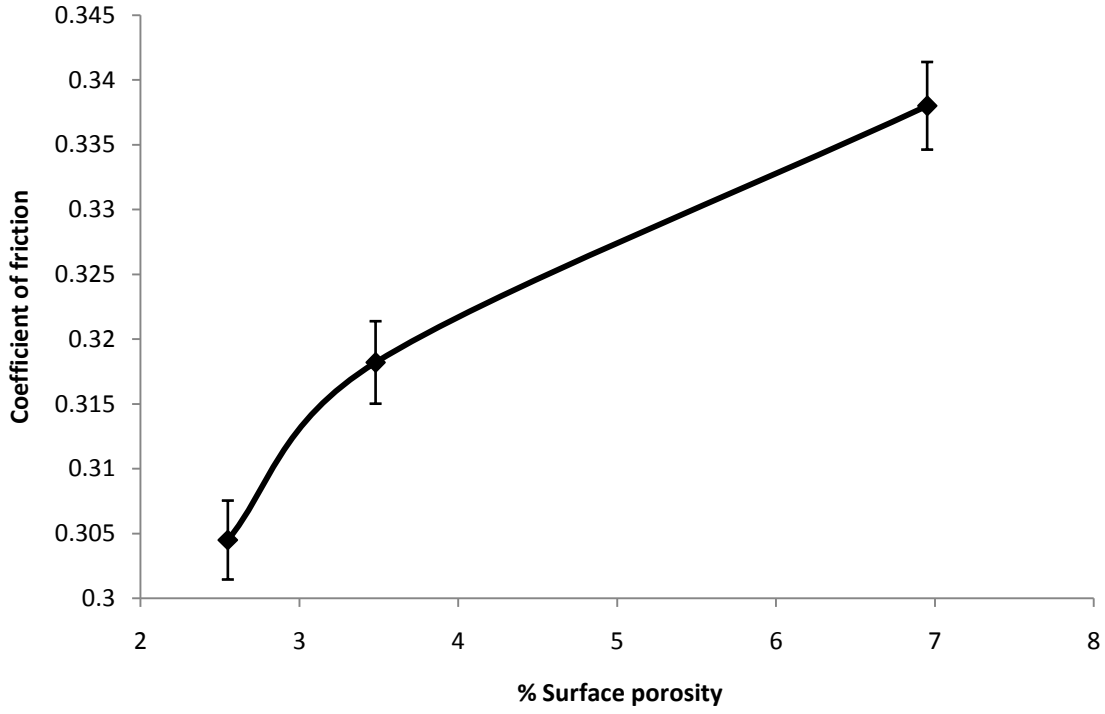

Figure 4.5 COF as a function of surface porosity for A380M aluminum alloy (At 10 N and 15 Hz)

Figure 4.6 depicts a representative plot that shows the variation of weight loss with sliding distance for as-received specimens tested under four different normal loads, 6 N, 10 N, 15 N and 20 N at 20 Hz. Appendix 'A' gives all the data collected during wear tests under various experimental conditions. The plots in Figure 4.6 reveal a somewhat linear increase (with no transition) in weight-loss with sliding distance. It was observed that, at any given sliding distance, weight-loss increases with applied load, as is evident by the upward shift in the weight-loss versus sliding-distance curves. This trend is in agreement with the work of other researchers (Tu, et. al, 2003; Deshpande & Lin., 2006; Ye, Li, & Eadie, 2001; Vardavoulias, et. al, 1993; Hiratsuka, 2005; Hamid, et. al, 2008; Uyyuru, et. al, 2006). Wear rates, calculated as the slopes of the weight-loss versus sliding-distance curves, under all conditions, are plotted as functions of applied loads, frequencies and surface porosities, as presented below.

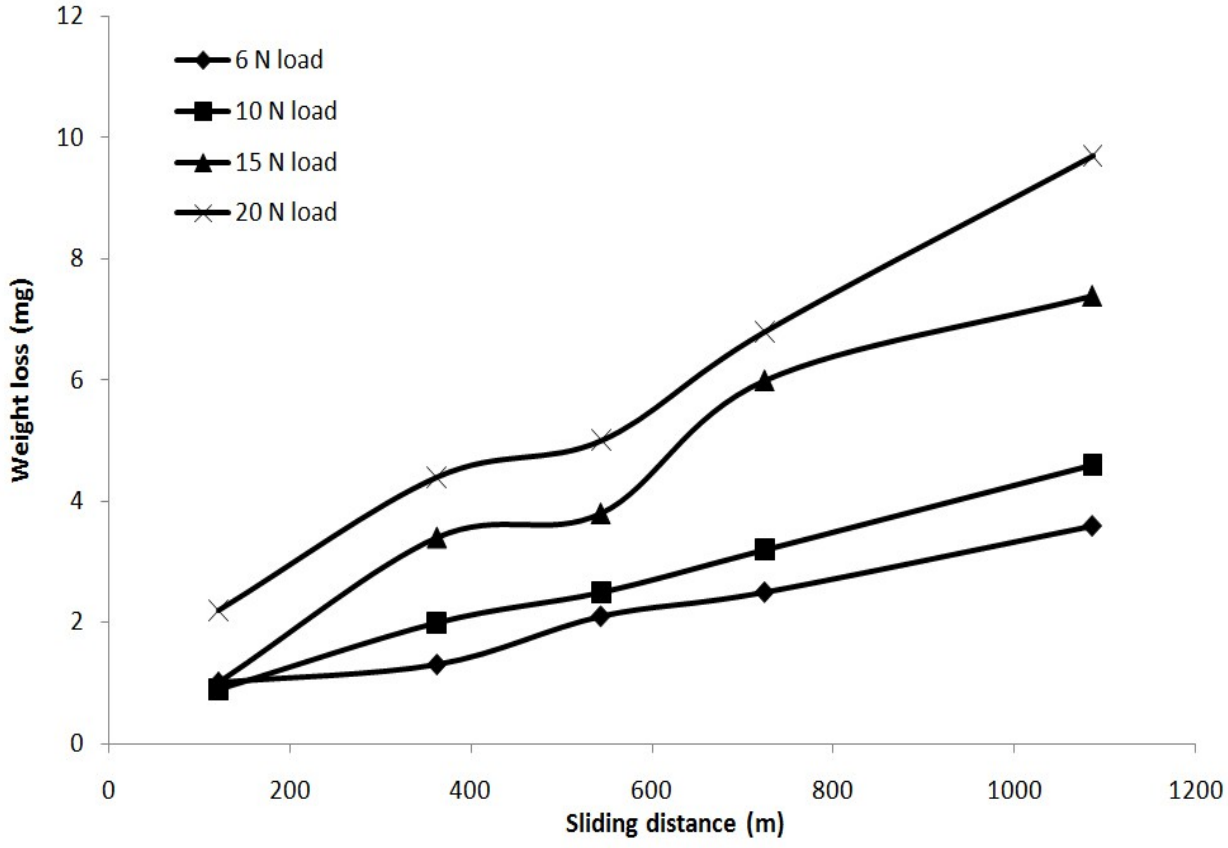

Figure 4.6 Weight-loss vs sliding distance at 20 Hz for as-received A380M

4.1.2.2 Effect of Normal Load

As shown in Figure 4.7 (a)-(c), the wear rate increases steadily with load. For as-received specimens, the wear rates almost double with an increase in normal load from 6 N to 20 N for all frequencies. Specimens prepared using cast condition 1 and cast condition 2 exhibit similar behavior (a steady increase in wear rate with increasing normal load) for all sliding frequencies. However, as clearly seen in Figure 4.7, wear rate tends to reach a steady state at loads higher than 15 N, at which the wear rate becomes less sensitive to load variations, except for the as-received specimens tested at 4 Hz. The increase in wear rate with an increase in normal load can be explained by hertzian analysis which will be discussed below. Increase in wear rate with normal load has also been observed by others (Hiratsuka, 2005; Alpas & Zhang, 1992; Hamid, et. al, 2008). However, with increasing normal load the wear is more severe for 4 Hz frequency than 10 Hz, 15 Hz and 20 Hz frequencies for as received, cast condition 1 and cast condition 2 specimens. The sensitivity of wear rate to frequency is discussed in the next section.

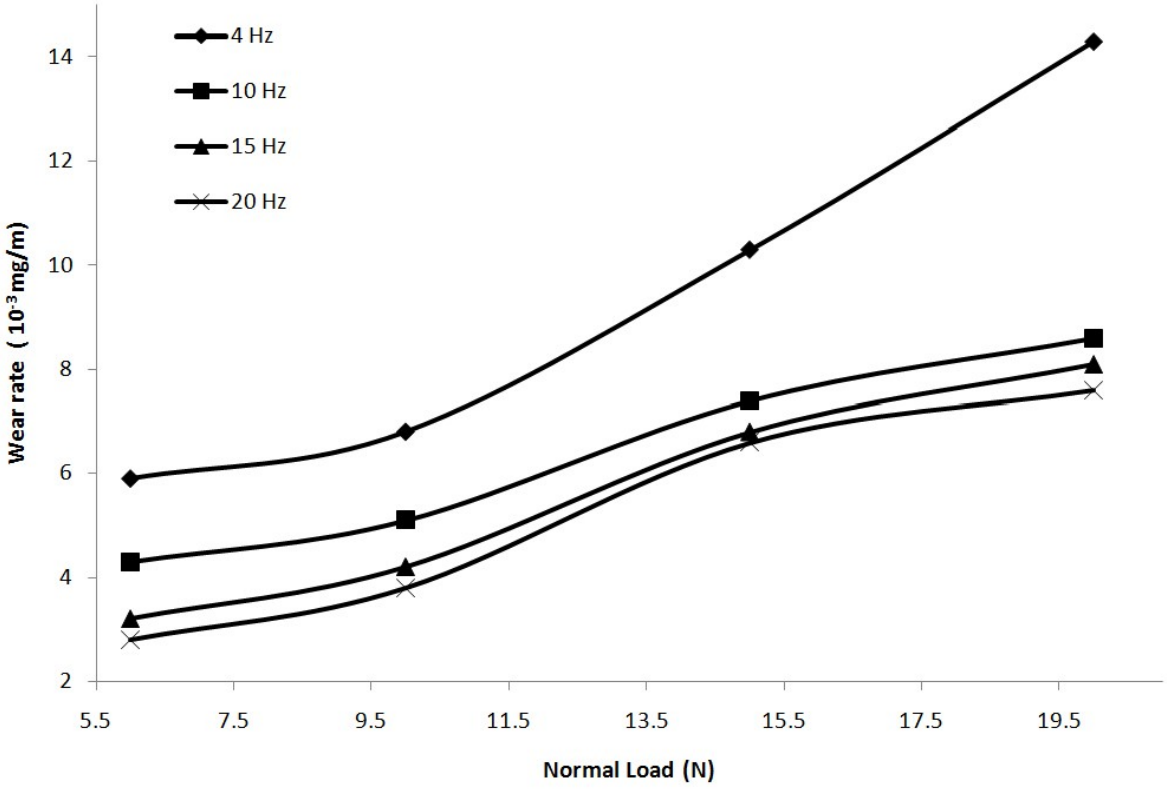

(a)

Figure 4.7 Wear rate as a function of normal load for A380M (a) as received

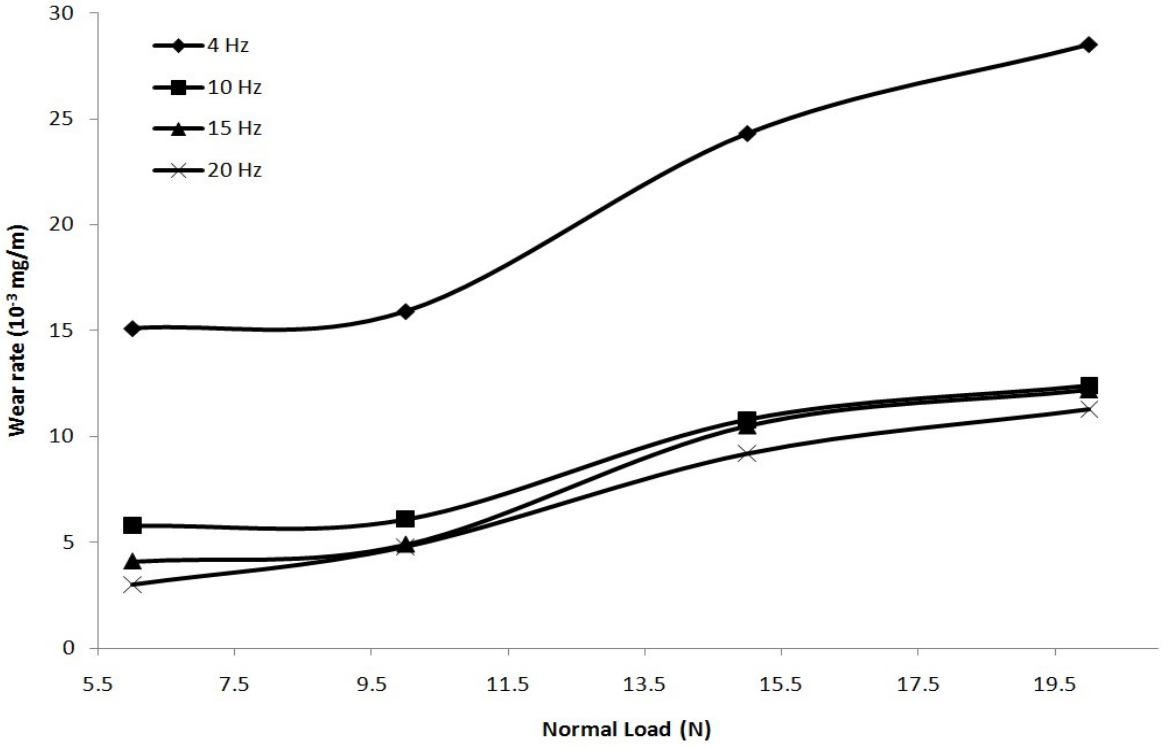

(b)

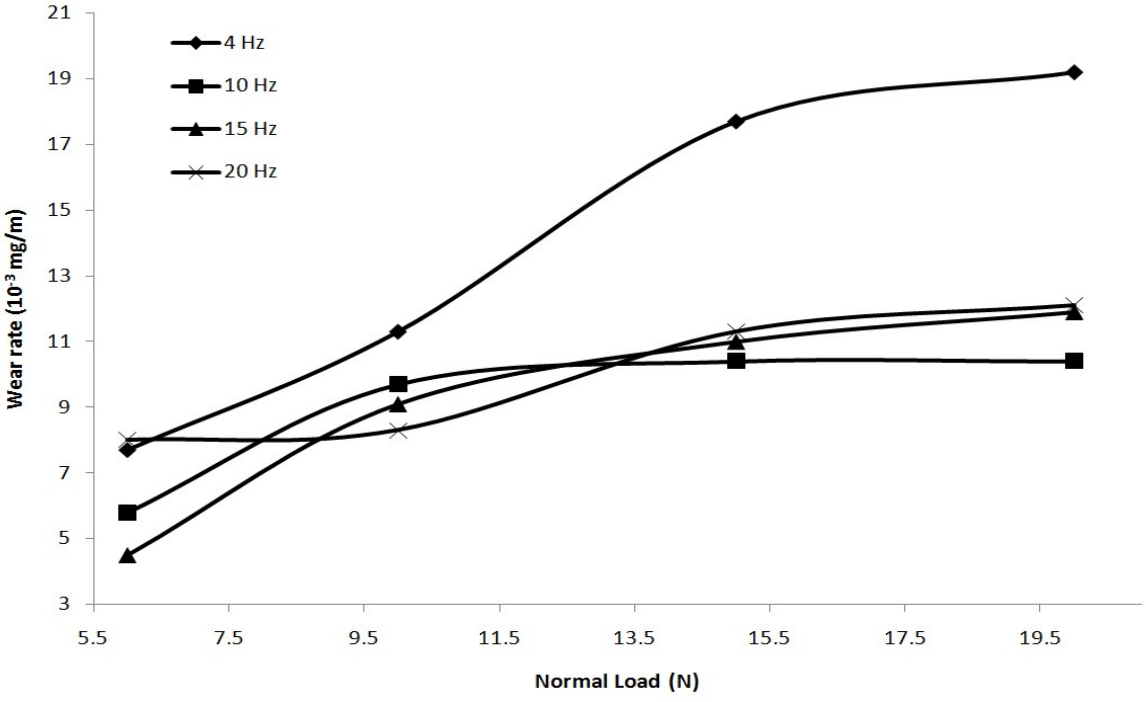

(c)

Figure 4.7 Continued. Wear rate as a function of normal load for A380M (b) cast condition 1, (c) cast condition 2

4.1.2.3 Effect of Frequency

There are two distinct regions observed in the wear rate versus sliding frequency curves in Figure 4.8. Region 1 shows a rapid decrease in wear rate with increasing frequency up to 10 Hz followed by a second region, at which point the effect of the applied frequency on wear rate appears to be negligible. The sharp drop in wear rate with increasing frequency is more prominent at higher normal loads. It is speculated that the initial drop in wear rate with increase in frequency is due to strain hardening. Alwahdi et al. (2005) reported that wear rate decreases with increasing strain hardening. At high frequency, however, wear rate reaches a steady-state condition (plateau) as the strain hardening effect is offset by thermal softening due to frictional heating. The competition between strain hardening and thermal softening as the reciprocating frequency increases has been previously reported (Hirst & Lancaster, 1960).

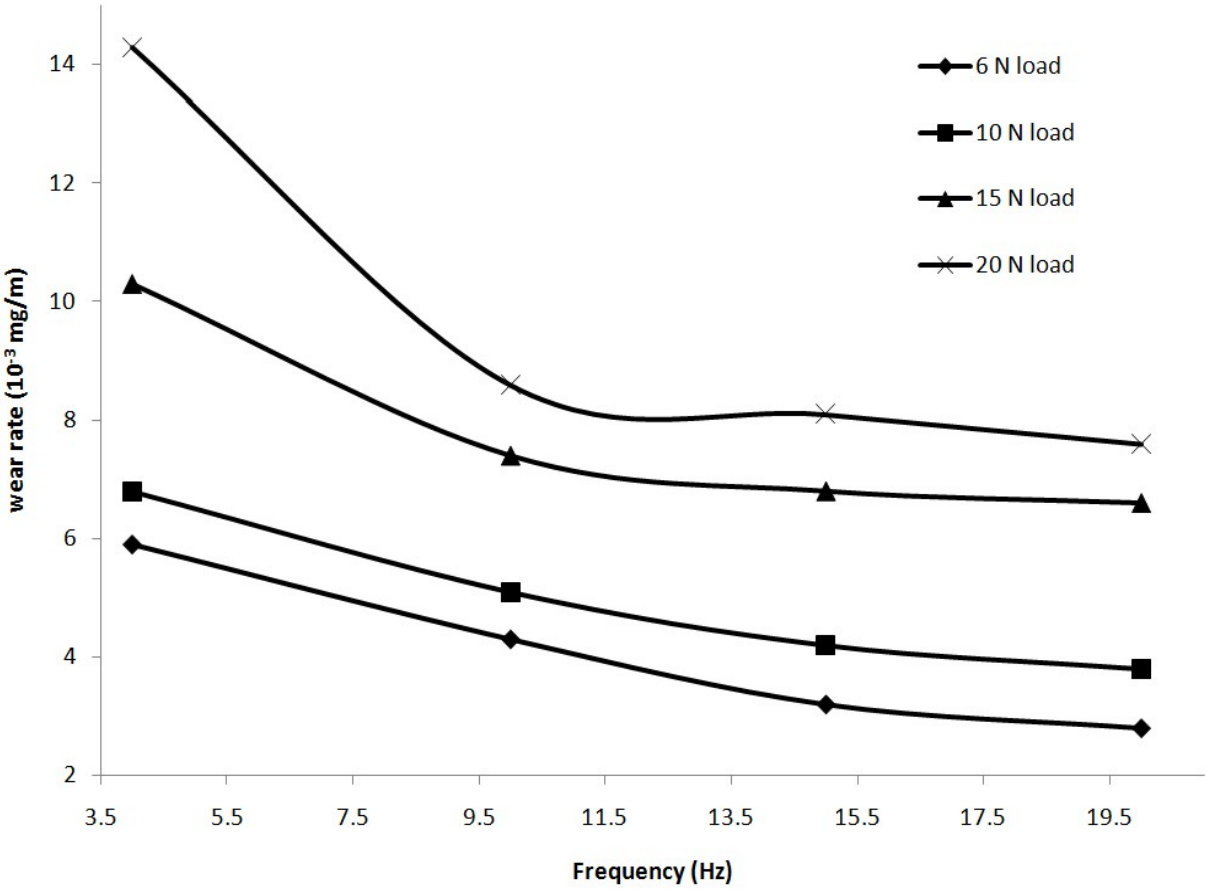

(a)

Figure 4.8 Wear rate as a function of frequency for A380M (a) as received

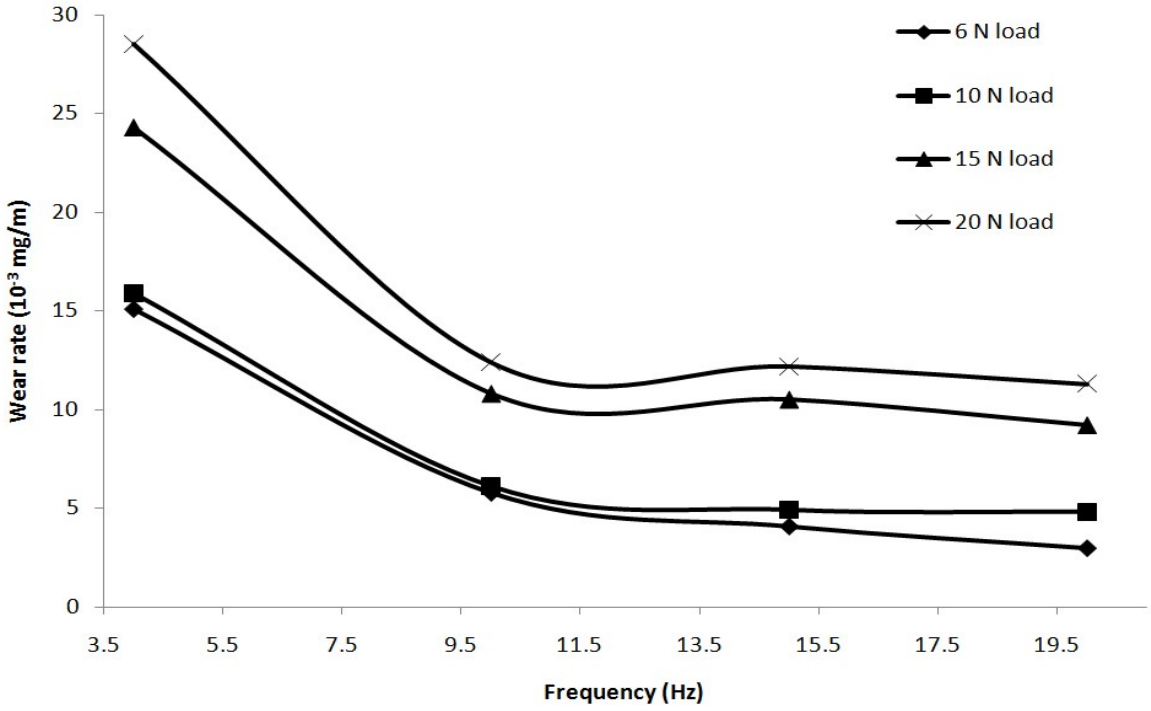

(b)

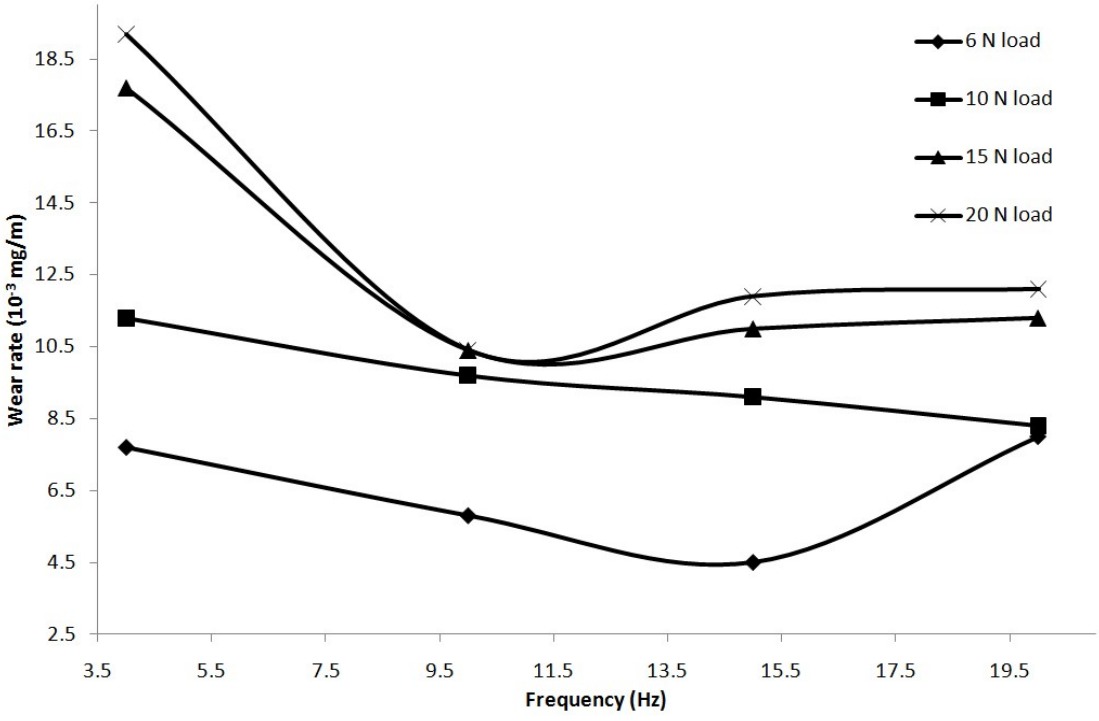

(c)

Figure 4.8 Continued. Wear rate as a function of frequency for A380M (b) cast condition 1, (c) cast condition 2

4.1.2.4 Effect of Surface Porosity

The wear rate at 15 Hz frequency of specimens containing 2.6 %, 3.5 % and 6.9 % porosity are plotted as a function of normal load as depicted in Figure 4.9 (a). It can be clearly seen from the figure that the wear rate rises with increasing normal load for all porosity levels. This rise in wear rate with applied load is prompted by high contact pressure and heavy plastic deformation. As well, wear rate increases with an increase in surface porosity, as shown in Figure 4.9 (b). It is found that, the wear rate increases about one and a half times with an increase in surface porosity from 2.6 % to 6.9 %.

As demonstrated above, a rise in porosity level leads to a drop in hardness of the material (Figure 4.3). Depending upon the sliding history and environment, the frictional force arises from three different sources (i.e., asperity deformation, ploughing by wear particles and hard asperities and adhesion). At any given loading contact, one or more of these mechanisms operates (Suh, 1980). At higher porosity, the surface roughness of the material increases; consequently, the possibility of the generation of wear debris increases as a consequence of asperity-asperity contact. A rise in the coefficient of friction with increasing porosity (Figure 4.5) confirms the formation of more asperity-asperity contact during sliding (higher energy required to shear off the junction). Fleming (1977) confirms that a characteristic crack propagation depth below the surface increases with an increasing coefficient of friction. In addition, the stress intensity factor and crack propagation rate increases with increasing COF. Hence, it can be concluded that an increase in porosity increases the wear rate due to a decrease in hardness of the specimens and a rise in asperity-asperity contact during wear. Moreover, increase in surface porosity decreases the required critical length for crack propagation, promotes link up of cracks and accelerates delamination wear. The increase in wear rate with increasing surface porosity can be explained more clearly from the optical and SEM micrographs as discussed in section 4.4 below.

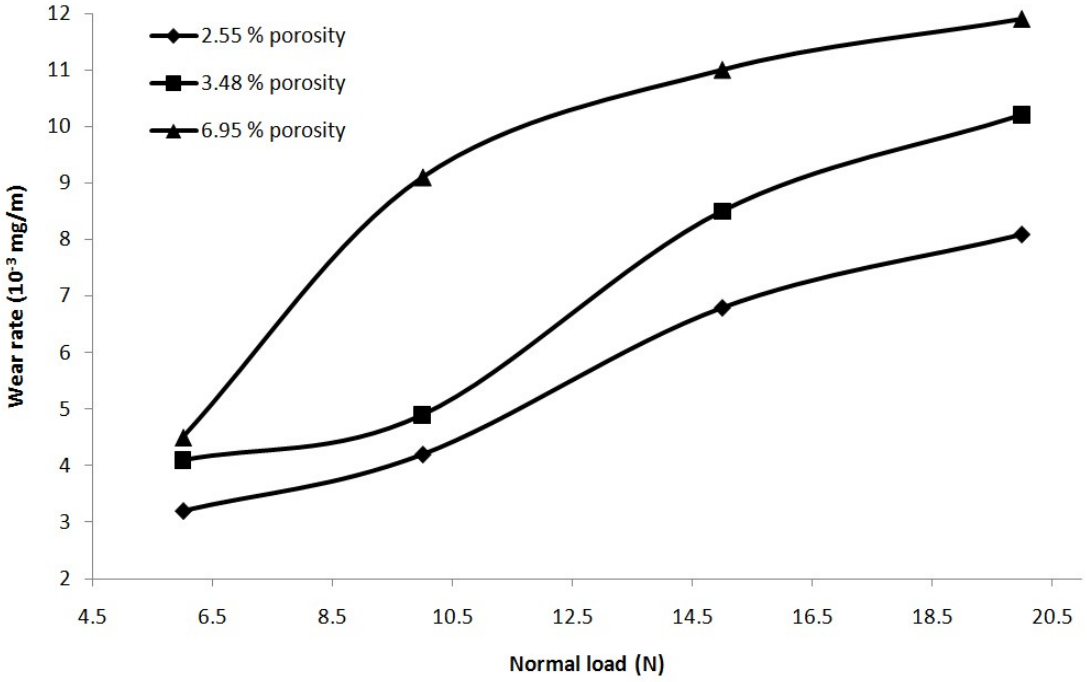

(a)

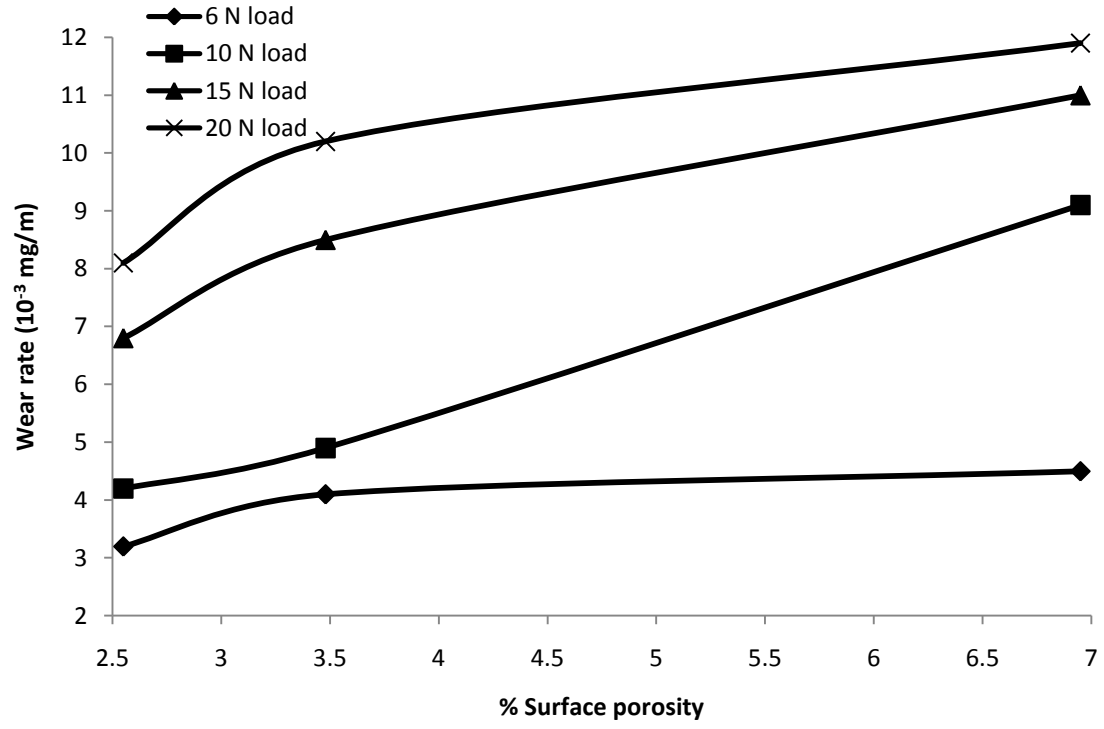

(b)

Figure 4.9 Wear rate for A380M at 15 Hz frequency versus (a) normal load, (b)surface porosity

4.2 Al-6 wt% Si Alloy

Optical micrographs of Al-6 wt% Si alloy, prepared by powder metallurgy method, are shown in Figure 4.10. The sintered Al-6 wt% Si alloy microstructures, in Figure 4.10 (a-c), reveal that the matrix and the Si grain sizes were essentially not affected by compactions which were about 85 μm and 17 μm respectively. However, the swaged specimen microstructure (Figure 4.10 (d)) exhibited finer matrix and smaller Si particles than prior to swaging. The size, shape and amount of pores are largely dependent on processing parameters. As all the specimens were sintered under the same sintering conditions, the compaction pressure plays the most significant role in determining pore size, shape and amount. Increasing the compaction pressure decreases the amount of porosity and reduces pore size (Figure 4.11), while the pore shape changes from a large irregular to a small round shape. As depicted in Figure 4.10 (a)-(d) and Figure 4.11, the average size of pores drops with the systematic increase in compaction pressure from 82.4 μm at 100 MPa to about 8.4 μm for 600 MPa followed by swaging. Although the pores have different shapes, they are evenly distributed in all specimens. The shape change of porosity during compaction has also been reported by others (Yalcin, 2009).

As the compaction pressure of the Al-6 wt% Si alloy powder is raised, both the volume and percentage of surface porosities drop (Table 4.2). The volume percent porosity ranges from 0.98% for a swaged specimen to 15.6 % for the 100 MPa pressed and sintered specimen, while surface porosities range from 1 to 6.7% for the same specimens, respectively. The low standard deviations of surface porosities indicate a uniform distribution of porosity throughout the structures. The basic properties of sintered Al-6 wt% Si are summarized in Table 4.3. The density of the specimens increases with an increase in compaction pressure and almost reaches the theoretical density of the alloy after swaging. Higher compaction pressure leads to greater uniformity, lower porosity and enhanced density of the alloy.

Table 4.2 Total % porosity of sintered Al-6 wt% Si specimens

Compaction Pressure	% porosity	
	Volume	Surface
100 MPa	15.67	6.71 ± .01
200 MPa	10.50	4.22 ± .01
600 MPa	5.52	2.35 ± .01
Swaged	0.98	1.02 ± .06

Table 4.3 Basic properties of Al-6 wt% Si alloy

Specimens	Green Density (g/cc)	Sintered Density (g/cc)
Pressed at 100 MPa	2.11	2.33
Pressed at 200 MPa	2.29	2.46
Pressed at 600 MPa	2.58	2.60
Swaged	2.74	

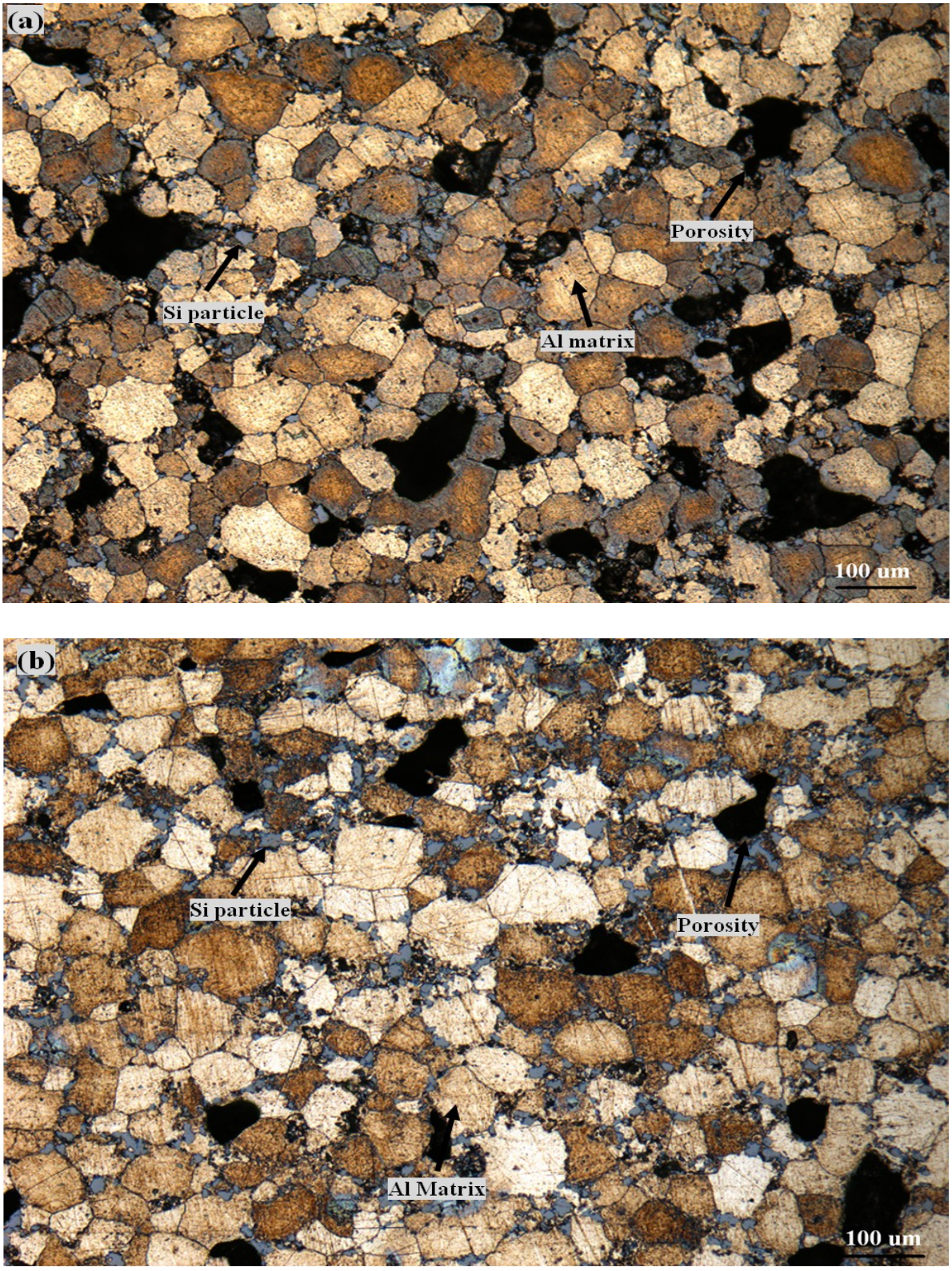

Figure 4.10 Optical micrograph of Al-Si alloy pressed at (a) 100 MPa, (b) 200 MPa

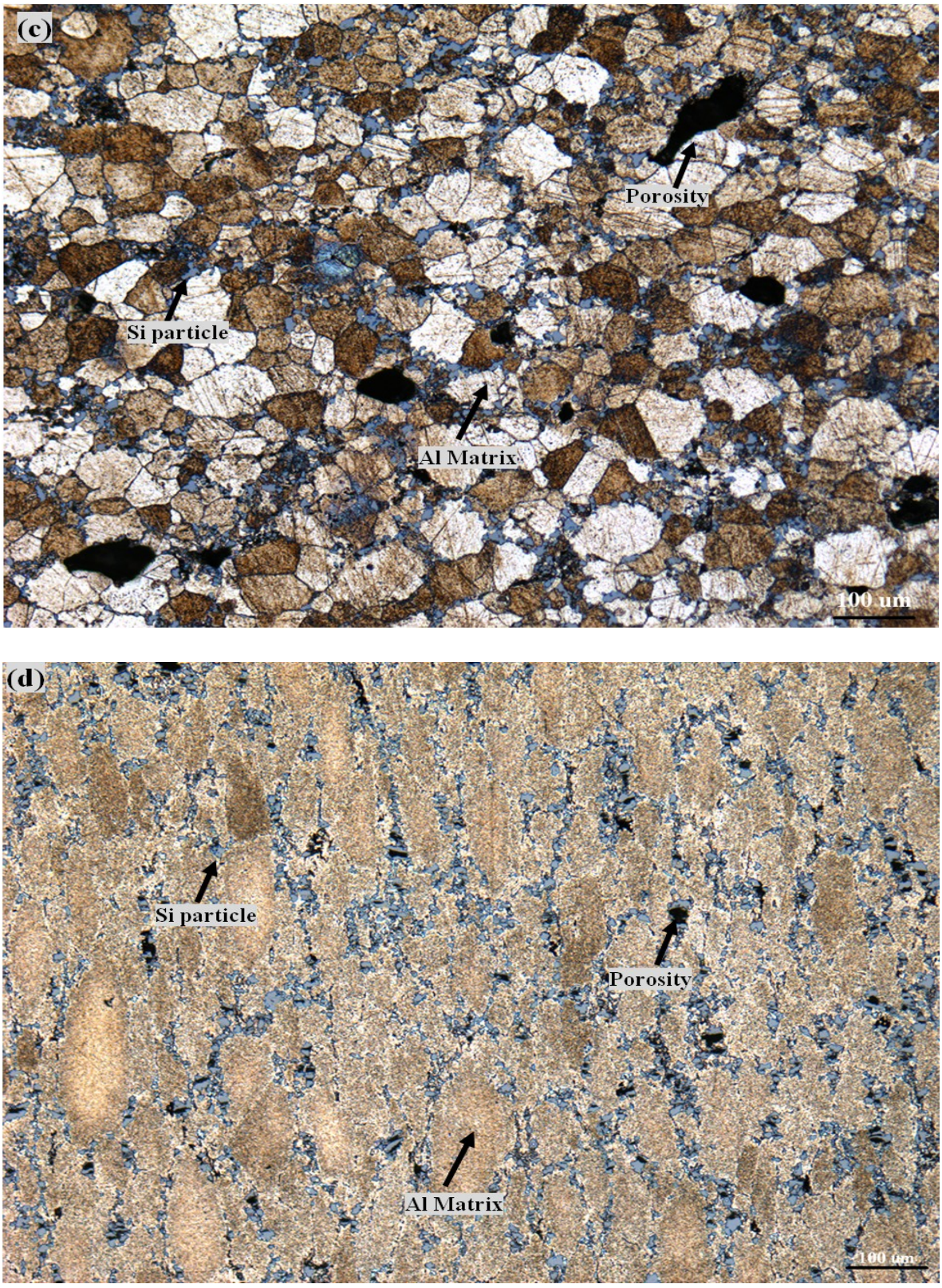

Figure 4.10 Continued, Optical micrograph of Al-Si alloy pressed at (c) 600 MPa and (d) Swaged

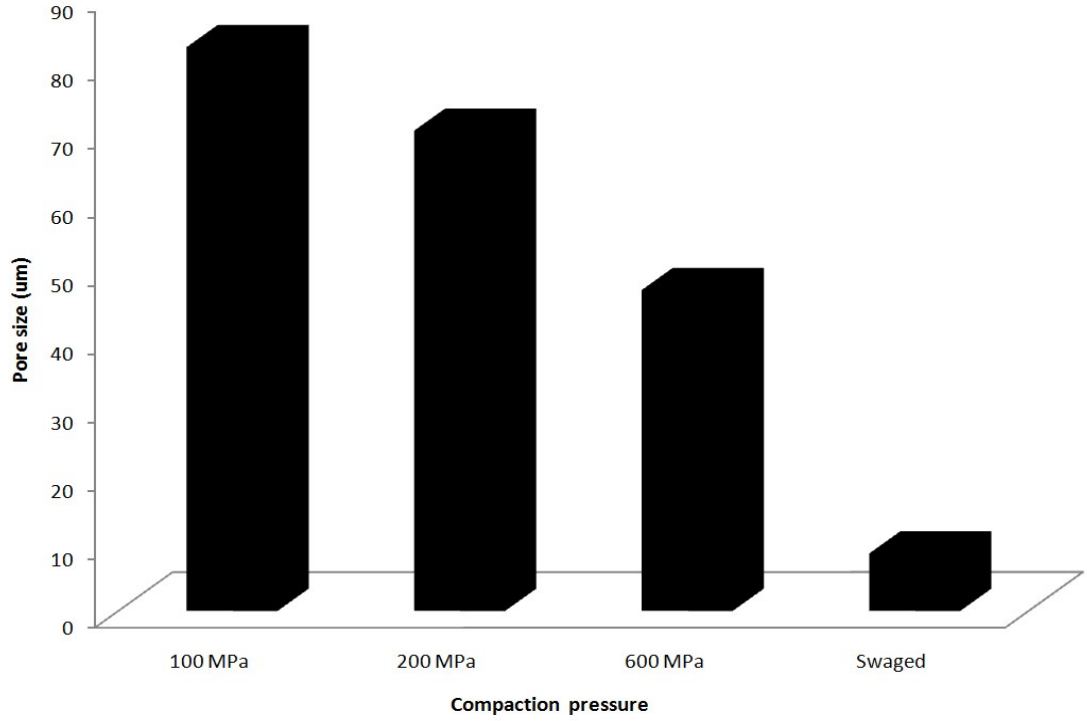

Figure 4.11 Dependence of average pore size on compaction pressure

The coefficient of friction is plotted as a function of surface porosity in Figure 4.12. The coefficient of friction for 1 % porosity is 0.31, and increases with increasing porosity; for 6.7% porosity, it is around 0.42. This is because; as the porosity increases more asperity-asperity contact occurs during sliding which requires higher energy to shear off asperity junctions. Higher COF indicates greater depth of deformation and plastic strain during wear. Increasing porosity also influence some physical properties, such as hardness of the material.

Figure 4.13 shows the variation of hardness with porosity at different processing conditions. As can be seen from the figure, the hardness of the alloy doubles as the surface porosity drops from about 6.7% to 1%. Specimens compacted at 100 MPa contain around 6.7% porosity and their Rockwell hardness is around 34 HRA. On the other hand, specimens compacted at 200 MPa, 600 MPa and swaged contain 4.2%, 2.3% and 1% surface porosity, respectively, and their Rockwell hardness is 49 HRA, 58 HRA and 62 HRA, in the same order. Decreasing hardness with increasing porosity content adversely affect the wear resistance of the alloy.

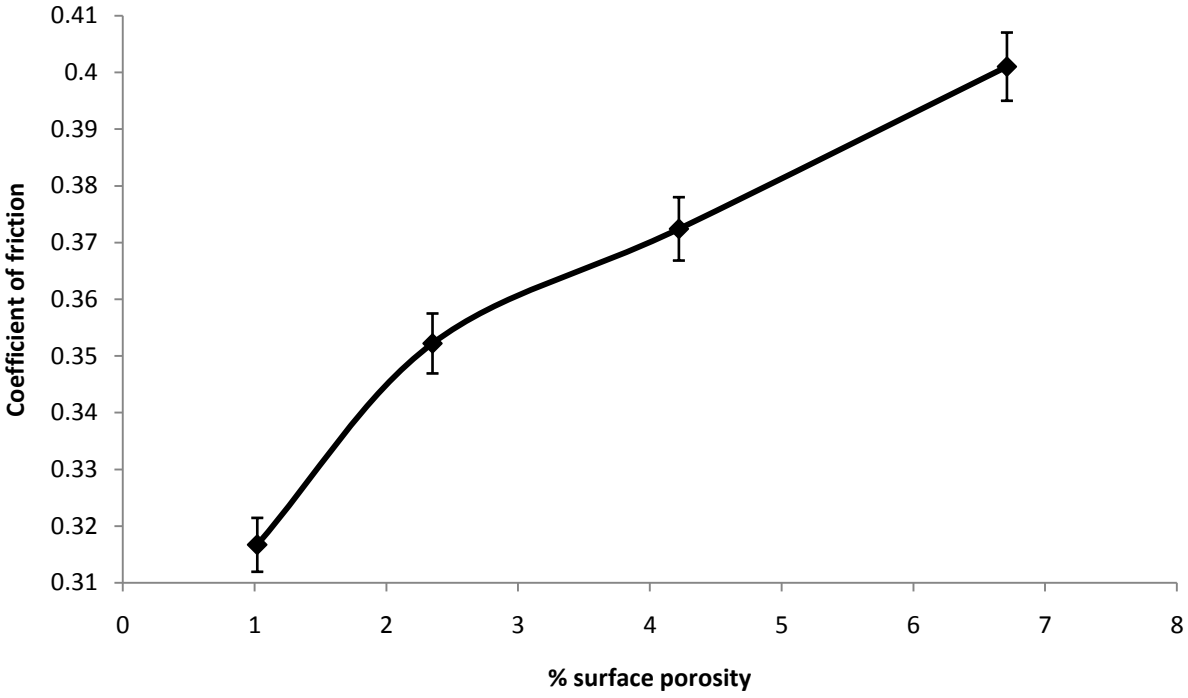

Figure 4.12 COF vs surface porosity for Al-6 wt% Si (at 10 N and 15 Hz)

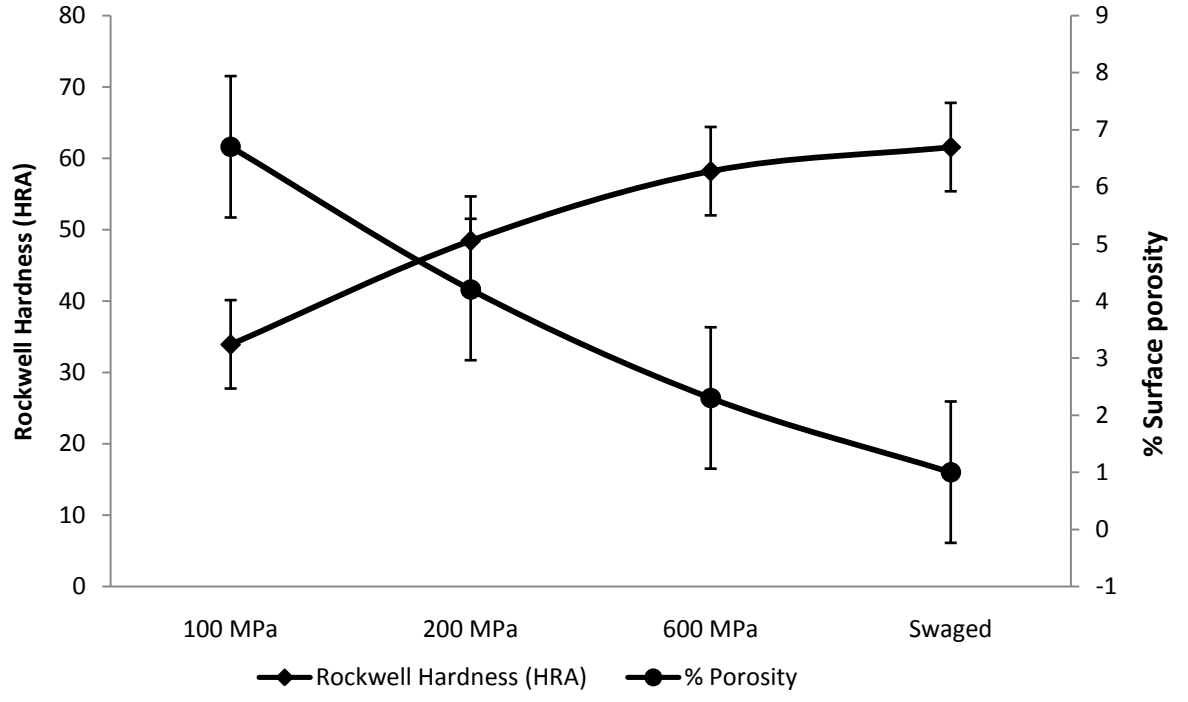

Figure 4.13 Variation of hardness and porosity with compaction pressure for Al-6wt% Si

The variation of wear rate with applied load and surface porosity are plotted in Figure 4.14. The wear rate rises linearly with increasing normal load for all porosity levels (Figure 4.14 (a)). However, the effect of surface porosity on wear resistance (Figure 4.14 (b)) shows an initial increase in wear rate, up to 4.2% porosity, followed by a drop at higher porosity level for all loads. For example, at 6 N load, the wear rate of specimen containing 1.0% porosity (pressed at 600 MPa and swaged) is 4.4×10^{-3} mg/m while at 4.2% porosity (pressed at 200 MPa) is 6.1×10^{-3} mg/m and average pore sizes are 8 μm and 70 μm, respectively. That is, about 3 and 8 folds increase in surface porosity and pore size, respectively, gave rise to about 40% increase in wear rate. Furthermore, contrary to expectations, at higher porosity wear rate drops. For example, at 6 N load, the wear rate of specimen containing 4.2% porosity (pressed at 200 MPa) is 6.1×10^{-3} mg/m while at 6.7% porosity (pressed at 100 MPa) is 4.1×10^{-3} mg/m and the average pore sizes are 70 μm and 82 μm, respectively. This is translated to 60% and 17% increase in surface porosity and pore size, respectively, accompanied by a 30% reduction in wear rate.

Hence, it can be conclude that, in the 1-4% porosity range, as compaction pressure is reduced, the porosity increases, leading to lower hardness and higher COF. As well, pores increase in size and become more irregular; consequently, wear rate increases (Figure 4.14). The increase in porosity leads to increased material removal as a result of the covering of pores and pore edge fracturing as will be discussed in section 4.4. Moreover, increased porosity in the subsurface raises the chances for crack nucleation, link-up of pores and delamination. Also irregular shape of pores leads to a higher probability of crack nucleation.

As % porosity rises over 4% as a result of lower compaction pressure, pores becomes large, and hardness drops; however, wear resistance increases (Figure 4.14). The effect of porosity on wear is not just due to softening but also to pore size. It has been observed that as pore size exceeds the contact area between the specimen and counter-face, wear rate drops. In order to explain the drop in wear rate at high porosity, a Hertzian contact analysis is carried out in an attempt to identify possible factors contributing to the wear rate of aluminum alloys. The analysis estimates the contact area between the specimen and the counter-face. The data required for the Hertzian contact analysis is summarized in

Table 4.4. Based on the Hertzian theory, the contact radius 'a' can be determined from (Johnson, 1987),

$$a^3 = \frac{3WR}{4E^*} \qquad \textbf{Equation 4.1}$$

where W is the total load on the contact spot, R is the effective radius related to the radius of the individual components by,

$$\frac{1}{R} = \frac{1}{R_1} + \frac{1}{R_2} \qquad \textbf{Equation 4.2}$$

In this research, all the samples are flat, which makes $R_2 = \infty$ and $R = R_1$. E^* is the effective modulus of elasticity:

$$\frac{1}{E^*} = \frac{1-{v_1}^2}{E_1} + \frac{1-{v_2}^2}{E_2} \qquad \textbf{Equation 4.3}$$

Here, v_1 and v_2 are Poisson's ratio of the bearing steel counter-face and the sample, respectively. Again, the maximum shear stress can be calculated from the following equation:

$$\tau_{max} = \frac{W}{2\pi a^2} \qquad \textbf{Equation 4.4}$$

Table 4.4 Data for Hertzian analysis

	Elastic Modulus, E (GPa)	**Poisson ratio, ν**	**Radius, R (mm)**
52100 bearing steel	210	0.3	3.15
Al alloy	90	0.3	∝

From Hertzian analysis, the contact radii are 0.06 mm, 0.07 mm, 0.08 mm and 0.09 mm, for 6 N, 10 N, 15 N and 20 N, respectively. That is, the contact diameter in this load range varies from 0.12 to 0.18 mm, as shown in Figure 4.15. The average pore size for the 100 MPa pressed and sintered specimens are 0.08 mm, and 60 % of the porosities are in the range of 0.14 mm. In other words, the ball slides into the pore itself, which eliminates the contribution of the pore covering and subsequent fracturing of material and wear occurs mainly by delamination. This ultimately leads to reduced wear (Figure 4.14).

Again, Hertzian analysis revealed that, under a certain normal load, maximum shear stress develops in the subsurface layer and increases with increasing normal load as shown in Figure 4.16. This explains the reason for the increase in wear rate with normal load. Shear stress causes plastic deformation in sub-surface layers to develop followed by crack initiation and crack growth. This ultimately leads to the formation of plate like particles and their removal by the extension of these cracks to the surface.

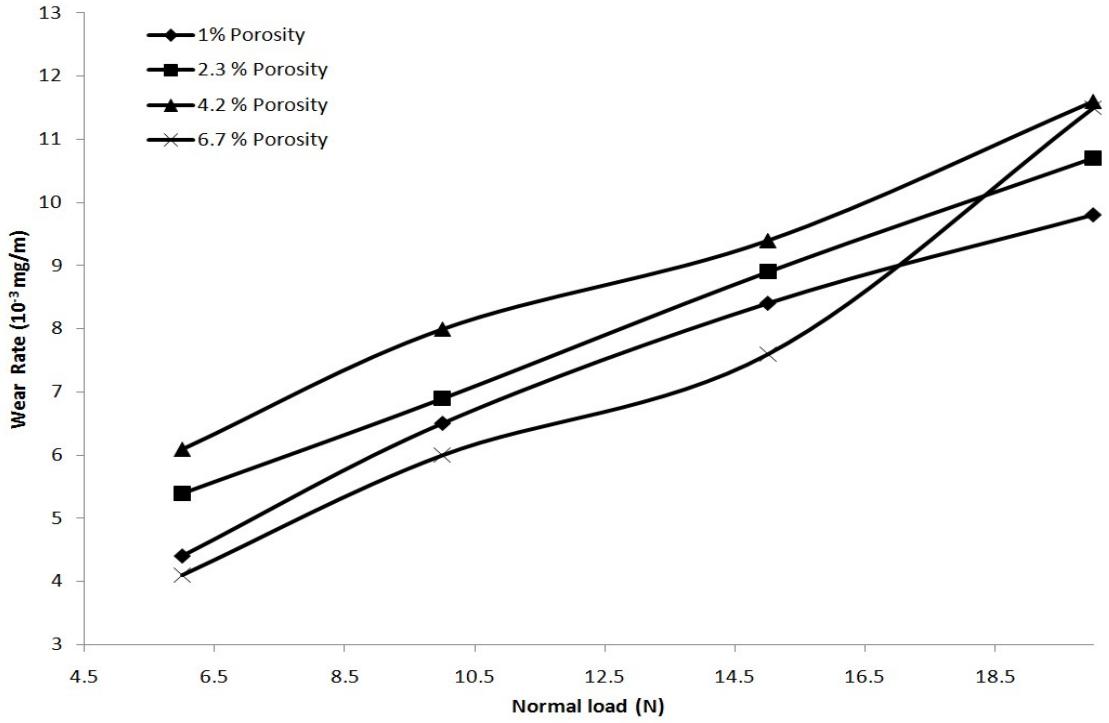

(a)

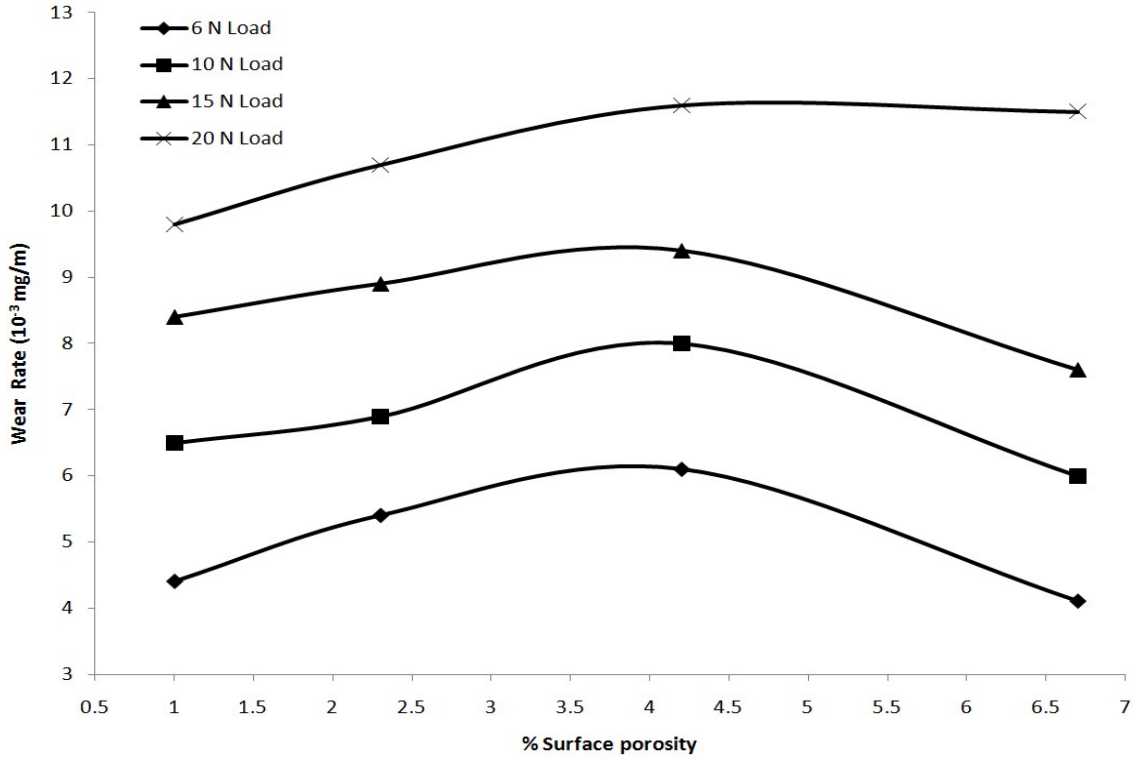

(b)

Figure 4.14 Wear rate for Al-6wt% Si at 15 Hz frequency versus (a) normal load, (b) % surface porosity

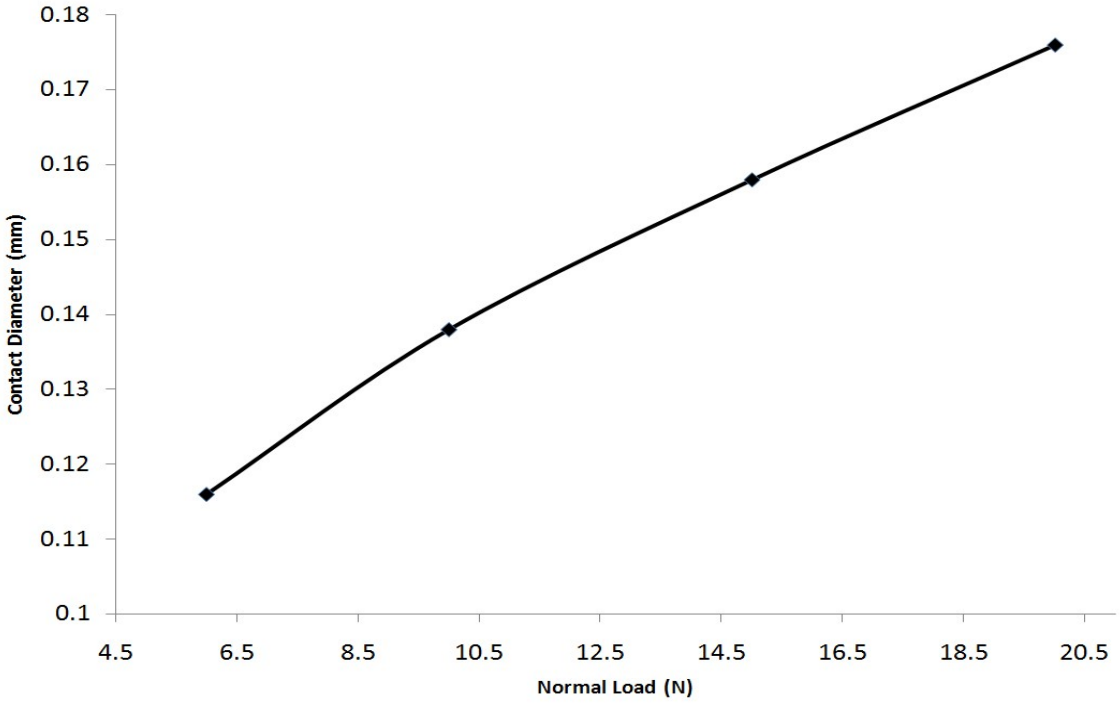

Figure 4.15 Contact diameter vs normal load (Hertzian contact analysis)

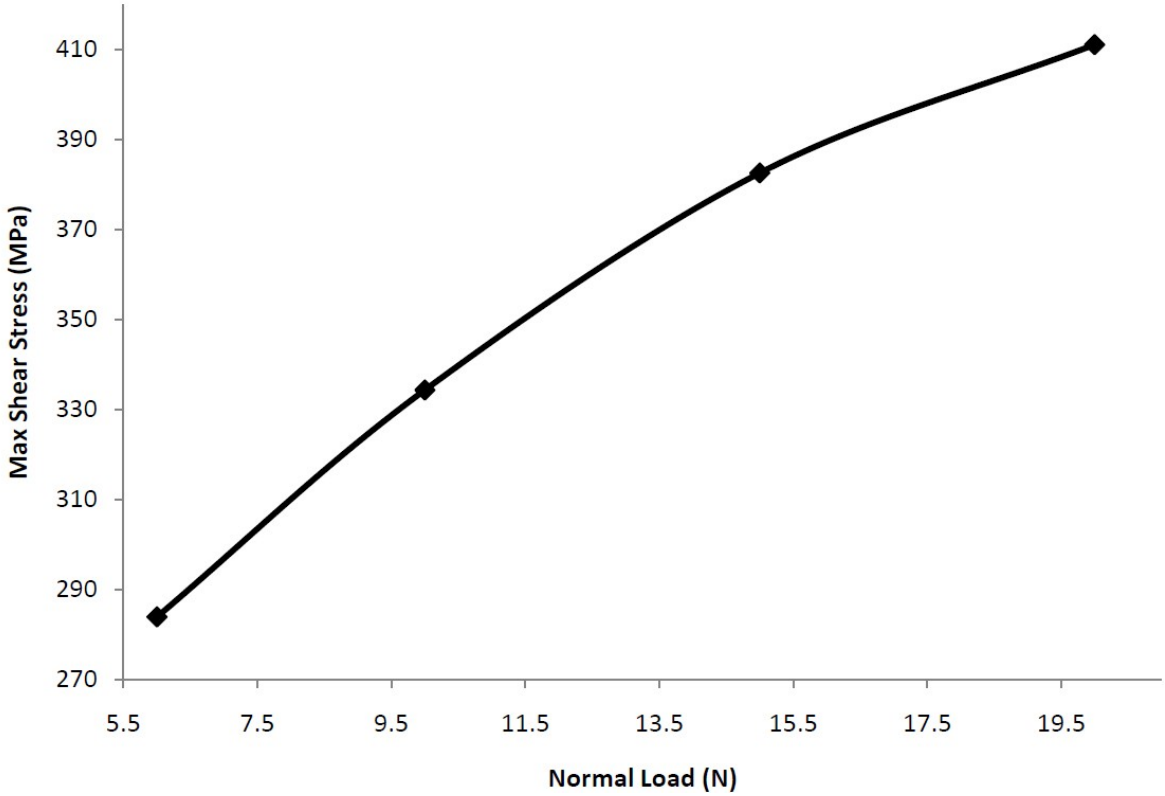

Figure 4.16 Maximum shear stress vs normal load

4.3 Effect of Hot Isostatic Pressing (HIP) on Wear

Specimens were subjected to hot isostatic pressing (HIP) to reduce surface porosity. Surface porosities of specimens before and after HIP were measured and plotted in Figure 4.17. An approximately 24%, 25% and 23% decrease in surface porosity was observed after HIP for cast condition 2, cast condition 1, and as-received specimens, respectively. It is noted that the reduction in surface porosity is somewhat constant (about 24%) regardless of the initial porosities. Figure 4.18 shows a relative comparison of surface porosity obtained before and after HIP for the specimens prepared using P/M. Surface porosities before HIP are around 6.7%, 4.2% and 2.4%, and after HIP, are 2.1%, 1.3% and 0.8% for 100 MPa, 200 MPa and 600 MPa, respectively. An approximate 68% decrease in surface porosity is observed after HIP for all of the P/M specimens. Similar to specimens prepared using casting process, the % reduction in surface porosity after HIP is constant regardless of initial porosity. Cast specimens usually contain two types of porosities, namely gas and combination of gas and shrinkage porosity. While porosity in the P/M samples form due to insufficient compaction pressure. Depending upon the initial amount of porosity, each specimen has certain percentage of small and large pores. During HIP, small pores dissolved into the matrix while the initial diameter of the large pores reduces. There seems to be a threshold pressure above which further reduction in % porosity would not be possible. Apparently, the pressure employed during the HIP treatment is higher than the 'threshold' pressure. This gives a constant amount of reduction in percent porosity for a given operating HIP condition. Data summarized in Table 4.5 is in agreement with the discussion above and shows the reduction in average pore size after HIP.

Table 4.5 summarizes the average Al and Si grain and pore sizes for A380M and Al-6 wt% Si before and after HIP treatment. The average pore sizes of as-received, cast condition 1 and cast condition 2 are 22.9 μm, 124.8 μm and 143.2 μm respectively, which drop to 14.1 μm, 90.6 μm and 108.8 μm, respectively, after HIP. Similarly, for Al-6 wt% Si alloy, the average pore sizes are 82.4 μm, 70.2 μm and 46.9 μm for specimens compacted at 100 MPa, 200 MPa and 600 MPa, respectively, drop to 34.6 μm, 23.5 μm and 20.4 μm, correspondingly, after HIP. The simultaneous application of heat and isostatic gas

pressure reduces the average size of internal voids and eliminates micro-porosity through a combination of plastic deformation, creep, and diffusion bonding. There is no substantial change observed in Si grain size after HIP, while significant grain growth occurs for the Al matrix due to prolonged heating at high temperature for both A380M and Al-6wt% Si. At high temperature and compaction pressure, some grains grow at the expense of other smaller grains.

Table 4.5 Summary of average grain and pore sizes for A380M and Al-6wt% Si alloys before and after HIP treatment

	Before HIP			After HIP		
A380M	Al grain size (μm)	Si particle size (μm)	Pore size (μm^2)	Al grain size (μm)	Si particle size (μm)	Pore size (μm^2)
As-received	6.7	2.5	22.9	15.6	2.8	14.1
Cast cond. 1	101.1	39.2	124.8	130.2	40	90.6
Cast cond. 2	179.1	51.1	143.2	210.7	53	108.8
Al-6 wt % Si	Al grain size (μm)	Si particle size (μm)	Pore size (μm^2)	Al grain size (μm)	Si particle size (μm)	Pore size (μm^2)
100 MPa	89.2	18.9	82.4	110.2	21.5	34.6
200 MPa	99.6	16.8	70.2	115.4	15.9	23.5
600 MPa	84.2	20.6	46.9	102.1	19.3	20.4

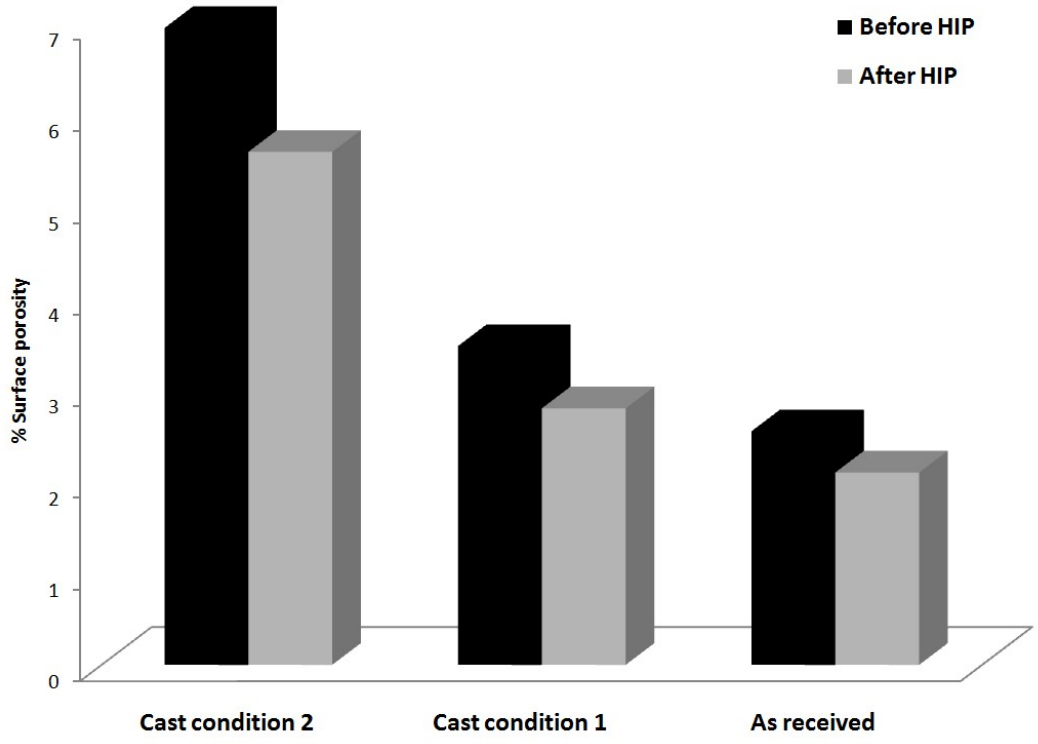

Figure 4.17 Variation of surface porosity before and after HIP for A380M

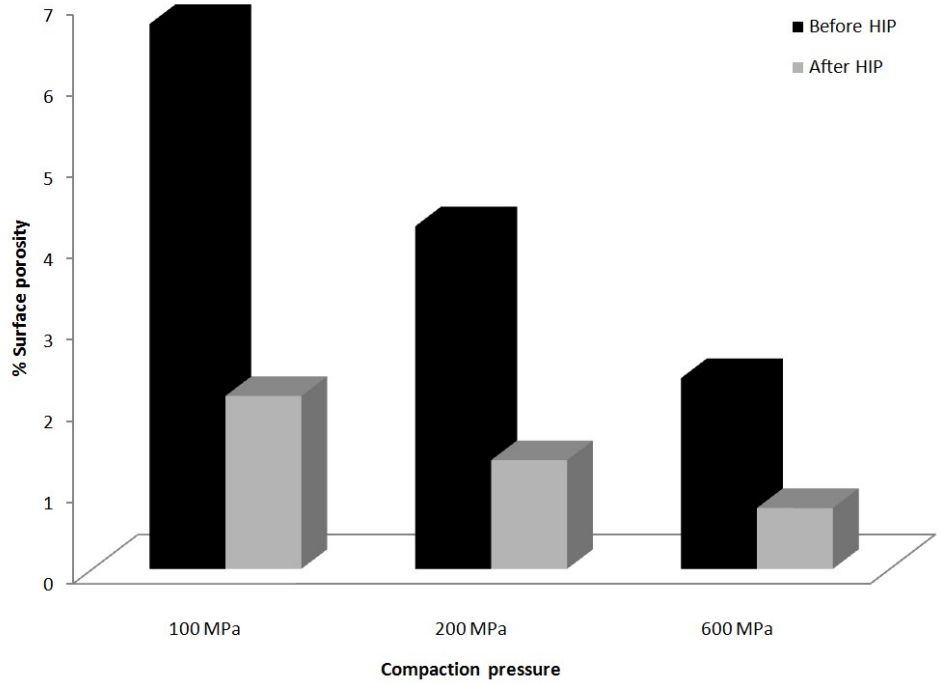

Figure 4.18 Variation of surface porosity before and after HIP for Al-6 wt% Si

Figure 4.19 (a)-(c) shows the microstructures after HIP for as-received, cast condition 1 and cast condition 2 specimens, respectively. As compared to the microstructure before HIP (Figure 4.1), it was observed grain boundaries are not as distinct as before HIP. The average Si particle size is essentially the same as before HIP, while the average grain size of the aluminum matrix increases. Figure 4.20 (a)-(c) shows the microstructures of specimens prepared by P/M, compacted at 100 MPa, 200 MPa and 600 MPa, respectively and HIPed. In Figure 4.10 (a)-(c), a distinct grain boundary was observed before HIP and the Si particles were distributed along grain boundaries, in contrast, less distinct grain boundaries were observed after HIP (Figure 4.20 (a)-(c)) and the Si particles are observed inside the aluminum grains. This points towards grain growth of Al matrix at high temperature and the Si particles along the grain boundary would disperse inside the new larger grains. This microstructural change affects some of the physical properties of the alloys.

The Rockwell hardness after HIP was measured and plotted in Figure 4.21 and Figure 4.22 for A380M and Al-6 wt% Si, respectively. After HIP, about 15 %, 12 % and 14 % decrease in hardness for as-received, cast condition 1 and cast condition 2 specimens, respectively were observed. On the other hand, there is 33 %, 36 % and 20 % decrease in hardness for 100 MPa, 200 MPa and 600 MPa specimens, respectively. It is suspected that, grain growth and softening at high temperature are the reason for drop in hardness.

The operating condition for HIP is shown in Table 4.6. It is pertinent to point out that the melting point and the recrystallization temperature for Al-Si alloys are around 560°C and 320°C respectively and the operating temperature for HIP is higher than the recrystallization temperature of the material. Recrystallization process replaced deformed grains by a new set of undeformed grains that nucleate and grow until the original grains have been entirely consumed. Recrystallization process usually accompanied by a reduction in the strength and hardness of the material.

Table 4.6 Operating condition for HIP

Samples	Operating conditions		
	Temperature (°C)	Time (Hrs)	Pressure (MPa)
A380M	515	3	101.7
Al–6 wt% Si	518	2	102.3

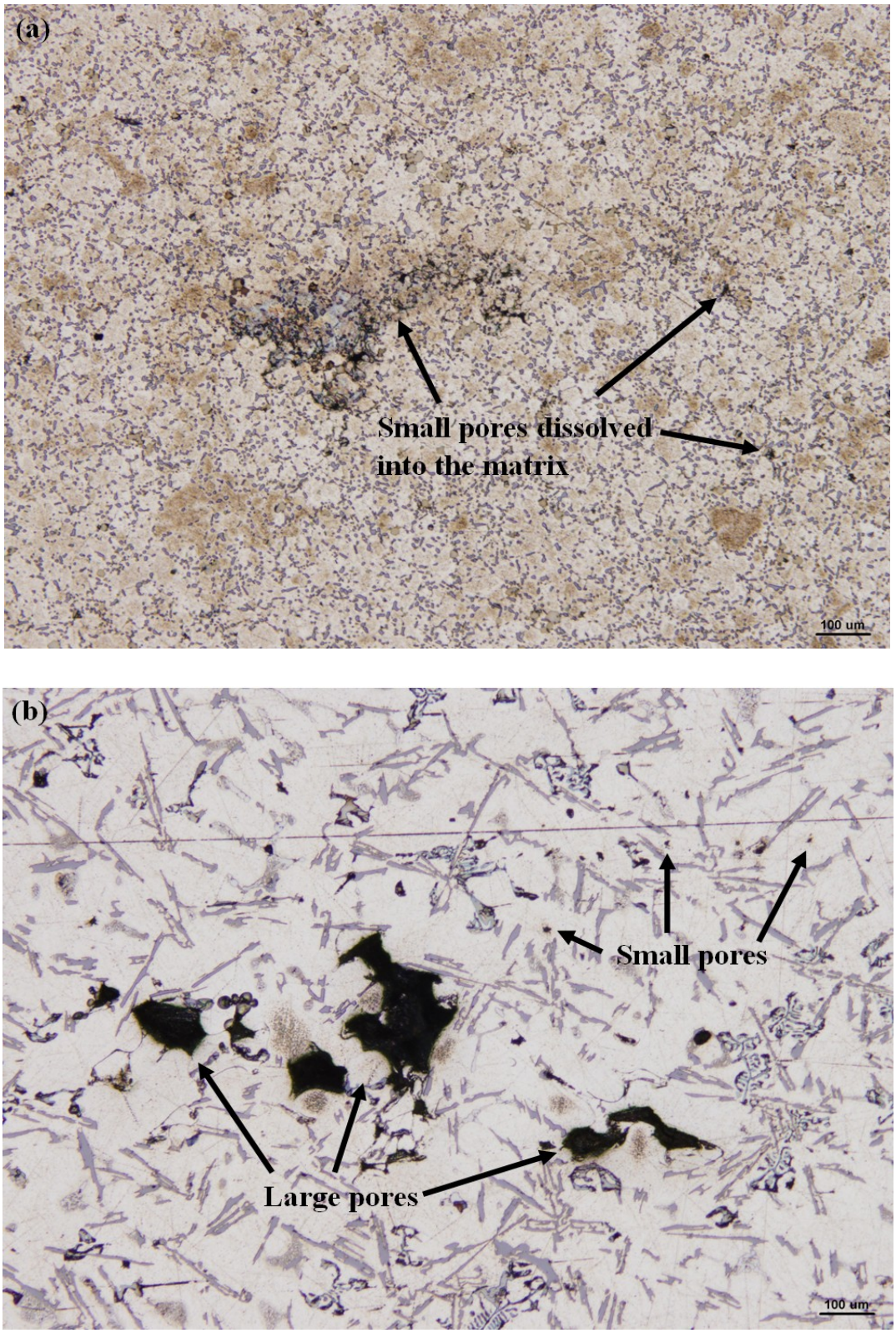

Figure 4.19 Microstructure of A380M after HIP in the (a) as-received, (b) cast condition 1

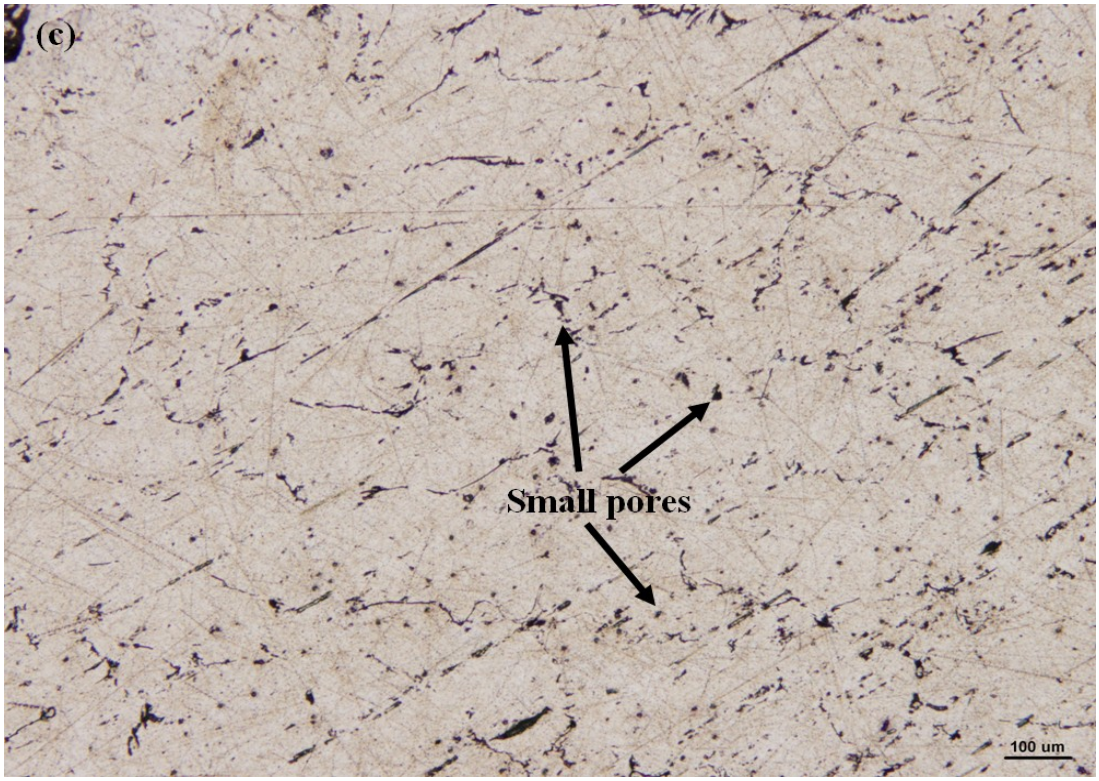

Figure 4.19 Continued. Microstructure of A380M after HIP, (c) cast condition 2

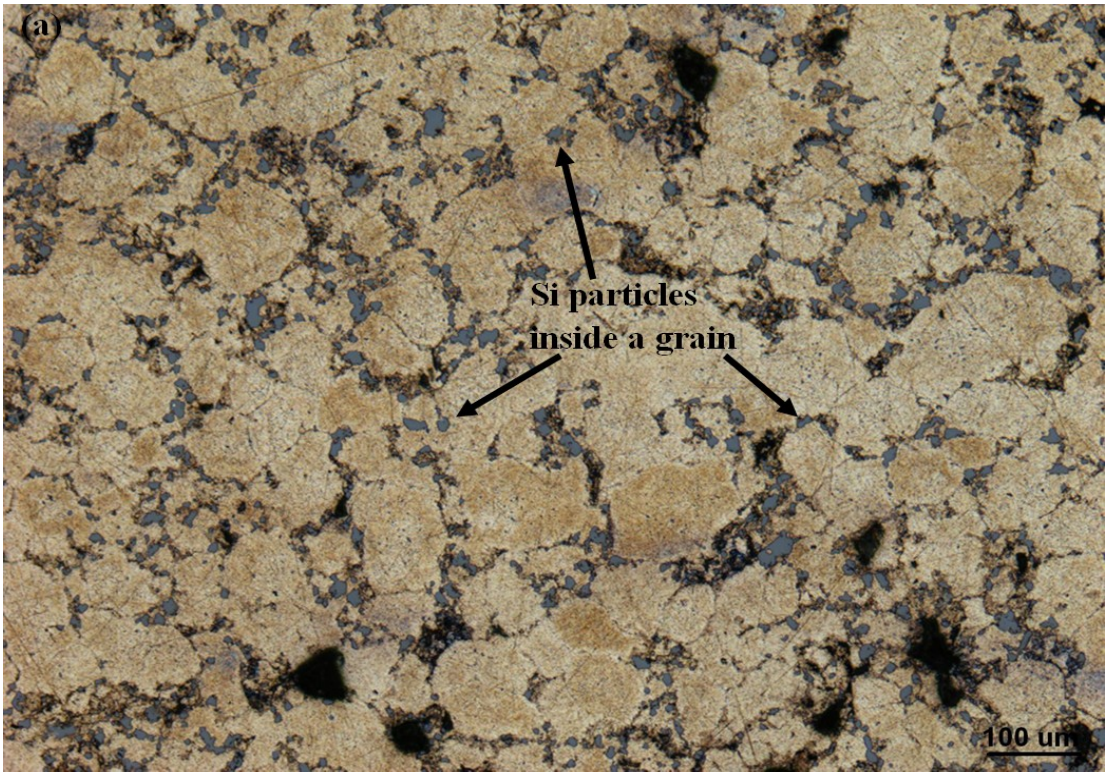

Figure 4.20 Microstructure of Al-6wt% Si after HIP compacted at (a)100 MPa

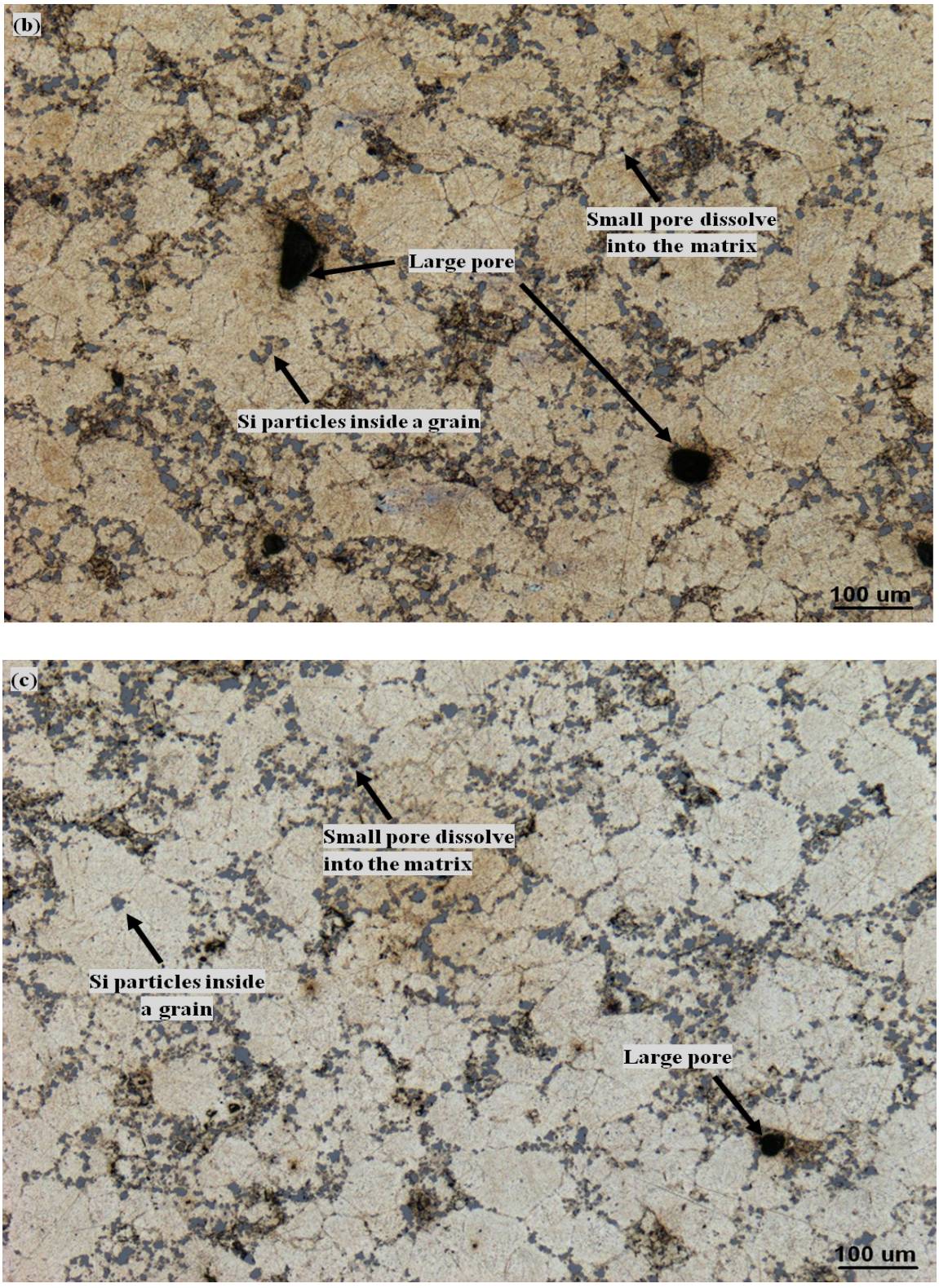

Figure 4.20 Continued. Microstructure of Al-6wt% Si after HIP compacted at, (b)200 MPa (c) 600 MPa

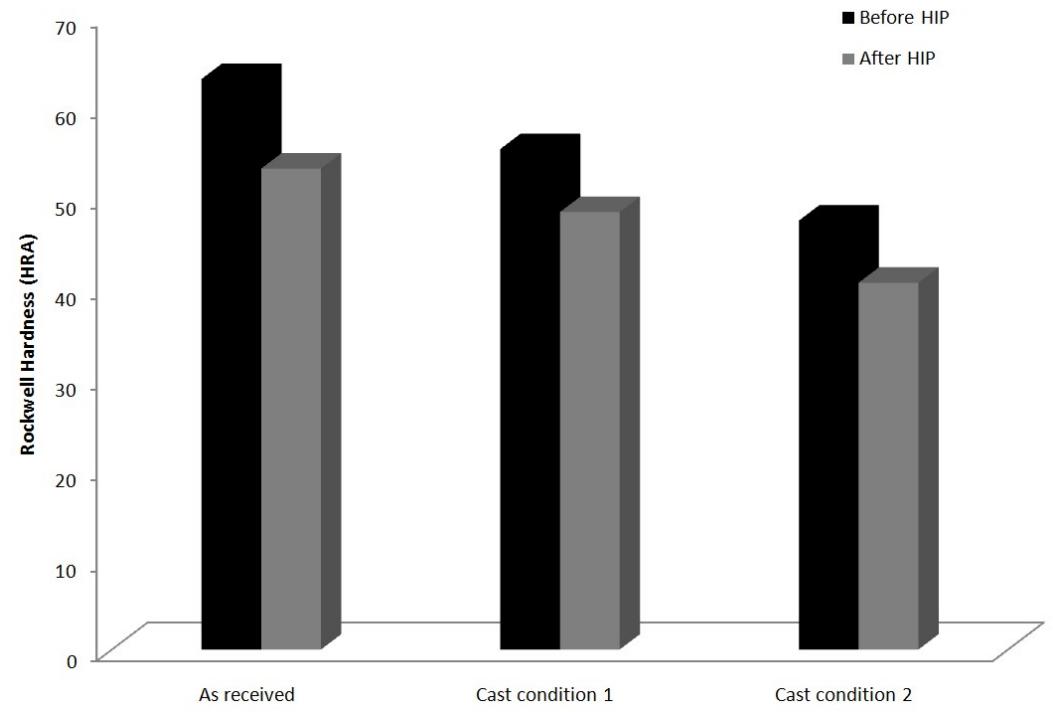

Figure 4.21 Rockwell hardness before and after HIP for A380M aluminum alloy

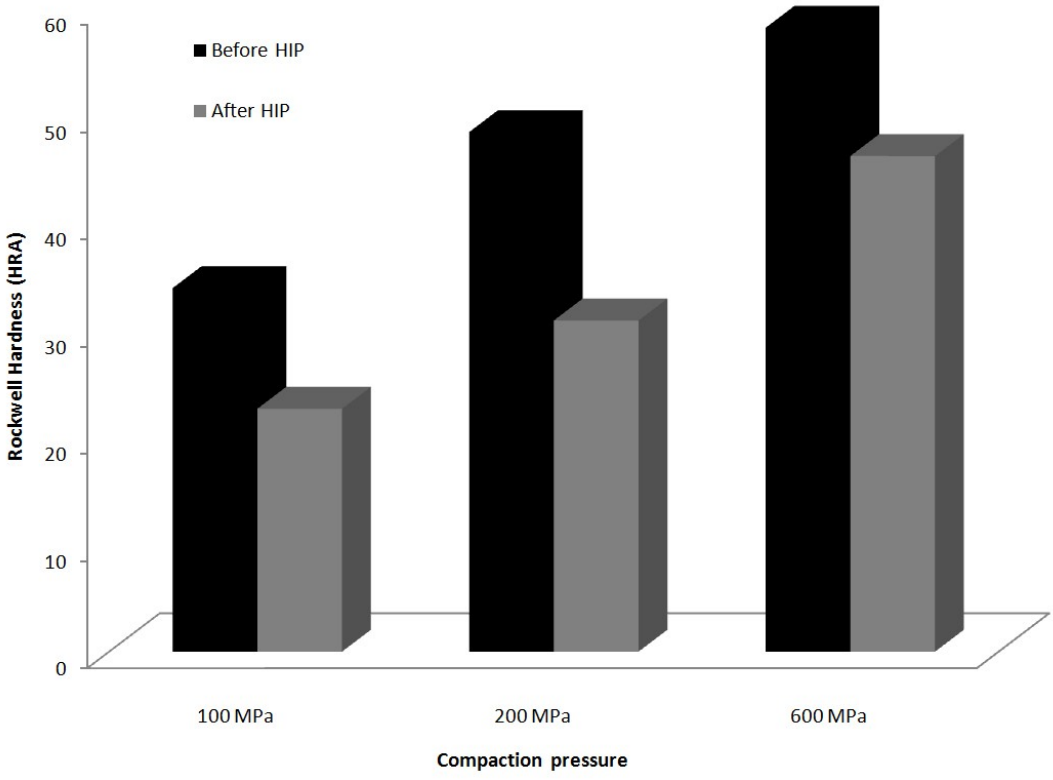

Figure 4.22 Rockwell hardness before and after HIP for Al-6 wt% Si alloy

The wear rates before and after HIP at 15 Hz frequency for as-received, cast condition 1 and cast condition 2 are shown in Figure 4.23 (a)-(c). It was observed that, for as received, cast condition 1 and cast condition 2 specimens, the wear rates after HIP are higher than prior to HIP treatment. For example at 20 N normal load, there is about 21%, 20% and 13% increase in wear rate after HIP for as-received, cast condition 1 and 2, respectively, although porosity drops by 24 %. Thus, it can be stated that, although the porosity of the specimen decreases, the wear rate increases after HIP for A380M alloy.

Figure 4.24 (a)-(c) shows the difference in wear rates (at a 15 Hz sliding frequency) for 100 MPa, 200 MPa and 600 MPa specimens tested before and after HIP. There is about 68% drop in surface porosity for 100 MPa, 200 MPa and 600 MPa pressed and sintered specimens after HIP this is accompanied by an increase in wear resistance (at 20 N) by 5%, 16% and 6%, respectively.

Comparing the data obtained after HIP, it can be seen that, for A380M aluminum alloy, the porosity decreases by about 24%, accompanied by hardness drop of about 13%. The combined opposing effects of reduced porosity and hardness result in an increase in wear rate. On the other hand, for Al-6 wt% Si alloy, a decrease in surface porosity after HIP increases the wear resistance although hardness drops. It can be concluded that competition between the beneficial effect of lower porosity and the detrimental effect of lower hardness determine the final wear rate.

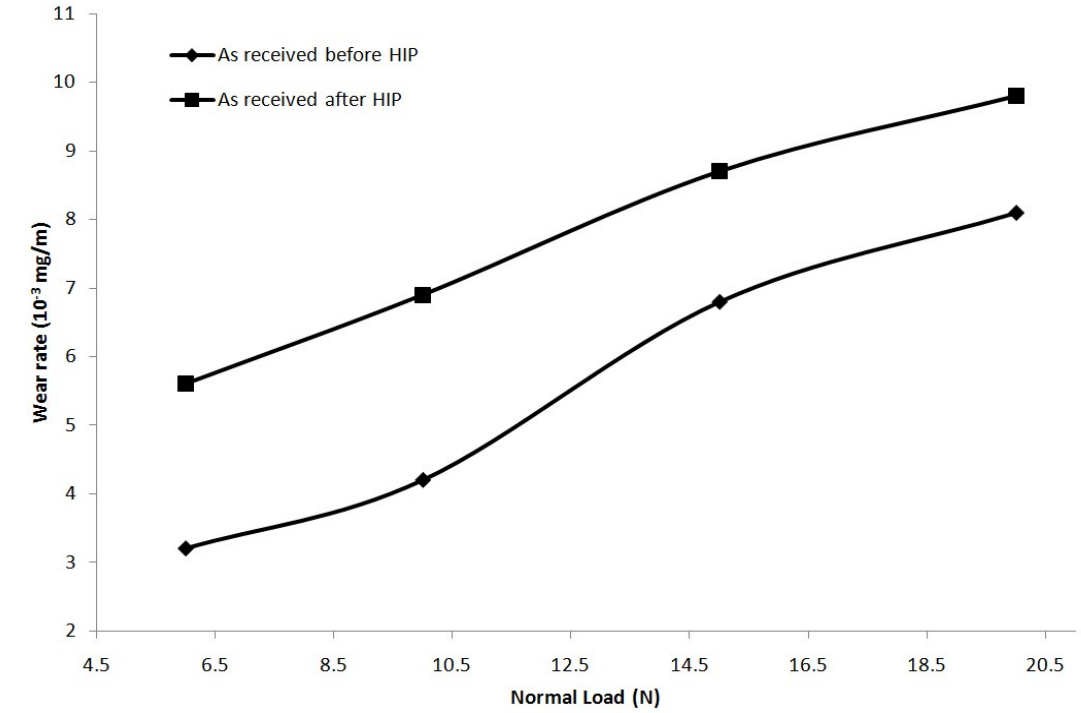

(a)

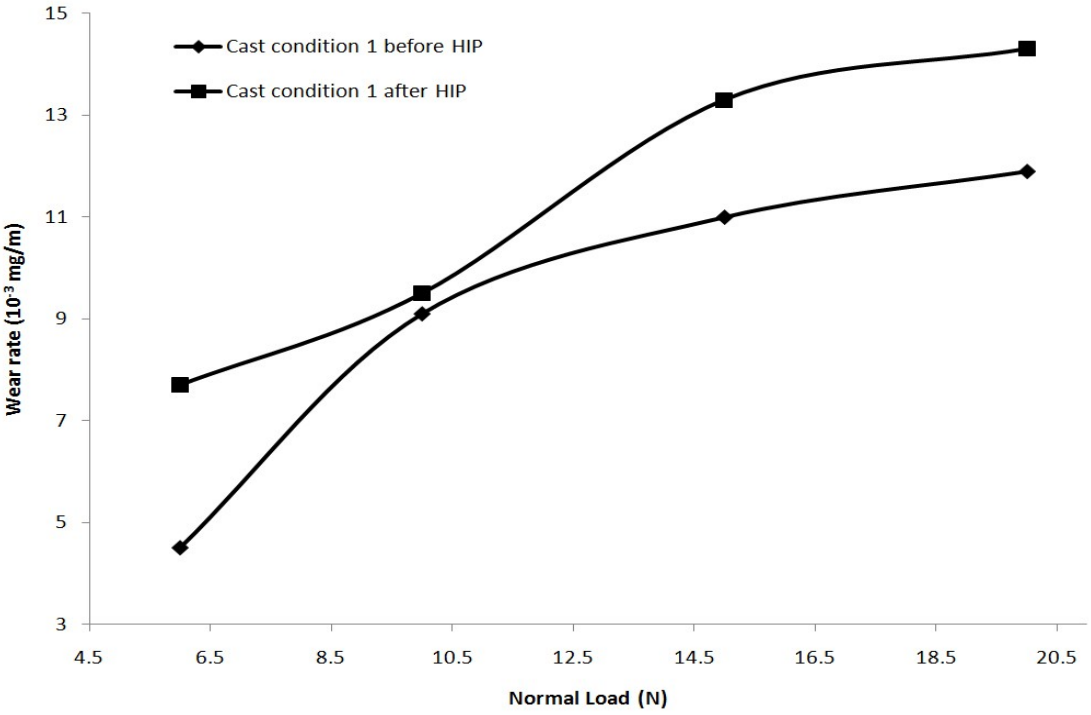

(b)

Figure 4.23 Variation of wear rate before and after HIP for A380M at 15 Hz frequency, (a) as-received (b) cast condition 1

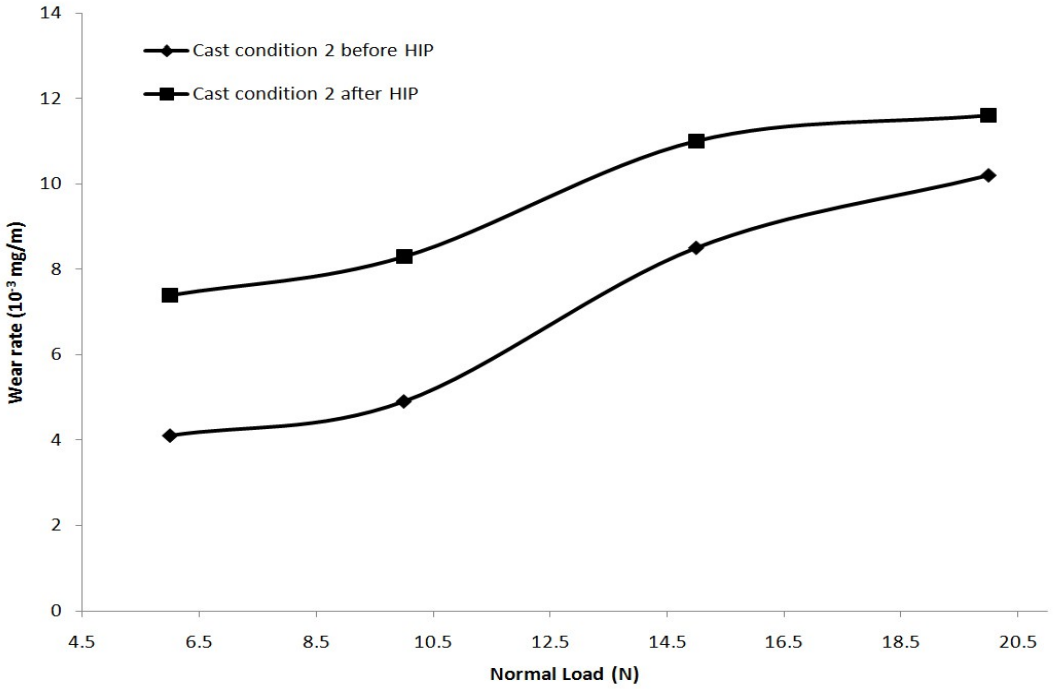

(c)

Figure 4.23 Continued. Variation of wear rate before and after HIP for A380M at 15 Hz frequency (c) cast condition 2

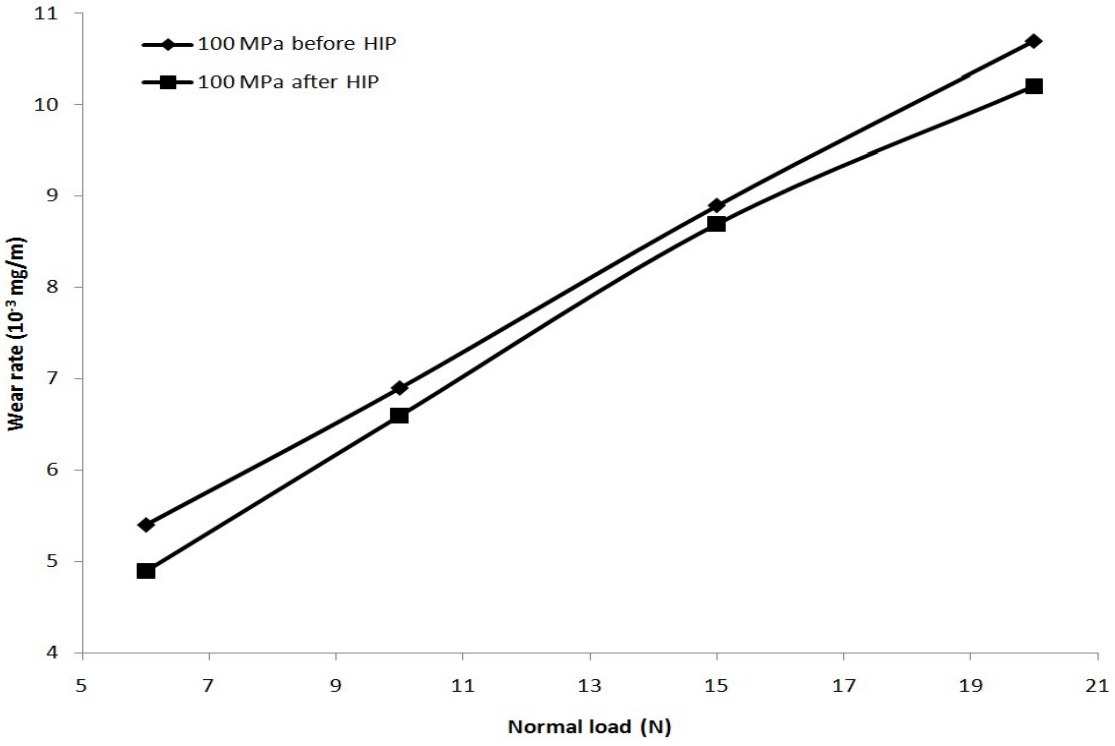

(a)

Figure 4.24 Variation of wear rate before and after HIP for Al-6wt% Si at 15 Hz frequency, (a) 100 MPa

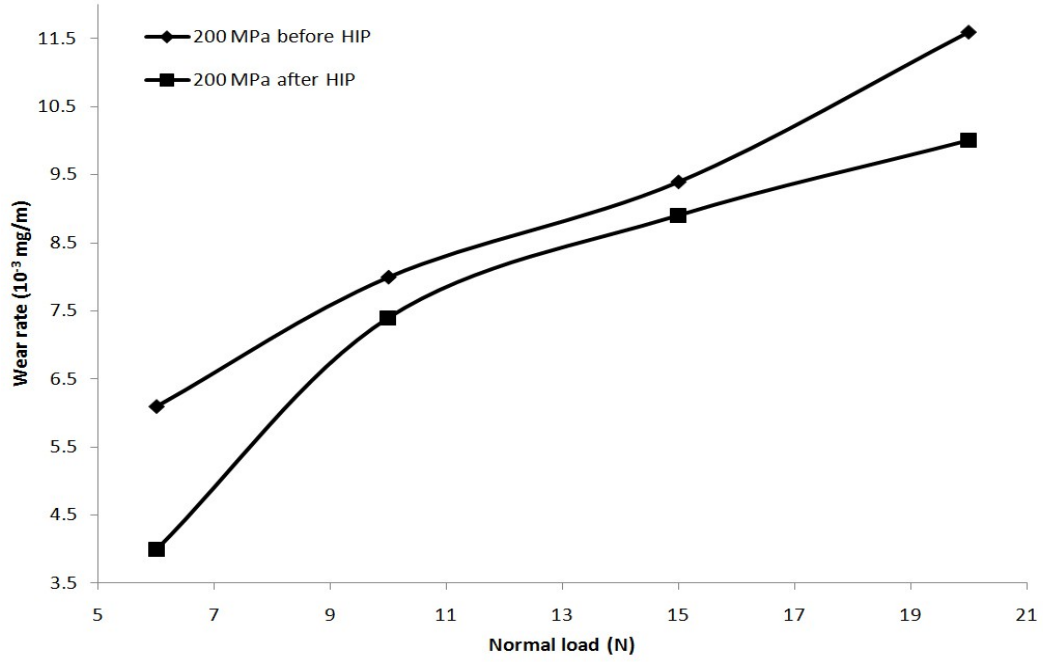

(b)

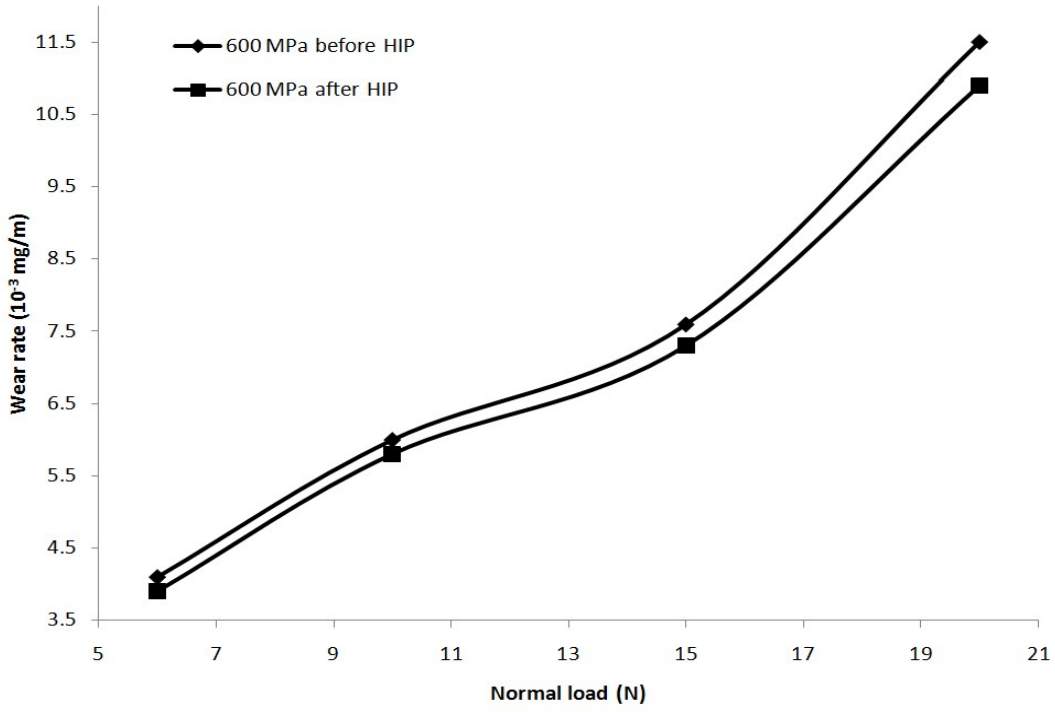

(c)

Figure 4.24 Continued. Variation of wear rate before and after HIP for Al-6wt% Si at 15 Hz frequency, (b) 200 MPa and (c) 600 MPa

4.4 Worn Surfaces Evaluation

Optical and scanning electron microscopy examinations of wear tracks reveal that delamination and heavy surface deformation and fracture are the dominant mechanisms during the wear process. Based on experimental observations in this study, several factors can be identified that affect the wear resistance of the cast and sintered Al-Si alloys, namely, amount of porosity, pore size and shape, hardness and operating conditions (load and frequency).

Figure 4.25 (a) is an optical micrograph of the specimen at the end of the reciprocating wear test. The image represents a transverse section of the wear track (along the wear track). The figure shows material extending in the sliding direction and partially covering pore cavity with a thin layer of deformed metal. The formation of the extruded metal over the pores occurs as a result of asperities ploughing through the surface and dragging material ahead of the slider. Moreover, Figure 4.25 (b) revels how plastic deformation in the vicinity of the pores contribute to pore closing. The extended material fractures and forms wear debris during subsequent passes of the slider. From this, it can be conclude that as the slider reciprocates on the surface it drag away the metal and covers the pores. Under the pressure of repeated sliding, this extruded metal fractures and forms wear debris. Furthermore, as pore edges represent stress concentration areas they tend to fracture with the reciprocating motion of the slider. This is evident from the cracks initiating from pore edge in Figure 4.26 (a). Figure 4.26 (b) shows the extension of these cracks due to the repeated motion of the slider.

Hertzian-type cracks develop as a result of surface tensile stresses that evolve during Hertzian contact. These types of cracks normally extend perpendicular to the sliding direction. Figure 4.27 (a) shows cracks perpendicular to the sliding direction which represents a clear evidence of Hertzian cracks developing during the wear process.

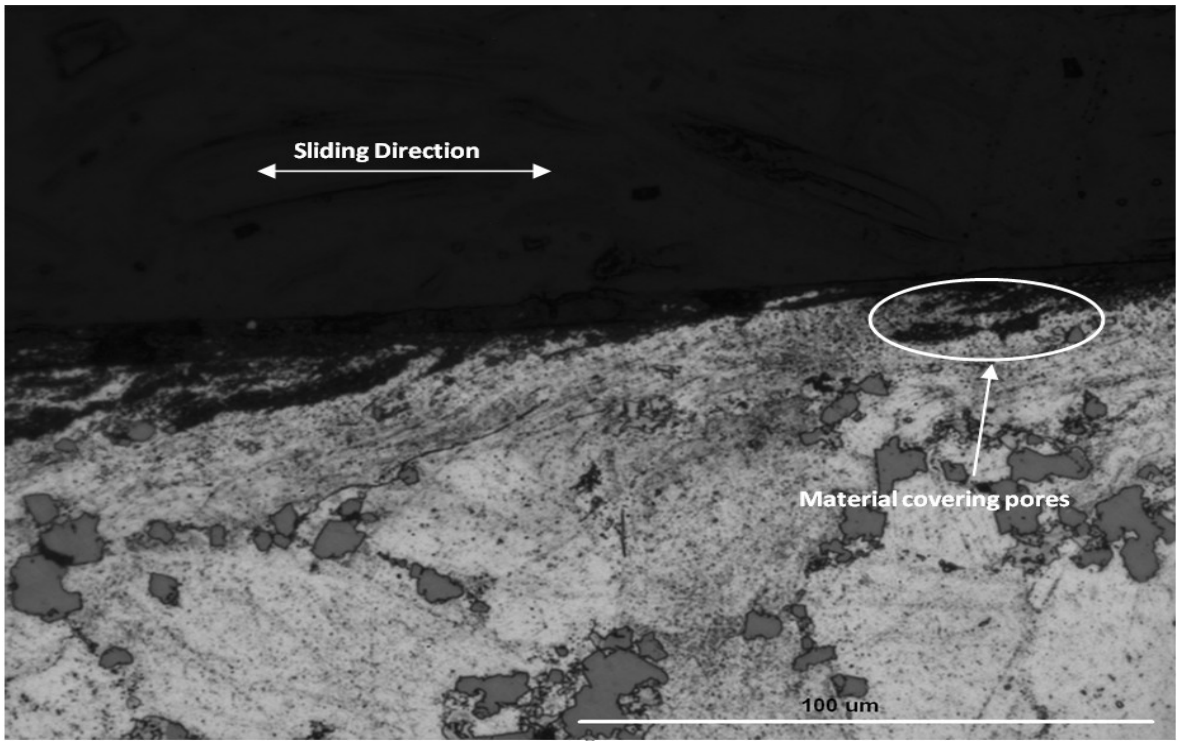

(a)

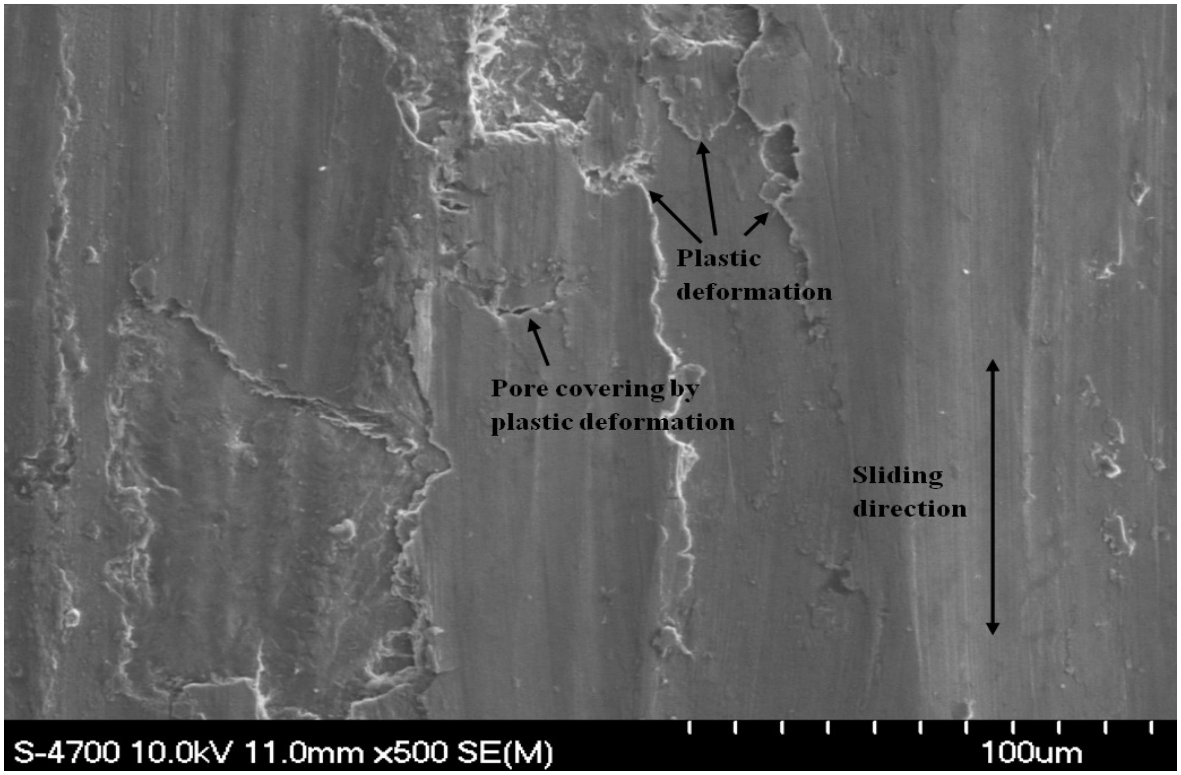

(b)

Figure 4.25 (a) Optical micrograph of transverse section of a wear track for Al-6wt% Si, (b) SEM micrograph of worn surface showing closing of pores by plastic deformation for A380M

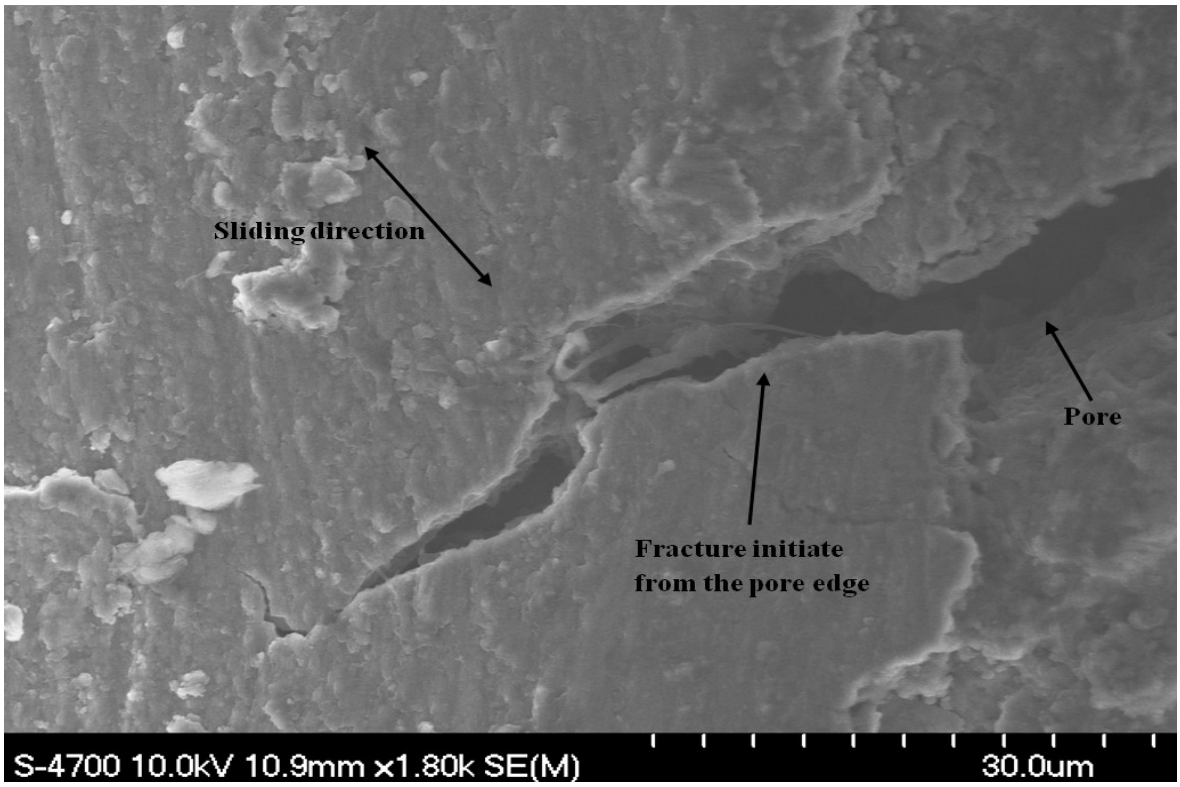

(a)

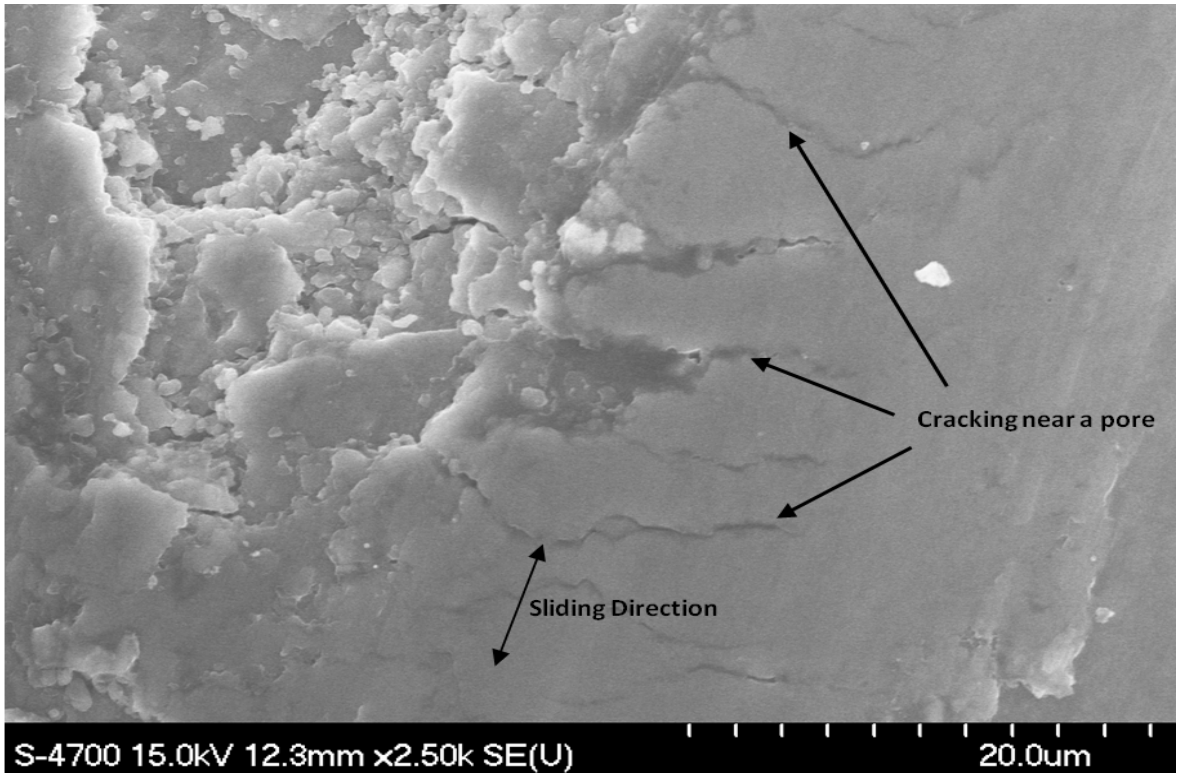

(b)

Figure 4.26 (a) Crack initiation from pore edge for A380M, (b) extension of the cracks for Al-6wt% Si

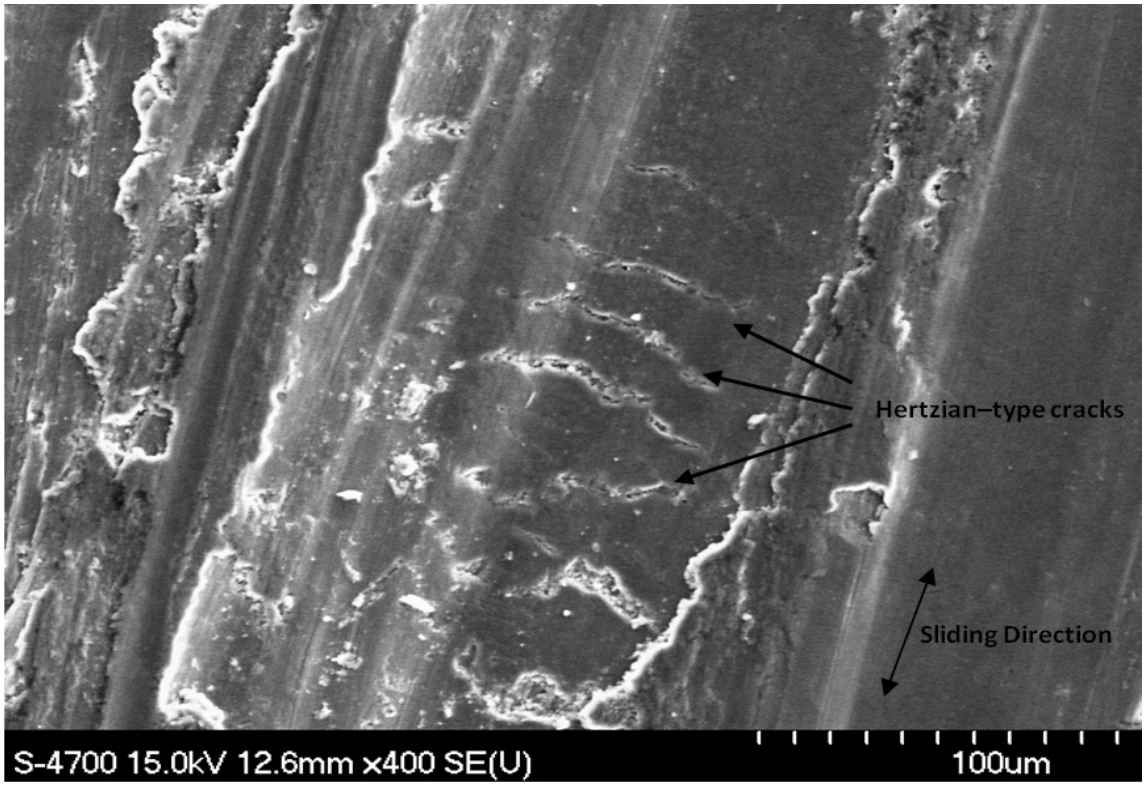

Figure 4.27 Hertzian type cracks for Al-6wt% Si

The other mechanism contributing to the observed wear is delamination. Initially, plastic deformation of surface layers due to cyclic normal and tangential loads take place, followed by crack or void nucleation in the deformed layers at pore sites (as pores act as high stress concentration zones). Cracks nucleate at depth where shear stress is maximum as predicted by the hertzian theory. Then cracks grow nearly parallel to the surface and eventually become unstable and extend to the surface leading to the formation of thin, plate-like (Figure 4.28) wear debris particles. Figure 4.29 (a) shows the plastic deformation on the surface of the wear track and exposed surface pit due to the delamination of wear debris. Plastic deformation, accumulated in the sub-surface layer, results in the detachment of wear debris as evident from Figure 4.29 (b).

Porosity in the subsurface layer accelerates the delamination wear process. Delamination wear occurs as a result of subsurface nucleation of cracks at pores (as they act as stress concentration regions) and propagation of these cracks (Figure 4.30(a)). There is a critical length of cracks beyond which cracks become unstable and propagate to the surface, generating wear debris. The cracks extend and create a network of cracks by

connecting different subsurface pores (Figure 4.30 (b)). Pores serve as the origin and end of crack propagation, hence reducing the required length of crack propagation.

Delamination from the subsurface layer can also take place by the initiation and joining of cracks at particle-matrix interfaces, as these areas are favorable sites for cracking. (Hamid, et. al, 2006). Figure 4.31 (a) shows an optical micrograph of a wear track cross section. The figure shows the debonding and breakaway of the Si particle in the subsurface layer creating a favorable site for crack initiation. This is in a good agreement with the work of Jahanmir and Suh (1977) who showed that for microstructures containing hard second-phase particles, if sufficient plastic deformation occurred during sliding wear, crack nucleation was favoured at these particles. Figure 4.31 (b) shows the debonding of the Si particle from the matrix and the link up of pores, which is further extended to the surface.

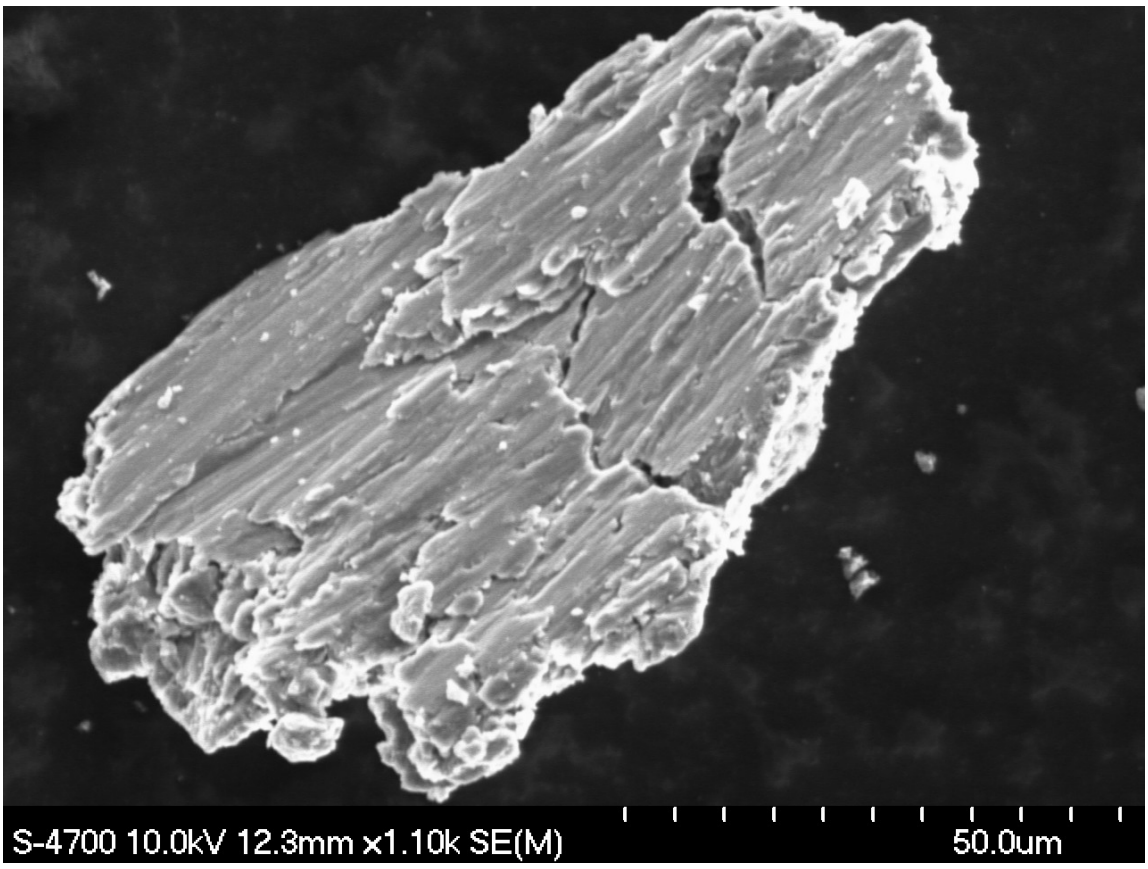

Figure 4.28 SEM image of plate like delaminated wear debris for A380M

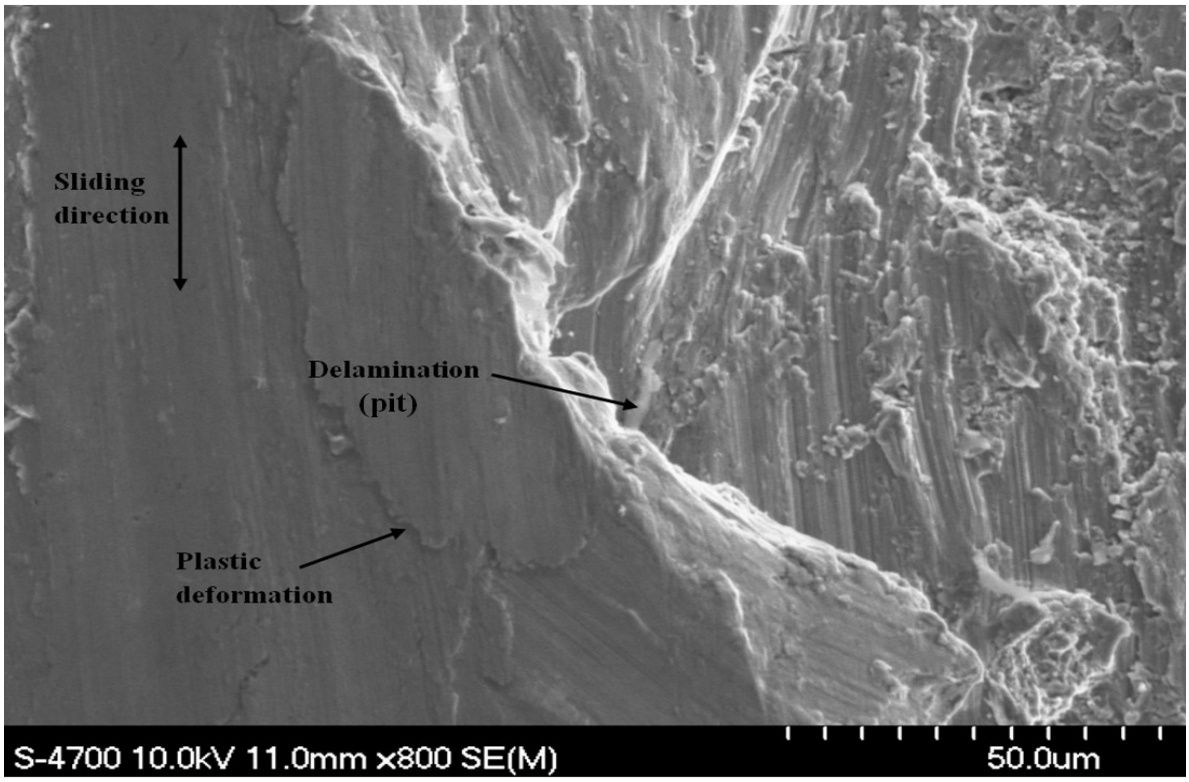

(a)

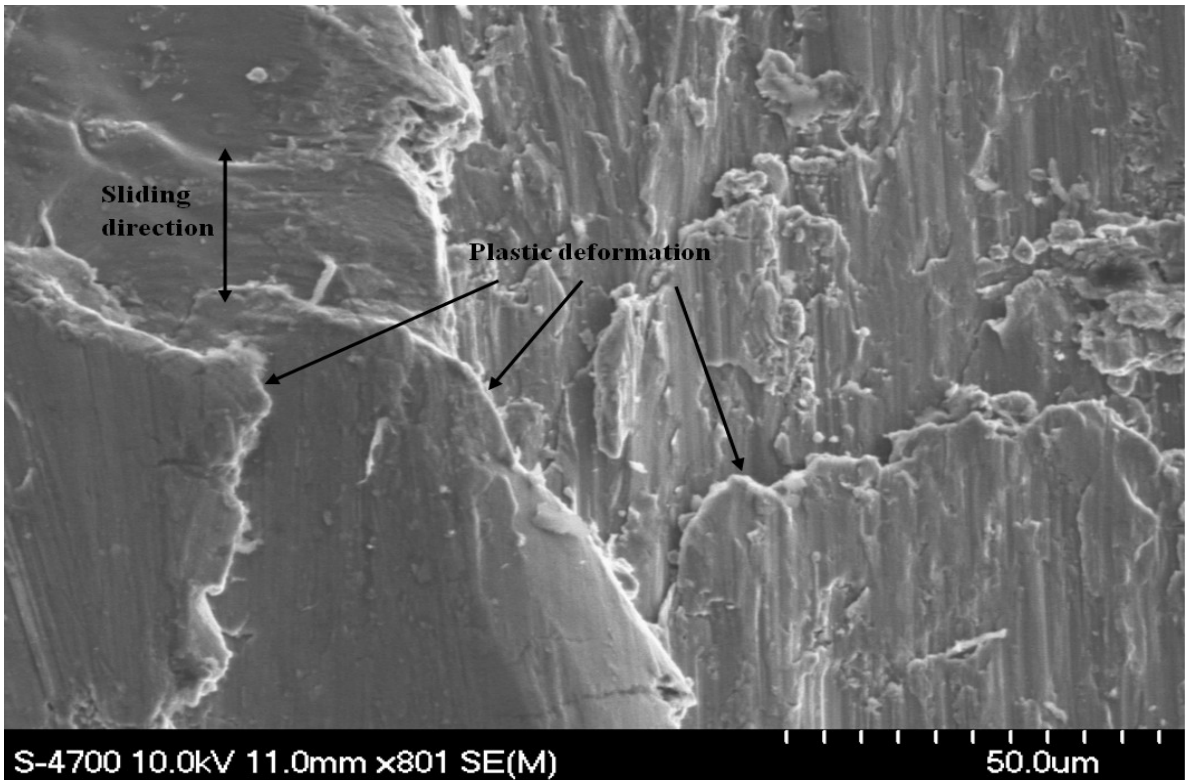

(b)

Figure 4.29 SEM image of wear track (a) plastic deformation and delamination, (b) evidence of plastic deformation in the sub-surface of A380M

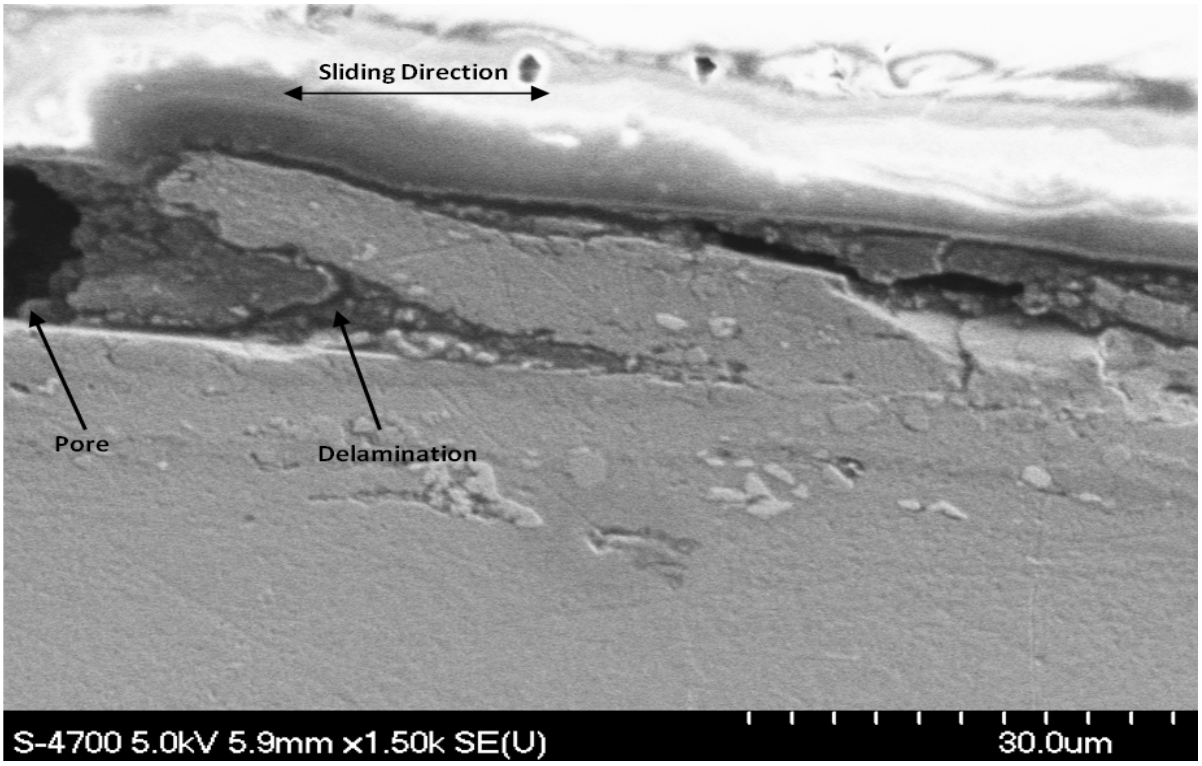

(a)

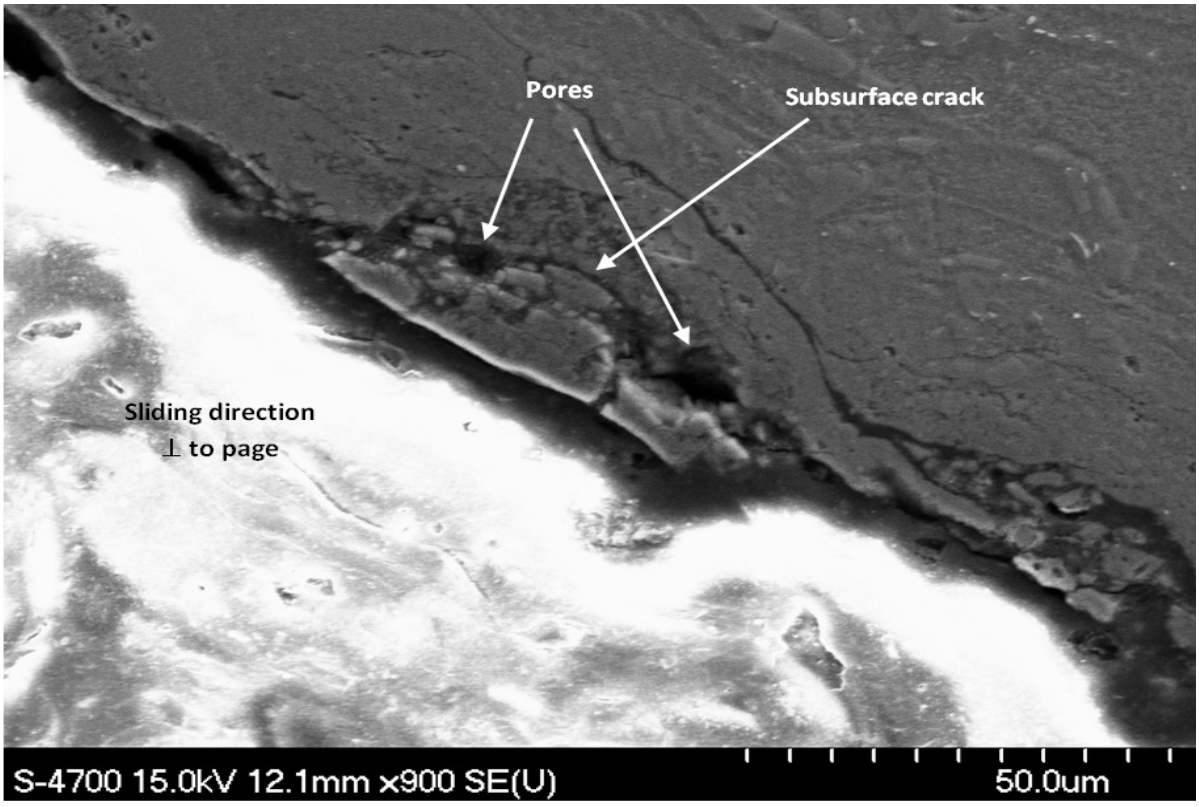

(b)

Figure 4.30 SEM image of Al-6wt% Si (a) transverse-section of wear track, (b) normal-section of the wear track

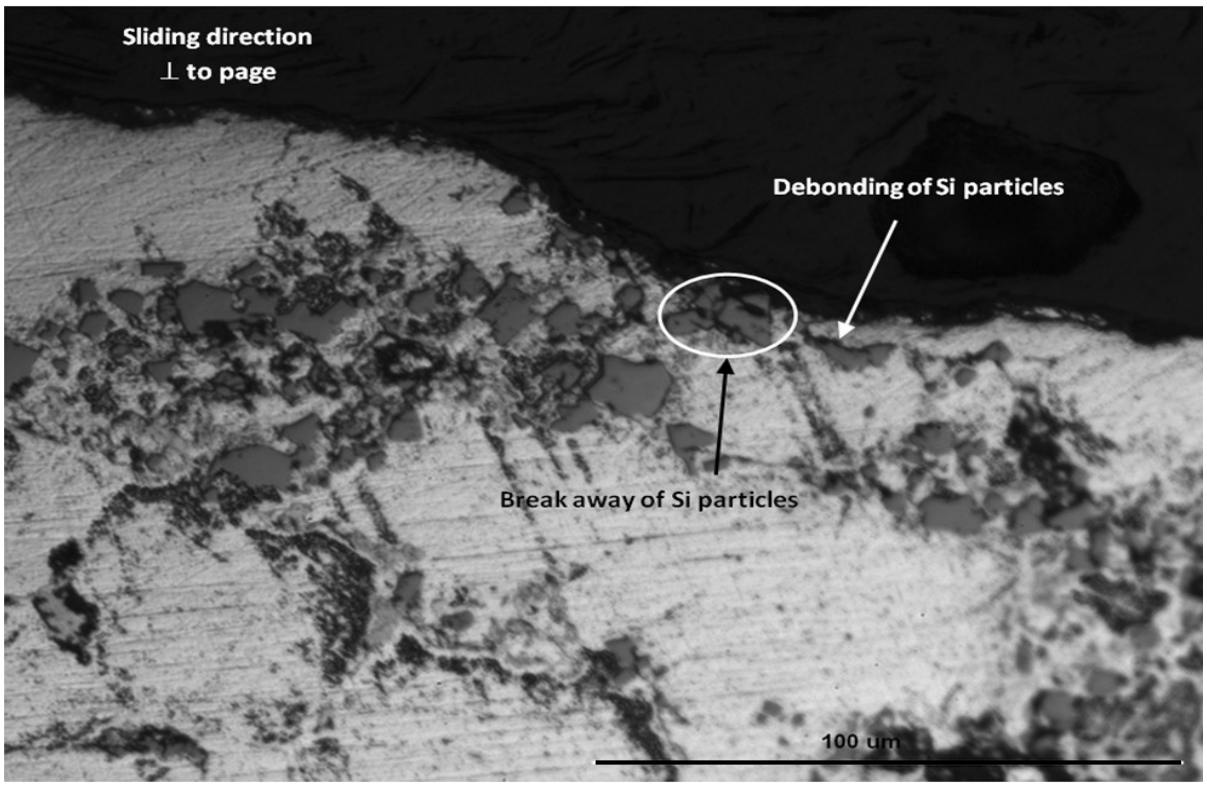

(a)

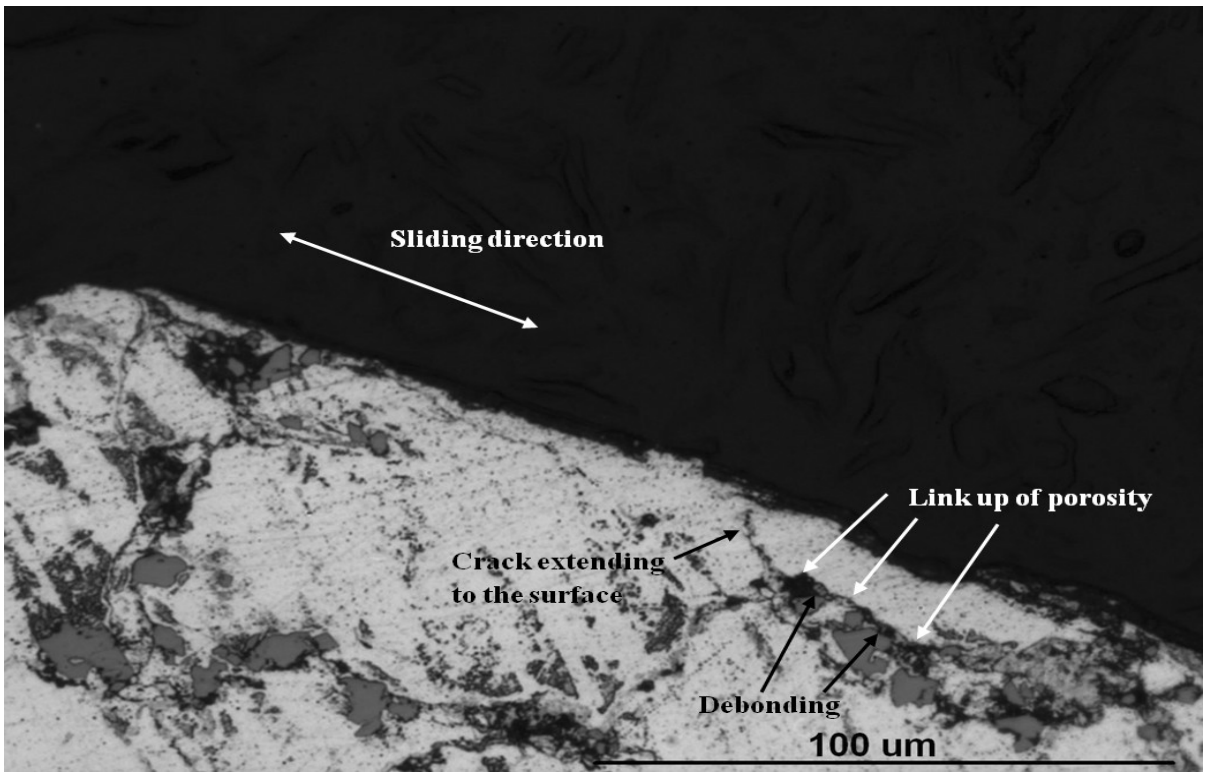

(b)

Figure 4.31 Optical micrograph of Al-6wt% Si (a) transverse-section of wear track, (b) normal-section of the wear track

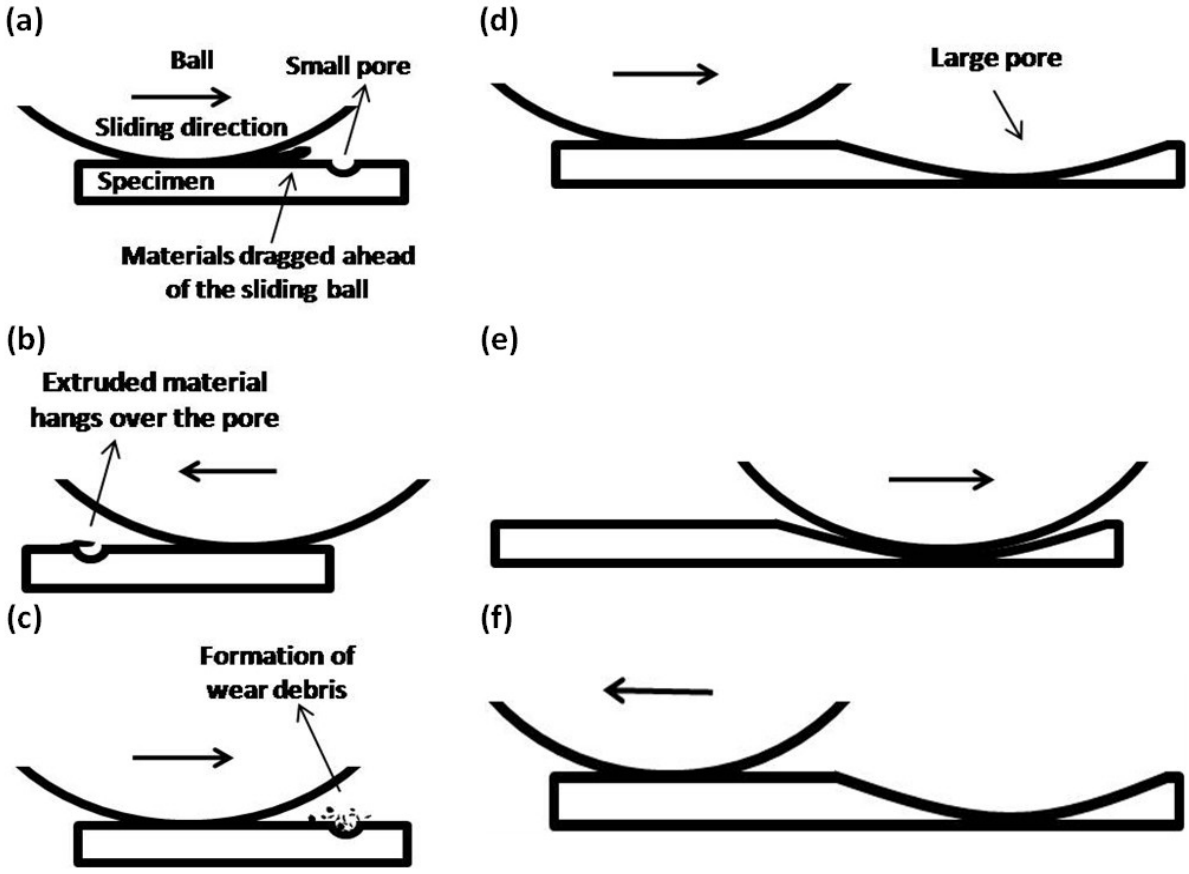

Figure 4.32 Schematic diagram depicting wear mechanisms in the presence of small and large pores.

Figure 4.32 is a schematic diagram showing the effect of pore size on wear mechanisms. Figure 4.32 (a-c) shows the covering of a small pore by deformed material ahead of the sliding counter-face and subsequent fracturing as a result of further passes of the slider. Figure 4.32 (d-f) shows the counter-face sliding inside a large pore, where the contact area and pore size are within the same order of magnitude. This model further explains the drop in wear rate at high porosity and large pore size for Al-6 wt% Si (Figure 4.11and Figure 4.14). Dubrujeaud et al. (1994) arrived at similar conclusions, that high porosity and large pore size have a beneficial impact on wear rate. However, they attributed the drop in wear rate at high porosity levels to lower contact pressure as a result of entrapment of wear debris in large pores.

Furthermore, the increase in wear rate for cast A380M alloy after HIP as porosity drops can be explained using the above model. As we discussed earlier, the decrease in hardness after HIP plays a vital role in lowering wear resistance. Moreover, as we see from Figure 4.19 and from Table 4.5, the average pore size of the specimens decreases after HIP. As soon as the pore size is lower than the critical contact area between the specimen and indenter ball at a given load, it may accelerate the wear process by plastic deformation and fracturing, through the mechanism described above.

SEM examination of the wear track after different sliding distance reveals that, in the initial stage of sliding, wear occurs by plastic deformation and delamination (Figure 4.33 (a)). As time progresses, the delaminated wear particles act as abrasive particles, break away into equiaxed irregular morphology, and some become entrapped in pores (Figure 4.33 (b)) and some become trapped between the sliding pair and wear occurs by three body abrasion mechanism (Figure 4.34). SEM examination of wear debris reveals two types of wear particles. The first type has an equiaxed irregular morphology (Figure 4.35 (a)), and the second type has a plate-like morphology (Figure 4.35 (b)). The coarse, plate-like particles are a result of delamination wear and the fine wear debris is believed to be a result of abrasive wear and break up of plate-like particles (Figure 4.35).

A notable feature of an XRD pattern of wear debris is the presence of a diffuse but distinct peak at Bragg's angle (2θ) between 10° and 15° (Figure 4.36). This suggests either the presence of an amorphous phase, such as Al_2O_3, or the formation of a nano-crystalline phase due to the heavy deformation during wear. EDX analysis of the wear track after 800 m sliding distance is shown in Figure 4.37 and reveals that the weight % of oxygen is around 3 % and 11 % in the matrix and inside the pore, respectively. Thus, it can be concluded that, after prolonged sliding, frictional heat generated in the contact surface increases the ambient temperature and a thin oxide layer is developed over the wear track, which in turn forms wear debris and is trapped in pores or in between the sliding pair.

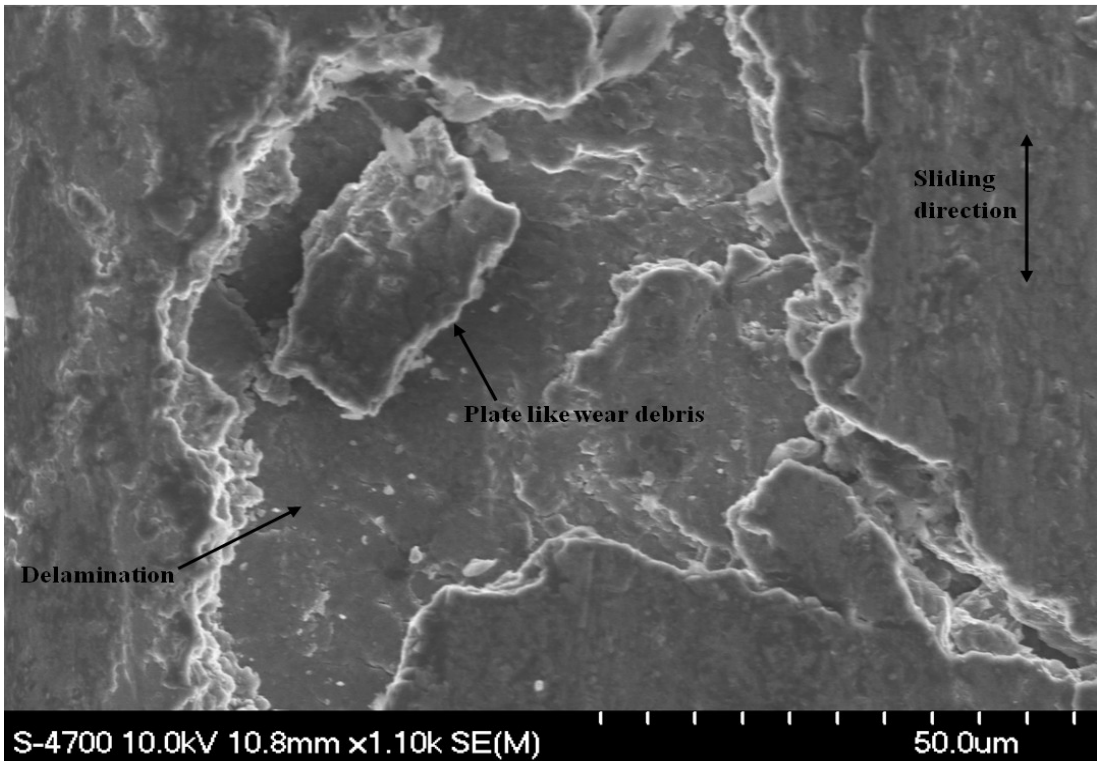

(a)

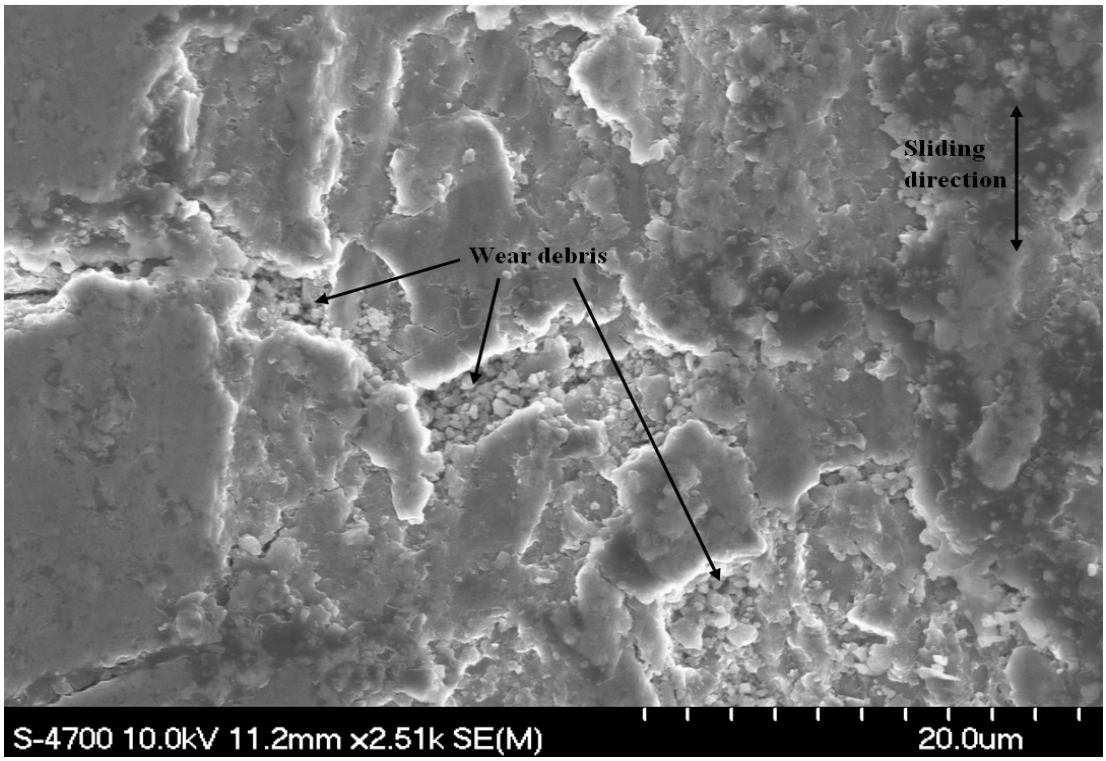

(b)

Figure 4.33 Wear track of A380M at (a) 90 m sliding distance, (b) 800 m sliding distance

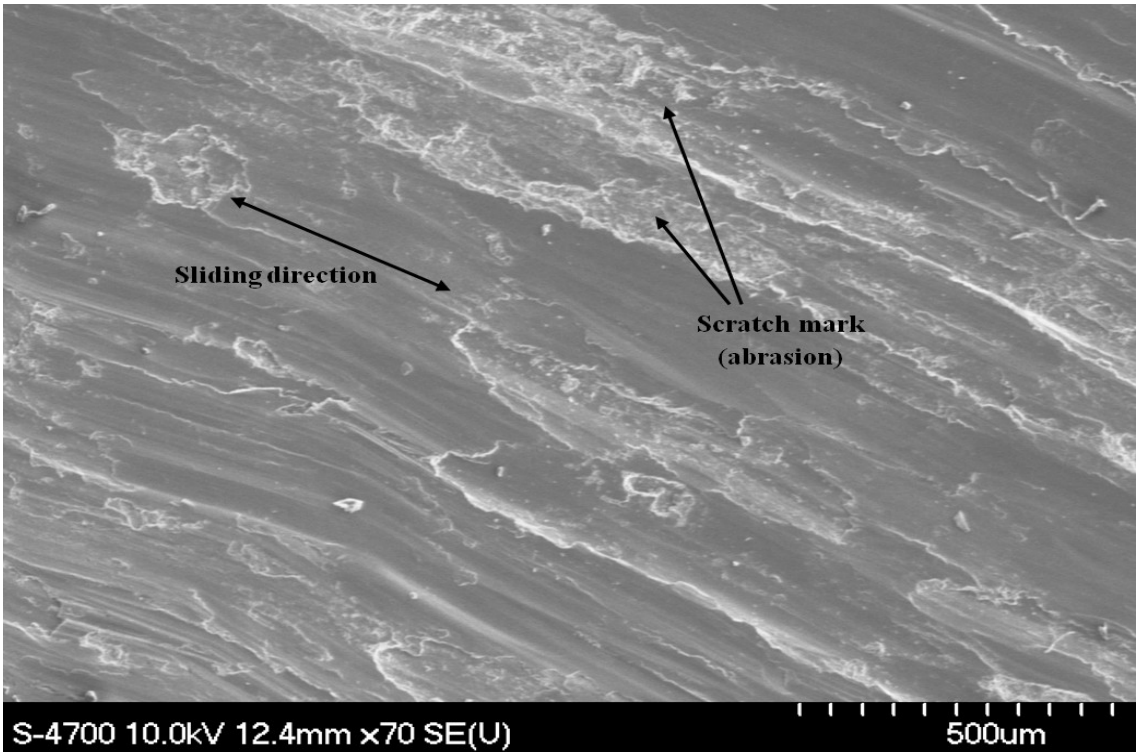

Figure 4.34 Abrasion wear by three-body abrasion mechanism for A380M

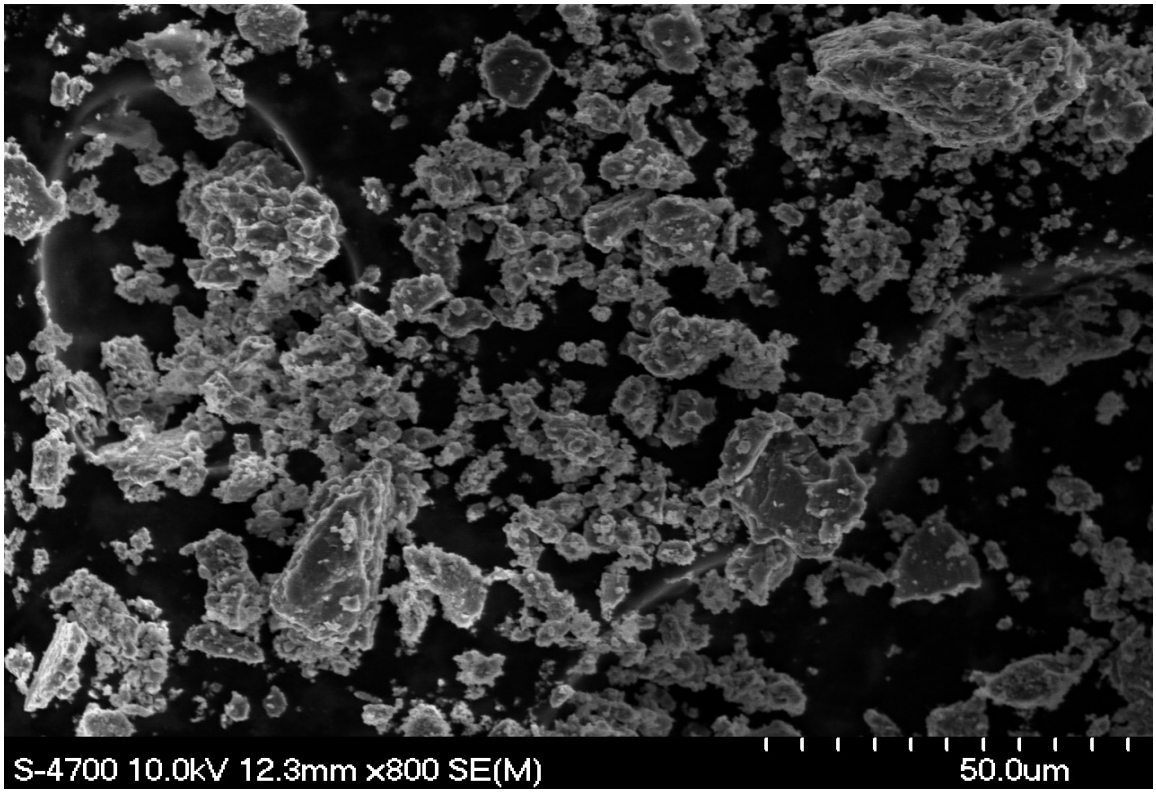

(a)

Figure 4.35 Wear debris of A380M collected at (a) 800 m sliding distance (equiaxed irregular morphology)

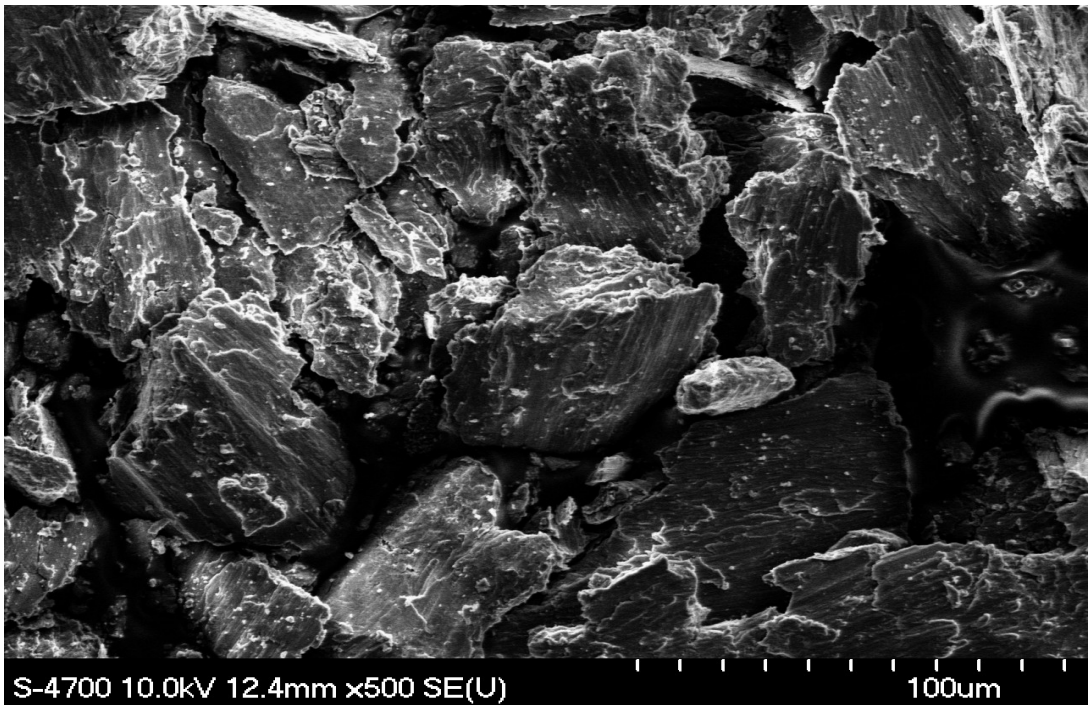

(b)

Figure 4.35 Continued. Wear debris of A380M collected at (b) 90 m sliding distance (Plate-like morphology)

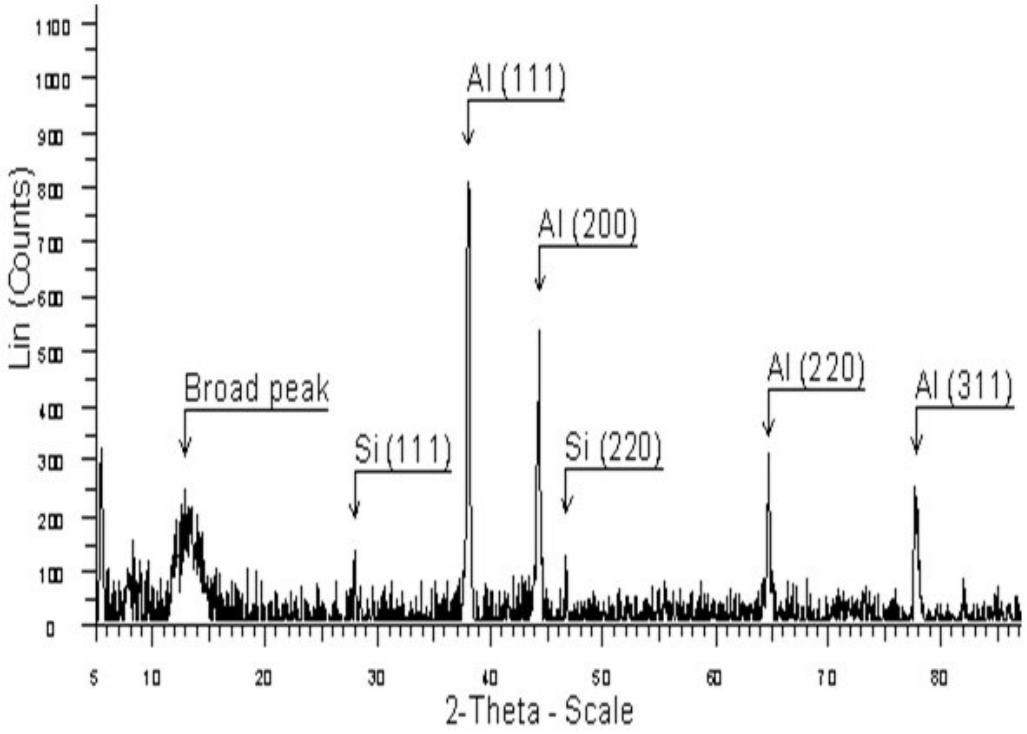

Figure 4.36 XRD pattern of wear debris

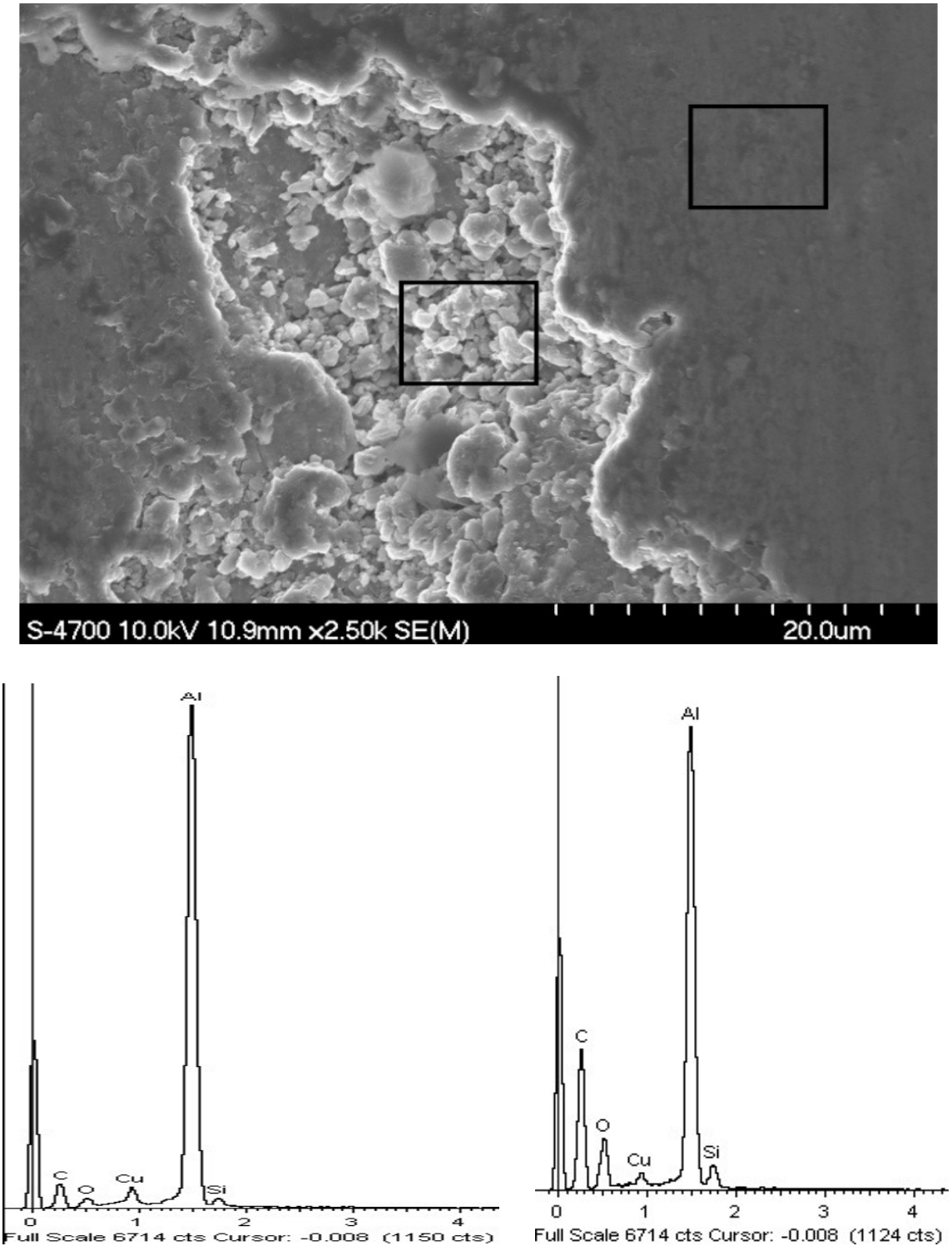

(a) (b)

Figure 4.37 EDS analysis of the wear track at 800 m sliding distance (a) in the matrix, (b)inside the pore.

CHAPTER 5 CONCLUSION

In the present project, the effects of surface porosity on the tribological properties of automotive Al-Si alloys were studied. The tribological behavior of A380M aluminum alloy with a surface porosity ranging from 2.6% to 6.7%, and an Al-6 wt% Si alloy with a surface porosity ranging from 1 % to 6.7%, have been investigated. The following main conclusions have emerged.

i. There is an inverse relationship between the hardness and porosity content of the specimens. The hardness of the specimens decreases with an increase in surface porosity. For A380M aluminum alloy, an approximate 33 % reduction in hardness was observed due to an increase in porosity from 2.6% to 6.9%. Again, for Al-6 wt% Si, the hardness of the alloy doubles as the surface porosity drops from about 6.7% to 1%.

ii. Wear of Al-Si alloy largely depends on operating conditions, such as normal load and sliding frequency. For A380M aluminum alloy, a linear increase in wear rate was observed with increasing normal load for all sliding frequencies. This is attributed to the rise in the maximum shear stress generated in the subsurface of the specimen with applied load. Increasing frequency resulted in decreasing wear rates due to the strain-hardening effect resulting from high strain rates. At high reciprocating frequency, frictional heat was generated at the contact surface layer, thus offsetting strain-hardening effects and ultimately leading to a plateau in wear rate.

iii. The amount of porosity plays a significant role during wear. Increase in porosity increases the wear rate of the material as a consequence of lower hardness and more asperity-asperity contact is followed by the generation of more wear debris. Furthermore, porosity in the sub-surface region minimizes the required length of crack propagation and creates a network resulting in delamination.

iv. The size and shape of pores have significant impact on material removal during wear. Below a certain critical pore size, wear occurs by two mechanisms: (a) partial covering of pores with a thin layer of deformed material and break up on

subsequent passes of the slider; and (b) nucleation of cracks at subsurface pores and connecting to other pores, ultimately leading to delamination of wear particles. As the porosity increases further, the wear resistance of Al-6wt%Si alloy increases, while hardness drops. When pore size is in the same order of magnitude as the contact area between the counter-face and the specimen, the counter-face slides into the pores and the pores become less effective in generating wear debris.

v. Lower porosity and higher hardness of the specimens are prerequisites for higher wear resistance. Higher compaction pressure at high temperature during HIP causes small pores to dissolve into the matrix and squeeze the large pores into smaller ones. Prolonged heating at high temperature causes grain growth of Al matrix at the expense of smaller grains. This microstructural change alters some physical properties, such as lowering the hardness of the specimens. Hence, the HIP treatment decreases the total amount of porosity at the expanse of decreased hardness. The competition between beneficial effect of lower porosity and the detrimental effect of lower hardness determines the final wear rate.

vi. Wear debris examination reveals two types of wear particles. The coarse plate-like particles are a result of delamination wear and the fine wear debris are believed to be a result of abrasive wear. Furthermore, it has been found that after prolonged sliding a thin oxide layer develops over the wear track as a result of frictional heating in ambient condition. This oxide film later breaks and forms hard wear debris which contributes to abrasive wear.

Although a fair amount of work has been performed in this study, more work is needed for a comprehensive understanding of the wear process. A number of recommendations for future work are listed below:

i. Developed a wear mechanism map defining the dominant wear mechanisms under different loads and frequencies and include the effect of porosity. Such map would be beneficial for the aluminum manufacturing industry.

ii. Apply cold isostatic pressing in order to avoid grain growth that occurs due to HIP.

iii. Perform high pressure water jet treatment to specimens as an alternative treatment to HIP to minimize porosity and increase wear resistance.

REFERENCES

(2010, May). Retrieved from www.wikipedia.org: http://en.wikipedia.org/wiki/Aluminium_alloy#cite_note-ReferenceA-0

Affatato, S., Spinelli, M., Zavalloni, M., Mazzega-Fabbroa, C., & Viceconti, M. (2008). Tribology and total hip joint replacement: Current concepts in mechanical simulation. *Medical Engineering & Physics , 30* (10), 1305-1317.

Aldham, D., Warburton, J., & Pendlebury, R. E. (1985). The unlubricated fretting of mild steel in air. *Wear , 106*, 177-201.

Alpas, A., & Zhang, J. (1992). Wear Rate Transition in Cast Aluminum- Silicon Alloys Reinforced with SiC Particles. *Scripta Metall , 26*, 505–509.

Alwahdi, F., Franklin, F., & Kapoor, A. (2005). The Effect of Partial Slip on the Wear Rate of Rails. *Wear , 258*, 1031–1037.

Amsallem, C., Gaucher, A., & Guilhot, G. (1973). The unlubricated frictional behaviour of sintered iron. *Wear , 23* (1), 97-112.

Anson, J., & Gruzleski, J. (1999). Effect of Hydrogen Content on relative shrinkage and Gas Microporosity in Al-7% Si Casting. *AFS Transactions , 107*, 135-142.

Antoniou, R., & Subramanian, C. (1988). Wear mechanism map for aluminum alloys. *Scripta Metallurgica , 22*, 809-814.

Archard, J. F. (1953). Contact and rubbing of flat surfaces. *Journal of applied physics , 24*, 981-988.

Archard, J. F., & Hirst, W. (1957). An examination of a mild wear precess. *Proc. R. Soc. Lond A. , 238*, 515-528.

Asensio-Lozanoa, J., & Suárez-Peña, B. (2006). Microstructure-properties correlation of pressure die cast eutectic aluminum–silicon alloys for escalator steps (Part II). *Materials Characterization , 56* (3), 178-184.

Ashby, M. F., & Lim, S. C. (1990). Wear mechanism maps. *Scripta Metallurgica , 24*, 805-810.

Ashby, M. F., Abulawi, J., & Kong, H. S. (1991). Temperature maps for frictional heating in dry sliding. *Tribology transition , 34*, 577-587.

ASM committee on Definitions of Metallurgical Terms. (1992). *Glossary of metallurgical terms and engineering tables.* (A. c. Metallurgical, Ed.) Metals park, Ohio: ASM.

ASM, H. (1992). *Friction, Lubrication, and Wear Technology* (Vol. 18). ASM International.

Bergmark, A., Alzati, L., & Persson, U. (2002). Crack initiation and crack propagation in copper powder mixed PM steel. *Powder Metallurgy Progress , 2* (4), 222-230.

Bhushan, B., & Gupta, B. K. (1991). *Handbook of Tribology: Materials, coatings, and surface treatments.* New York, NY, USA: McGraw-Hill.

Bindumadhavan, P., Chia, T., Chandrasekaran, M., Wah, H. K., Lam, L. N., & Prabhakar, O. (2001). Effect of particle-porosity clusters on tribological behavior of cast aluminum alloy A356-SiCp metal matrix composites. *Materials Science and Engineering , A315*, 217-226.

Biswas, S. K., & Bai, B. N. (1981). Dry wear of al-graphite particle composites. *Wear , 68* (3), 347-358.

Bocchini, G. (1986). The influence of porosity on the characteristics of sintered materials. *Int. J. Powder Metall , 22* (3), 185-202.

Boileau, J., & Allison, J. (2001). *The Effect of Porosity Size on the Fatigue Properties in a Cast 319 Aluminum Alloy* (Vol. 110). SAE transactions.

Bowden, F. P., & Tabor, D. (1950). *Friction and Lubrication of Solids, part 1.* Oxford, England: Clarendon press.

Bowden, F. P., & Tabor, D. (1964). *Friction and lubrication of solids, part 2.* Oxford, England: Clarendon press.

Chen, Q., Li, D., & Cook, B. (2009). Is porosity always detrimental to the wear resistance of materials?—A computational study on the effect of porosity on erosive wear of TiC/Cu composites. *Wear , 267*, 1153-1159.

Childs, T. H. (1988). The mapping of metallic sliding wear. *Proc. I. Mech. E. , 202* (C6), 379-395.

Danninger, H., Jangg, G., Weiss, B., & Stickler, R. (1993). Microstructure and mechanical properties of sintered iron part I: basic considerations and review of literature. *Powder Metall Int. , 25* (3), 111-117.

Deshpande, P., & Lin., R. Y. (2006). Wear resistance of WC particle reinforced copper matrix composites and the effect of porosity. *Materials science and engineering , A418*, 137-145.

Deuis, R. L., Subramanian, C., & Yellup, J. M. (1997). Dry sliding wear of aluminium composites—A review. *Composites Science and Technology , 57* (4), 415-435.

Dubrujeaud, B., Vardavoulias, M., & Jeandin., M. (1994). The role of porosity in the dry sliding wear of a sintered ferrous alloy. *Wear , 174*, 155-161.

Dwivedi, D. (2006). Wear Behavior of Cast Hypereutectic Aluminum Silicon Alloys. *Material design , 27*, 610–616.

Dwivedi, D. (2006). Wear Behavior of Cast Hypereutectic Aluminum Silicon Alloys. *Mater. Des. , 27*, 610-616.

EAA. (2009). Retrieved from European Aluminium Association: http://www.eaa.net/en/about-aluminium/production-process/castings/

Erikson, A. R., & Wiech, R. E. (1984). *Metals Handbook* (Vol. 7). Metals park , Ohio: ASM.

ESRF. (2006). Retrieved from In situ Microtomography Study of Metallic Powder Sintering: http://www.esrf.eu/UsersAndScience/Publications/Highlights/2002/Materials/MAT3

ESRF. (2006). Retrieved from In situ Microtomography Study of Metallic Powder Sintering : http://www.esrf.eu/UsersAndScience/Publications/Highlights/2002/Materials/MAT3

Finkin, E. F. (1978). An explanation of the wear of metals. *Wear , 47* (1), 107-117.

Fleming, J. R., & Suh, N. P. (1977). Mechanics of crack propagation in delamination wear. *Wear , 44* (1), 39-56.

Gerard, D., & Koss, D. (1990). Low Cycle Fatigue Crack Initiation: Modeling the Effect of Porosity. *Int. J. Powder Metall , 26* (4), 337-343.

German, R. M., & Munir, Z. A. (1975). Morphology relations during bulk-transport sintering. *Metallurgical and Materials Transactions A , 6* (12), 2229-2234.

German, R. M., & Munir, Z. A. (1975). Morphology relations during surface-transport controlled sintering. *Metallurgical and Materials Transactions B , 6* (2), 289-294.

German, R. (1994). *Powder Metallurgy Science* (2nd ed.). New Jersey: Metal Powder Industries Federation.

Gohar, R., & Rahnejat, H. (2008). *Fundamentals of tribology.* London: Imperical college press.

Gomes, J., Ramalho, A., Gaspar, M., & Carvalho, S. (2005). Reciprocating wear tests of Al–Si/SiCp composites: A study of the effect of stroke length. *Wear , 259* (1-6), 545-552.

Gruzleski, J., & Closset, B. (1990). *The Treatment of liquid Aluminum-Silicon Alloys.* Des plaines, IL, U.S.A: American Foundarymen's Society.

Gui, M., Kang, S. B., & Lee, J. M. (2000). Influence of porosity on dry sliding wear behavior in spray deposited Al–6Cu–Mn:SiCp composite. *Materials Science and Engineering, , 293*, 146–156.

Hamid, A. A., Ghosh, P., Jain, S., & Ray, S. (2006). Influence of particle content and porosity on the wear behaviourof cast in situ Al(Mn)–Al2O3(MnO2) composite. *Wear , 260*, 368-378.

Hamid, A. A., Ghosh, P., Jain, S., & Ray, S. (2008). The influence of porosity and particles content on dry sliding wear of cast in situ Al(Ti)–Al2O3(TiO2) composite. *Wear , 265*, 14-26.

Hanbing, X., Xiaogang, J., Thomas, T. M., & Qingyou, H. (2004). Degassing of molten aluminum A356 alloy using ultrasonic vibration. *Materials letters , 58* (29), 3669-3673.

Harsha, A. P., & Tewari, U. S. (2003). Two-body and three-body abrasive wear behaviour of polyaryletherketone composites. *Polymer Testing , 22* (4), 403-418.

He, Y., Winnubst, L., Burggraaf, A. J., & Verweij, H. (1997). Influence of Porosity on Friction and Wear of Tetragonal Zirconia Polycrystal. *Journal of the American Ceramic Society , 80* (2), 377-380.

Helwig, H.-M., Hiller, S., Garcia-Moreno, F., & B, J. (2009). Influence of Compaction Conditions on the Foamability of AlSi8Mg4 Alloy. *Metallurgical and Materials Transactions B , 40*, 755-767.

Hiratsuka, M. (2005). Role of wear particles in severe-mild wear transition. *Wear , 259* (1-6), 467-76.

Hirst, W., & Lancaster, J. (1960). The Influence of Speed on Metallic Wear. *Proc. Roy. Soc. , A259*, 228-241.

Hoffman, G., Lipp, K., Michaelis, K., Sonsino, C. M., & Rice, J. A. (1999). Testing P/M materials for high loading gear applications. *Int. J. Powder Metall , 35*, 35-44.

Hokkirigawa, K. (1991). Wear mode map for ceramics. *Wear , 151*, 219-228.

Hurricks, P. L. (1970). The mechanisum of fretting- A review. *Wear , 15*, 389-409.

Jahanmir, S. (1980). On the Wear Mechanisms and the Wear Equations. *Fundamentals of Tribology* , 455-469.

Jahanmir, S., & Suh, N. P. (1977). Mechanics of subsurface void nucleation in delamination wear . *Wear , 44*, 17-38.

Jasim, K. M., & Dwarakadasa, E. S. (1993). Effect of sliding speed on adhesive wear of binary Al-Si alloys. *Journal of materials science letters , 12*, 650-653.

Johnson, K. (1987). *Contact Mechanics* (First ed.). UK: Cambridge University Press.

Jun-an, W., & Danninger, H. (2001). Factors Influencing the Wear Behavior of Sintered Steels. *Journal of Shanghai University , 5* (3), 241-246.

Kalpakjian, S., & Schmid, S. R. (2003). *Manufacturing process for engineering materials.* Upper Saddle River, NJ: Pearson Education.

Kato, H., Eyre, T. S., & Ralph, B. (1994). Wear mechanism map of nitrided steel. *Acta Metall. Mater , 42*, 1703-1713.

Kaufman, J. G., & Rooy, E. L. (2004). *Aluminum alloy casting : Properties, processes, and applications.* AFS.

Kaufman, J. G., & Rooy, E. L. (2004). *Aluminum alloy casting: properties, processes and applications.* Materials park, OH: ASM International.

Khorasani, A. N. (1996). Gas porosity in aluminum silicon alloys. *Metal casting and surface finishing , 42* (9-10), 34-39.

Kim, M., Kwon, H., Kim, D., & Loper, C. (1997). *Porosity formation in Relation to the Feeding Behavior of Al-Si Alloys* (Vol. 105). AFS Transactions.

Kiuchi, M., & Kopp, R. (2002). Mushy/Semi-Solid Metal Forming Technology – Present and Future. *CIRP Annals - Manufacturing Technology , 51* (2), 653-670.

Kong, H. S., & Ashby, M. F. (1992). Wear mechanisms in brittle solids. *Acta Metall Mater , 40*, 2907-2920.

Kopeliovich, D. D. (2008). Retrieved from SubsTech: http://www.substech.com/dokuwiki/doku.php?id=mechanisms_of_wear

Liang, Y., Li, S., Jin, Y., Jin, W., & Li, S. (1996). Wear behaviour of a TiNi alloy. *Wear , 198*, 236-241.

Lim, S. C. (1998). Recent developments in wear mechanism maps. *Tribology International , 31* (1-3), 87-97.

Lim, S. C., & Ashby, M. F. (1987). Wear mechanism maps. *Acta metall , 35* (1), 1-24.

Lim, S. C., Lee, S. H., Liu, Y. B., & Seah, K. H. (1996). Wear maps for some uncoated cutting tools. *Tribotest , 3*, 67-87.

Lim, S. C., Liu, Y. B., Lee, S. H., & Seah, W. K. (1993). Mapping the wear of some cutting tool materials. *Wear , 162-164*, 971-974.

Lim, S., & Brunton, J. (1986). The unlubricated wear of sintered iron. *Wear , 113* (3), 371-382.

Ling, F. F., & Saibel, E. (1957). Thermal aspects of galling of dry metallic surfaces in sliding contact. *Wear , 1* (2), 80-91.

Liu, Y., Asthana, R., & Rohatgi, P. (1991). A map for wear mechanisms in aluminum alloys. *Journal of materials science , 26*, 99-102.

Lumley, R., Polmear, I., Groot, H., & Ferrier, J. (2008). Thermal characteristics of heat-treated aluminum high-pressure die-castings. *Scripta Materialia , 58* (11), 1006-1009.

Ma, Y. (2008). *Integrated Study of the Influence of Casting and Heat Treatment Parameters on Microstructures of Multiphase Multi-component Aluminum Alloys.* University of Connecticut.

Mahmoud, T. S., Mahmoud, F. H., Zakaria, H. M., & Khalifa, T. A. (2008). Effect of squeezing on porosity and wear behaviour of partially remelted A319/20 vol% SiCp metal matrix composites. *Proceedings of the Institution of Mechanical Engineers, Part C: Journal of Mechanical Engineering Science , 222*, 295-303.

Mashl, S. J. (1999). Hot isostatic pressing of casting. In *ASM handbook* (Vol. 15, pp. 408-416). ASM International.

Mashl, S. J. (2008). Hot isostatic pressing: more than a niche technology. *International journal of powder metallurgy , 44* (5), 27-30.

Mathers, G. (2002). Materials standards, designations and alloys. *The welding of aluminum and its alloys* , 35-49.

Menezes, P. L., Kishore, & Kailas, S. V. (2009). Role of surface texture of harder surface on subsurface deformation. *Wear , 266*, 103-109.

Method for Determination of Density of Compacted or Sintered Powder Metallurgy Products-Standard 42. (2002). *Standard Test Methods of Metal Powders and Powder Metallurgy Products* , 59-61. Princeton, NJ.

Moore, A. J., & Tegart, W. J. (1952). Relation between Friction and Hardness. *Proc. R. Soc. Lond A. , 212*, 452-458.

Mukhopadhyay, G. (2007). *An Overview of Die Casting Processes and Alumaximization.* Metal World.

Nathan, G. K., & Jones, W. J. (1966-67). Influence of the hardness of abrasives on the abrasive wear of metals. *Proceedings of the institution of mechanical engineers , 181* (30), 215-221.

OCPL. (2003). Retrieved from www.oilcheck.com.au: http://www.oilcheck.com.au/Tutorial/17_delamination_wear.htm

ODC. (2004). Retrieved from Ortal Die Casting: http://www.ortal.co.il/Index.asp?CategoryID=77&ArticleID=72

Oliver, W. C., & Pharr, G. (1992). Improved technique for determining hardness and elastic modulus using load and displacement sensing indentation experiments. *J. Mater. Res. , 74*, 1564–1580.

Pall. (2007). Retrieved from The Chain Reaction of Wear: http://www.pall.com/hydraulic_3779.asp

Polmear, I. J. (1995). Light Alloys: Metallurgy of the Light Metals. London: Edward Arnold.

Powder Metallurgy Design Solutions. (1999). Metal Powder Industries Federation.

Price, P. E., & Kohler, S. P. (1984). *Cold isostatic pressing of metal powders* (Vol. 7). Metals park, Ohio: ASM.

Price, P. E., & Kohler, S. P. (1984). *Hot isostatic pressing of metal powders* (Vol. 7). Metals park, Ohio: ASM.

Riedel, H., Kozák, V., & Svoboda, J. (1994). Densification and creep in the final stage of sintering. *Acta Metallurgica et Materialia , 42* (9), 3093-3103.

Rigney, D. A. (1988). Sliding wear of metals. *Annual reviews inc* , 141-163.

Rosenfield, A. R. (1987). A shear instability model of sliding wear. *Wear , 116*, 319-328.

Sadik, B. (2009). Investigation of Tribological and Mechanical Properties of Metal Bearing. *Bull. Mater. Sci. , 32* (4), 451-457.

Saka, N., Eleiche, A. M., & Suh, N. P. (1977). Wear of metals at high sliding speeds. *Wear , 44* (1), 109-125.

Sarkar, A. D., & Clarke, J. (1979). Wear Characteristics of as-cast Binary Aluminium-Silicon Alloys. *Wear , 54* (1), 7-16.

Sarkar, A., & Clacke, J. (1980). Friction and Wear of Aluminium-Silicon Alloys. *Wear , 61* (1), 157-167.

Schaffer, G., & Hall, B. (2002). The Influence of the Atmosphere on the Sintering of Aluminum. *METALLURGICAL AND MATERIALS TRANSACTIONS A , 33*, 3279-3284.

Sigworth, G., Wang, C., Huang, H., & Berry, T. (1994). *Porosity Formation in Modified and Unmodified Al-Si Alloy Casting* (Vol. 102). AFS Transactions.

Simchi, A., & Danninger, H. (2004). Effects of porosity on delamination wear behavior of sintered plain iron. *Powder metallurgy , 47*, 73-80.

Simchi, A., & Danninger, H. (2004). Effects of porosity on delamination wear behaviour of sintered plain iron. *Powder Metallurgy , 47* (1), 73-80.

Soemantri, S., McGee, A. C., & Finnie, I. (1985). Some aspects of abrasive wear at elevated temperatures. *Proceedings of the international conference on wear of materials* , 338.

Standard Practice for Determining the Inclusion or Second-Phase Constituent Content of Metals by Automatic Image Analysis. (2008). *Annual book of ASTM Standards* .

Standard Terminology Relating to Wear and Erosion. (1987). *Annual book of standards , 03.02*, 243-250.

Stolarski, T. (1994). Analysis of the resistance to motion in a sliding contact. *Wear , 171* (1-2), 203-209.

Straffelini, G., & Molinari, A. (2001). Dry Sliding Wear of Ferrous PM Materials. *Powder Metallurgy , 44* (3), 248-252.

Styles, K. T. (1980). The influence of fret corrosion upon the fatigue life of machine components. *Met. Australs* , 4-6.

Subramanian, C. (1991). Effects of sliding speed on the unlubricated wear behaviour of Al-12.3wt.% Si alloy. *Wear , 151* (1), 97-110.

Suh, N. P. (1977). An overview of the delamination theory of wear. *Wear , 44* (1), 1-16.

Suh, N. P. (1973). The delamination theory of wear. *Wear , 25*, 111-124.

Suh, N. P. (1980). Update on the Delamination Theory of Wear. *Fundamentals of Friction and wear of Materials* , 43-71.

Surface Engineering. (2005). Retrieved from Surface engineering forum: http://www.gordonengland.co.uk/wear.htm

Surface Engineering. (2007). Retrieved from Surface Engineering & Alloy Company: http://www.surfaceengineering.com/Solutions-Adhesive.htm

Tabor, D. (1983). Proc. Int. Conf. Tribology. in the 80s,. (p. 1). Cleveland, OH: NASA Lewis Research Center.

Tahat, M. S. (2010). Aluminium-silicon alloy and its composites reinforces by silicon carbide particles. *Microelectronics International , 27* (1), 21-24.

Tehrani, P. H., & Saket, M. (2009). Fatigue crack initiation life prediction of railroad. *Journal of Physics , 181*, 1-8.

Tekmen, C., Ozdemir, I., Cocen, U., & Onel, K. (2003). *Materials Science and Engineering , A360*, 365-371.

Tian, C., Law, J., van der Touw, J., & Murray, M. (2002). Effect of melt cleanliness on the formation of porosity defects in automotive aluminium high pressure die castings. *Journal of Materials Processing Technology , 122* (1), 82-93.

Tingler, K. (2008). *A Developmental Study in Tensile Properties of Plaster cast A356 Aluminum Alloy at Room and Elevated Temperature.* Oklahoma, OK: Oklahoma State University Stillwater.

Torabian, H., Pathak, J., & Tiwari, S. (1994). Wear characteristics of Al-Si alloys. *Wear , 172* (1), 49-58.

Tu, J., Rong, W., Guo, S., & Yang, Y. (2003). Dry sliding wear behavior of in situ Cu–TiB2 nanocomposites against medium carbon steel. *Wear , 255*, 832-835.

Tylczak, J. H., & Oregon, A. (1992). *Abrasive wear* (Vol. 18). ASM International.

Uyyuru, R., Surappa, M., & Brusethaug, S. (2006). Effect of reinforcement volume fraction and size distribution on the tribological behavior of Al-composite/brake pad tribo-couple. Wear, 260 (2006) . *Wear , 260*, 1248–1255.

Van Horn, K. R. (Ed.). (1967). *Aluminum* (Vol. 1). Metals Park, Ohio: American society for metals.

Vardavoulias, M., Jouanny-Tresy, C., & Jeandin, M. (1993). Sliding-wear behaviour of ceramic particle-reinforced high-speed steel obtained by powder metallurgy. *Wear , 165* (2), 141-149.

Wang, J. A., & Danninger, H. (2001). Factor Influencing the wear behavior of PM steels. *ACTA Metallurgica Sinica , 14* (1), 33-41.

Wang, J., He, Y., & Danninger, H. (2003). Influence of Porosity on the Sliding Wear Behavior of Sintered Fe-1.5Mo-0.7C Steels. *Journal of Materials Engineering and Performance , 12* (3), 339-344.

Wang, Y., & Rodkiewicz, C. M. (1994). Temperature maps for pin-on-disk configaration in dry sliding. *Tribology International , 27*, 259-266.

Waterhouse, R. B. (1977). The role of adhesion and delamination in the fretting wear of metallic materials. *45*, 355-364.

Wilson, S., & Alpas, A. T. (1997). Wear mechanism maps for metal matrix composites. *Wear , 212* (1), 41-49.

Yalcin, B. (2009). Effect of Porosity on the Mechanical Properties and Wear Performance of 2% Copper Reinforced Sintered Steel Used in Shock Absorber Piston Production. *J. Mater. Sci. Technol. , 25* (5), 577-582.

Ye, H., Li, D., & Eadie, R. (2001). Influences of Porosity on Mechanical and Wear Performance of Pseudoelastic TiNi-Matrix Composites. *Journal of Materials Engineering and Performance , 10* (2), 178-185.

Appendix A: Raw Data

Reciprocating ball-on-flat test results

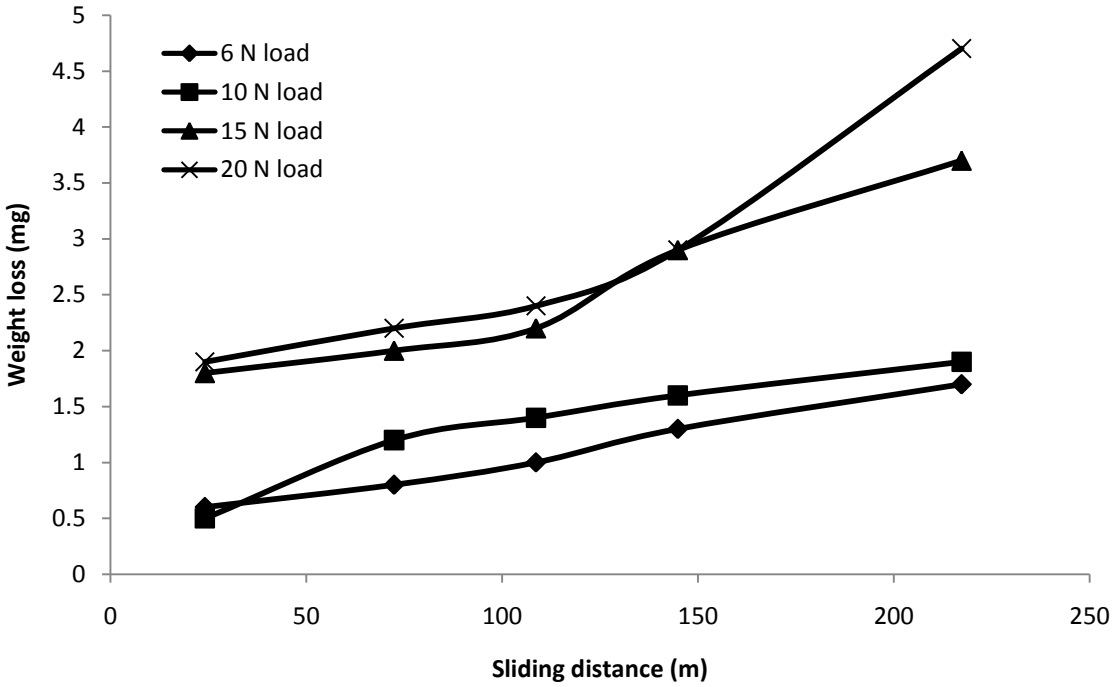

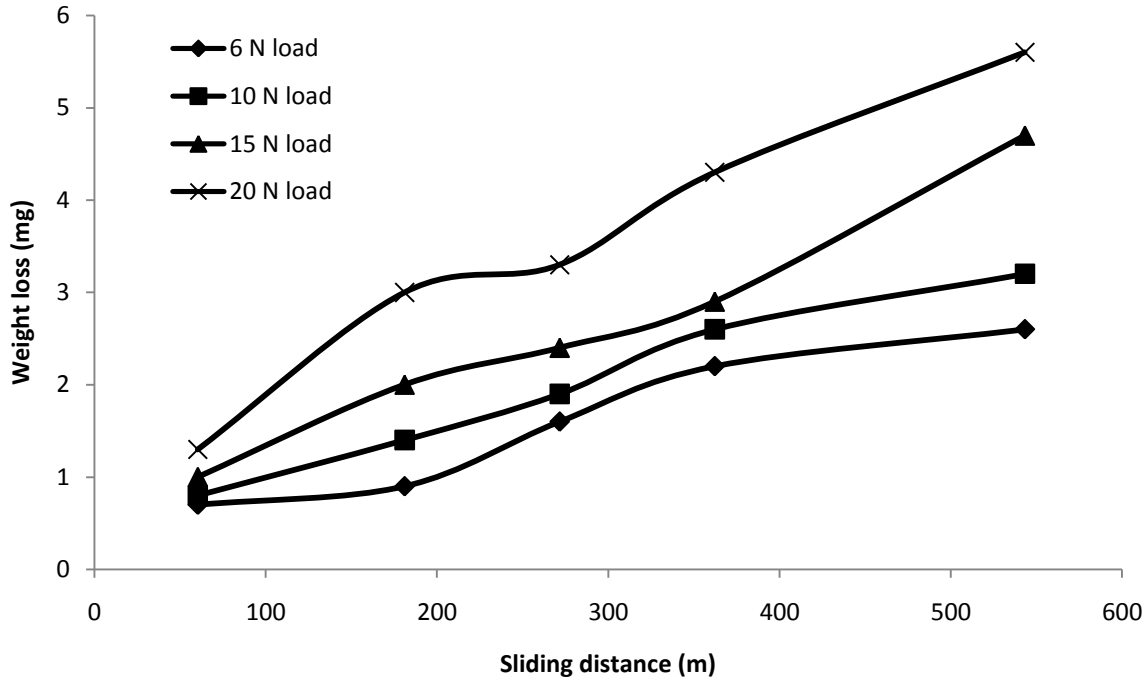

Figure A 1 Weight loss vs sliding distance for as received specimens at a frequency of (a) 4 Hz, (b) 10 Hz

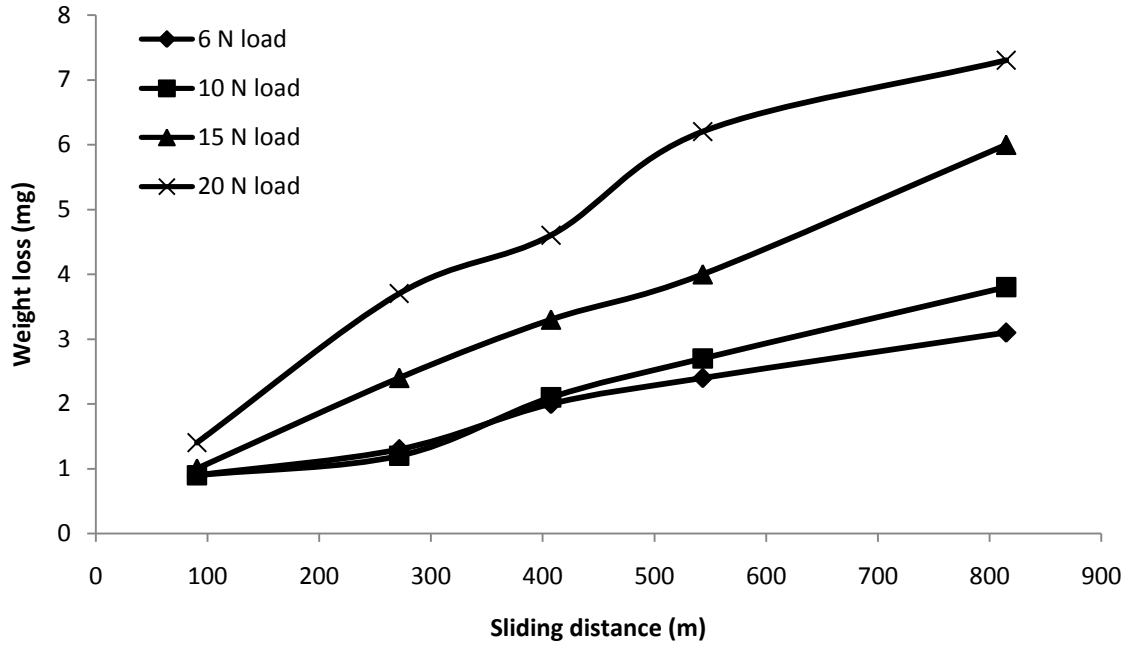

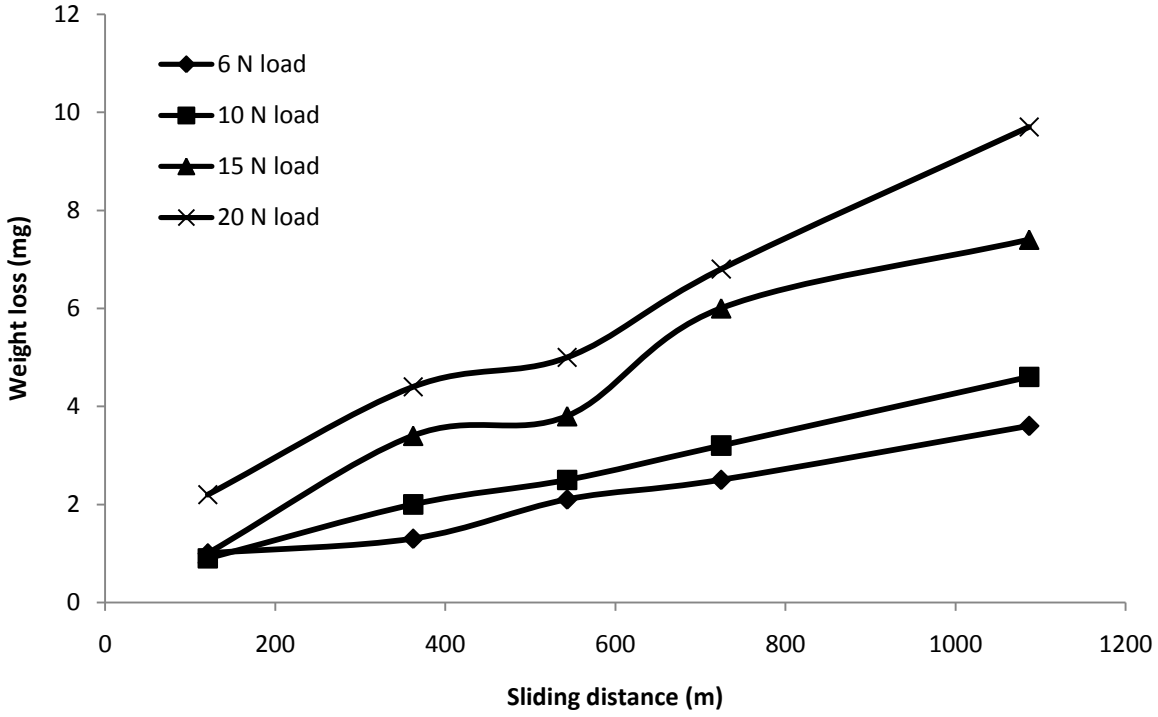

Figure A 1 Continued. Weight loss vs sliding distance for as received specimens at a frequency of (c) 15 Hz, (d) 20 Hz

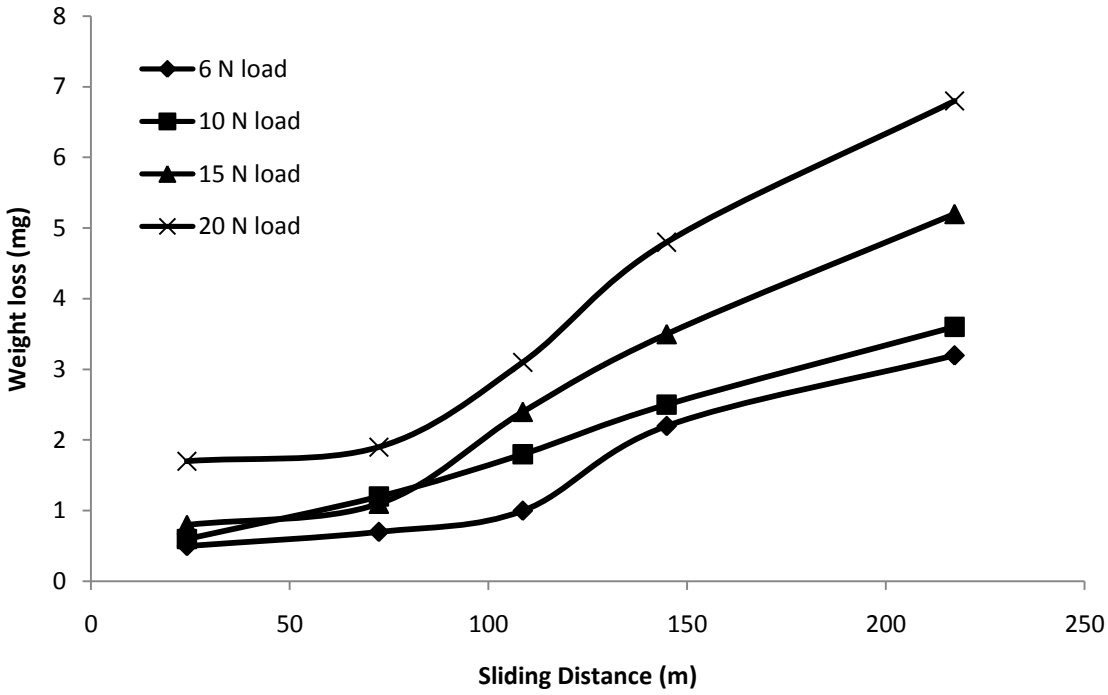

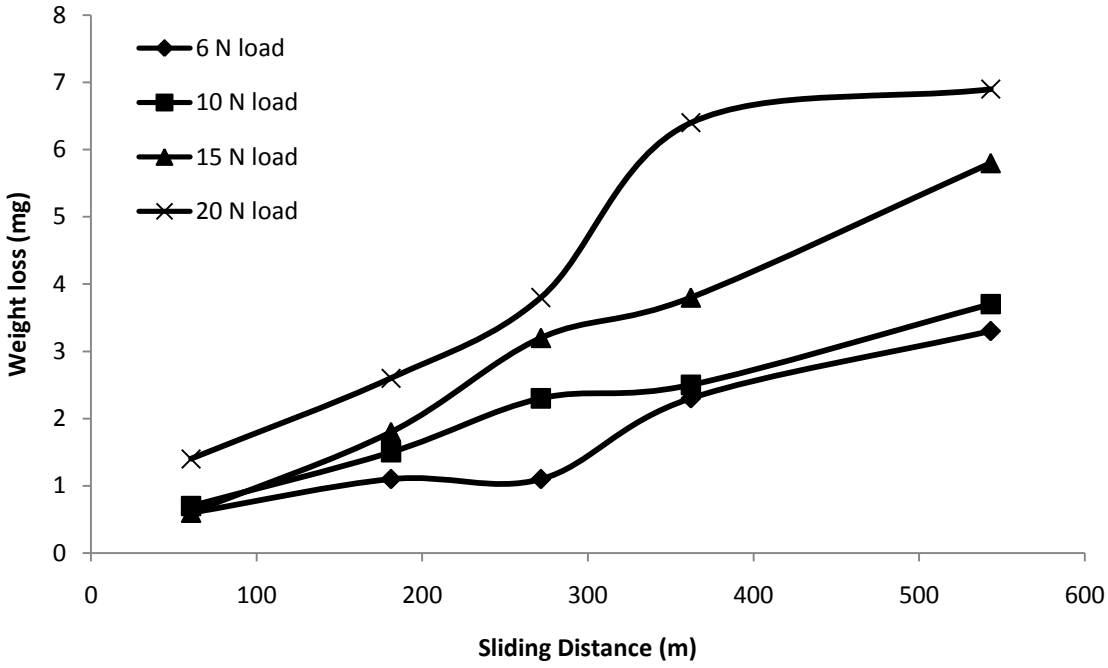

Figure A 2 Weight loss vs sliding distance for cast condition 1specimens at a frequency of (a) 4 Hz, (b) 10 Hz

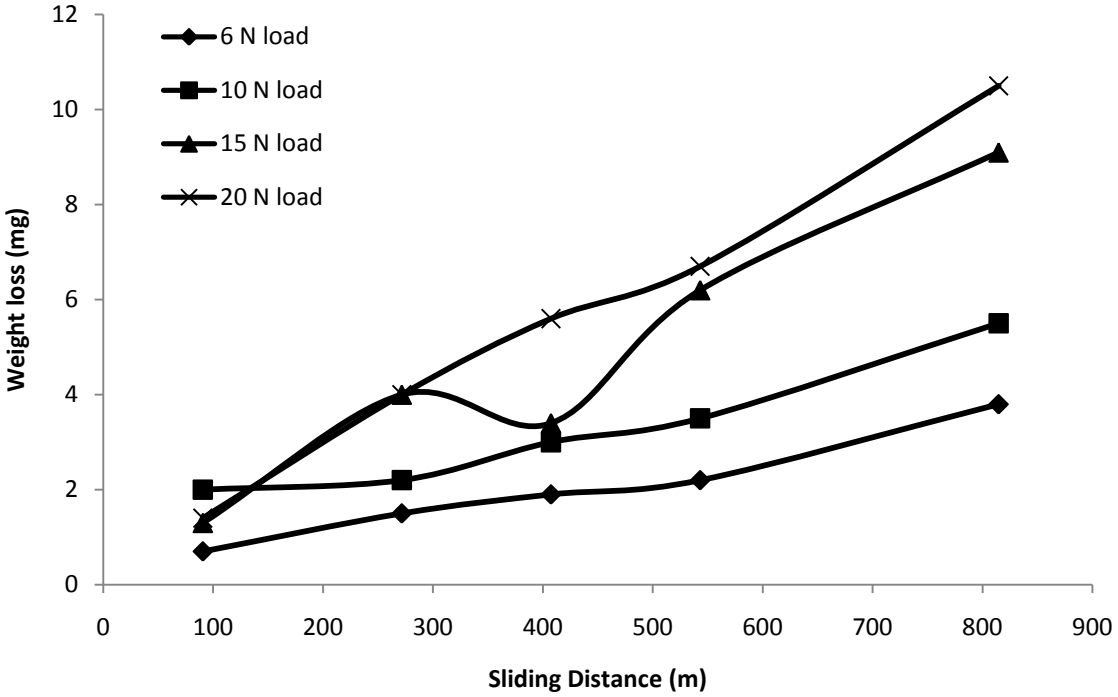

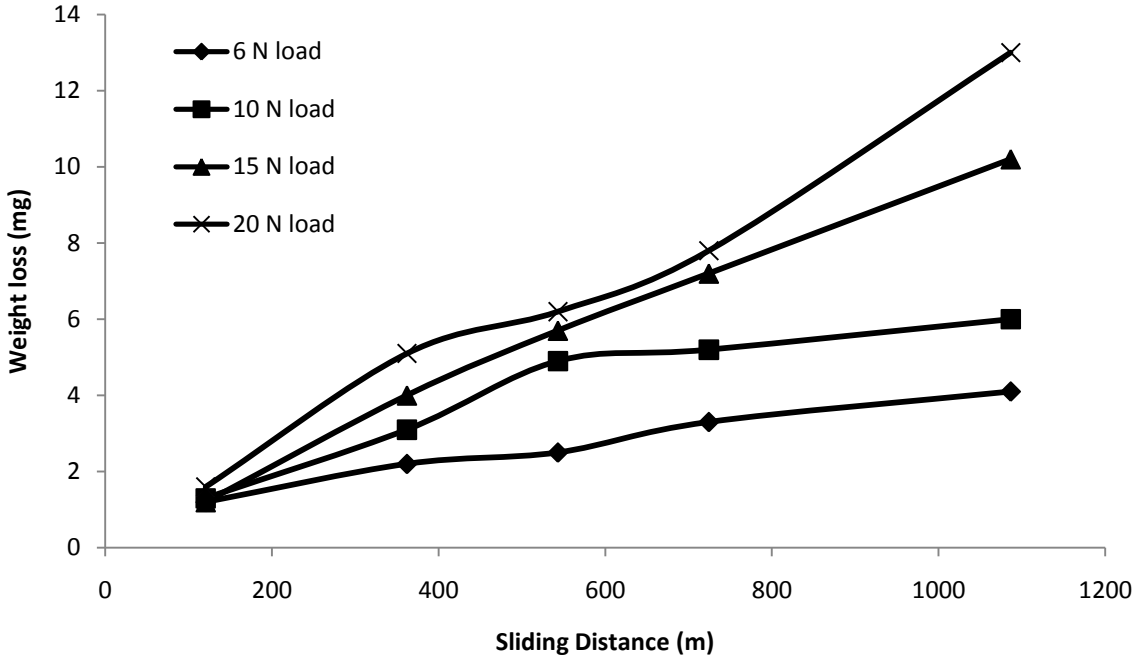

Figure A 2 Continued. Weight loss vs sliding distance for cast condition 1specimens at a frequency of (c) 15 Hz, (d) 20 Hz

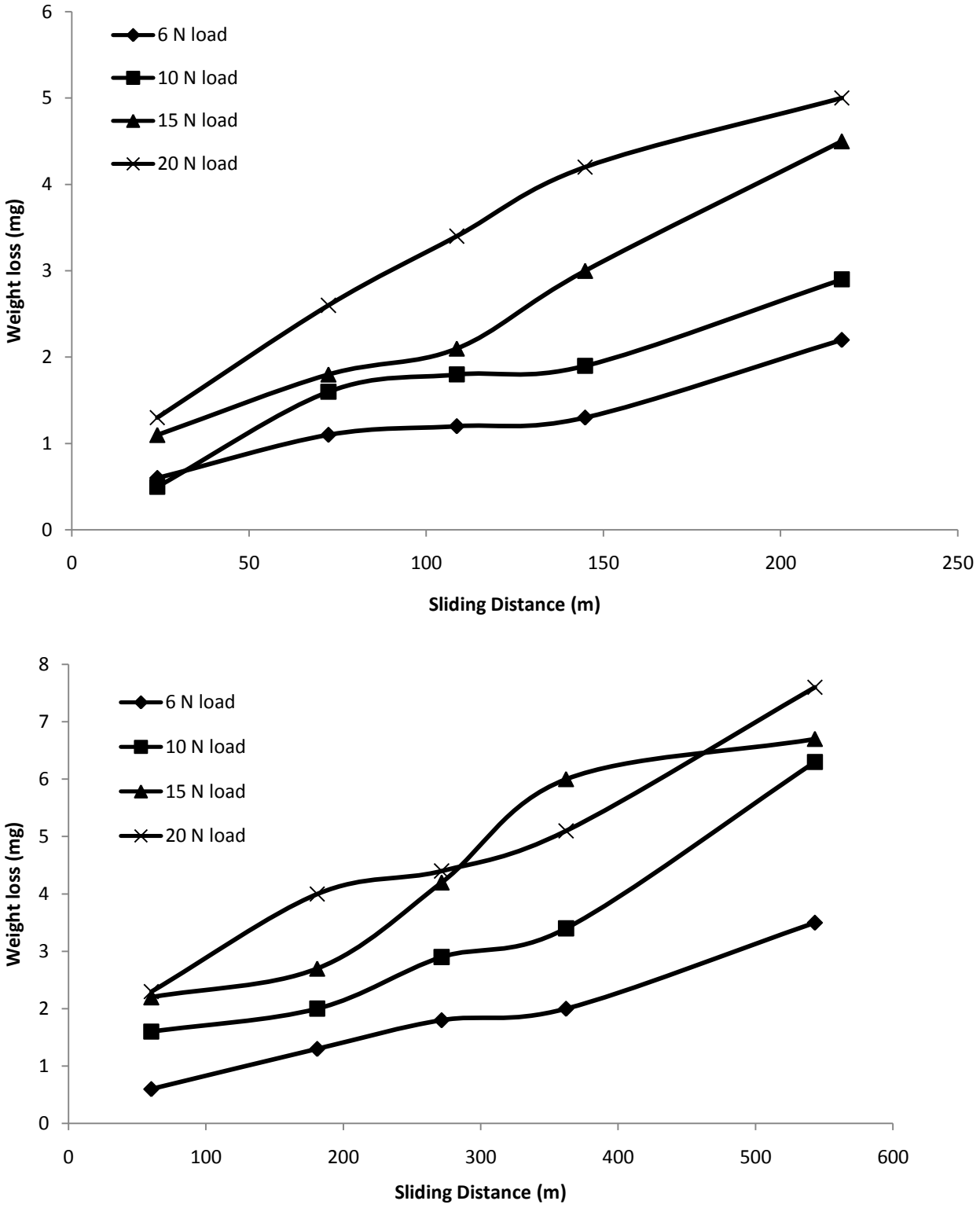

Figure A 3 Weight loss vs sliding distance for cast condition 2 specimens at a frequency of (a) 4 Hz, (b) 10 Hz

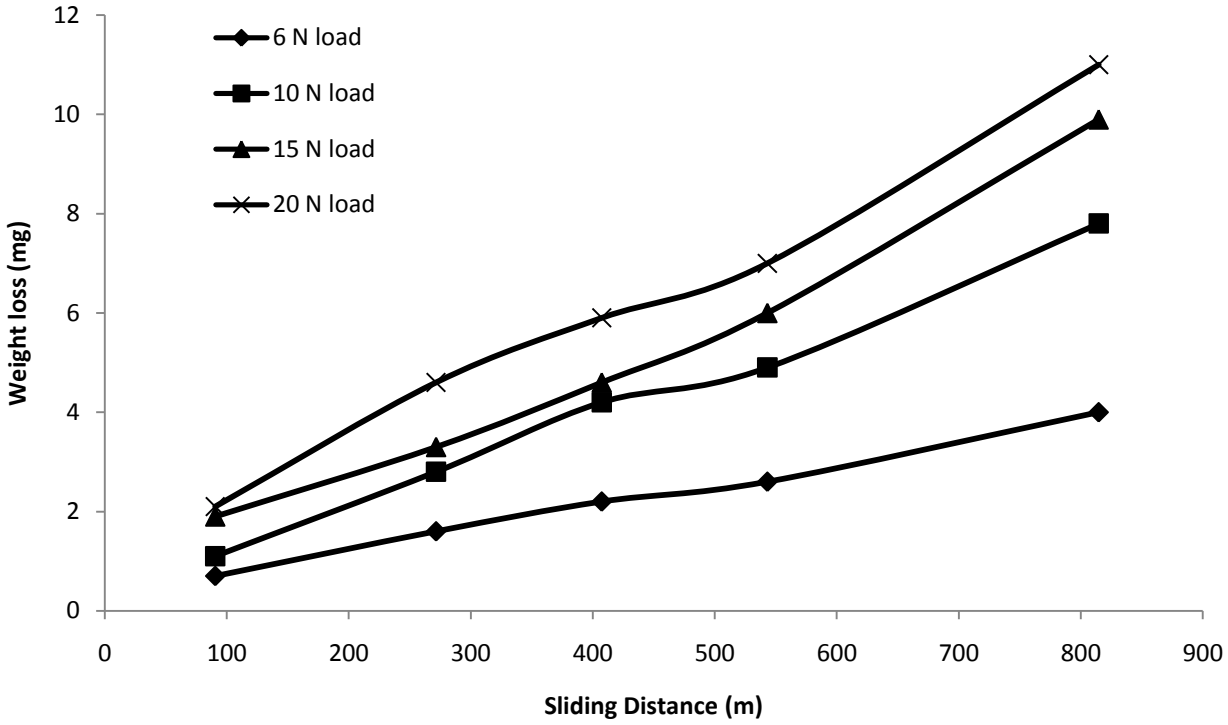

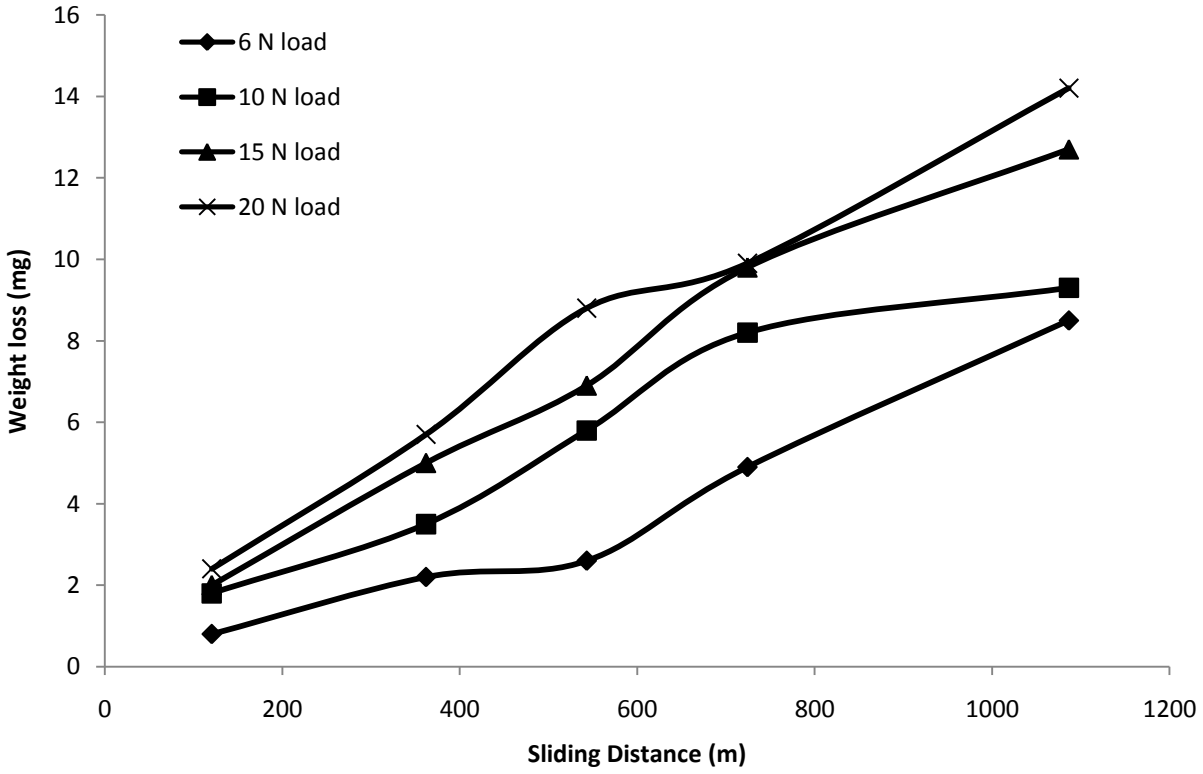

Figure A 3 Weight loss vs sliding distance for cast condition 2 specimens at a frequency of (c) 15 Hz, (d) 20 Hz

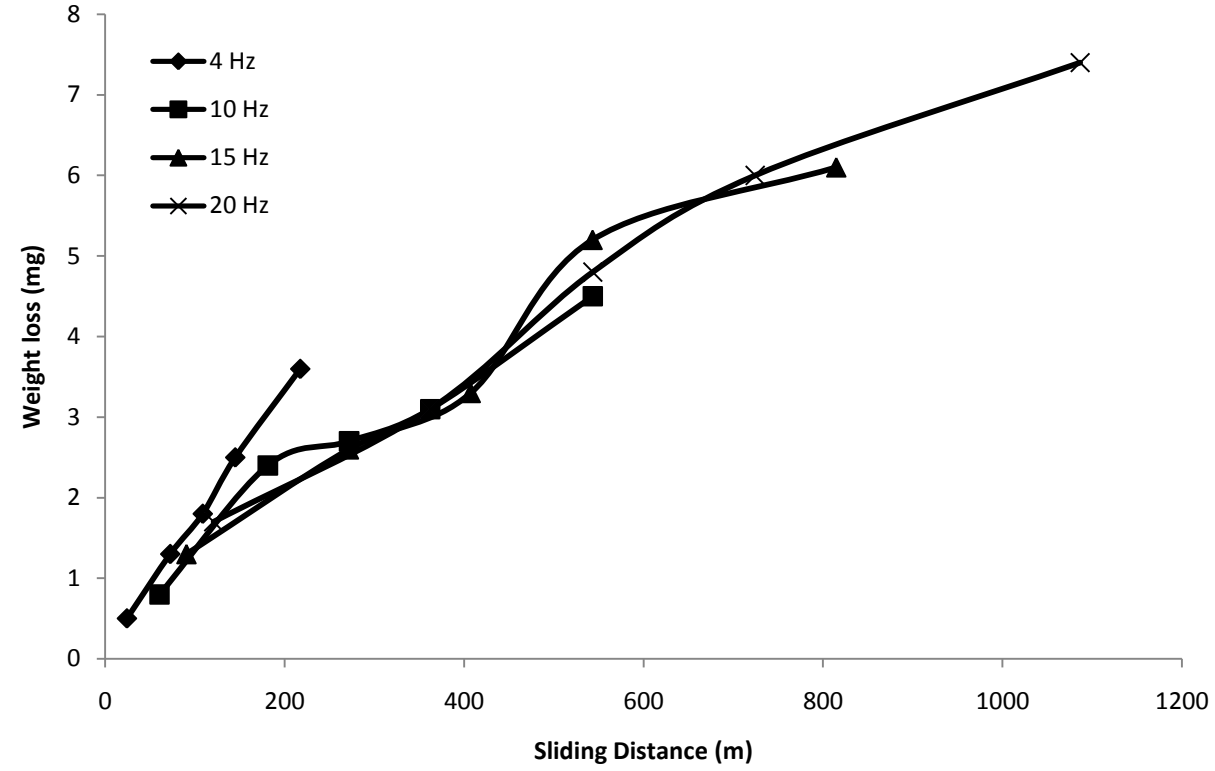

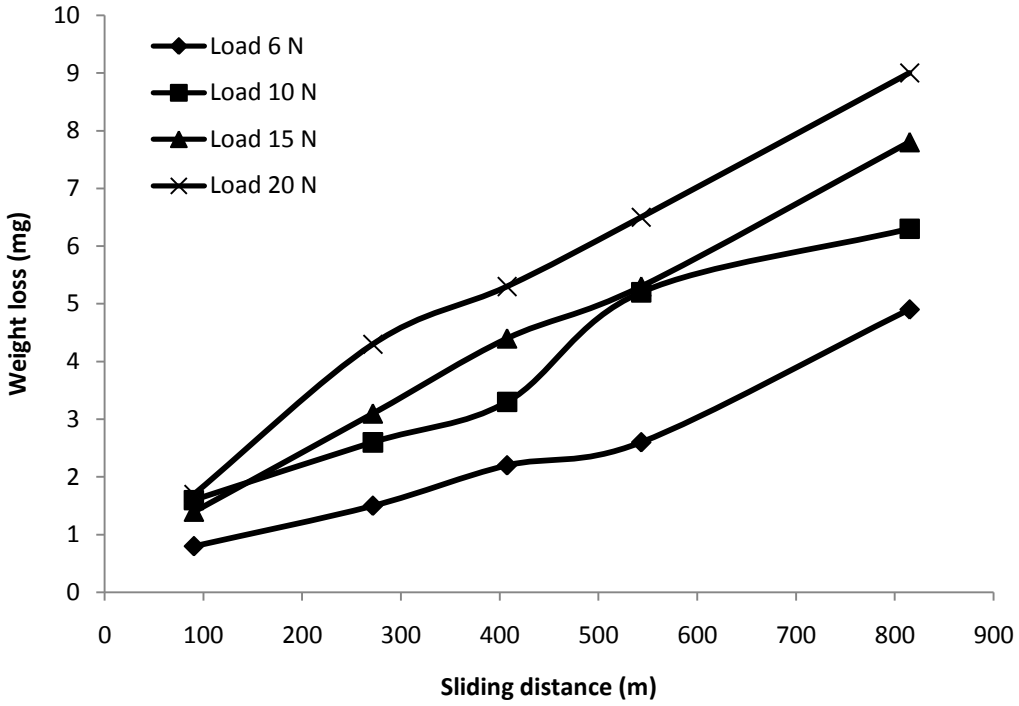

Figure A 4 Weight loss vs sliding distance for as received A380M specimens after HIP at (a) 10 N normal load, (b) 15 Hz frequency

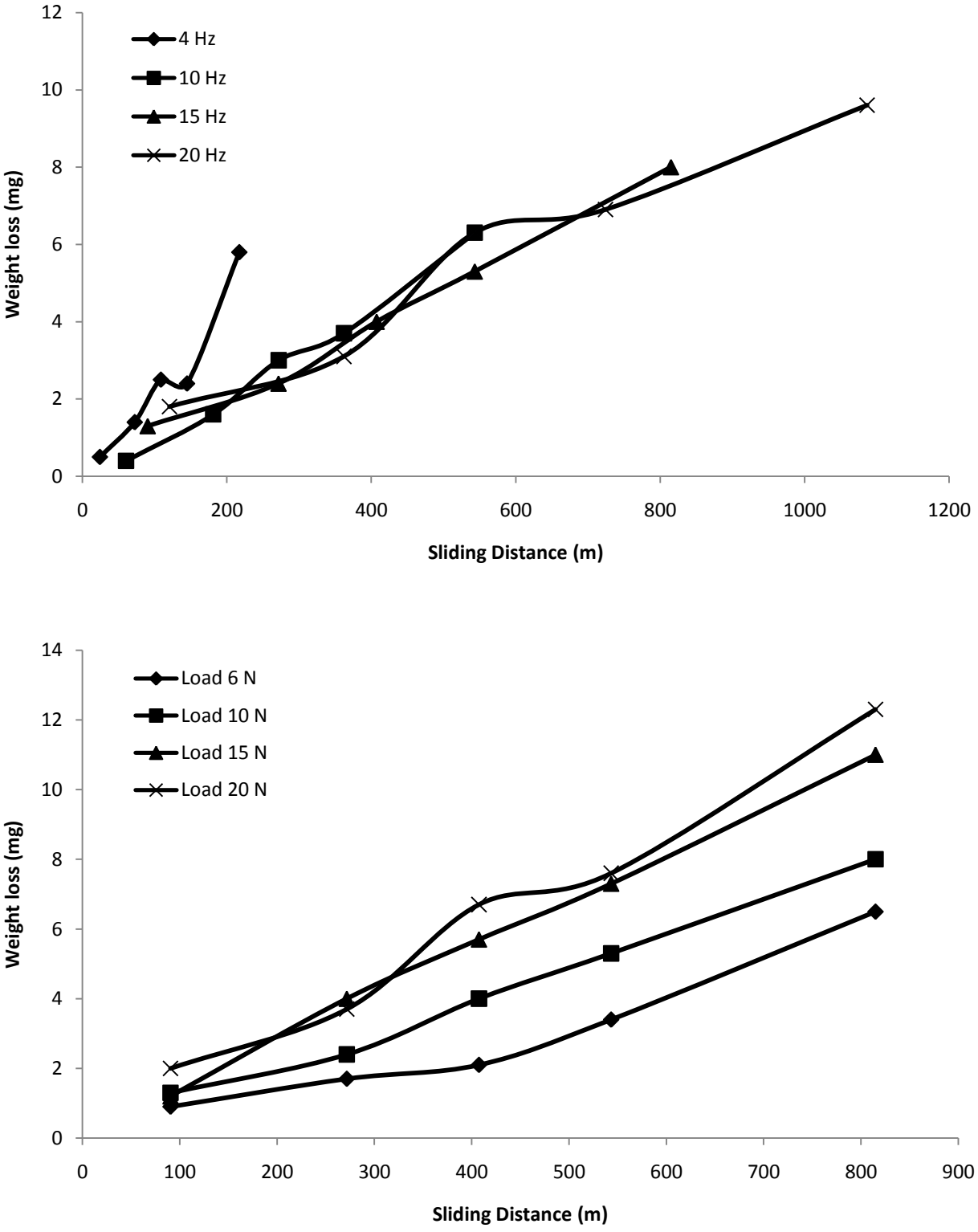

Figure A 5 Weight loss vs sliding distance for A380M, cast condition 1 specimens after HIP at (a) 10 N normal load, (b) 15 Hz frequency

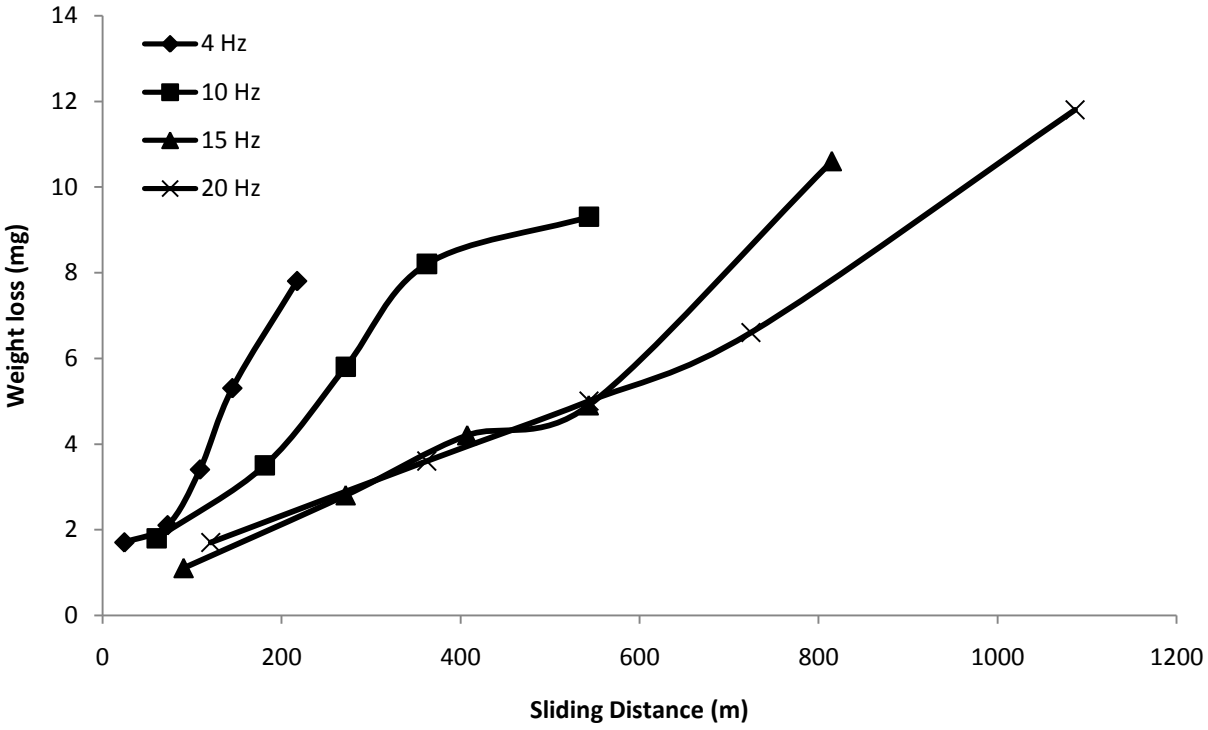

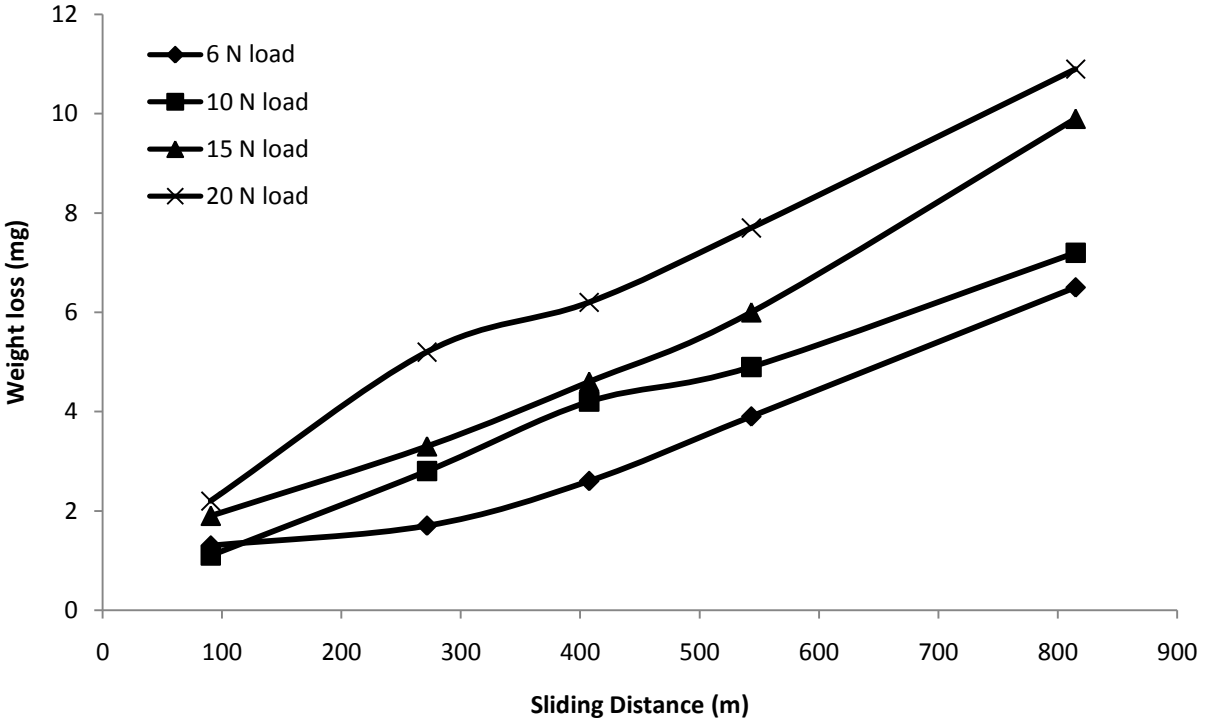

Figure A 6 Weight loss vs sliding distance for A380M, cast condition 2 specimens after HIP at (a) 10 N normal load, (b) 15 Hz frequency

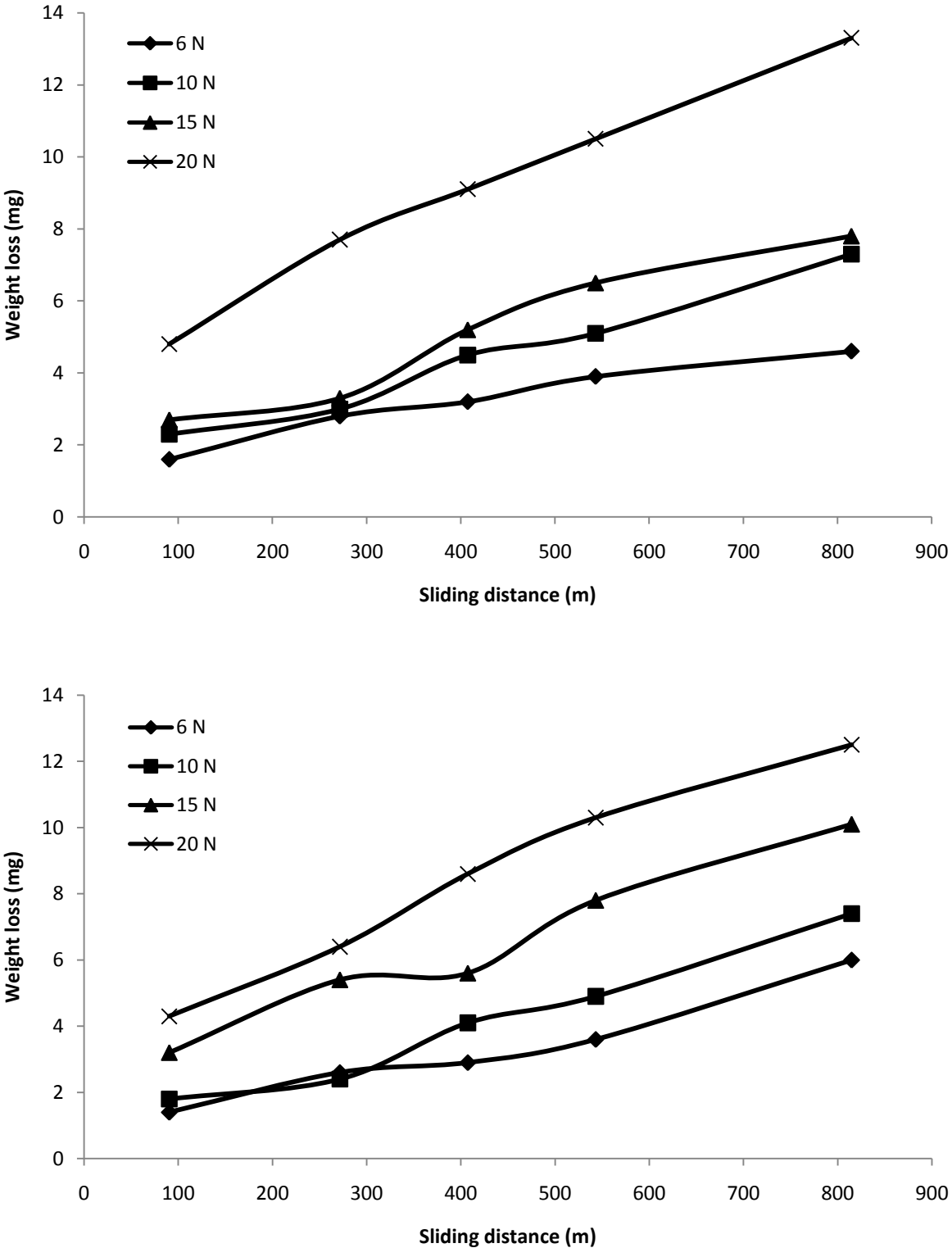

Figure A 7 Weight loss vs sliding distance at 15 Hz frequency for Al-6wt% Si specimens compacted at (a) 100 MPa, (b) 200 MPa

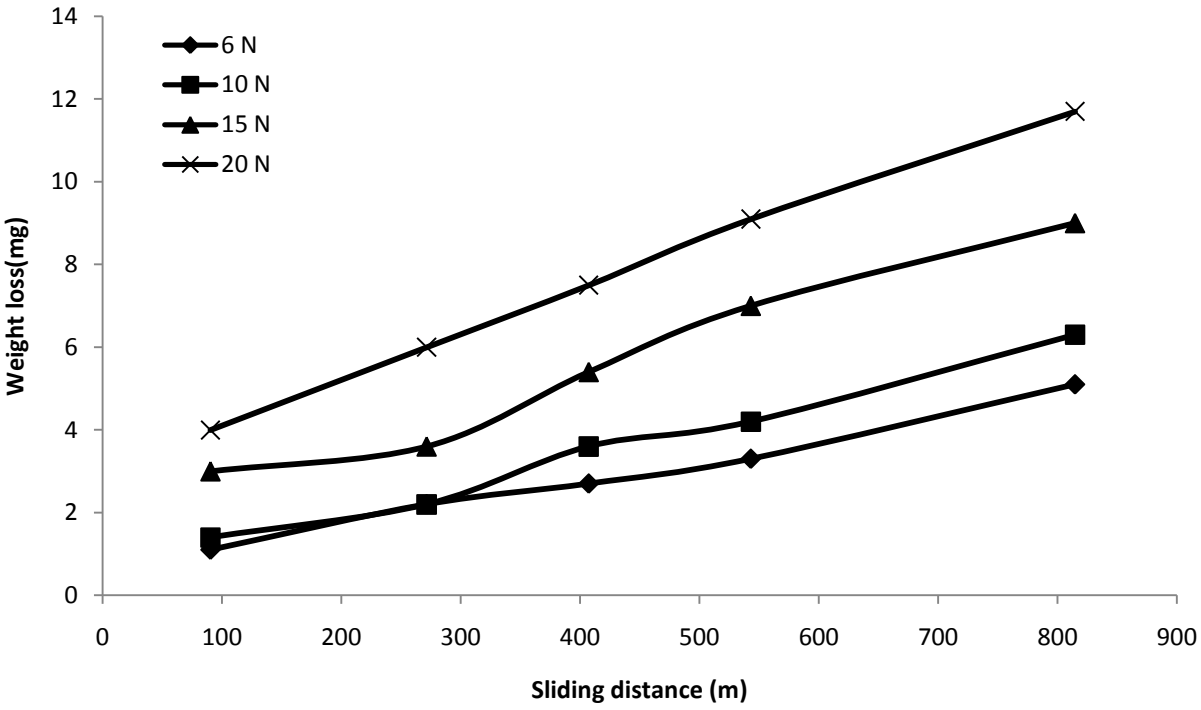

Figure A 7 Continued. Weight loss vs sliding distance at 15 Hz frequency for Al-6wt% Si specimens compacted at (c) 600 MPa

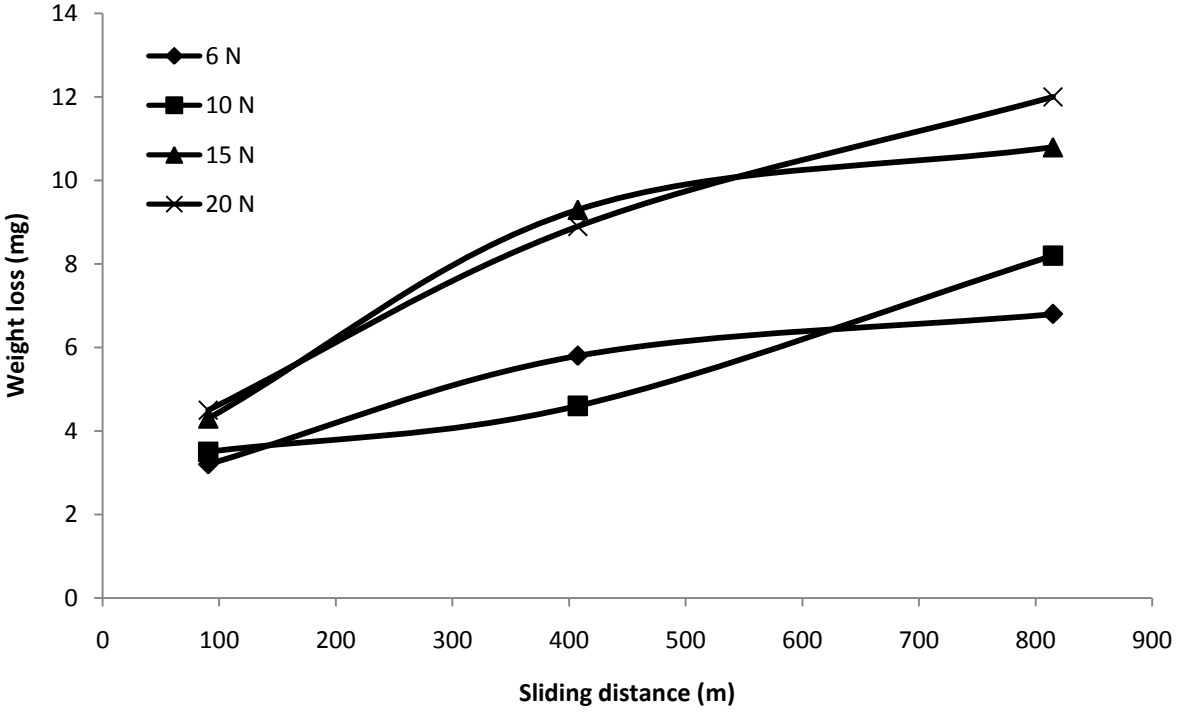

Figure A 8 Weight loss vs sliding distance at 15 Hz frequency for Al-6wt% Si specimens after HIP compacted at (a) 100 MPa

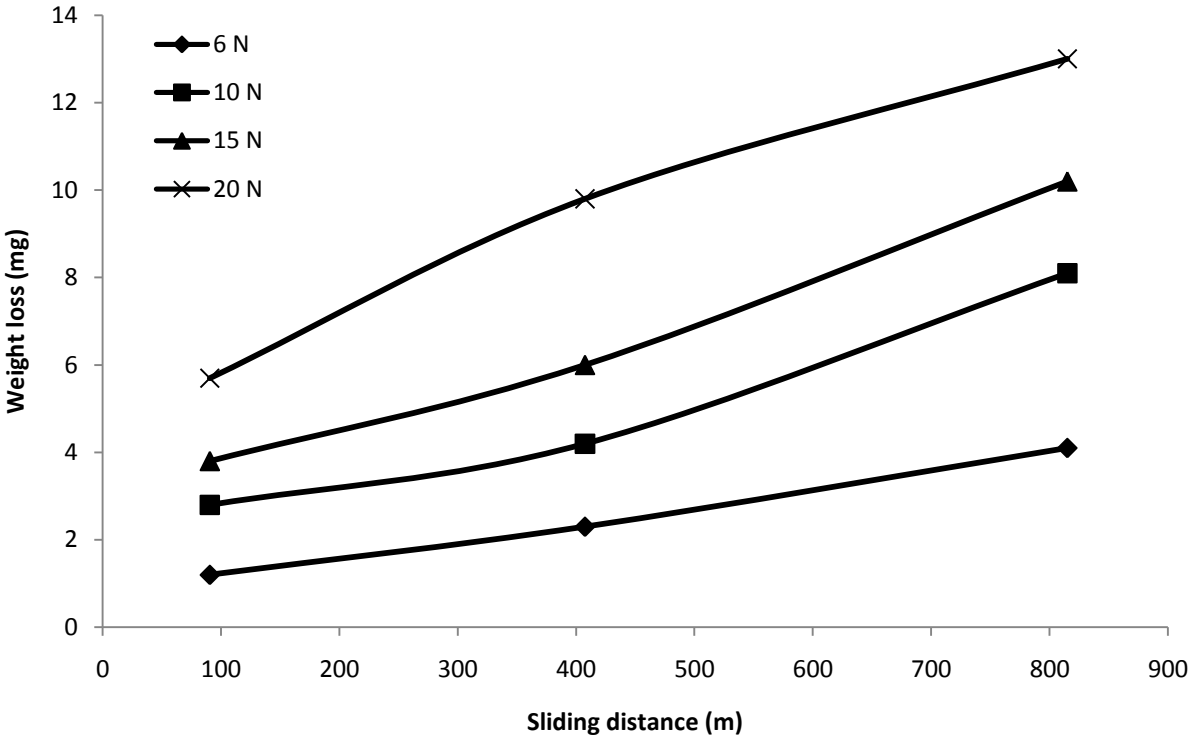

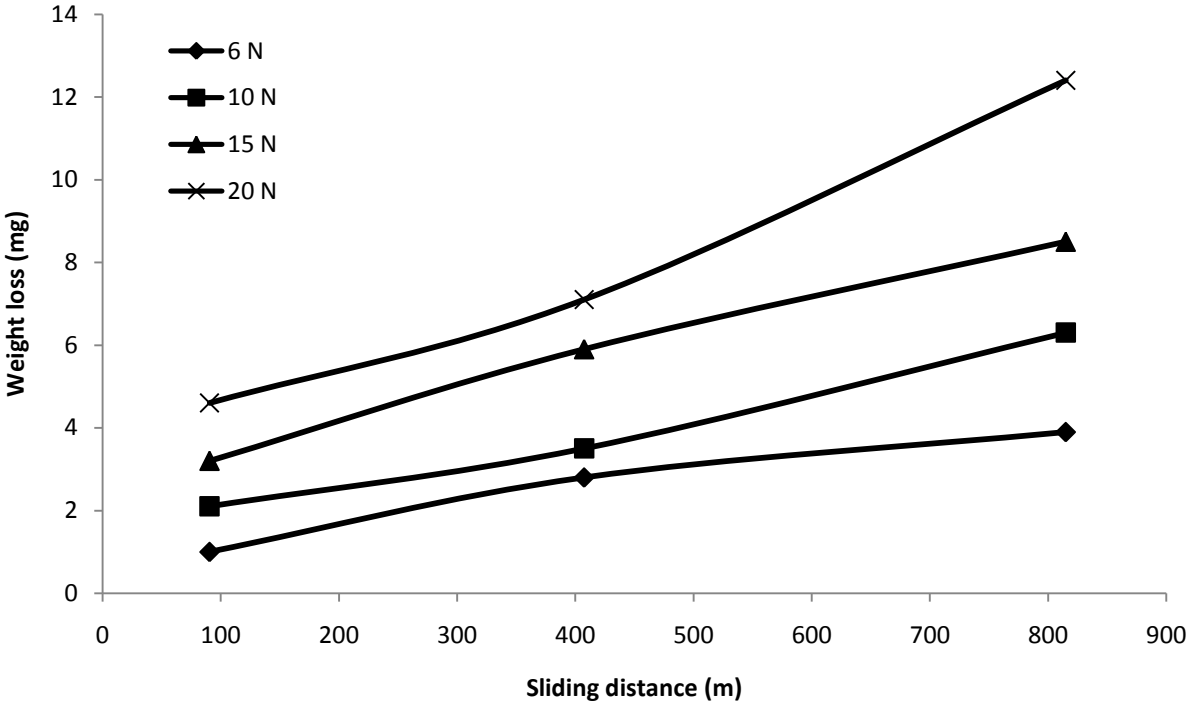

Figure A 8 Continued. Weight loss vs sliding distance at 15 Hz frequency for Al-6wt% Si specimens after HIP compacted at (b) 200 MPa, (c) 600 MPa